Structural Model and Fracture Analyses for a Major Gas Emplacement in Devonian Sandstones of the Subandes

by

Juan Francisco Pedro Iñigo

Thesis

Presented to the Faculty of the Graduate School of
The University of Texas at Austin
in Partial Fulfillment
of the Requirements
for the Degree of

Master of Science in Geological Sciences

The University of Texas at Austin
December 2009

Structural Model and Fracture Analyses for a Major Gas Emplacement in Devonian Sandstones of the Subandes

Approved by
Supervising Committee:

Stephen E. Laubach, Supervisor

Mark Cloos

Brian K. Horton

Dedication

To my wife Lara for her unconditional love and for joining me in this adventure

Acknowledgements

I want to thank Dr. Stephen Laubach and Dr. Randall Marrett for their support and help in the past two years. Their teachings, corrections and comments helped me enormously to improve this thesis. Also I want to specially thank John Hooker “The Dude” for his friendship and all his help with multiple tasks of my thesis both in the field and in the lab; as well as for multiple discussions, which enrich my understanding of fractured reservoirs. I also want to thank the members of my committee Dr. Brian Horton and Dr. Mark Cloos for their valuable comments and corrections.

In addition, I want to thank a number of institutions which made possible this thesis either by giving me economic support or by releasing data for analyses: Jackson School of Geosciences, FRAC Consortium, Pan American Energy, Repsol-YPF, GDL Foundation and the Fulbright Commission. Some aspects of this work were supported by the Chemical Sciences, Geosciences and Biosciences Division, Office of Basic Energy Sciences, Office of Science, U.S. Department of Energy Grant No.DE-FG02-03ER15430, and by industrial associates of the Fracture Research and Application Consortium.

Finally, I want to thank the people who collaborated in some way or another in this thesis: Massimo Bonora for helping me with the 3D kinematic structural model; Aysen Ozkan for helping me with petrographic description; Dr. Mike Murphy and the University of Houston for allowing me to use their Move software license; Bob Ratliff

for providing a free license of Lithotec software; Jose Luis Silvestro and Asterio Ayaviri from Repsol-YPF for providing information for analyses; Marcos Cohen, Maria Emilia Gayol and Gabriela Bernatek of Pan American Energy for providing data; Dr. Jon Holder for his help with subritical crack index tests; and all of my new friends from around the world who gave me many durable memories from this two years in Austin.

December 2009

Abstract

Structural Model and Fracture Analyses for a Major Gas Emplacement in Devonian Sandstones of the Subandes

Juan Francisco Pedro Iñigo, MSGeoSci
The University of Texas at Austin, 2009

Supervisor: Stephen E. Laubach

The fold and thrust belt of the Subandean Ranges (central and southern Bolivia, and northern Argentina) contains both gas and condensate production and reserves in Devonian quartzose sandstones within deep structures. Reservoir sandstones present values of permeability close to 0.01 mD, implying that reservoir drainage must be controlled by a fracture system that enhances permeability. Hydrocarbon production in naturally fractured reservoirs is affected by fracture quality (degree of openness), spatial arrangement, size distribution (including aperture, height and length), fracture abundance, and arrangement with respect to stratigraphic and macro-structural features. Systematic study of fractures in the subsurface is complicated by the small probability that a well will intersect sufficient fractures for direct analysis of their attributes. Because of this fracture data obtained from logging and coring must be complemented with alternative methodologies. In my study I performed a workflow that includes geologic mapping of outcrop analogs of subsurface units, fracture characterization in outcrops and thin sections, the construction of kinematic structural model using algorithms for 3D analysis, petrographic description of composition and diagenesis, and statistical multivariate analyses in order to define how structural, lithologic and diagenetic features affect fracture distribution.

From the construction of a structural model and the analyses of its properties, I generated semi-quantitative models of fracture attributes based on classic fold-related fracture concepts. This model was tested with direct fracture observations from core and outcrop, coupled with microstructural imaging using SEM-CL, to document fracture attributes. The models all show high curvature and strain values homogeneously distributed along the azimuth and close to the hinge of the anticline, which implies this domain should be most fractured. On the other hand, microfracture studies reveal that although highest strain values are found in the hinge, low strains also are found along the hinge even for samples with similar lithologies.

The study of macro and microfractures in outcrop and core samples allowed me to clearly identify two opening mode fracture sets for the Devonian sandstones. These present an orthogonal arrangement and variable cross cutting relations. The dominant set (defined as Set I) has a WNW strike and is perpendicular to the structural trend of the Subandean Ranges; the subordinate set (defines as Set II) has a NNE strike, and is parallel to the previously mentioned structural trend. Set I has higher strain accumulation, log-normal spacing distribution, and is strongly controlled by the primary quartz content of the rocks. Set II also has a log-normal spacing distribution, and presents structural control.

Table of Contents

List of Tables

List of Figures

CHAPTER 1: INTRODUCTION

Fold and thrust belt (FTB) zones constitute one of the most challenging geological environments for hydrocarbon exploration and production owing to structural complexity. Nevertheless, the fact that they contain 14% of the known global recoverable hydrocarbons and 28% of the world's giant gas fields found so far (Cooper, 2007), makes them a desirable target. The potential size of the exploration and development discoveries implies that risks associated both with exploration and reserves development of hydrocarbons should be taken. The Subandean Ranges, located in Central and South Bolivia and North Argentina, is a fold thrust belt having considerable production potential. At least three hydrocarbon plays are known in the structures that form these ranges. These are known as the Devonian, Carboniferous and Tertiary plays. Notably, most of the gas and condensate production and reserves of NW Argentina and Bolivia are related to the Devonian play. The reservoirs in this play are quartzose sandstones located in the deep structures of the Subandean Ranges (Kozlowski et al., 2005). Proven gas reserves in the Argentinean portion of the basin are as much as 52,615 MMm^3 (millions of cubic meters), while probable and possible are 8,253 and 9,979 MMm^3 respectively. The daily production in Argentina is as much as 16,019 Mm^3/d (thousand of cubic meters per day). This play represents 12% of the Argentinean gas production (IAPG). A central issue for the successful exploration and development of these reservoirs is understanding the role of natural fractures.

1.1 Statement of the Problem and Motivation

The fact that the reservoir sandstones in the Argentinean NW and Bolivian Devonian basin have values of permeability for intact rock close to 0.01 mD, yet production rates indicate that reservoir drainage must be controlled by a fracture system that enhances permeability (Kozlowski et al., 2005). Numerous studies and models applied in this basin that led to wells being drilled have diverse results. Some of these wells have, no doubt, contacted natural fracture systems, given their high production rates. However, in a basin where drilling one well can cost as much as 60 million dollars, is imperative to achieve an improved characterization and understanding of the fracture system that controls the reservoir quality so that fractured regions can be better targeted. It is not the aim of my thesis to solve all of the geological uncertainties associated to gas production in the Bolivian and Argentinean Devonian basin, but rather to employ diverse methodologies that would allow achieving a better understanding of the fracture system developed in these sandstones.

1.2 The Sampling Problem

It is always best to study fractures in the subsurface, because rocks at the surface have undergone a different loading and diagenetic history. Consequently, fractures in outcrop can differ markedly from those in the subsurface (Laubach et al., 2009). However, sampling fractures in the subsurface is limited, especially for near vertical wells with steeply dipping fractures. This can be understood via considering the probability of a steeply inclined well intersecting a steeply inclined fracture, which is given by $P_i = D/S_i$, where D is the diameter of the well and S_i the fracture spacing for a particular layer (Narr, 1991). Because D is commonly small relative to S_i, large numbers of boreholes are needed to define fracture arrays using only logging and coring data (Figure 1.1). Based on the hypothesis that fracture attributes such as kinematic aperture and spacing follow quantitative patterns across broad ranges of scale, one way to overcome the scarcity of subsurface information about fractures is to elucidate quantitative relationships among fractures of different scales. Then, scaling relationships determined at one scale range are the basis for fracture predictions at other scales (Laubach, 1997; Marrett et al., 1999).

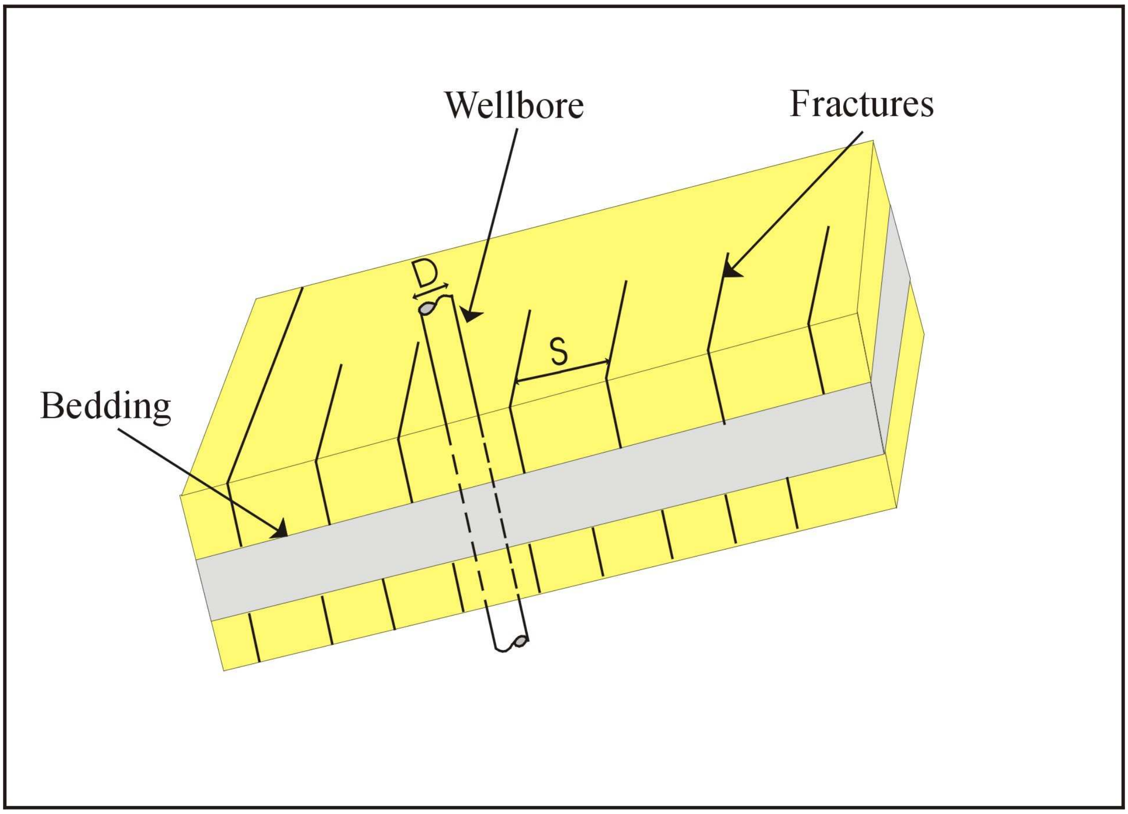

Figure 1.1: Fracture distribution in reservoir and relation between spacing and well diameter (modified from Narr, 1991).

1.3 Objectives

Fracture-related hydrocarbon production is affected by fracture orientation, fracture quality (degree of openness), spatial arrangement, size distribution (including aperture, height and length), fracture abundance, and arrangement with respect to stratigraphic and macro-structural features. The objective of my thesis is to analyze all of these features and define the structural, stratigraphic and diagenetic parameters that control them. To accomplish this I performed a workflow that includes geologic mapping of outcrop analogs of subsurface units, fracture characterization in outcrops and thin sections, the construction of kinematic structural models using algorithms for 3D analysis, petrographic description of composition and diagenesis, rock property testing in the laboratory, statistical multivariate analyses comparing field-scale structure to fractures and rock properties, and some simple modeling of fracture-related fluid flow. The ultimate objective is to better predict and understand the attributes of fractures array and quality, and hopefully reduce geologic risk in further basin development. To conduct each of these analyses I used a variety of geologic software. Table 1.1 enumerates all of the software employed and presents a web address where more information can be retrieved.

Software	**Used for**	**Web Address**
Litho Tect™	2D Structural construction and restoration	*www.geologicsystems.com*
3D Move®	3D structural model construction and restoration. Curvature and strain analyses	*www.mve.com*
Stereowin	Macrofracture and microfracture orientation analyses	*www.geo.cornell.edu/geology/faculty/RWA/programs.html*
FaultKinWin	Fault kinematic and orientation analyses	*www.geo.cornell.edu/geology/faculty/RWA/programs.html*
Scandium®	SEM-CL image acquisition	*www.soft-imaging-web.de/en/us/eng*
Photoshop®	Image mosaic assemblage	www.adobe.com
Didger3®	Microfracture interpretation	*www.goldensoftware.com*
GoMezure™	Microfracture distribution and orientation analyses	www.beg.utexas.edu/indassoc/fraccity/public
Correlation Count	Microfracture distribution analyses	ftp://ftp.geo.utexas.edu/outgoing/Marrett/CorrCount/

Table 1.1: Software employed in my thesis and web addresses to retrieve more information.

1.4 Thesis Organization

Chapters 2, 3 and 4 of my thesis constitute a theoretical introduction both to the zone of my study and to fracture and structural modeling concepts from a bibliographic review. Chapter 5 is a description of the methodologies employed, which are further developed in each of the subsequent chapters. Chapters 6 through 12 constitute the bulk of the analyses I performed. Chapter 6 is a description of the structures I analyzed both for outcrop and in the subsurface using core. The workflow employed in the structural model and fracture analyses related to this methodology are presented in Chapter 7. Chapters 8 and 9 constitute a characterization of macro and microfractures respectively, where orientation, size and spacing distributions are defined. I present a petrographic characterization of the studied rocks in Chapter 10. Rock mechanics studies are presented in Chapter 11. Chapter 12 is a description of aggregate fracture properties such as porosity and permeability, and how these are affected by cement precipitation within the fractures. Finally Chapter 13 and 14 are the discussion and conclusions of my work respectively.

Three appendices contain supplementary data. Appendix A is a stratigraphic description of the rocks present in the Devonian basin. Appendix B and C constitute the raw data for fracture population and point counting for petrographic description respectively.

CHAPTER 2: GEOLOGIC BACKGROUND

2.1 Sedimentary Basin History

The Devonian basin analyzed in this study extends for hundreds of kilometers in Bolivia, but only its southernmost portion goes into Argentina. Some authors like Millani (1997) have related the distal deposits of this basin to the huge Parana basin, located in eastern Argentina and Brazil. The Devonian basin strictly speaking comprises the deposits of the Icla, Santa Rosa, Huamampampa and Los Monos formations (a detailed characterization of these, as well as a stratigraphic column can be found in Appendix A). The term Northwest basin is frequently used in Argentina to define these deposits. However, this term is used to characterize a geographic feature and does not address the differences between the different basins in the region, which have deposits that range in age from Upper Devonian to Late Miocene. Based on their genesis, subsidence mechanism, and facies arrangements three different basins can be characterized in the studied zone. In order to better understand the overall geologic history that affected the Devonian deposits, it is best to first define the three sedimentary cycles that were present in this region.

2.1.1 SILURIAN-DEVONIAN CYCLE

The Ocloyic deformation phase, associated with the Famatinian cycle that took place during the Asghillian along the margin of South America, is interpreted as the origin of the Silurian-Devonian sedimentation cycle (Ramos, 1986). This tectonic event produced an elongated intracontinental basin with sediments discordantly deposited on top of Cambrian-Ordovician strata (Starck, 1999a). The presence of a strong asymmetry in sediment distribution, and the predominant sediment transport from the west margin (Figure 2.1), is the principal evidence cited to characterize this basin as a retroarc foreland basin associated with the deformation of Ordovician deposits and the uplift of the Protopuna (Ramos, 1986; Palma and Irigoyen, 1987; Stark, 1999a). Other authors, such as Fernandez Seveso et al. (1998) present an alternative interpretation for the basin and suggest a regional sag marine basin controlled by thermal cooling, and associated with a previous rift stage restricted to the Ordovician and Early Silurian.

The sedimentary fill of this cycle totals about 3,500 m (11,480 ft) of interbedded quartzose sandstone and pelitic units that comprise a shallow marine platform (Starck et al., 2002a). According to Starck (1999b), the end of this basin is given by the diastrophic Chanic phase, which has shortening characteristics that separate the Silurian-Devonian cycle from the Gondwanian cycle. The origin of this deformational phase is though to be related to the accretion of microterranes to the margin of Gondwana. The large distance between the basin and the margin could explain the absence of evidence of collisional tectonism. A pre-Carboniferous unconformity was produced associated with this orogenic phase. As a consequence of this, Silurian-Devonian sediments were gently tilted. The amount of erosion associated with this unconformity is extremely variable since in the eastern part of the Subandean Ranges, Carboniferous deposits of the Tupambi Formation are located above thick deposits of the Devonian Los Monos Formation, which corresponds to the Aguaragüe Supersequence. On the other hand, to the west in the Caspala region of the Cordillera Oriental geologic province, Carboniferous sediments are above the Ordovician Cinco Picachos Supersequence. The degree of erosion between these two positions is intermediate, with a clear increment towards the SW (Stark et al., 1992). The effect of the Chanic diastrophic phase in addition to eustatic sea level fall during the early Carboniferous produced a non-depositional and erosive hiatus of approximately 50 Ma (Starck, 1999a). The Chanic diastrophic phase is recorded as an abrupt change from marine Silurian-Devonian deposits to purely continental Carboniferous-Permian sediments (Starck, 1999a).

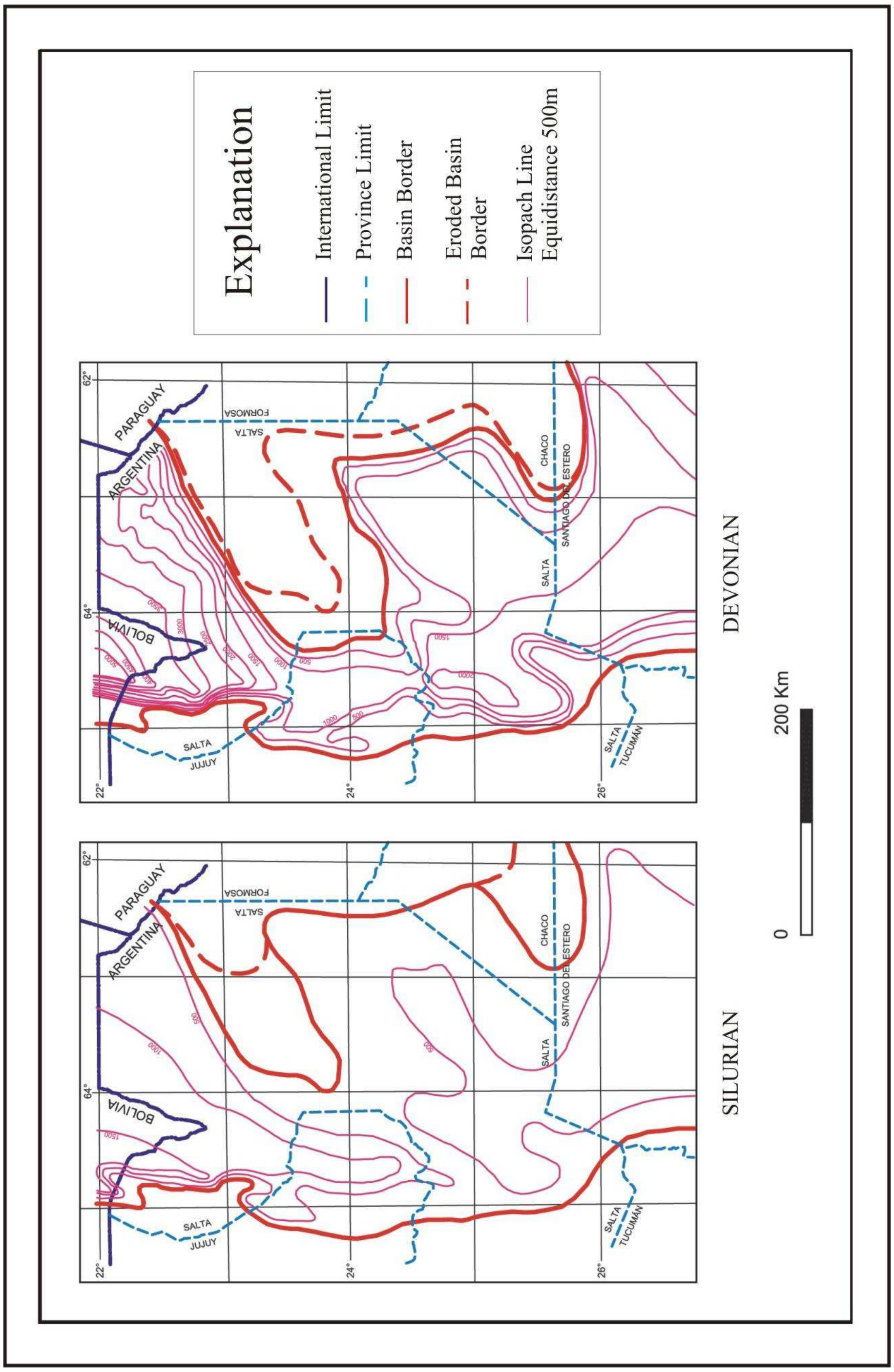

Figure 2.1: Isopach map showing asymmetry and predominant sedimentation from the west for the Devonian basin (modified from Di Marco, 2004).

2.1.2 CARBONIFEROUS-PERMIAN CYCLE

A second stage in the evolution of the NW region, is given by the Tarija Carboniferous-Permian intracratonic basin, associated with thermal phenomena (Figure 2.2). This basin has markedly less subsidence than the Devonian basin, with maximum rates around 0.016 mm/yr (Ramos, 1999). Maximum total subsidence is located close to the international limit between Argentina and Bolivia (Stark, 1999a).

The sedimentary deposits that fill this basin have a thickness close to 2,500 m (8,200 ft) and are mostly continental (Starck et al., 2002b). The oldest units in this cycle had a strong glacial influence during deposition, while the younger units were deposited in warmer conditions corresponding to an arid environment (Starck, 1999a). The culmination of this sedimentary sequence is marked by the deposits of the Vitiacua Formation, which corresponds to a Permian marine ingression (Ramos, 1999).

The closure of the Tarija basin is associated with the Araucana phase, which generated the partitioning of Gondwana and the Paleozoic-Eomesozoic basins, during the Late Jurassic. This phase also produced the end of the tectonic-sedimentary Gondwanian cycle. The sediments of the Tarija basin were affected by a strong erosive discordance, along a NNE strike. The top of the structural highs along the extensive Argentinean Cretaceous rift, were eroded forming unconformities which are more extensive to the south (Starck, 1999b). Those sediments that were not eroded are part of the Salta Group that constitutes basement of the Cretaceous extensive rift. This diastrophic and erosive event truncated the borders of the basin.

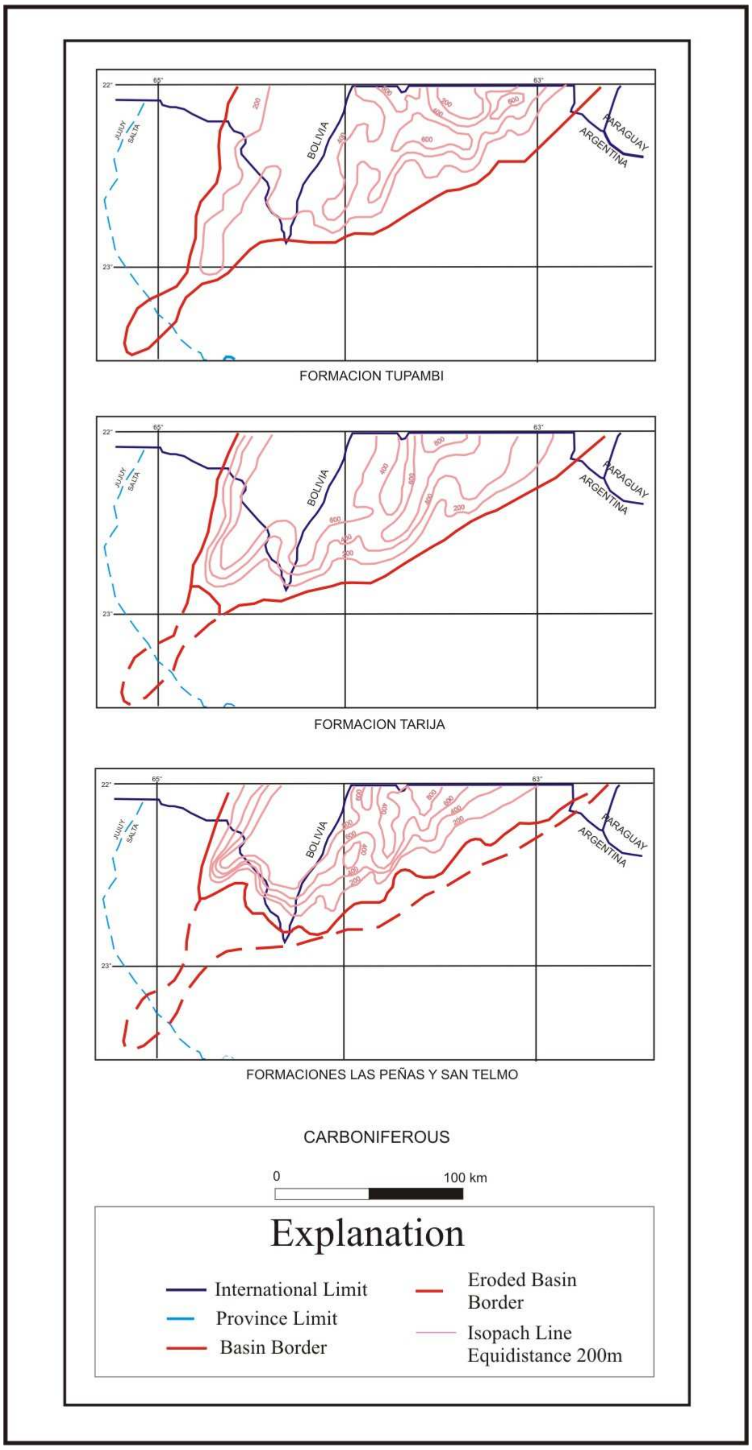

Figure 2.2: Isopach map for the Carboniferous-Permian Tarija basin (modified from Di Marco 2004).

2.1.3 TERTIARY CYCLE

A final stage in the geologic development of the Subandean region is recorded in the Tertiary deposits. These can reach up to 5,000 m (16,400 ft) of thickness, and are located on top of strata deposited in previous cycles, with a minor unconformity between them. These deposits are clastic rocks, which record synorogenic depositional patterns (Starck et al., 2002b).

The formation of the Subandean Ranges and the deposition of the Tertiary cycle are related to a shallowing of the Nazca plate, as it subducts beneath the South American plate during the Early Miocene. This phenomenon created the Neogene Subcycle that corresponds to the Andean Cycle of Groeber (1929). This shallowing process was associated with the migration of the Miocene volcanic arc towards the foreland and consequently the eastward movement of the associated orogenic front and foreland basin (Ramos, 1999b). The steepening of the Nazca plate appears to have generated an injection of magma causing acid volcanism, perhaps even a crustal delamination process. The consequent uplift of the brittle-ductile transition caused an important deformation event that affected the Puna, the Cordillera Oriental and the Subandean Ranges.

2.2 Tectonic Environment

2.2.1 EXTENT OF THE GEOLOGIC PROVINCE

The Subandean belt system is defined as the frontal zone of a Neogene foreland thin skin fold and thrust belt (Mingram and Russo 1972; Roeder, 1988). It is limited to the west by the Cordillera Oriental and to the east by the Chaco Plain where the foreland deposits were not affected by the Andean orogeny (Baby et al., 1992; Kozlowski et al., 2005). In the north-south direction the system extends hundreds of kilometers in Bolivia up to Peru and into Argentina up to the parallel 23°30’ (Baby et al., 1992; Moretti et al., 1996; Aramayo Flores, 1999; Echeverria et al., 2003) (Figure 2.3). However, my study focus is on the southern Subandean Ranges that extend up to the parallel 18° in Bolivia. The ranges reach their maximum development in the Bolivian zone, with a width of 150 km (Baby et al., 1992; Moretti et al., 1996). They narrow towards the south as they go into Argentina.

2.2.2 BRIEF CHARACTERIZATION OF THE ANTICLINES THAT FORM THE RANGES

The system is characterized by folds and thrusts that record eastward vergence (Ramos, 1999a). Fault bent folds, fold propagation folds and duplex systems are the most common structures of these ranges. Aramayo Flores (1999) suggests that it is the presence of quartzose sandstones intercalated with shales that defines the characteristics of the structures. Where quartzose rigid sandstones transmit the forces and generate the structure previously mentioned; while the plastic shales act as detachment levels.

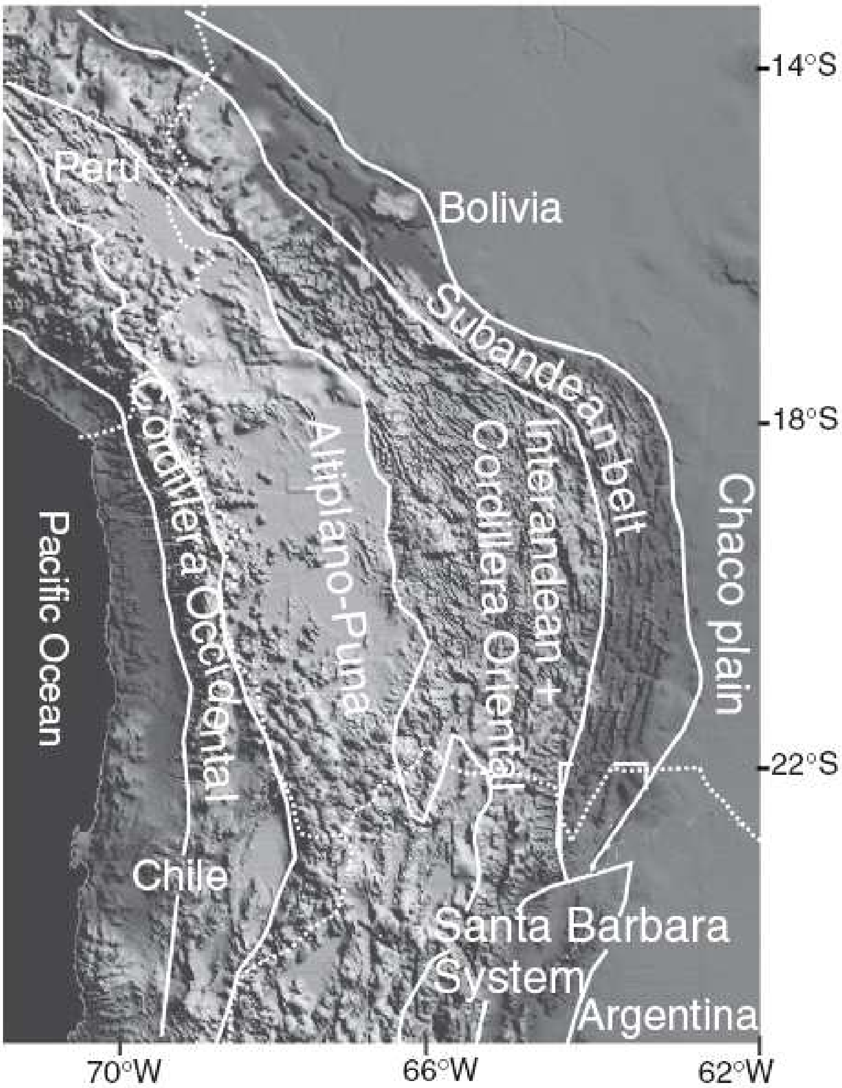

Figure 2.3: Satellite image showing the Suabandean Belt extent and bordering geologic provinces (modified from Echeverria et al., 2005).

We should mention that shales can also absorb deformation through ductile flow into the core of the anticlines.

Based on structural features, the Subandean ranges can be divided into western and eastern ranges (Figure 2.4). The limit between the two is located in the Sierra Baja de Oran in Argentina (Starck et al., 2002b) and close to the Mandiyuti thrust in Bolivia (Baby et al., 1992). The anticlines that form the western Subandean ranges are given by harmonic folds associated with fault bend folding or imbricate fan structures, like those in the region of the Pescado anticline and Sierra de Pintascayo in Argentina. To the east, the shale levels of the Los Monos Formation gain thickness, favoring the development of antiformal stacks and ductile shale flow (Aramayo Flores, 1999). This produces a displacement between deep structures given by fault propagation folds and duplex with passive roofs, which generate wide and concentric anticlines (Kley & Monaldi, 1999); and shallow, concentric and tight anticlines that outcrop as box structures (Hernandez et al, 2002 and Starck et al, 2002b). The anticlines that form the eastern Subandean Ranges are aligned in structural axes that have hundreds of kilometers of length. Individual structures are separated by structural saddles and can be substantially offset forming en echelon structures (Starck et al., 2002b).

The fracture analysis I did comprises both outcrop studies in the Abra del Condor anticline located in the western Subandean Ranges of Bolivia, and subsurface studies of gas fields located in the eastern Subandean Ranges. Therefore, I consider it necessary to define all of the genetics units that form these ranges, independently from the distribution

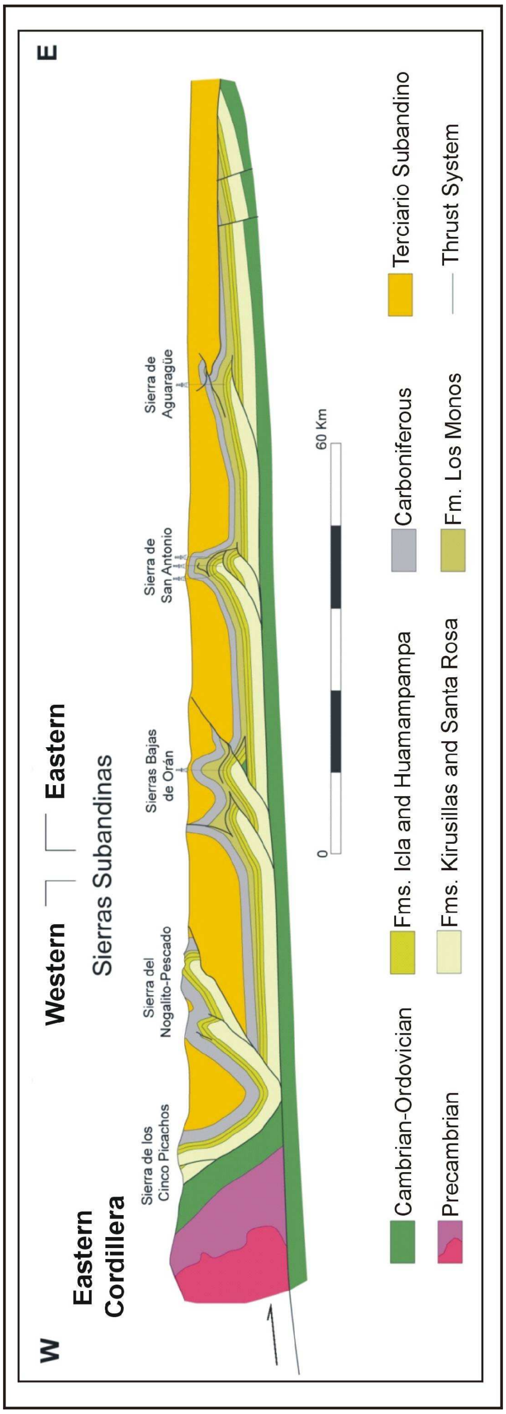

Figure 2.4: Cross section showing structural differences between Western and Eastern Subandean Ranges (modified from Starck et al., 2002b).

of each of them. Several authors define for the Subandean Ranges four structural levels, genetically related and separated by shale deposits which constitute detachment levels (Starck, 1999a; Starck *et al,* 2002b; Kley y Monaldi, 1999; Hernández, *et al.*, 2002) (Figure 2.5). Each of these levels is formed by formations of different ages and lithologies, which respond differently to deformation (Aramayo Flores, 1999). Below a characterization for each of these levels is presented.

2.2.2.1 Structural Basement

Structural basement comprises all the rocks younger than Silurian and not involved in the deformation (Starck et al., 2002b). It is formed in Bolivia by the Early Silurian Formation Cancañiri; Ordovician Formations Cieneguillas and Iscayachi; Cambrian Formations Sama/Torohuayco/Camacho; and Pre-Cambrian San Cristobal Formation (Moretti et al., 1996; Moretti et al., 2002; Dunn et al., 1995). In Argentina basement is the Zapla Silurian Formation; the Caspala, Acoyte and Santa Rosita Ordovician Formations and Chalhualmayoc, Campanario and Lizoite Cambrian Formations.

2.2.2.2 Basal Detachment

This basal detachment is located within the shales of the Silurian Kirusillas Formation and limits the Silurian-Neogene deformed sedimentary column. The detachment horizon has great continuity and efficiency, controlling the deformation of the Subandean Ranges from the south latitude parallel 23°30’ in Argentina to the latitude 18° in Bolivia; and even further to the north it has been correlated to the Silurian detachment of the El Carmen Formation, in the Boomerang Ranges zone of Bolivia (Sheffels 1988, in Welsinsk et al., 1995). The efficiency of detachment is probably related to high pore pressure, given as a consequence of the thick sedimentary column that overlies it (Starck et al., 2002b). Outcrop data, in the limit between Cordillera Oriental and the Subandean Ranges; seismic data in the eastern Subandean Ranges and the Chaco Plane; and data obtained from structural cross sections, allowed definition of a regional dip of 2° or 3° toward the NW for this surface. This dip is probably related to thrust-related loading and the asymmetry of Tertiary subsidence, which increases as we move to the hinterland. Starck et al. (2002b) also suggests that tilting of strata could be related to the aperture of the Argentinean Cretaceous rift.

This regional inclination explains why this level is located between 7,000 and 8,000 m below sea level (23,000 to 26,000 ft) in the Subandean Ranges region and between 12,000 and 13,000 m below sea level (39,000 to 43,000 ft) in the Cordillera Oriental province (Aramayo Flores, 1999).

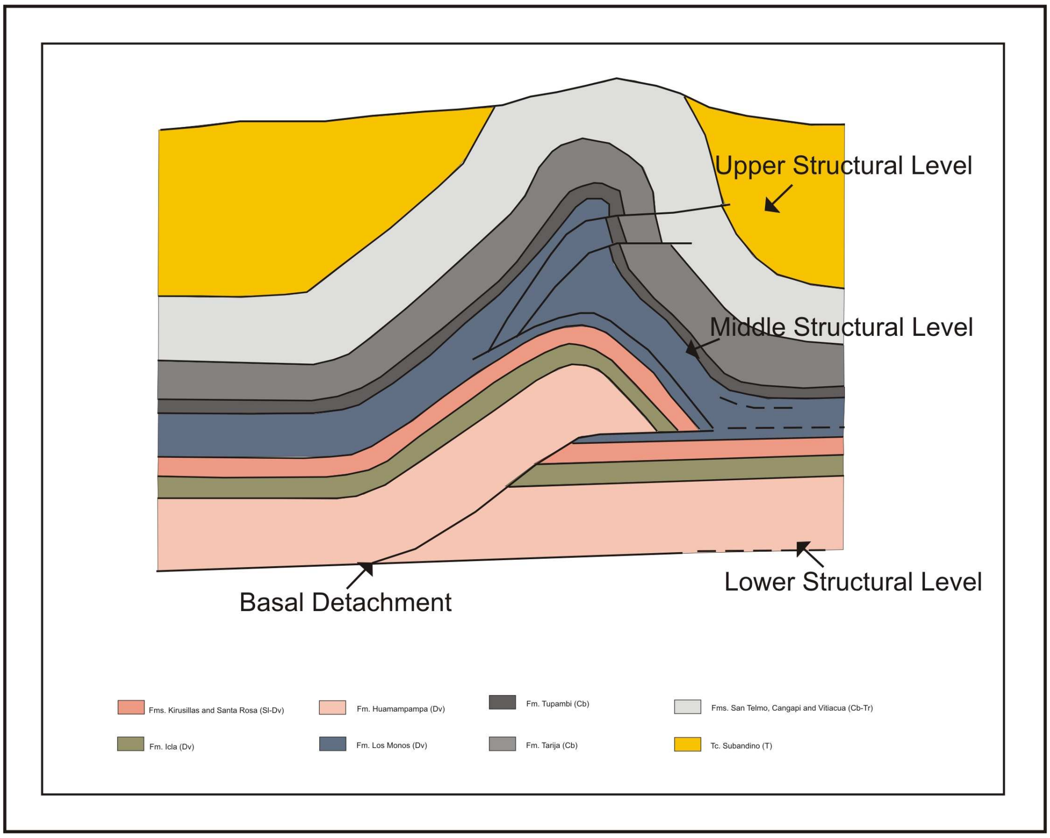

Figure 2.5: Schematic cross section showing the different structural levels that compose the Suabandean Ranges (modified from Starck et al., 2002b).

2.2.2.3 Lower Structural Level

The lower structural level constitutes the main focus of my thesis and therefore it is described in more detail than the others. Bounded by stratigraphic discontinuities, this level involves Silurian horizons that correspond to the uppermost part of the Kirusillas Formation and Devonian Santa Rosa, Icla and Huamampampa formations. In the Eastern Subandean Ranges, a thickness of ~2,500 m (8,200 ft) is bounded by the Silurian detachment level at the base and a detachment level located in the inferior third of the Los Monos Formation. The anticlines that form this structural level were generated by fault bend folding (Starck et al., 2002b). However, in some regions of the eastern Subandean ranges (like in Ramos, San Pedrito and Macueta anticlines) the structures have complex designs that differ from what expected in standard fault bend fold systems. Some authors like Stark (2002b) and Aramayo Flores (1999) propose that these structures are associated not only with fault bend folding processes but also with duplex stacking and plastic fluency or shear non parallel to the stratification in the core of the anticlines. These processes are superimposed and related to final phases of the structural evolution when the lower structural level became locked against the superior detachment level. As a result tight anticlines that present steep limbs are formed. Structures further to the east, near Aguaragüe and Campo Durán/Madrejones, are simpler fault bend folds with a flat-ramp-flat geometry. In this zone, anticlines have gently dipping back limbs and moderately dipping forelimbs.

The closure of these anticlines in a N-S sense is determined by the plunge of the axes which parallel the geometry of the ramp of the system (Starck et al., 2002b). The location of the structural saddles and the depth of the structural closures is extremely important in the overall oil system since this defines the spilling point of the hydrocarbon accumulation in the Devonian play.

2.2.2.4 Middle Structural Level

As well as the upper structural level, this unit is restricted to the eastern Suabandean Ranges, and was not analyzed in this thesis. However, a brief description is presented to better understand the Subandean system.

This genetic unit is enclosed within the Los Monos Devonian shales that have a thickness between 500 and 700 m (1,640 to 2,300 ft). It extends from a basal detachment level located 200 to 250 m (740 ft) above the base of this formation, and an upper detachment level located 200 m (650 ft) below the top of the formation (Aramayo Flores, 1999). Both detachment levels control the structural development of this unit, and are related to overpressure in the shales of the Los Monos Formation, associated with the quick deposition of the Terciario Subandino sediments, tectonic compaction and the generation of oil and its later cracking to gas (Vaamonde, 2002).

Several authors (Moretti et al, 1996; Aramayo Flores, 1999; Hernández et al., 2002; Starck, 1999a and Starck et al., 2002b) propose that this unit controls the geometry of the structure in the Subandean Ranges, and favors the development of a disharmony between the deep and shallow structures in the eastern region. The basal detachment is an underthrust, which produces a displacement to the west of the sedimentary column; favoring a mechanical insertion of the lower structural level as a structural wedge. The displacement of the sedimentary column to the west stops when it finds a blind point, where a thrust is generated cutting upwards and to the east, and defining the detachment of the upper structural level (Starck et al., 2002b). As a consequence of the deformation, the shales of the Los Monos Formation are affected by processes of tectonic thickening, such as sheet stacking and ductile shale flow. It is because of this that the thickness of this formation is locally duplicated or triplicated in the eastern Subandean ranges (Aramayo Flores, 1999).

2.2.2.5 Upper Structural Level

The upper structural level is characterized by the presence of concentric, tight and very asymmetric anticlines, associated to the ductile accommodation of the sediments in the intermediate structural level. The degree of asymmetry is controlled by the prime deformation process (Starck et al., 2002b). Symmetric anticlines are produced where deformation is controlled by eastward thrusts. Asymmetric and tight anticlines are produced where vertical growth processes prevail. The detachment level of this unit are the overpressured shales of the Los Monos Formation. The complexity of the structures in this unit is explained as a consequence of an initial thrusting process followed by a folding process, in which even the detachment level became folded.

2.2.3 TIMING AND KINEMATICS INVOLVED IN THE DEFORMATION

Synororgenic sedimentation in the Subandes started with the formation of the Cordillera Oriental 27 Ma ago (Sempere, 1990). The basal deposits of the Tranquitas/Petaca Formation record the beginning of the Tertiary sedimentary cycle around 16.4 Ma. Jordan and Alonso (1987) state that the end of the deformation of the Cordillera Oriental took place at 10 Ma, and deformation propagated from this point to the Subandean Ranges. However, the main deformation of the Subandean Ranges and consequently the deposition of synorogenic sediments began at 8 Ma in the western region of the ranges, reaching the Aguraragüe zone in Argentina approximately 2 Ma ago. This indicates a shortening velocity of 10 mm/yr (Starck et al., 2002b).

Most of the deformation of the Aguaragüe range where the orogenic front is currently located probably took place between 3 Ma and 1.2 Ma (Echeverria et al., 2005; Hernandez et al., 2002). However, neotectonics structures including out of sequence thrusts, suggests that deformation in the area is still active. Starck et al. (2002b) report the presence of recent alluvial deposits that are tilted on the margin of the Tarija River. These neotectonic structures in the western region of the Subandean ranges are deforming jointly with structures near the eastern front of deformation.

Currently the Subandean ranges record a shortening velocity of 8 mm/yr (Hernandez et al., 2002). The active deformation front is located in Argentina east of Campo Duran. The buried thrust front is defined by a belt of seismic epicenters (Suayter in Ramos, 1999a). The foreland basin associated with the current fold and thrust belt, is located to the east. Cenozoic sediments reach a maximum thickness of 4,000 m at the foot of the Aguaragüe range.

CHAPTER 3: THEORETICAL BACKGROUND ON FRACTURES

3.1 Fracture Definitions and Classifications

Fractures can be defined as discontinuity surfaces, where rocks or minerals have lost cohesion. They are formed by two planar surfaces (fracture walls) that meet at a common front. Generally the relative displacement of originally adjacent points on fracture walls is small compared to their length (Pollard & Aydin, 1988). According to the type of motion that the fracture walls experienced during fracture formation, three different fracture modes are defined. Mode I or opening mode fractures are characterized by movement perpendicular to the walls of the fractures (Figure 3.1a); Mode II and Mode III constitute shear fractures, where the displacement is parallel to the fracture surfaces. Mode II fractures present sliding perpendicular to the edge or front of the fracture (Figure 3.1b); while Mode III have sliding parallel to the fracture front (Figure 3.1c). Under this classification Mode II and III fractures should be considered faults.

Another distinction among fractures can be made according to the presence or absence of cement. The term joint is used to define fractures that exhibit small displacement perpendicular to their surfaces, no or very little displacement parallel to their surfaces and no cement filling them. Veins on the other hand include extension fractures characterized by the presence of minerals deposits (rarely veins can also form by replacement processes so some veins may not be fractures at all). In fractures such deposits can range from inconspicuous, small and/or isolated crystals lining open fractures, to massive cements that completely fill them (Laubach, 2003). As truly barren fracture walls are rare in fractures that grow in diagenetically reactive subsurface environments, the terms *vein* and *joint* are not helpful in many geologic fracture studies. The term *opening-mode fracture* has possibly misleading implications about fracture-cement content and, but best fits the structures studied here (Hooker et al., 2009). Therefore, I compare my results to the theory and previous studies of joints or opening-mode fractures. According to literature most joints are oriented perpendicular to the layering and are roughly rectangular in two dimensions (Pollard and Aydin, 1988; Narr and Suppe, 1991; Bai et al., 2000; Nelson, 2001). This seems to be the case for most fractures in my study.

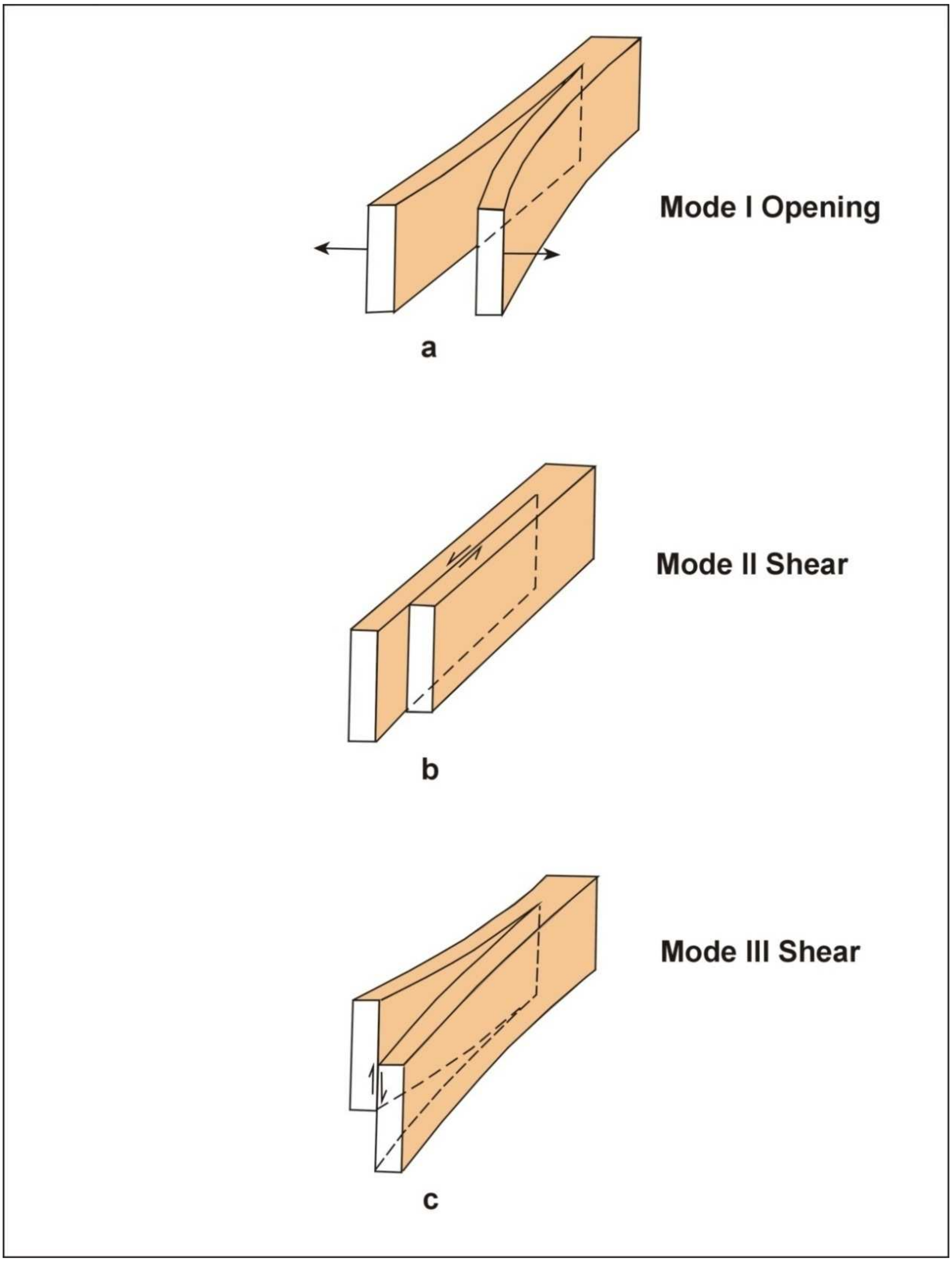

Figure 3.1: Fracture classification (Modified from Twiss and Moores 1992). a: Mode I (opening mode); b: Mode II; c: Mode III. Modes II and III are faults.

3.2 Origin of Joints (Opening-Mode Fractures)

The origin of joints is related to the presence of flaws or Griffith cracks in a rock, that reduce the strength of the material. Cracks propagate due to high concentrations of local tensile stress near the crack tips (Twiss and Moores, 1992). Different applied stress fields ranging from compressive to tensile and the original orientation of the flaws with respect to these stress fields, will define which cracks propagate and which mode of fracture will develop. Further propagation of joints is related to mechanical interaction, since the stress field associated to a joint can have an important effect on the growth of neighboring joints (Olson and Pollard, 1989) where the distance between them is small with respect to their dimensions (length or height). Where fractures grow toward one another, hooked patterns of interaction develop. The amount of hooking or straight overlap between fracture segments reflects the magnitude of far-field fracture parallel compression. Less hooking indicates greater fracture parallel compression (Olson and Pollard, 1991). Joints can terminate by dying out at discontinuities such as lithologic boundaries or faults, by curving and dying out at another joint or by segmenting into an echelon set of small extension fractures.

From the above explanation it seems clear that fracture type and orientation can porvide a large amount of information about the tectonic force field related to their origin. On the other hand, the inception and growth of opening-mode fractures can result from very small strains and it is not the case that large structures or tectonic events are needed to produce opening-mode fracture arrays that can considerably affect such important parameters as permeability (Philip et al., 2005; Olson et al., 2009). Fracture type and orientation, along with relative timing from crosscutting and abutting relations (Price, 1966; Hancock, 1985) is the basis for classifying fractures in different sets for further analysis, such as size distribution or spacing. However, we should also mention that kinematics alone are not enough to depict all fracture characteristics. Diagenesis also plays a major role in fracture origin, evolution and patterning. Evidence of this are the studies of Laubach (1988), Lander et al. (2002), Laubach et al. (2004), and Laubach and Ward (2006) among others. Therefore, other fracture attributes such as cross cutting relationships, cement presence and type, and fracture texture should be also taken into account to better define fracture sets.

3.3 Tectonic and Non Tectonic Fractures

Marrett and Laubach (2001), point out that fractures in folded sedimentary rocks are usually explained as the results of tectonic events (such as folding). Fractures are often inferred to be byproducts associated with the formation of large folds and faults (Stearns, 1968; Lisle, 1994; Fischer and Wilkerson, 2000; Keating and Fischer, 2008). However, owing to the negligible strains represented by most opening-mode fracture arrays alternative origins need to be considered. For example burial and uplift processes can also account for fracture arrays (i.e., Narr and Currie, 1982; Hancock, 1985). Examples of non tectonic fractures include those given by Laubach and Lorenz (1992) who report fractures forming as a consequence of burial processes, for example stretching linked to lengthening during subsidence. Engelder and Fisher (1996), discuss fractures forming by mechanisms such as regional stretching during uplift of sedimentary rocks in cratonal basins; and elastic contraction related to cooling of hot rocks. Pore fluid pressure effects can also drive fracture growth, including natural hydraulic fracture (Engelder and Lacazzette 1990; Olson et al., 2009).

3.3.1 FAULT RELATED FRACTURES

A *tectonic* origin for fractures, in petroleum industry usage, usually implies an origin related to faulting or folding (Nelson, 1985), despite the fact that plate scale stress fields are primarily of tectonic origin (Zoback and Zoback, 1980). In the following I use tectonic in this sense although in a broader usage the role of tectonics is rather more difficult to isolate. Before a tectonic (fold or fault related) origin is assumed for fractures, we should first determine how the fractures are related to larger structural features. In the case of faults, there are several fracture-fault attributes that we should expect to find. The first is that the structures be contemporaneous. This is typically a challenging criteria to demonstrate. Crosscutting relations can rule out contemporaneous faults and fractures, for example when joints cut across fault rocks. In some cases similar timing may evident if distinctive cement sequences or datable cements are present in fractures and faults (e.g., Laubach and Diaz-Tushman, 2009). Another criterion is kinematic compatibility, faults and fractures that share the same sense of movement (Hancock, 1985). For example in the case of faults it is common to find two small shear fractures one parallel and presenting the same sense of shear as the main fault and one set with opposite sense of shear at an angle of about 60°. These subsidiary fractures can be predicted by the

Coulomb fracture criterion (Stearns, 1968; Nelson, 2001). Opening mode fractures that present en echelon arrays can also be found in shear zones, developing perpendicular to the minimum compressive stress (Twiss and Moores, 1992).

3.3.2 FOLD RELATED FRACTURES

Although subject to much recent criticism (Marrett and Laubach 2001; Bergbauer and Pollard 2004), one of the most accepted models of fold related fractures is that one of Stearns (1968), who showed that fracture orientation and intensity are commonly symmetrically related to position along the fold. He characterized four fracture arrangements given by sets of conjugate shear fractures and extension fractures bisecting them (Figure 3.2). A more recent treatment of this type of behavior is in Hancock (1985). Deformational models which comprise changes in stress magnitude and orientation as the structure forms over time, account for fracture distributions in the Stearns' model. Twiss and Moores (1992) show how principal stress orientation, magnitudes and signs, change over time in parallel layer folding formed by compression. An elastic layer model can account for fracture Stearns' 3a and 3b fracture types (Figure 3.3). The distribution of strain in folds formed by orthogonal flexure mechanisms is shown in Figure 3.4. Stearns' type 1 and 2 fractures are usually explained through the strain distribution involved in flexural flow deformation processes, where slip is parallel to bedding planes (Figure 3.5). In order to account for the generation of three types of fractures, Hudleston et al. (1996) suggest that in multilayer folding flexural slip mechanisms (presented in chapter 4) bedding planes and less stiff layers distort by flexural flow and competent layers by orthogonal flexure. An alternative interpretation to account for the presence of the three types of fractures is that of Couples et al. (1998) who suggest a model where slip surfaces are activated in a hierarchical fashion favoring overprinting of strain. In their model Type 3 fractures are the result of mechanical units that are individually deformed by orthogonal flexure; while Type 1 and 2 would be related to active slip horizons along the margins of areally limited bedding parallel slip events. The movement of discrete rock blocks occurs in an inchworm-like fashion. Figure 3.6 constitute a summary of the different types of fracture we should expect in a fold according to the relative position in the overall structure.

However, these simple models have several important limitations. Bergbauer and Pollard (2004) argue that Stearns' model fails to address the presence of prefolding fractures. They suggest that these fractures in strata probably control the development of new fractures, which may lack consistency with the symmetric distribution presented by Stearns. In addition, they mention that in laboratory experiments only one fracture orientation develops in a sample; contradicting Stearns' model where all three fractures orientations can be formed in a single bed.

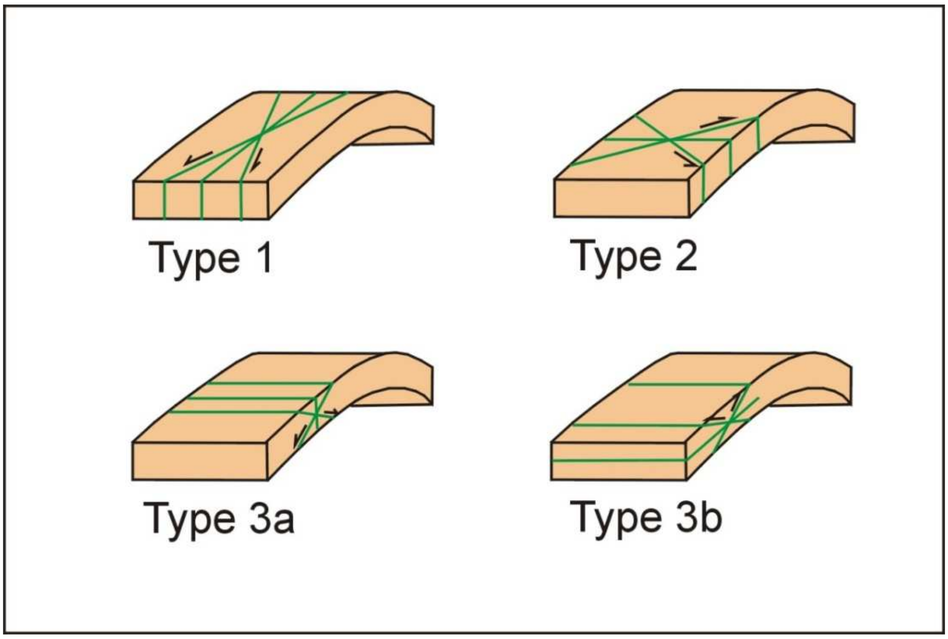

Figure 3.2: Stearns' fracture model, showing the different fractures arrangement that can be found in a fold (Modified from Stearns 1968).

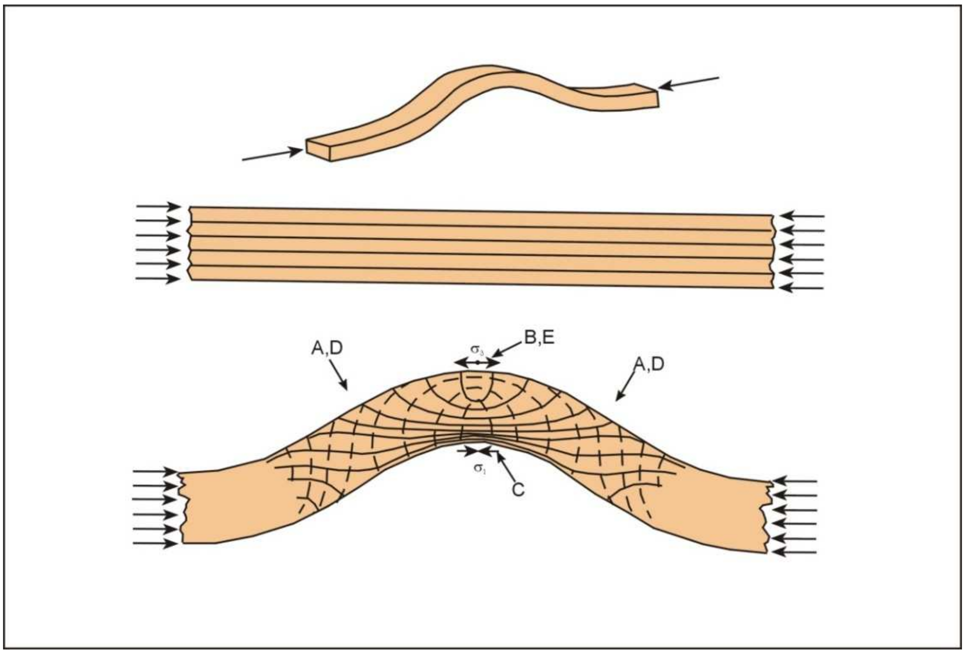

Figure 3.3: Changes in stress distribution through time during folding (Modified from Twiss and Moores (1992)

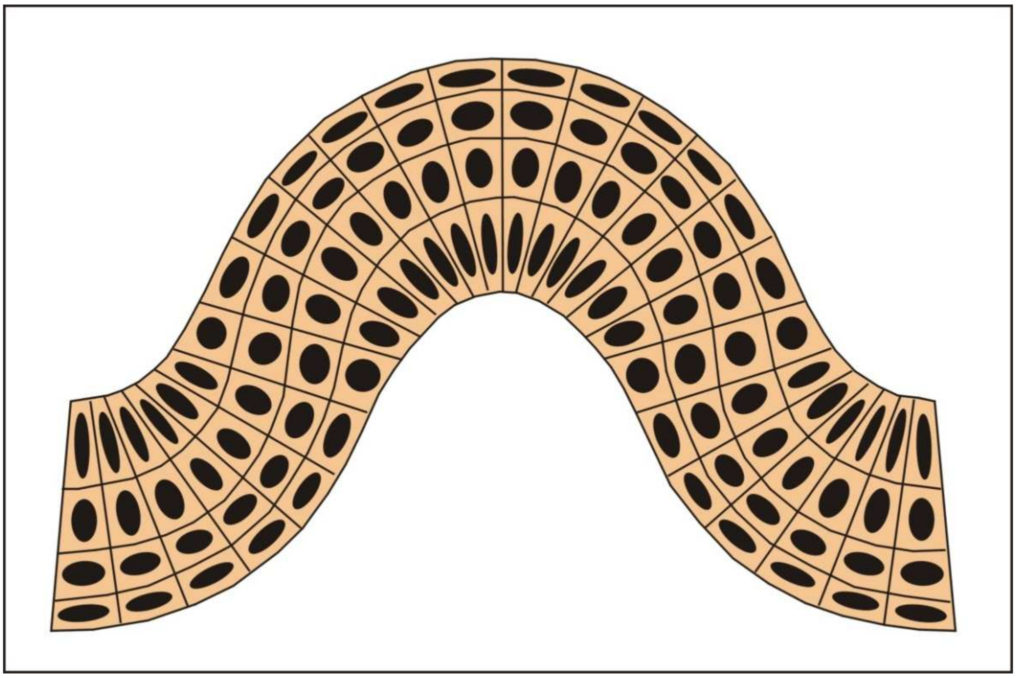

Figure 3.4: Tangential longitudinal strain distribution (Modified from Twiss and Moore, 1992).

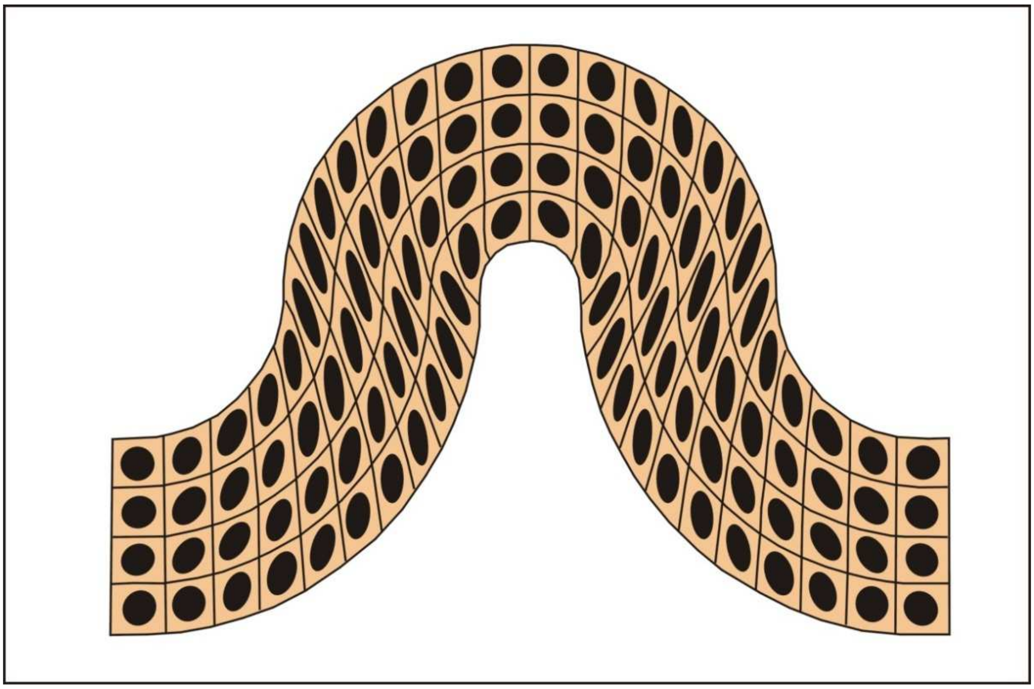

Figure 3.5: Flexural flow strain distribution (Modified from Twiss and Moore, 1992).

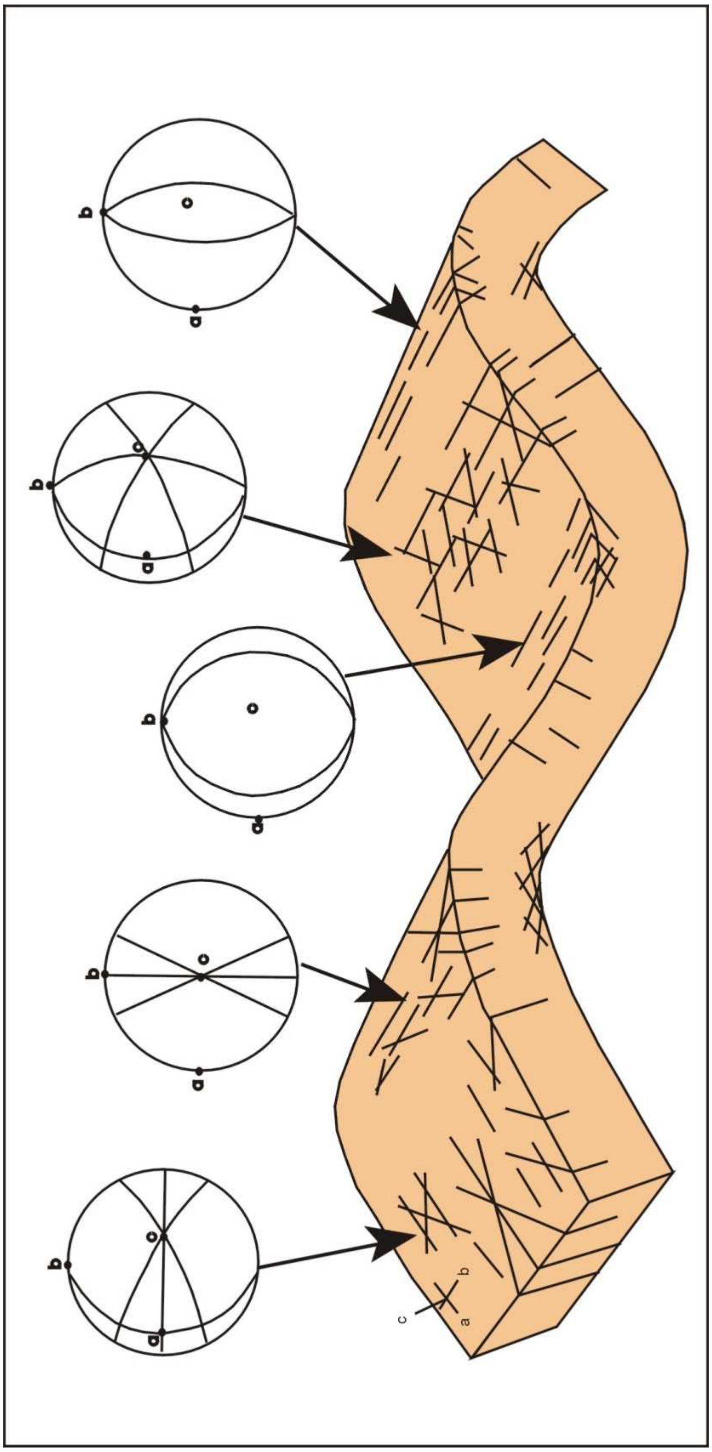

Figure 3.6: Distribution of fractures through a fold (Twiss & Moores, 1992).

CHAPTER 4: STRUCTURAL MODELS AND THEIR RELATION TO FRACTURE PREDICTION

One way to suplement sparse information in subsurface data sets and to improve our understanding of the overall fracture system is to work with semi-quantitative fold-fault models to predict fracture attributes based on the premise that fractures are related to the folding and or faulting process. These models include classic fold-fracture concepts presented in Chapter 3 as well as general models of fold and fault development that predict strains and fracture patterns. An essential step, described later, is to test the predictions derived from the models against field observation. Fold and fault models are widely used in the oil industry to make predictions of fracture patterns and distributions to enhance the development of subsurface hydrocarbon fields because direct characterization of a fracture population is limited or impossible. Twiss and Moores (1992) describe three geologic-structural models that can be used to characterize structural features and tectonic processes in the earth. Most of the methodological approaches and analyses used in this thesis, in order to better understand and predict fractures features and distribution, are subsumed within these models. Therefore, a theoretical background of the models and the fracture prediction related analyses performed using them, are presented in this chapter. Based on geometric, kinematic or mechanical approaches, each of these models assesses different features of the overall structural geology under study. As we move from the purely geometric models to the mechanical analyses, larger amounts of data are needed and more restrictions apply, presumably leading to better results (more accurate predictions). Analyses such as curvature, Gaussian curvature and strain distribution can be used to infer distribution of fractures through a fold, and to predict features such as intensity and orientation. Table 4.1 is a summary of the key attributes and limitations of these models. In addition, I present below a brief introduction to the models considered in this study, as well as references that provide a fuller account of each method.

Geologic Model	**Fracture Related Analyses**	**Required Data**	**Limitations**
Geometric	Simple Curvature/Gaussian Curvature	Outcrop maps-Wellbore information-Seismic observations	Structural evolution is not considered-Only synfolding fractures can be inferred
Kinematic	Strain	Idem above plus kinematic geometric rules	Do not consider mechanical properties of rocks
Mechanic	Kinematic-Mechanic analyses/Linear elastic fracture models	Idem geometric models plus rock properties and continuum mechanic laws	Large amount of data required

Table 4.1: Summary of geologic models; data requirements and limitations.

4.1 Structural Geometric Models

Geometric models constitute a first approach to making three-dimensional interpretations of the extent and orientation of folds and faults within the earth. These models are generally constructed from data that includes outcrop maps, seismic reflector observations, wellbore information, and other information including previously documented structural style observations (Twiss and Moores, 1992). Such models have been used to infer many attributes of fractures (Lisle, 1994; Stewart and Podolski, 1998; Bergbauer and Pollard, 2003). Nevertheless, one big disadvantage of these models is that they only apply to folds and faults in their final form, that is they are static models. Thus these models allow analysis of only the final stage of the deformation history, and do not account for previous steps during deformation.

4.1.1 CURVATURE ANALYSIS

Curvature analyses are applied to assess fracture intensity related to bending processes, and how this changes through a fold. The axiom of this type of model is to relate the distribution and density of fold-related fractures to the magnitude of local bending strains, based on the assumption that folded rock layers are analogous to elastically deformed plates (Fischer and Wilkerson, 2000; Lisle, 1994; Narr, 1991). The spatial variability of curvature magnitude throughout a fold controls the occurrence and density of fractures (Fisher and Wilkerson, 2000); zones with higher amounts of strain should have the highest fracture abundance.

Curvature models commonly fail to adequately predict fracture patterns, one reason is that the progressive development of the fold is not taken into account. This static view of folds can lead to erroneous results, since zones that have undergone significant amounts of deformation in the development of the folds may end up in regions of low curvature in the static model, and thus will be misinterpreted as low strain and thus possibly low intensity fractures zones (Sanders et al., 2004) (Figure 4.1). Another reason is that preexisting fractures may be passively incorporated in folds (Marrett and Laubach, 2001), and become reactivated by folding (Laubach, 1988). Fractures can also become superposed on folds (Bergbauer and Pollard, 2004). The main failing of these models is that they do not account for fold evolution. Moreover, some analyses as those performed by Keating and Fischer (2008) in analog models suggests that a direct proportionality between curvature and strain is not valid in some cases, such as basement involved fault related folds. In spite of these disadvantages, curvature analyses continue to be used and have proven to be useful (Hennings et al, 2000) to define abundance for fractures in hinge related zones.

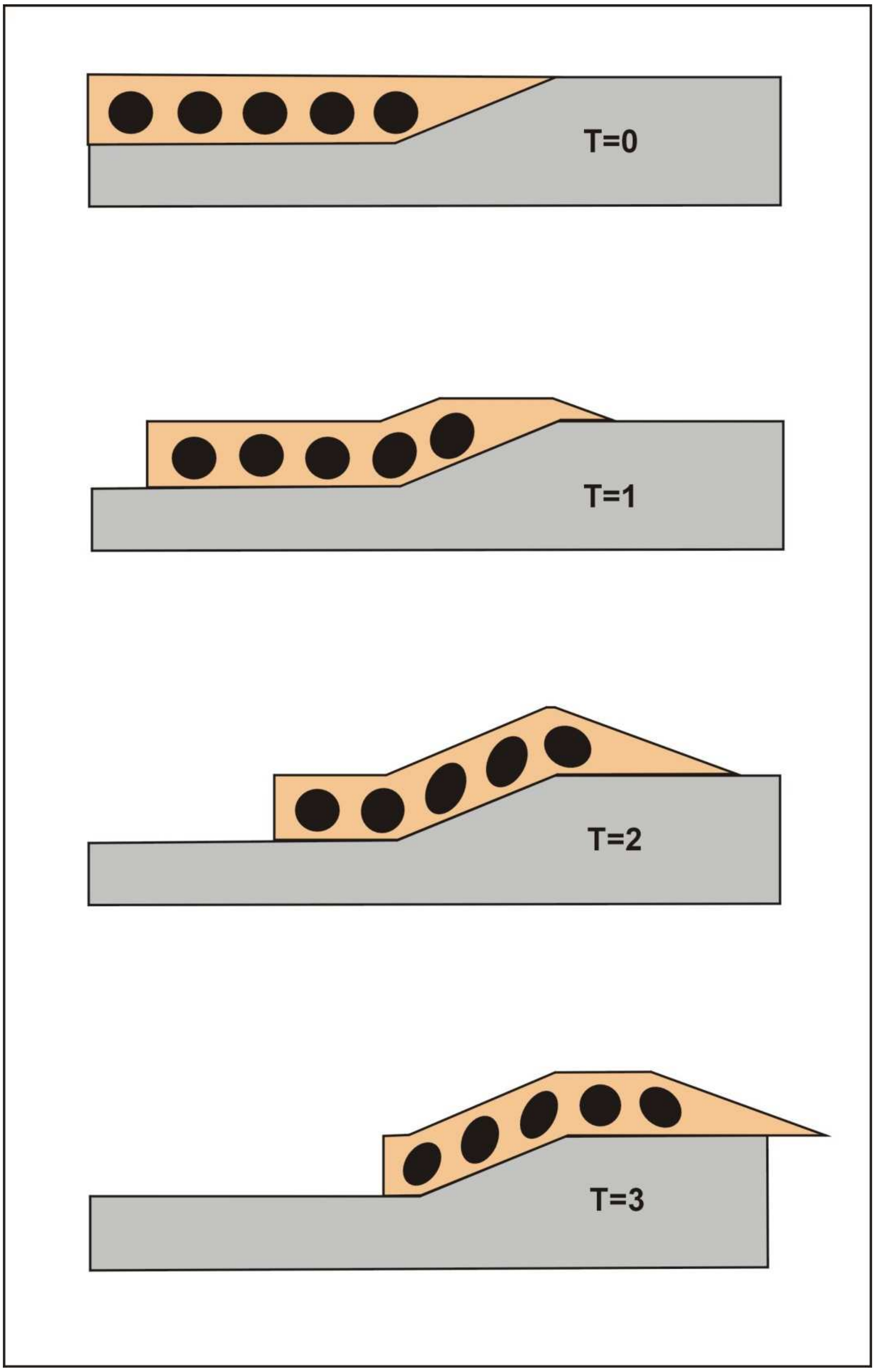

Figure 4.1: Conceptual strain development above a thrust fault, where spheres and ellipses represent deformation present in each step (From Sanders et al., 2004).

Two different types of curvature analyses can be applied to geometric models in order to predict fracture distribution.

4.1.1.1 Simple Curvature

Curvature concepts are easy to understand on perfectly cylindrical folds, given by the presence of identical cross sections when sectioned serially (Lisle and Robinson, 1995) (Figure 4.2). Such folds will have a unique curvature value defined as the inverse of the radius of curvature in any single section plane parallel to the line of the greatest curvature (Figure 4.3). This value presents units of 1/length; for three consecutive points in a horizon the radius of curvature is defined as the distance from the point to the unique center of curvature (Equations 1 through 4 in Figure 4.3). Most folds in nature do not present these characteristics. However, small departures from perfect cylindricity in nature should not greatly affect this type of analyses. Curvature is usually approximated as the rate of change of dip across a surface, given by the second partial derivative (Hennings et al., 2000; Johnson and Johnson, 2000). However, Bergbauer and Pollard (2003) showed that this approach can lead to significant errors when working with surfaces that have slopes with moderate to high dips. In contrast they propose a methodology based on differential geometry, similar to the one defined by Samson and Mallet (1997), Stewart and Podolski (1998), Fischer and Wilkerson (2000); and later employed in other works such as Mynatt et al. (2007), and Pearce et al. (2006). In these studies, the curvature is defined in terms of the rate at which the tangent plane turns with respect to distance along the surface (Figure 4.4); this defines the curvature vector k, composed by the normal curvature vector k_n and the tangent vector k_g. Only k_n is necessary to define the curvature value, and this can be calculated by dividing the second and first derivatives of a surface (Bergbauer and Pollard, 2003).

All 3D structural analyses in this thesis were done using commercial software 3D Move® (see Chapter 7). In this software, the methodology described by Stewart and Podolski (1998) is followed, employing differential geometry and neighboring grid nodes as a way to calculate curvature.

As stated in Stewart and Podolski (1998), and Bergbauer and Pollard (2003) this curvature analysis will be dependent on data manipulation such as gridding and smoothing processes. However, the fact that maximum curvature values are located along the hinge of the structure where previous studies in the Subandes found the highest fracture abundance (Sanguinetti et al., 1998; Araujo and Clivio, 2001; Cohen 2003; Sanders et al., 2004; Kozlowski et al., 2005) suggests that these curvature values can be considered as valid predictors of fracture occurrence and abundance.

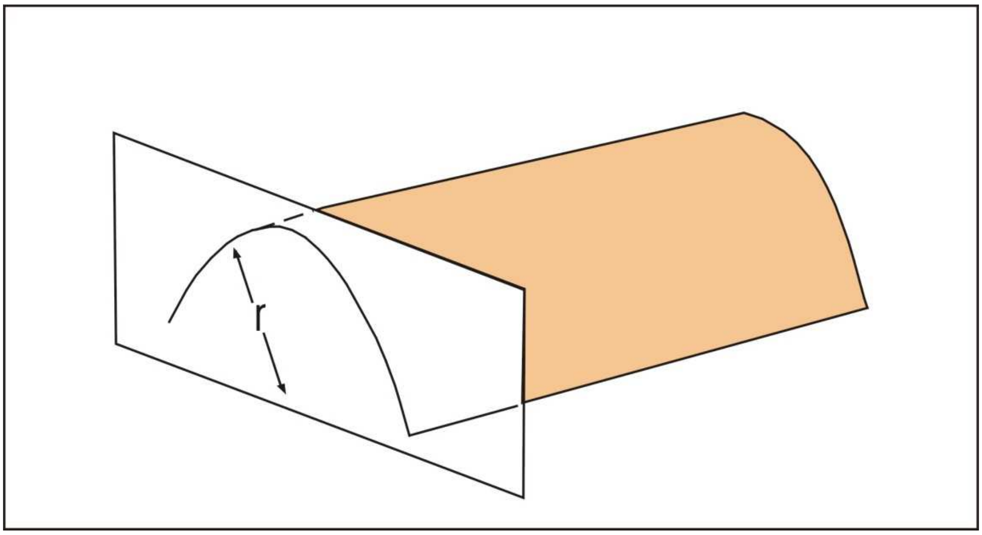

Figure 4.2: Curvature distribution in cylindrical folds (From Lisle and Robinson, 1995).

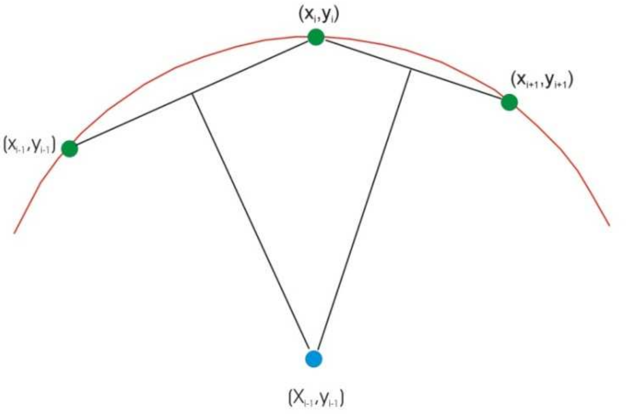

$$x_i \text{ center} = \frac{1}{2}\,\frac{(y_i-y_{i-1})[(y_{i+1}-y_i)^2+x_{i+1}{}^2-x_i^2]+(y_{i+1}-y_{i-1})^2+x_{i-1}{}^2-x_i^2]}{(y_i-y_{i-1})(x_{i+1}-x_i)-(y_{i+1}-y_i)(x_i-x_{i-1})} \quad \text{(Eq. 1)}$$

$$y_i \text{ center} = \frac{1}{2}\,\frac{(x_i-x_{i-1})[(x_{i+1}-x_i)^2+y_{i+1}{}^2-y_i^2]+(x_{i+1}-x_{i-1})^2+y_{i-1}{}^2-y_i^2]}{(x_i-x_{i-1})(y_{i+1}-y_i)-(x_{i+1}-x_i)(y_i-y_{i-1})} \quad \text{(Eq. 2)}$$

$$Ri=[(x_i-x_{i\,\text{center}})^2+(y_i-y_{i\,\text{center}})^2]^{1/2} \quad \text{(Eq. 3)}$$

$$C_i=\frac{1}{R_i} \quad \text{(Eq. 4)}$$

Figure 4.3: Curvature in 2D and the defining equations (From Lisle and Robinson, 1995).

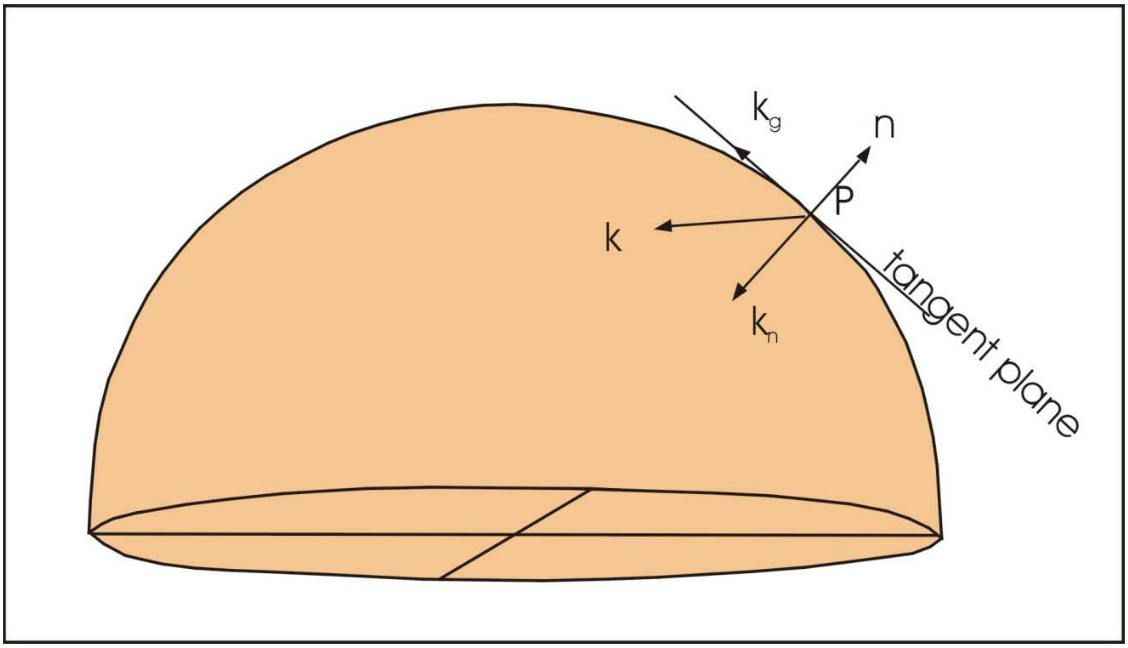

Figure 4.4: Curvature definition with respect to a surface (Modified from Bergbauer and Pollard, 2003).

4.1.1.2 Gaussian curvature

Lisle (1992 and 1994) presented a model in which fracture intensity through a fold was predicted by the curvature at points on the folded surface. This method differs from the one presented above because the curvature considered is the double (or three dimensional) type, expressed quantitatively by means of the Gaussian curvature (Figure 4.5). Gaussian curvature is defined as the product of the two principal curvatures k_1 and k_2, the extreme values of curvature measured along two orthogonal curves through a point (Lisle, 1992 and 1994) and have values of 1/area. According to Lisle (1994) the idea that curvature of folded surfaces can give information on the stretching involved in the folding process, arises from a folding mechanism in which the limbs rotate, but where the bedding surfaces do not stretch. This is called *isometric folding* and includes mechanisms such as flexural slip and flexural-flow folding, explained below. Before isometric folding the Gaussian curvature of all points in a planar structure is zero. This will be expected to change during folding, although according to the Gauss' theorem, in such a way as to give a zero product. This is true if at least one of the principal curvatures is zero, and they do not posses double curvature (Figure 4.6). This analysis suggests that zones that depart from isometric bending can have higher strain and thus higher fracture intensity. Thus, the analyses of bedding plane strains and fracture prediction are based on the measurement of Gaussian curvature and its distribution on the folded surface. However, this type of analysis only works well if isometric folding is likely to happen.

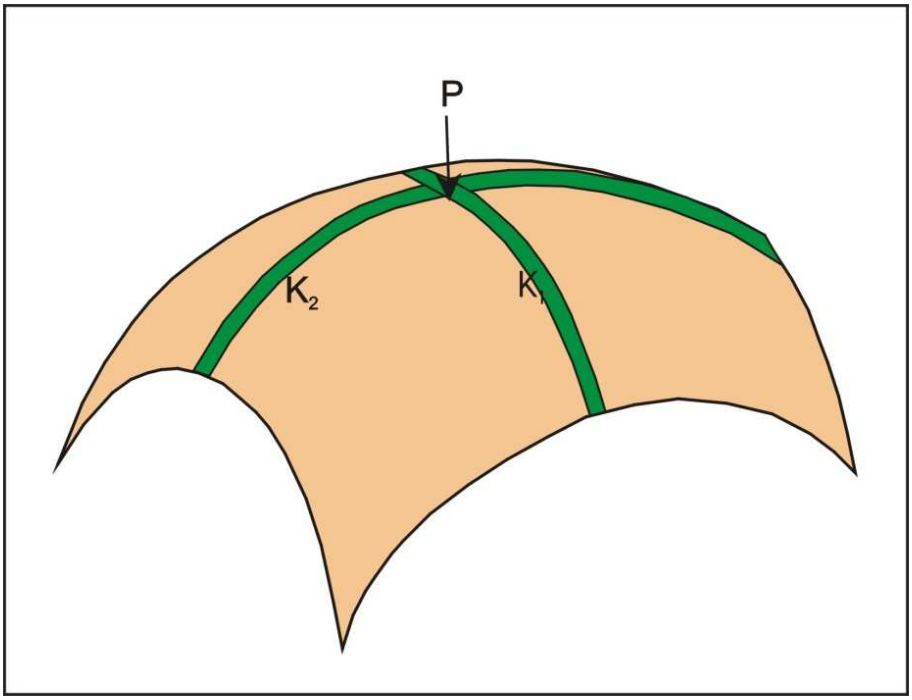

Figure 4.5: Gaussian curvature (From Lisle, 1994).

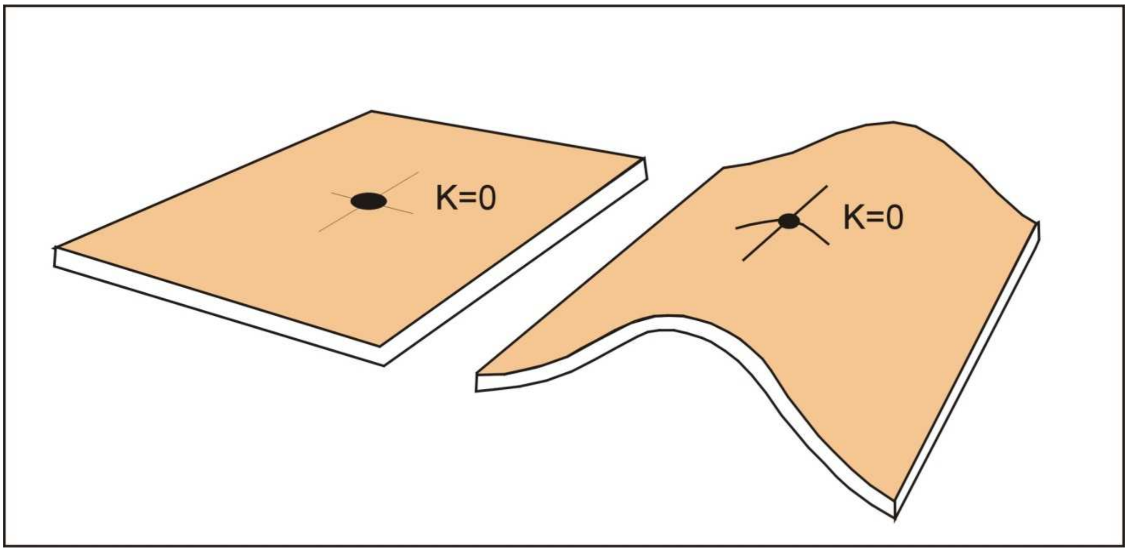

Figure 4.6: Gaussian curvature isometric folding (Lisle, 1994).

They are most applicable to folds where layers have a strong anisotropy that results in slip along the anisotropy planes.

4.2 Structural Kinematic Models

Kinematic models predict a specific history of deformation of how a system went from an undeformed to a deformed state. They describe how the elements of a fold move relative to one another, simplifying mechanical processes into a practical set of geometric rules (R. Ratliff, LithoTect tutorial 2006). They do not asses how or why the motion occurred or what the physical properties of the system were (Twiss and Moores, 1992). They may incorporate mechanical stratigraphy (in a qualitative sense) (Donath, 1971; references in Laubach et al. 2009) but do not use rigorous mechanics. In order to explain or predict the geometry of a structure and the folding processes associated with its formation, kinematic model rules are applied as a way to validate a bidimensional or tridimensional interpretation. Both restoration (going in one or multiple steps from the deformed to the undeformed state) and forward modeling (going in one or multiple steps from the undeformed to the deformed state) can be applied to 2D structural cross sections and 3D structural models. This is performed through the use of algorithms in commercial software such as 2D and 3D Move®, LithoTect^{TM}, Gocad® or Kine 3D® (users guides listed in References). A kinematic modeling methodology was applied in this thesis as a way to constrain the deformation and kinematic history of a subsurface anticline, which is a hydrocarbon field in the Subandean Ranges. By means of kinematic models, I assessed how the deformational processes could have affected the generation, and distribution of fractures in the Devonian sandstones of the Huamampampa Formation. An explanation of the workflow followed, and the results obtained are presented in Chapter 7.

A variety of kinematic models can be applied to characterize deformation processes. Morretti (2008) mentioned Flexural Slip, Simple Shear (both vertical and inclined), Ductile Flow and Rigid Block Rotation as the most common models used for structural interpretation. It is important to bear in mind that in spite of the constraints this method gives us, balance and restoration of a structural interpretation, can be accomplished by more than one kinematic model. Hence the input of the interpreter is essential when it comes to choosing the most appropriate model for the geologic features of the area under study (R. Rattliff, LithoTect tutorial, 2006). The results obtained cannot be considered as unique, and even when using the same kinematic model many deformation histories can lead us to the same present day geologic distribution. Below a short summary of the model used in this thesis.

4.2.1 FLEXURAL SLIP

Flexural slip is assigned to a stack of layers responding to either compressive or tensile forces by sliding along the interlayer surfaces. This mechanical process is registered when layers present high competence separated by low competence layer boundaries, such as those of the Devonian sandstones of the Subandean Ranges. This high competence contrast produces a relative slip, parallel to the layer boundaries, towards the fold hinge for the layer in the convex side, and a slip towards the limb for that one in the concave side (Twiss and Moores, 1992) (Figure 4.7).

As we mentioned in Chapter 3, natural multilayers respond to bending or buckling folding by a combination of simple shear processes and orthogonal flexure; where the first takes place along the layer boundaries, and the second within the individual competent layers. Therefore, pure flexural slip deformation models would only help us to assess the presence of Stearns' type 1 and 2 fractures; but assuming this type of deformation would not preclude the possibility of finding Type 3 bending related fractures.

4.2.2 Flexural slip algorithm

In addition to the features described above, some other aspects strictly related to the use of this kinematic model as an algorithm in commercial software, need to be mentioned to fully understand the theory behind the modeling applied in this thesis. The flexural slip kinematic model is usually used in commercial software, combined with the geometry of the faults and decollement levels (Moretti, 2008) as an algorithm to explain folding processes such as fault bend folding (Suppe, 1983) that were used to characterize the folds that form the Subandean ranges, both in this thesis and in many other previous works (Aramayo Flores, 1999; Stark et al., 2002b; Giraudo et al., 1999; Moretti and Delos 2006; Sanders et al., 2004). When working with flexural slip kinematic models in the construction and restoration of structural cross sections, certain rules must be followed such as: preservation of length, thickness and consequently area of the layers that parallel the slip system (Rattlif, LithoTect tutorial, 2006) (Figure 4.8); beds need to be parallel and horizontal prior to the deformation; deformation processes are restricted to the hanging wall, while the beds in the footwall remain undeformed. In addition to these, a simple flat-ramp-flat geometry needs to be interpreted, and the cut off angle of the ramp needs to be less than 30°, if oblique or backshear is not to be invoked (2D Move tutorial).

4.2.3 FAULT-PARALLEL FLOW ALGORITHM

The fault-parallel flow algorithm is based on Eagan's et al work (1997) and is present in Midland Valley commercial software (2D Move® and 3D Move®). This algorithm was used in my thesis to model deformation history in 3D. A similar approach to describe the evolution of structures in the Subandean ranges was used by Sanders et al. (2004). This algorithm also evokes layer parallel shear as the deformation mechanism. It is used for complex fault geometries, and is based on particulate laminate flow over a fault ramp, where the fault is divided into dip domains and flow lines are constructed for each domain, equally spaced with respect to the fault (Figure 4.9). Then the hanging wall is transported along these flow lines (Move tutorial). As in the flexural slip algorithm some rules apply to fault parallel flow models. In 2D, the area of the hangingwall is maintained. In 3D the volume is maintained (it is important to notice that the area of a surface in 3D need not be preserved); the footwall remains undeformed and is not translated.

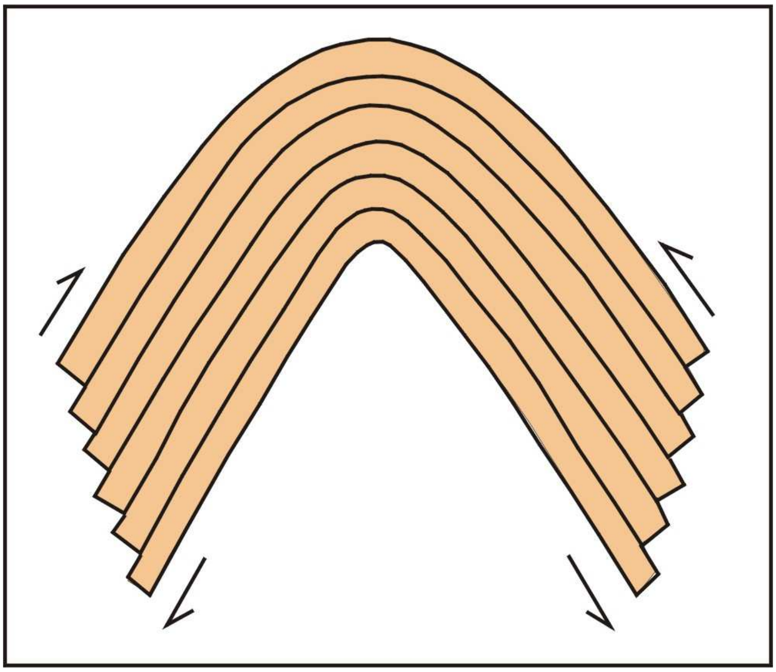

Figure 4.7: Movement of beds during flexural slip folding.

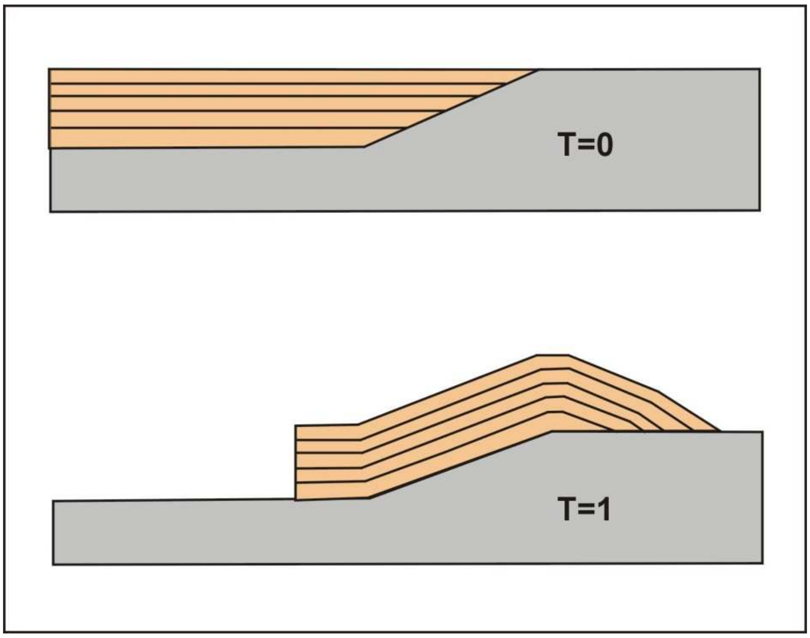

Figure 4.8: Flexural slip system with slip parallel to bedding and simple shear curvilinear slip (Modified from R. Ratliff, Lithotec tutorial 2006).

4.2.4 STRAIN ANALYSES

The models presented above not only allow us to define a specific deformation history but also allows us to make predictions of fractures through the study of the strain history. The strain of a body is defined as a change of size, shape or both during deformation. The deformation history of a structure will be represented in the strain path, which registers the changes in strain in the different deformation stages; therefore, strain measurements can be used to analyze different strain-related features (such as fractures) during geologic evolution. These measurements include both volumetric (Figure 4.10) and shear strain values (Figure 4.11). The volumetric strain of a body assesses the changes in volume through the volumetric stretch s_v and the volumetric extension e_v (Twiss and Moores, 1992), where

$$Sv = \frac{v}{V}$$

and

$$e_v = \frac{v\text{-}V}{V}$$

V, the undeformed volume of the body, and v, the deformed one. Shear strain e_s comprises the changes in shape of a body, given by changes in the angles between lines that were originally perpendicular; and is defined as

$$e_s = 0.5 \tan \psi$$

Where ψ represents the shear angle. Figure 4.11 is a representation of these strain measurements for a cube. The importance held by strain measurement is that changes in the vertices location of the volumes will constrain: volumetric dilatation, principal strain magnitudes (maximum and minimum values in the strain tensor) and orientations, and plane strain ratios (ratios between the principal strain values if strain is defined in a single plane and no deformation occurs normal to that plane). These model calculations can be used to assess potential for fracture development and fracture abundance, if the assumption is true that strain present in the deformation is strictly related to the development of fractures. Previous analyses both in the Subandean Ranges (Sanders et al., 2004; Moretti and Delos, 2006), and other naturally fractured settings (Masaferro et al., 2003; Hennings et al., 2000; Jamison, 1997) have applied this methodology to quantify fracture intensity and distribution.

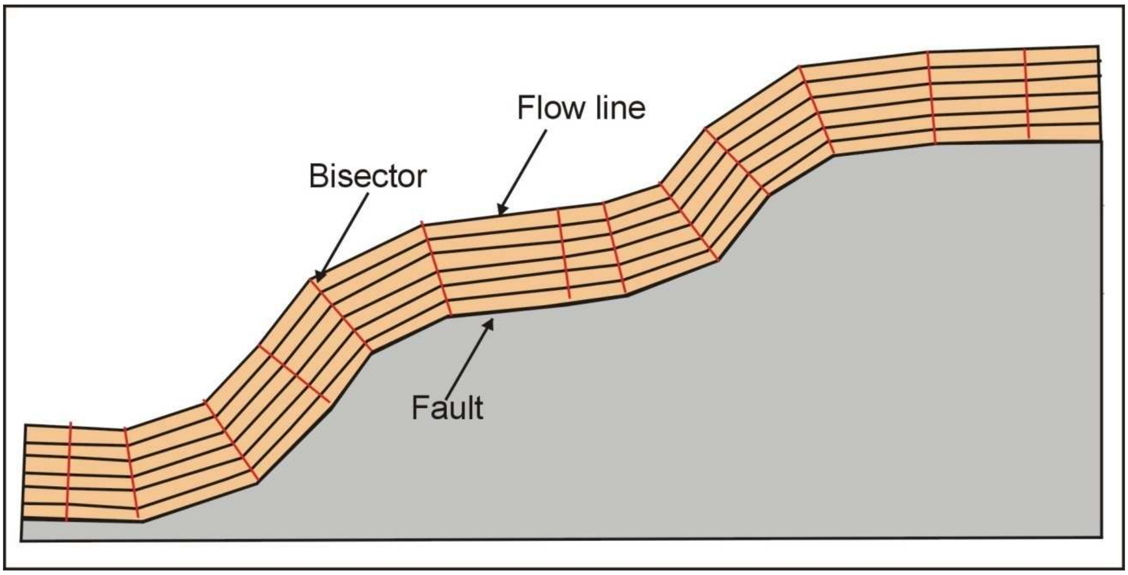

Figure 4.9: Fault parallel flow deformed cross section, showing flow lines (From Move tutorial).

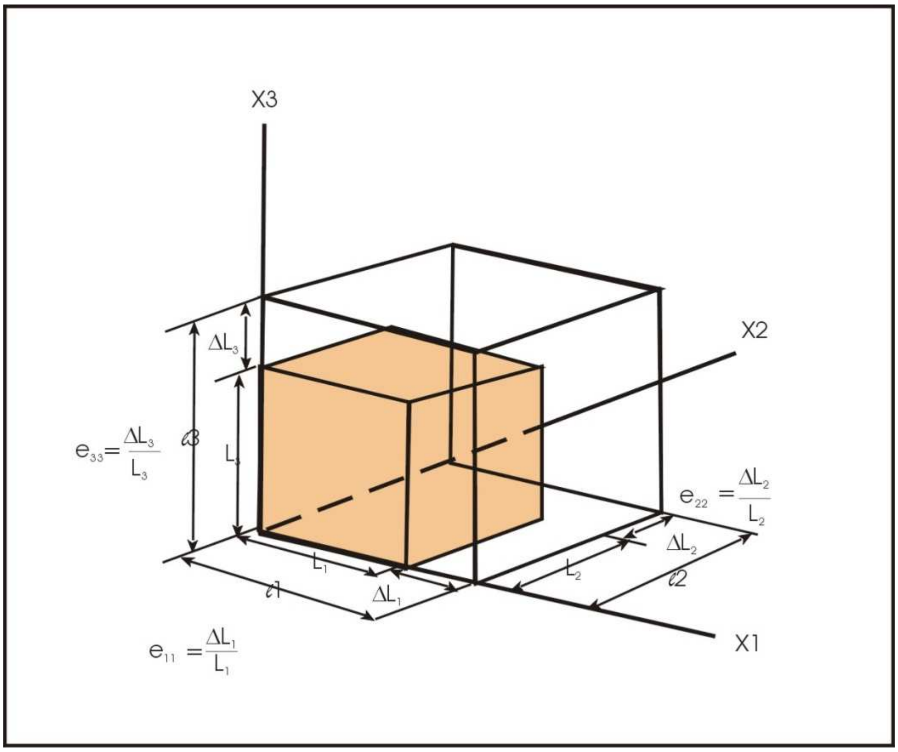

Figure 4.10: Strain associated to volumetric change of a body (From Twiss and Moores 1992).

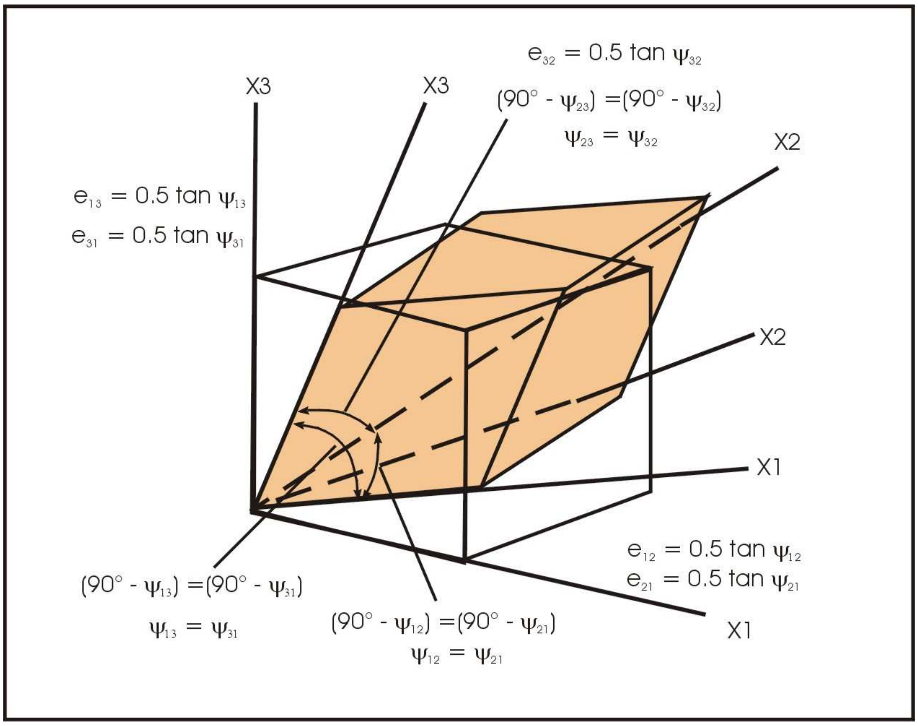

Figure 4.11: Strain associated to shape change of a body (From Twiss and Moores 1992).

4.3 Structural Mechanic Models

These models are based on the basic laws of continuum mechanics, -conservation of mass, momentum, angular momentum, and energy,- and on how rocks behave in response to applied forces (Twiss and Moores, 1992). This approach represents the next step in structural modeling and fracture analysis. Some studies such as those of Casey and Butler (2004), Moretti et al. (2006), and Gusofski et al. (2009) have made an incursion into combinations of kinematics and mechanics analyses, where rock behavior is taken into account through linear-elastic Hookean laws that control material strength heterogeneities (Mouron, 2005 in Gusofski et al., 2009; Moretti et al., 2006), and not just approximated by deformational models e.g. flexural slip or simple shear (Moretti et al., 2006). No further references will be made to these models since this type of analysis was not applied in my thesis, owing to the fact that commercial software that comprises this methodology such as Kine3D®, GOCAD®, or Dynel® were not available. However, as I describe, mechanical properties of Subandean Devonian sandstones should be considered, since they seem to have a major impact on fracture intensity, analyzed here through primary lithology and diagenesis and their impact on relative microfracture abundance.

CHAPTER 5: METHODOLOGY

A wide variety of methodologies were applied in this thesis in order to better understand, and hopefully make predictions, about the fracture system of the Devonian sandstones in the Subandes. In order to accomplish this, I amalgamated information from multiple sources, ranging from the macroscale to the microscale, studying subsurface reservoir samples and outcrop analogs, and analyzing both structural and diagentic features. A summary of the methodologies employed in this thesis is presented below; in addition, each of the successive chapters presents a more detailed description on how these were applied to my data.

5.1 Macroscale

5.1.1 OUTCROP STUDIES AS RESERVOIR ANALOGS

Due to the problem of sampling large but sparse macrofractures in the subsurface (see Chapter 1) most questions cannot be answered confidently based only on macrofractures detected in core and logs. To the extent that such data were available for my study, they were most useful as a check on inferences based on study of microfractures in core samples. Consequently, the emphasis of my macrofracture analysis was on natural outcrops of the Huamampampa sandstones near Abra del Condor (see Chapter 6 for location). I consider these outcrops to be an analog of the Devonian reservoir rocks. Yet it is worthwhile to bear in mind that the data obtained from the outcrop studies should be carefully evaluated when comparing it to subsurface reservoir.

The geological history of the rocks exposed is different from that of those in the subsurface. Some of the differences between outcrop and subsurface fractures in these rocks are presented in Chapter 9.

Although it was not among the original tasks envisioned for my thesis, I conducted geological mapping in Abra del Condor to define the structural geometry of the rocks in outcrops. This field mapping was needed because published maps depicted contradictory interpretations (Florez Niño et al., 2005; Ayaviri, 2002), and these published accounts differed from my initial interpretations of the Abra del Condor's geology. Through the course of a field trip during the month of August 2008, a large amount of strike and dip information was obtained with a magnetic compass, and lithological characterization and correlation was performed on the different geologic formations, with location determined with satellite positioning (GPS). Using these data and aerial photos of the zone (scale 1:50,000), a new geologic map was composed using the software LithoTech^{TM}. The bitmap file of the aerial photos was aligned to the world coordinates and a planimetric view was created using the Warp Bitmap algorithm of Didger®3.

I also described and mapped fractures and the following features were registered: azimuth and dip, morphology, mode (opening, sliding), composition and texture of cement within the fractures if present (rare), cross cutting relationships when more than one set was present, kinematics for faults, and qualitative distribution of the fractures relative to large-scale structural and stratigraphic parameters within the outcrops. Bed unfolding methodologies such as those described by Bergbauer and Pollard (2004) and

Bellahsen et al. (2006) were performed to better understand the relationship of fractures to the overall structure. Unfortunately, the absence of cement filling the fractures, that would have allowed us to unequivocally quantify the fracture size distribution through the kinematic aperture (Marrett et al., 1999), precluded performing fracture characterization using 1D scanline methodologies such as those described by Ortega et al (2006).

To complement the analysis done in the field by macroscopic observation, we collected seven oriented samples (see chapter 8 for locations), representative of the different structural domains and stratigraphic levels in Abra del Condor. Microfracture studies performed on these samples allowed me not only to better characterize fracture properties and quantify the impact of geologic large scale features using microfractures, but also to perform a direct comparison of outcrop and subsurface fractures.

5.1.2 STRUCTURAL MODEL ANALYSES

In addition to the observation of fracture distribution in the outcrop analog, I used structural analyses to assess the relation of the fracture system with the present day geometry and deformation history of one anticline in the basin. A kinematic structural model was constructed for an anticline that hosts a subsurface hydrocarbon field of the Devonian basin in NW Argentina, and taken here as a prototype of the anticlines that form these ranges. Semi-quantitative models of fracture attributes based on analyses and concepts presented in chapters 3 and 4 were used to relate the structural form and evolution to the overall fracture distribution.

A first step was to build sequenced structural cross sections in 2D using both 2D Move® and LithoTect^{TM} commercial software. These cross sections were based on outcrop, seismic and well data. In order to validate the interpretation a restoration in 2D was done, using the software mentioned above and applying the algorithms presented in chapter 4. Then the sections were integrated in 3D, in order to generate a tridimensional structural model. Finally, the subsequent forward modeling deformation evolution, and quantitative analyses of fracture distribution were done using 3D Move® software. Details on the workflow and analyses I applied are presented in chapter 7.

Even when large amounts of data can be obtained using the methodologies presented above, we should bear in mind that a wide spectrum of deformation paths could have produced fractures and folds in the Subandes. Moreover, this approach ignores the mechanical properties of the rock (governed by depositional rock type, diagenesis and mechanical layer thickness). Such factors and subsequent diagenesis can affect the spatial arrangement, size distribution and intensity of fractures and their degree of remaining porosity. Complementary data obtained both from observation in the field and microfracture studies in subsurface core were performed to test the predictions obtained from the model.

5.1.3 ROCK MECHANICS STUDIES

Rock property, bed thickness, and interface controls on fracture characteristics are evident in differences in fracture patterns in layered sequences. Owing to the inherent difficulty in sampling subsurface fracture patterns in a meaningful way, identifying links between stratigraphic layer properties and distributed fractures is valuable for extrapolating fracture attributes in sparsely sampled rocks and unsampled areas (e.g., Narr, 1991; Morettini et al., 2005). Mechanical properties of strata that influence growth of opening-mode fractures include tensile strength, elastic stiffness, brittleness, fracture mechanics properties, thickness of layers, and nature of interfaces. Mechanical properties can be measured on rock samples or inferred from well logs (e.g., Ameen et al., 2009) or seismic data. As part of my modeling study I measured Young’s modulus and subcritical crack index in the Petroleum and Geosystems Engineering rock mechanics laboratory. Most of my subsurface core samples were tested (see chapter 11 for details about these tests and samples). These results were coupled with information gathered from other methodologies, and used in order to assess the variability of fracture abundance through fracture related strain measurements. Multivariate statistical analyses were employed to evaluate to what degree what factors affect the overall fracture distribution.

5.2 Microscale analyses

5.2.1 SEM-CL MICROSCOPY

Scanning electron microscope (SEM) based cathodoluminescence (scanned CL) was used to image and study *microfractures,* defined as those fractures visible only under magnification. Microfractures constitute another way to overcome the sampling problem, since microfractures are much more abundant than macrofractures and can be studied even in small volumes of rock (Laubach, 1997; Hooker et al., 2009). The basis for such analysis is that some attributes of microfractures such as orientation, kinematic aperture and spacing distribution, can be used as a proxy to better understand macrofractures characteristics (Laubach, 1989, 1997 and 2003; Marrett el al., 1999; Gomez and Laubach 2006). Both subsurface and outcrop samples were analyzed; from these I obtained contiguous thins sections parallel to bedding, obtained following the methodology described by Gomez and Laubach (2006) and further described in chapter 9.

Cathodoluminsecence (CL) is the emission of light from crystals stimulated by bombardment with an accelerated electron beam. CL can be collected in ways that are either quantitative (actual spectra of intensity versus wavelength) or qualitative (images) (Boggs and Krinsley, 2006). Images in this thesis were obtained using an Oxford Instruments Mono CL2 cathodoluminiscence detector system, attached to a Philips XL30 scanning electron microscope (SEM) at 15 kV. The detectors record CL emissions in the range of ultraviolet through visible into near infrared (185-850 nm) and convert them to grey scale intensity values. Secondary electron images were also obtained for some samples; these can be used to create topographic images in which porosity is visible.

Image acquisition was operated by Scandium® software, which controls the microscope stage and allowed me to automatically collect consecutive images in a predefined line. The measurement of microfracture attributes in a 1D scanline can provide information on fracture kinematics, strain, aperture scaling, orientation and spacing (Marrett et al., 1999). Scanlines were defined perpendicular to the macrofracture principal orientation, assessed in the field for outcrop samples and in electrical borehole image (FMI) logs for subsurface core. For those core samples where logs were not available or in the circumstance that cores were not oriented, two perpendicular scanlines were defined in order to avoid undersampling of the fracture population.

Mosaics along the scanlines were created from individual images using Photoshop®; microfractures were digitized on these images using Didger®3 software, following the methodology described by Gomez and Laubach (2006). In order to quantify features such as kinematic aperture distribution, orientation and spacing, a GoMezure^{TM} spreadsheet template was employed; further description of this analysis and the results for the Devonian sandstone microfracture properties are presented in chapter 8.

The presence of cement within the fractures, as well as remaining porosity and an emergent threshold fracture size was also analyzed in CL images. The cement detected is mostly quartz. Emergent threshold is a kinematic aperture for which fractures of a certain size or larger will register remaining porosity (Laubach, 2003). Porosity and permeability were assessed, based on observations of individual fractures and generalized fracture size distribution evidence from scaling relations following the methodology described by Marrett (1996).

5.2.2 PETROGRAPHIC TRANSMITTED LIGHT MICROSCOPY

Grain compositions, cement types and porosity both within the fractures and the host rock were analyzed in sixteen thin sections of samples both from outcrop and subsurface core, using light microscopy and a counter stage (300 hundreds points were counted per sample). These data coupled with structural information was used in multivariate analysis to assess the impact of primary lithological composition and diagenesis on fracture strain magnitude and fracture intensity.

Finally, superficial assessments of the likely presence of late or postkinematic carbonate cement deposits filling fractures (fracture quality) were made by estimating the degradation index (ratio between postkinematic cement to porosity), following the methodology described by Laubach (2003).

CHAPTER 6: FOLDS OF THE SUBANDEAN RANGES

A key step in my analysis of fractures was to define fold geometry and kinematics. As stated in Chapter 5, fracture analyses were performed with a wide variety of methodologies in different geologic environments. I should mention that in spite of having data from such a wide range of settings, the structural characteristics for the Lower Structural Level (See Chapter 2) that constitutes the main focus of my study, do not greatly differ. The main difference is changes in the structural and stratigraphic thickness of the geologic units from one site to the other.

6.1 Abra del Condor and Piedra Larga Anticlines

Abra del Condor and Piedra Large are the anticlines that I studied in outcrop. In order to better understand fracture distribution in this region I reinterpreted the geology in the vicinity of these folds and modified published maps, based on mapping I did in the field or interpreted from aerial photography. The region of Abra del Condor and Piedra Larga is located 35 km (21 miles) in a straight line to the NE of the city of Tarija in the south of Bolivia, and around 26 km (16 miles) from the closest subsurface hydrocarbon field of the Devonian basin I studied in this thesis.

Outcrops in this area include the Devonian Los Monos, Huamampampa, Icla and Santa Rosa formations which have a thickness of 220 m, 370 m, 180 and 300 m respectively (Florez Niño et al., 2005). The thickness of the Los Monos Formation is a minimum value since the formation top is not present in the area. To the east of the

Piedra Larga thrust, Carboniferous outcrops of the Tarija, Taiguati and Escarpment formations as well as the Permian Cangapi and the Triassic Vitiacua formations are present. Figure 6.1 is a geologic map that is based on previously published data and maps and my reinterpretation. For details on the stratigraphy of these units see Appendix A.

From a structural point of view, the Abra Del Condor region is characterized by an anticline-syncline pair (see Figure 6.1). These highly asymmetric doubly plunging folds trend NNE with an average strike between N20°E and N30°E. As the rest of the Subandean Ranges, reviewed in Chapter 2, the development of this fold pair is related to the Miocene Andean orogeny and fold orientation is perpendicular to the direction of orogenic shortening that has not changed since the Cretaceous (Horton, 2001). Current maximum horizontal stress indicators from borehole breakouts shows that the current tectonic compression parallels the shortening direction inferred from fold orientation (Cohen, 2002; World Stress Map, 2008).

The Abra del Condor anticline can be interpreted as a minor or parasitic fold in the hanging wall of a larger structure related to the emplacement of the Piedra Larga thrust. The structure could be defined as a fault propagation fold, where the fault dies in the subsurface, as a detachment fold; or simply as a consequence of flexural slip deformation related to the overall shortening process. Figure 6.2 constitutes a schematic cross section (for position, see figure 6.1) of the northern region of Abra del Condor.

The presence of an anticline nose with a south plunging component, defined from the attitude of the beds in the northern outcrops of the Huamampampa Formation, suggests that this zone could be divided in a northern and a southern region (structural domain)(see figure 6.1). The relation between these two regions is not completely clear, Florez Niño et al (2005) proposed the contact is a fault interpreted to have a combination of dip and strike displacement. However there is poor exposure in this region, and I was unable to identify this fault in outcrop. The interpretation of Florez Niño et al (2005) presents incongruences from a stratigraphic point of view, since I recognized conglomerate deposits (Figure 6.3) within what they defined as Los Monos Formation. This unit is interpreted as a distal marine in the eastern Subandean Ranges (Starck, 1999a; Disalvo and Villar, 1999), and becomes more proximal towards the west, with an intercalation of sands and shale (Dunn et al., 1995). The presence of conglomerate may mean that Florez Niño et al. (2005) are incorrect about their identification of Los Monos Formation.

However, what I defined as Los Monos is clearly shalier than the outcrops Florez Niño et al. (2005) defined as part of this unit (Figure 6.4). I consider this conglomerate to be the uppermost portion of the Huamampampa formation. The upper Huamampampa was deposited in a coastal environment, with a mixture of continental and marine deposits (Starck et al., 1992). I also observed conglomerate in a similar stratigraphic position in the back limb of Abra del Condor (Figure 6.5). Based on this fact and on the geomorphologic features observed in aerial photos (Figure 6.6), I redefine the contact as a left lateral strike slip fault that loses its displacement to the west (see Figure 6.1)

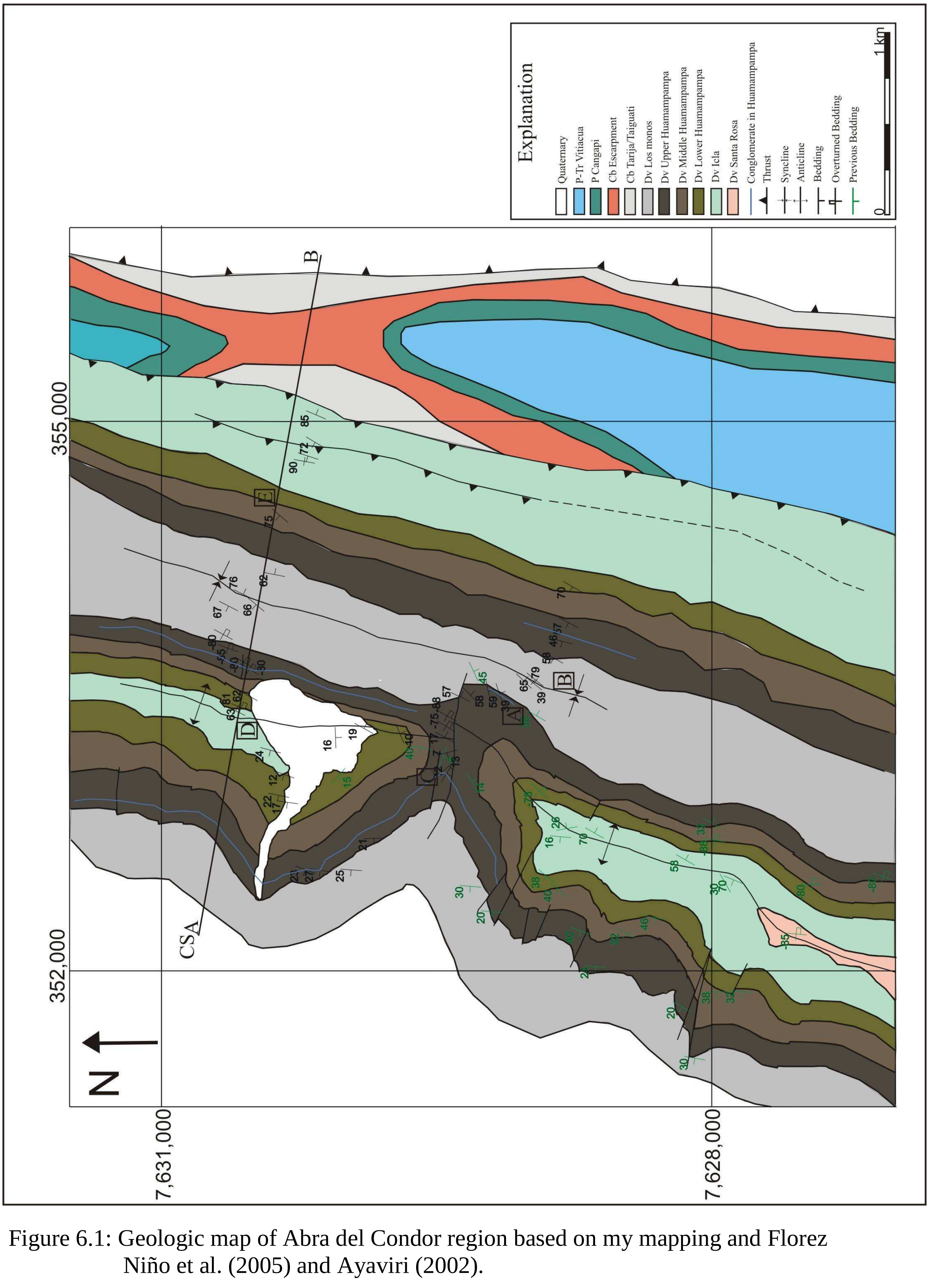

Figure 6.1: Geologic map of Abra del Condor region based on my mapping and Florez Niño et al. (2005) and Ayaviri (2002).

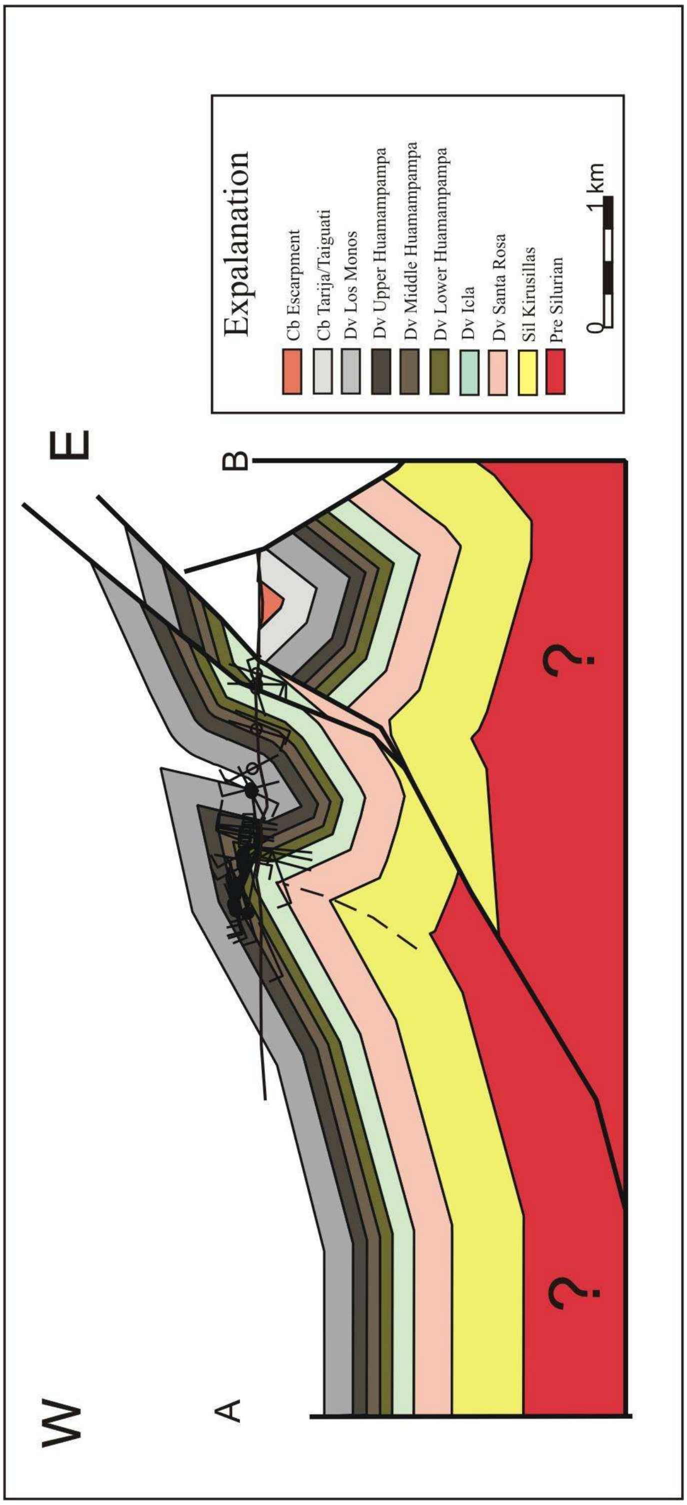

Figure 6.2: Schematic cross section for the Abra del Condor region based on my field observation. My interpretation shows how the Piedra Larga thrust cuts the Huamampampa Formation.

Figure 6.3: a: West view of conglomerate next to the Huamampampa top in the Abra del Condor Forelimb (For location see letter A in Figure 6.1). Hammer for scale. b: Detail of the conglomerate.

The Abra del Condor fold has gently dipping beds in the backlimb, between 15° to 40 towards the WNW. The forelimb has steep to overturned beds with dip values between 65° to the ESE, and up to 75° to the WNW when beds are overturned (see figure 6.1 and 6.2). The interlimb angle *i* varies between 40° and 70°, depending on the zone analyzed, defining a close to almost tight fold according to Fleuty's classification (1964). The hinge zone is poorly exposed (Figure 6.7). In spite of poor exposure I managed to obtain adequate strike and dip data from the Icla Formation outcrops, in the northern region. Using the π methodology and software StereoWin, the attitude of the fold axis (Figure 6.8) was defined as plunging 6° to the azimuth 206°. Since the axis is almost horizontal I redefine its strike as N26°E. Similar characteristics to those observed in Abra del Condor were defined for the hinge region of the Huamampampa outcrops in the Sierra del Pescado anticline, located in the northernmost region of the Salta Province of Argentina, and cut by the Pescado and Bermejo River (Antonellini, 1998). However, in that area a complete dip reversal occurs in a distance of less than 10 m.

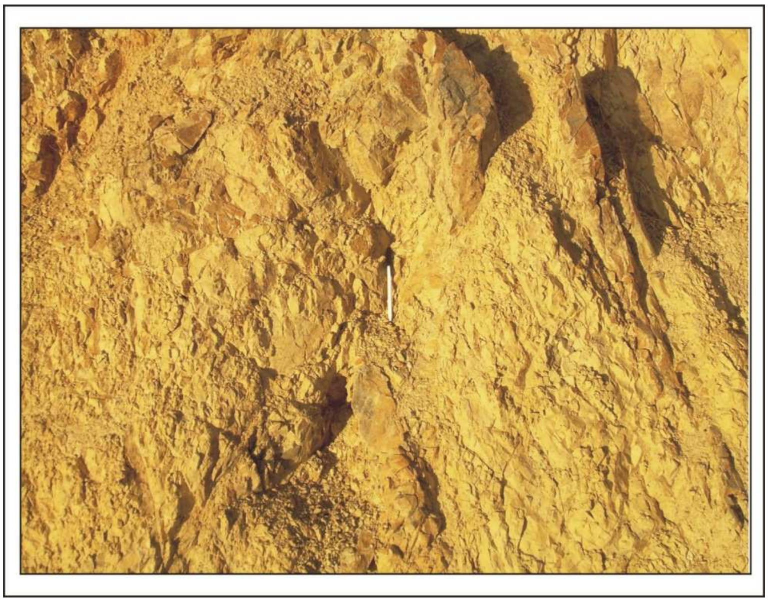

Figure 6.4: East view direction for shales of the Los Monos Formation in the syncline of Abra del Condor. Pen for scale. For location see letter B in Figure 6.1.

Figure 6.5: West view direction for conglomerate near to the top of the Huamampampa Formation in the backlimb of the Abra del Condor anticline. Round pebbles are in the conglomerate. Pen for scale. For location see letter C in Figure 6.1

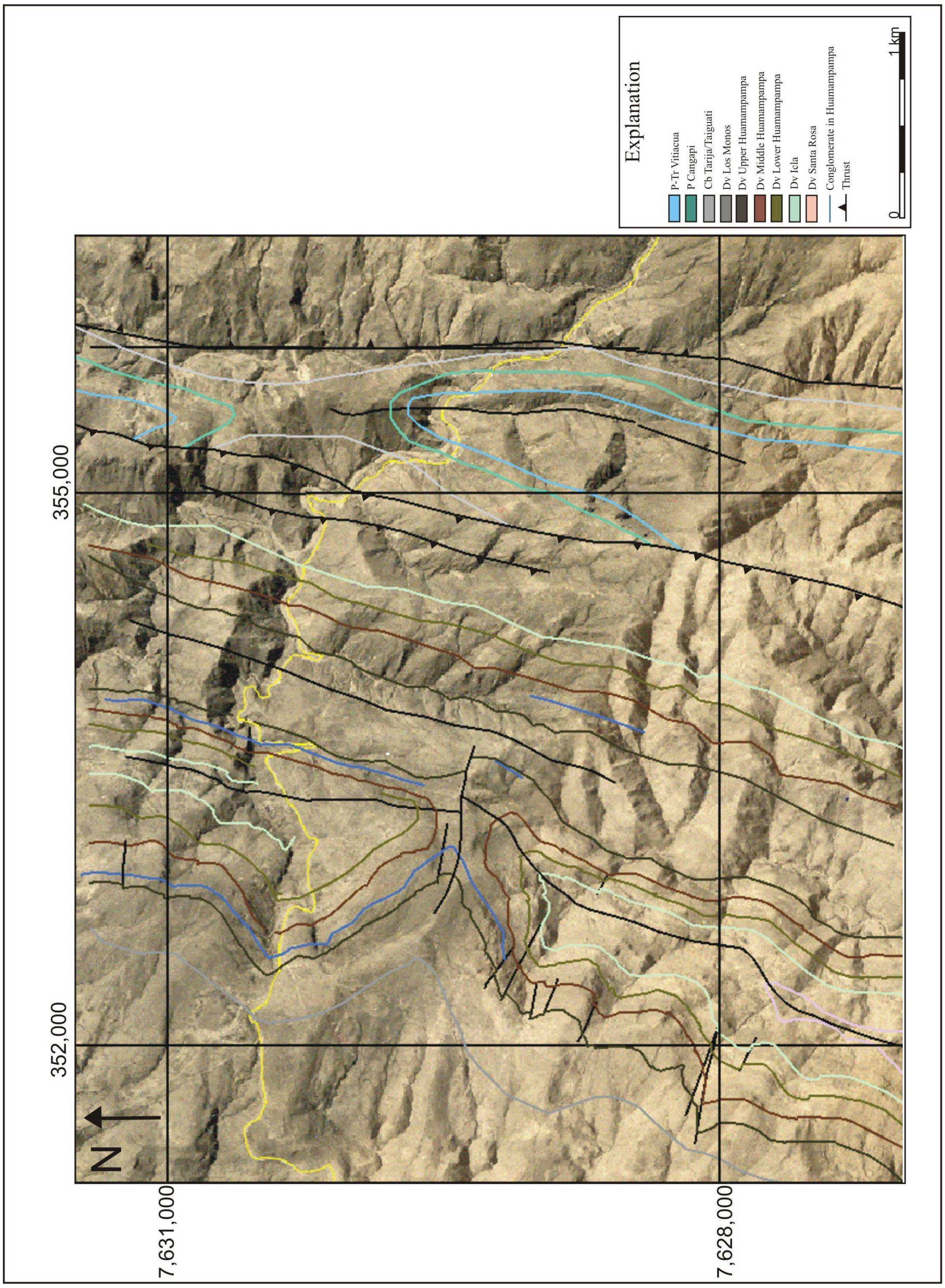

Figure 6.6: Aerial photos and my geologic interpretation of the Abra del Condor region.

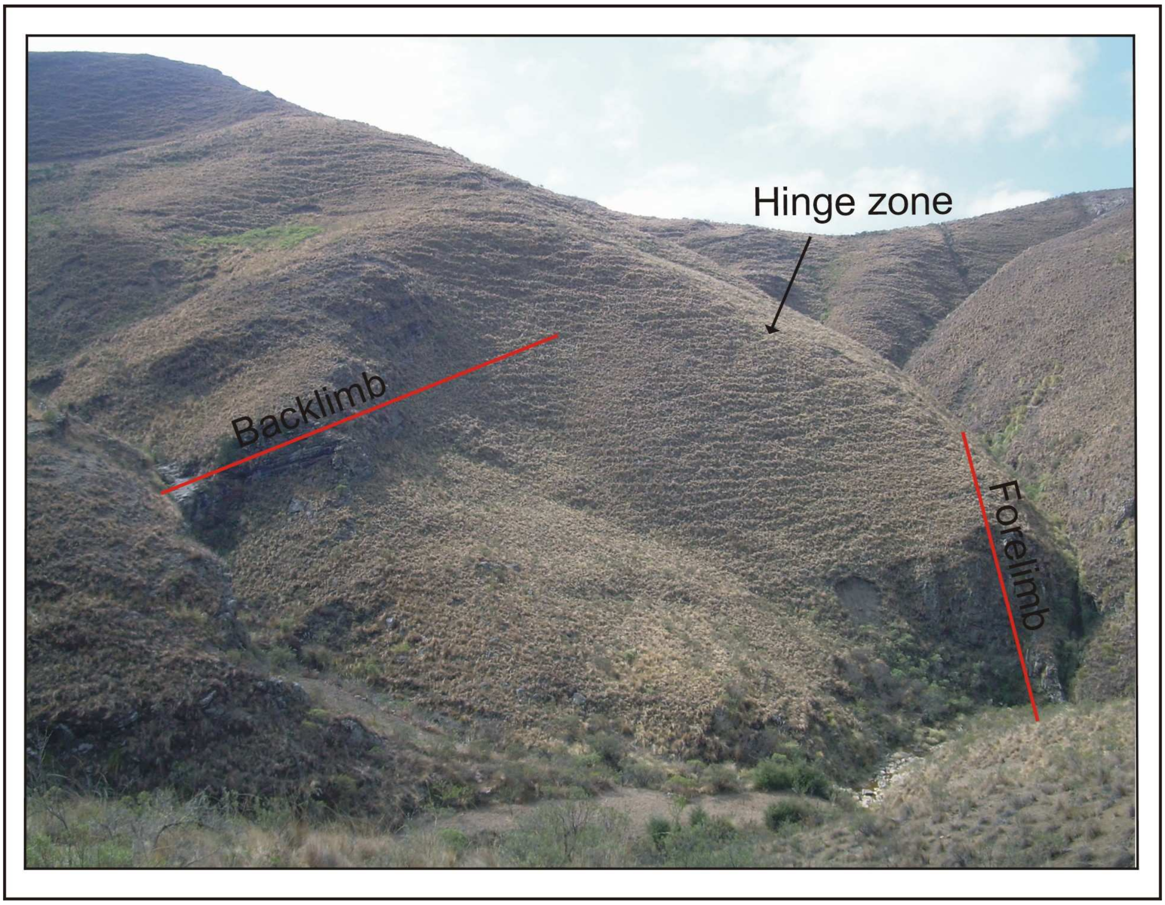

Figure 6.7: View NNE of the Abra del Condor anticline hinge in Icla Fm. In spite of poor exposure, the strong asymmetry of the overall structure is evident. For location see letter D on Figure 6.1. Red lines parallel bedding.

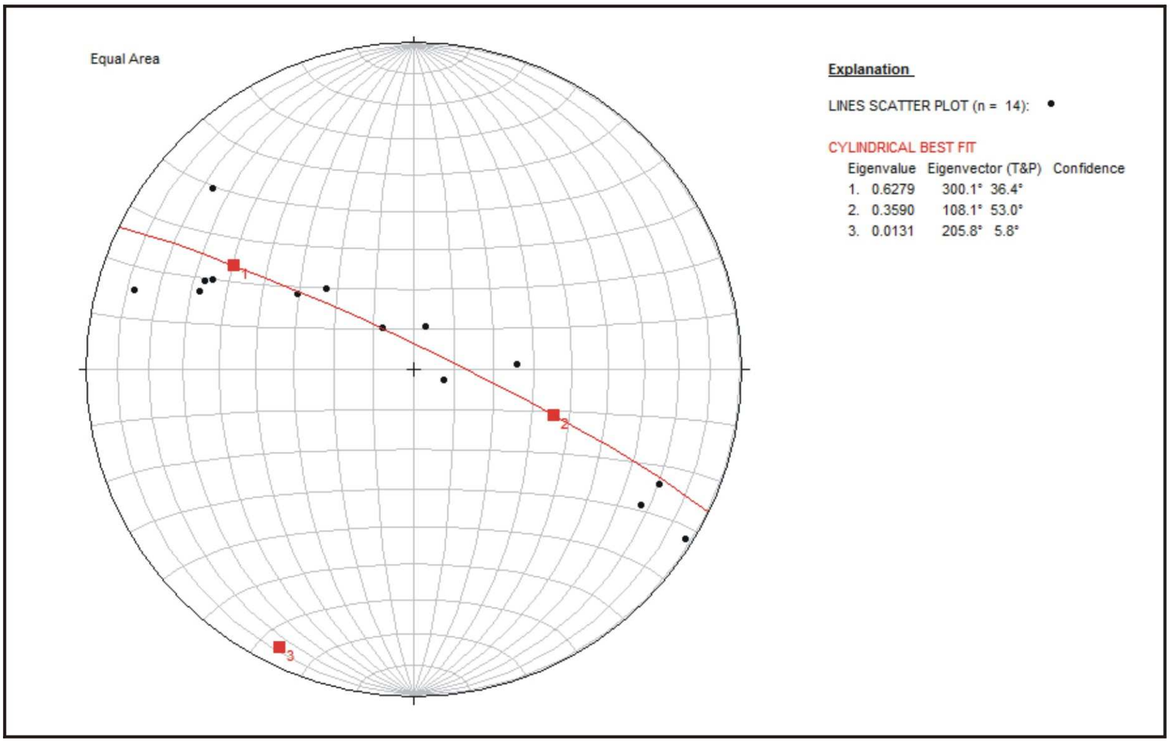

Figure 6.8: Schmidt equal area stereonet showing the attitude of the Abra del Condor axis. The circular best fit technique was used to define trend and plunge. North is top of diagram. Lower hemisphere projection.

The correlative syncline of the Abra del Condor structure exposes Los Monos shales. This syncline is a complex structural distribution; extremely tight with vertical to overturned limbs, and almost isoclinal geometry in the north of the studied area but becoming broader and more open to the south (see figure 6.1). Further to the north, outside of the area of my study it appears that this syncline is broader with steeply dipping limbs (Figure 6.9).

The structure to the east is the Piedra Larga anticline. This fold is limited underneath by the Piedra Larga thrust, which superimposes Devonian Icla deposits on top of Tarija Carboniferous rocks. The stratigraphic displacement is around 1,000 m (3,300 ft) (see Figures 6.1 and 6.2). This structure has a steep backlimb in the north with dip values of 75° to 90° to the WNW and moderate to high dip values in the south of about 55° to 70° to the WNW, increasing closer to the thrust. High dip values are probably associated with a flat or a very low angle ramp relation of the sedimentary column with respect to the Piedra Larga thrust. A main difference from the interpretation of Florez Niño et al. (2005) is that I do not recognize a well developed forelimb for this anticline. I believe the west dipping deposits of the hinge and the backlimb are truncated by the Piedra Larga thrust (see figure 6.2). My interpretation was inferred from the dip values and the distribution of cross stratification in the Huamampampa Formation that allowed me to define the top of the beds to the west in regions close to the thrust, implying that these are not overturned (Figure 6.10). This interpretation is in accordance with that of Ayaviri (2002).

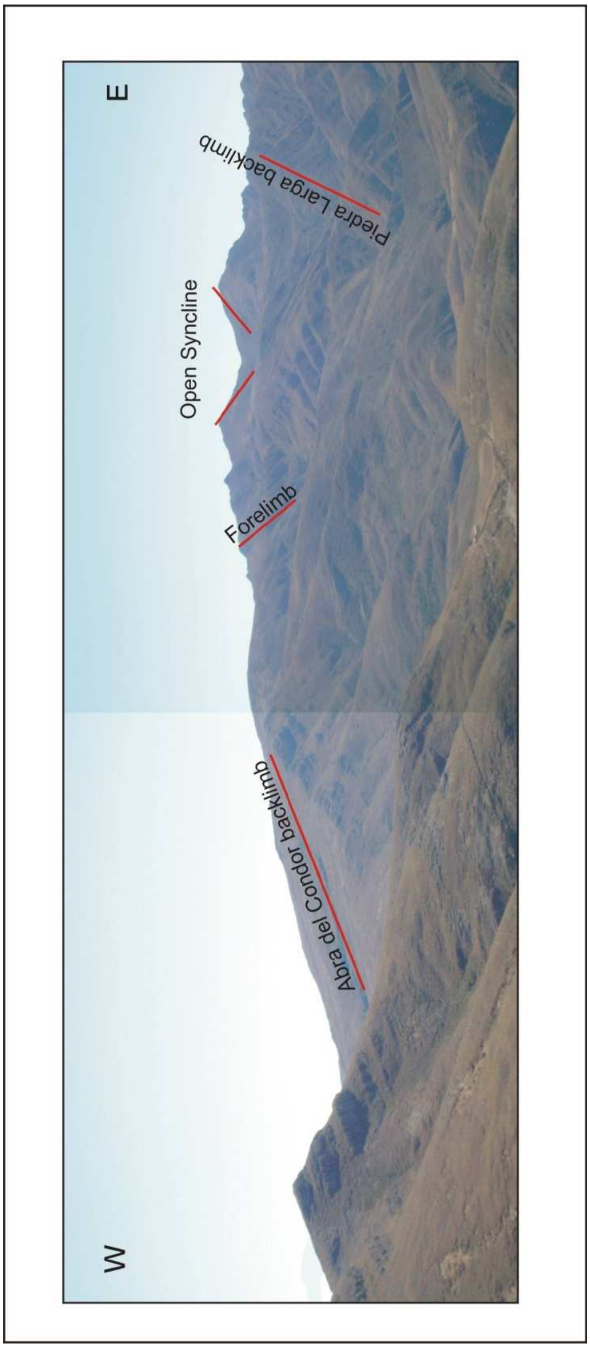

Figure 6.9: North regional view of the Abra del Condor region. The Abra del Condor anticline has a gentle backlimb and a steeper forelimb. An open syncline is present in the distance. The steep backlimb of the Piedra Larga anticline appears to the east. This picture is outside the geologic map of Figure 6.1 (further to the north).

Figure 6.10: South view of cross bedding stratification for the Huamampampa formation, showing the top of the beds to the West. Green and yellow lines are bedding. This allows me to interpret these strata as part of the steep Piedra Larga backlimb. Hammer for scale. For location see letter E in Figure 6.1

6.2 SUBSURFACE ANTICLINE

Subsurface fracture data was obtained from multiple cores of gas and condensate fields within the Devonian basin. The characteristics of the anticlines that form the eastern Subandean Ranges, where Devonian reservoirs are located, include a common geologic history and present an overall similar structural geometry along the structural axis. I worked on one of these anticlines to qualitatively assess fracture distribution and its relation to the structural evolution using kinematic models (see Chapter 4 and 5), and then test the results obtained against data from microfracture studies in core (see Chapter 9 and 13). The structure for which I built a structural model is part of a gas field in the Argentinean NW; I will refer to this structure as the “Subsurface Anticline” hereafter.

As stated in chapter 2, the sedimentary rocks that composes the Lower Structural level in this region of the Subandean ranges, constitutes about 2,500 m of sedimentary rocks subdivided into the Kirusillas, Santa Rosa, Icla, Huamampampa and Los Monos Devonian formations. The thicknesses of these units are defined from regional studies, seismic and wellbore data. In order to simplify my structural analysis this column was divided into a 1,500 m mechanical stratigraphic unit formed by the Kirusillas and Santa Rosa Formations; a 900 m mechanical stratigraphic unit formed by the Icla and Huamampampa Formations; and a 200 m thick unit that corresponds to the Los Monos Formation. These subdivisions are related to the stratigraphic distribution of these formations; where the Kirusillas and Santa Rosa formations constitute the Cinco Picachos Supersequence and the Icla and Huamampa formations of the Las Pavas Supersequence.

The Subsurface Anticline has a doubly plunging structure, which follows the northeastward regional trend, with strike values around 10° to 15°. Analogously to the Abra del Condor anticline, this fold is asymmetric with dip values around 40° to the west-west north in the back limb. The forelimb dips from 60° to 80° to the east-east south. Figure 6.11 is a cross section of this fold. Deeper in the fold the forelimb is steeper and in some locations overturned. The interlimb angle *i* has values between 60° and 80°, putting this anticline in the upper limit of close folds of Fleuty's classification (1964).

The deformation history interpreted for this structure is based on the inference of a fault propagation fold. Such a fold would produce an increment in the fold amplitude and would explain the asymmetric geometry and the steep forelimbs (Mitra, 1990). This fold was affected later by a fault bend folding process. The tectonic transport direction, was along a strike of 106° aas indicated by the perpendicular to the fold axis orientation. The displacement on the fault is variable along the fold, reaching a maximum of 6100 m in the center of it, diminishing toward the anticline noses. The combination of fault propagation and fault bend folding processes resulted in an average shortening of 30%. My kinematic interpretation differs from that of Starck et al. (2002b) for the Subandean Ranges presented in Chapter 2. Since the asymmetry and overall geometry of the fold is not explained in my thesis as a consequence of deformation in the final stages of evolution, but related to a simpler chronological deformation process.

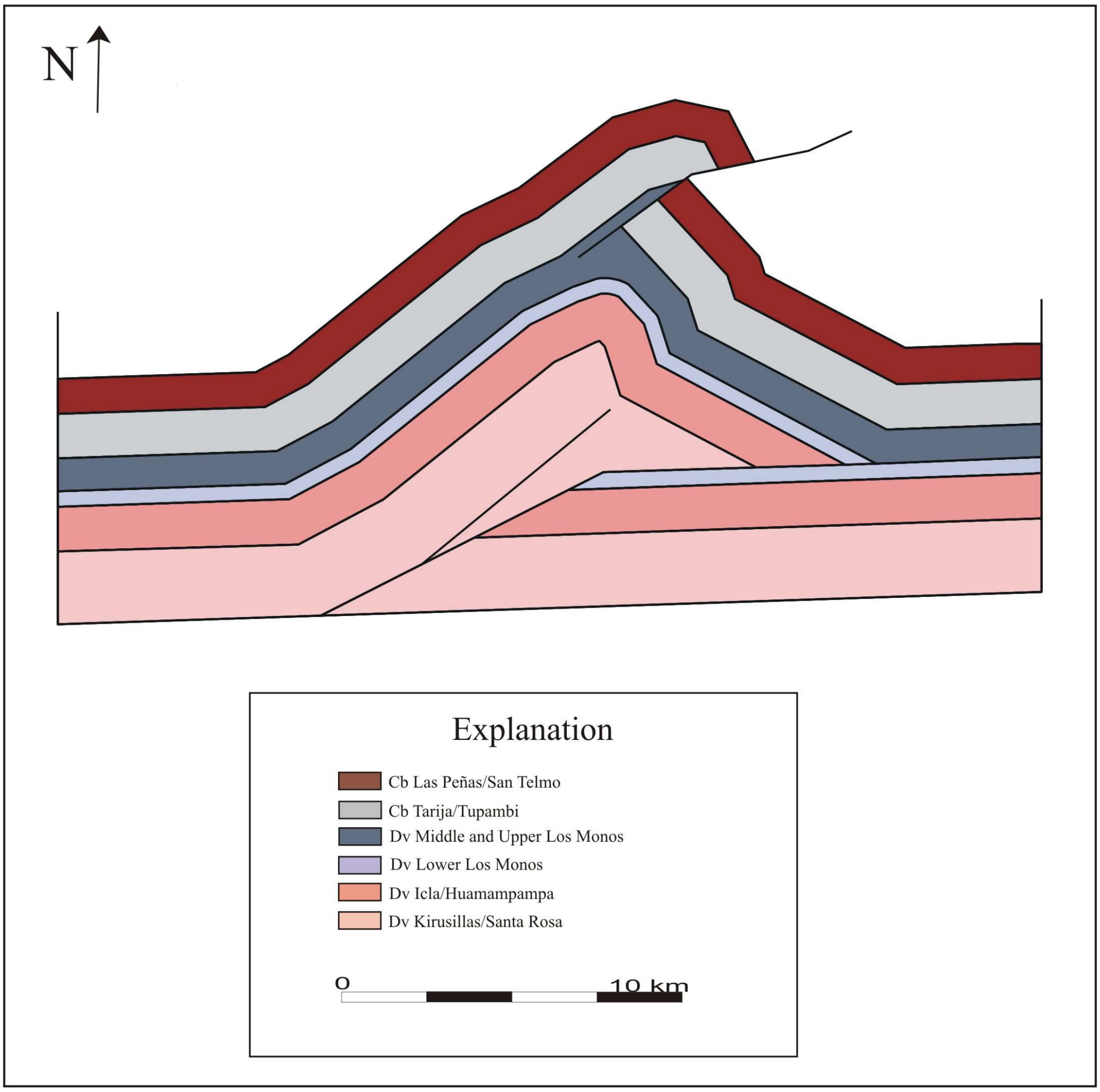

Figure 6.11: Cross section of the Subsurface Anticline, showing the stratigraphy and distribution of the limbs. No vertical exaggeration.

CHAPTER 7: STRUCTURAL MODEL

7.1 Sequenced Cross Sections

Based on outcrop, seismic and wellbore data I constructed a sequenced six cross section for the Subsurface Anticline (see Chapter 6) (Figure 7.1) that account for the present day geometry and the deformation evolution that cause the fracture system to form. As previously stated, this structure constitutes a double plunging anticline; therefore, I built four cross sections in different positions along the strike of the structure, and two more cross sections were made in the north and south closures of the anticline. These cross sections were built using algorithms described by Suppe for fault bend folds (Suppe, 1983), and for fault propagation folds (Suppe and Medwedeff, 1990). I used the commercial software 2D Move® and LithoTect^{TM}. Later, I integrated the results of the two-dimensional models in 3D to build a tridimensional geologic model. Fracture-related analyses (models of fracture occurrence in the presence of folds) presented in chapter 3 were later applied to this structural model.

Although the cross sections on figure 7.1 represent the Lower, Middle and Upper structural levels (see Chapter 2) of the Subandean ranges for this zone, the main focus of my structural analysis was on the Lower Structural Level where the Devonian reservoir is located. I used the present day geometric distribution of the middle and superior structural levels as a constraint to validate the interpretation of the overall structure. Within the Inferior Structural Level, the top of the Devonian Huamampampa sandstones constitutes the main focus of my study since it is the principal reservoir of the Devonian basin. For this reason I used it as the regional datum (McClay, 1992) for restorations in 1D and 2D; for the construction of 2.5D surfaces (explained below) and 3D volumes, their subsequent forward modeling and fracture related properties analyses.

As it was described in chapter 6, I interpret the fold to have formed as a result of fault propagation (Mitra, 1990), which generates an initial structure with a steep forelimb. At the Huamampampa horizon, beds are deformed but not transported along the fault. Later fault bend folding is marked by a second eastward verging thrust with a cut off angle of 24°. This thrust transports the previous fold with variable displacement along the fault. For simplicity in figure 7.1, neither of the backthrusts in the Middle Structural Level (see Chapter 2) are shown, and I only interpret the top of this level.

7.2 Line Balance Restoration

A first step to validate my interpretation was to perform a line balance single step palinspastic restoration for each of the six cross sections, using line length restoration methods (Figure 7.2). LithoTect^{TM} commercial software was used to perform the restoration, taking as a premise that the length of the lines and the thickness of the beds are preserved before and after the deformation. A pin line was set on the not deformed horizons of the easternmost region of each section, and a loose line was set on the opposite end. In Figure 7.2, a consistent difference is registered between the length of the Lower Structural Level and the one of Middle and Upper levels; the latter two always shorter than the first. Since abundant well data and outcrop information was used as a constraint to build these sections, I do not consider this an error in my interpretation. I believe part of the shortening registered in the Lower Level was transmitted to the following structural trend located to the east. This is not an isolated structure, but a part of the overall Subandean Ranges system. Therefore, even when most of the shortening of the Lower Structural Level is transmitted to the Middle and Upper levels, some of the movement can be passed onto the following structure developed in the deformation sequence.

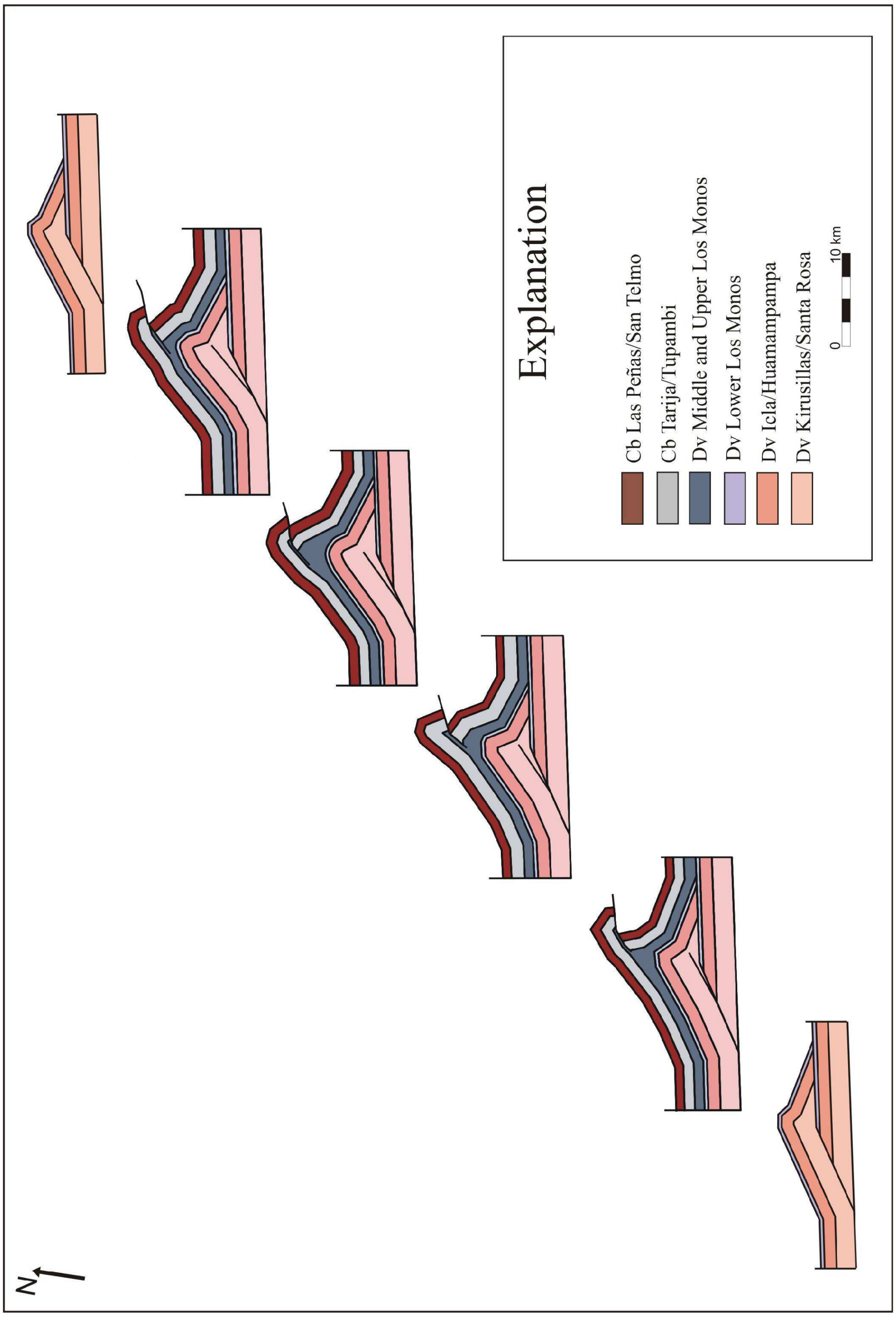

Figure 7.1: 2D cross Section 1 through 6 used to construct the 3D structural model.

7.3 Restoration in 2D

The next step of my analysis was to perform a sequential restoration of the cross sections in 2D. The intermediate stages of the deformation between the fully deformed and the fully restored stages are presented (Figure 7.3). The use of sequential restoration gives an insight on the structural evolution, enabling assessment of the consecutive steps that can lead to the final geometric distribution (Groshong, 2006). This constitutes a more rigorous analysis to support my interpretation. I performed a sequential restoration in four steps, only for the Lower Structural Level (Figure 7.3). Although this structure is the consequence of two deformation processes in sequence, the limitations of the 2D algorithms in the software force me to restore the cross sections as if the fault propagation fold and the fault bend folding were contemporaneous. I used a combination of geometry field interpolation, flexural slip and area balance in LithoTect™ to restore the sections. In order to account for unfolding, the Santa Rosa/Kirusillas package by the fault propagation fold, I used geometry field interpolation. A parallel complex geometry was employed it to hypothesize the earlier stages in the evolution of the main structure (Figure 7.4). The resulting horizons were later used as a template to transform the remainder of the structure.

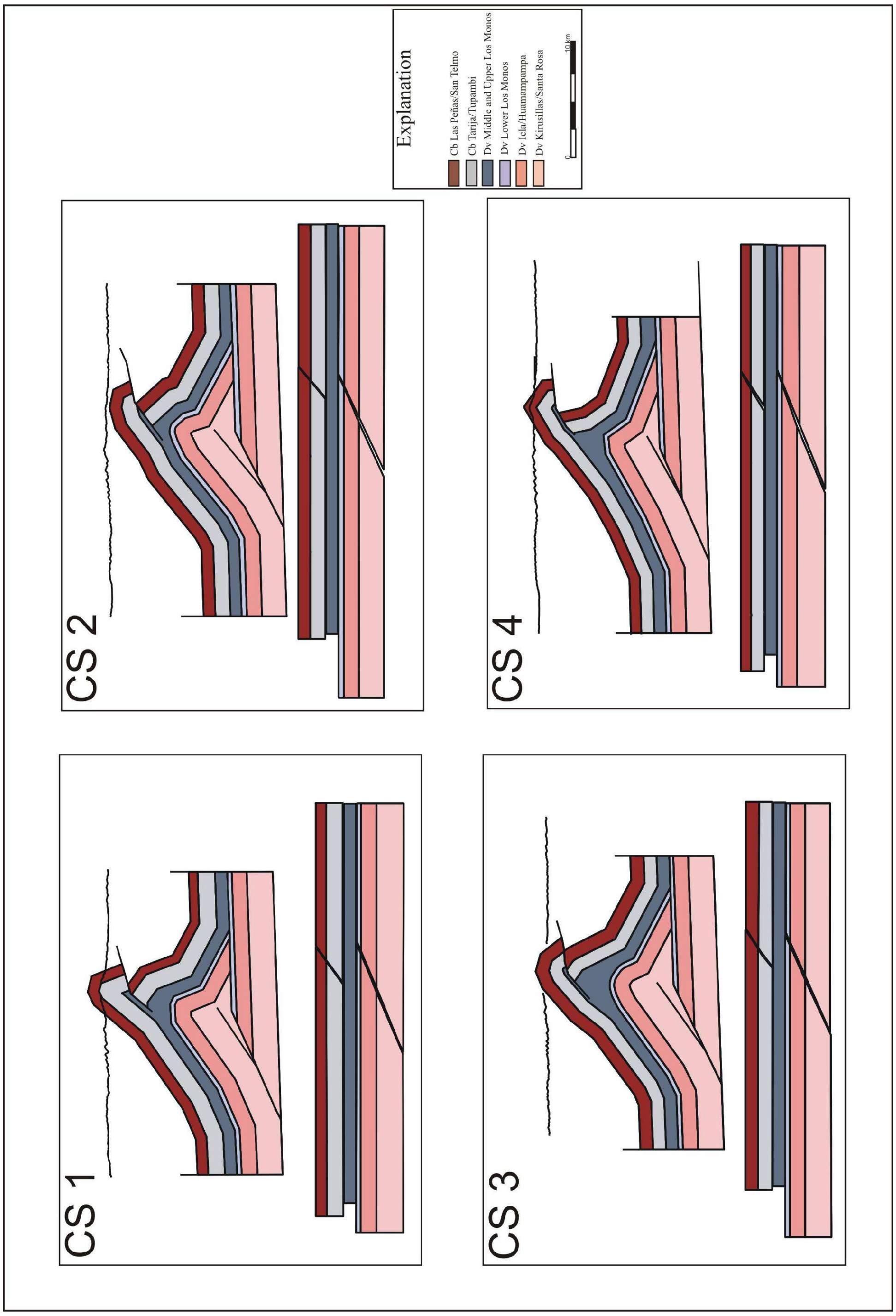

Figure 7.2: 1D line length restoration of cross sections 1 through 4 in single step.

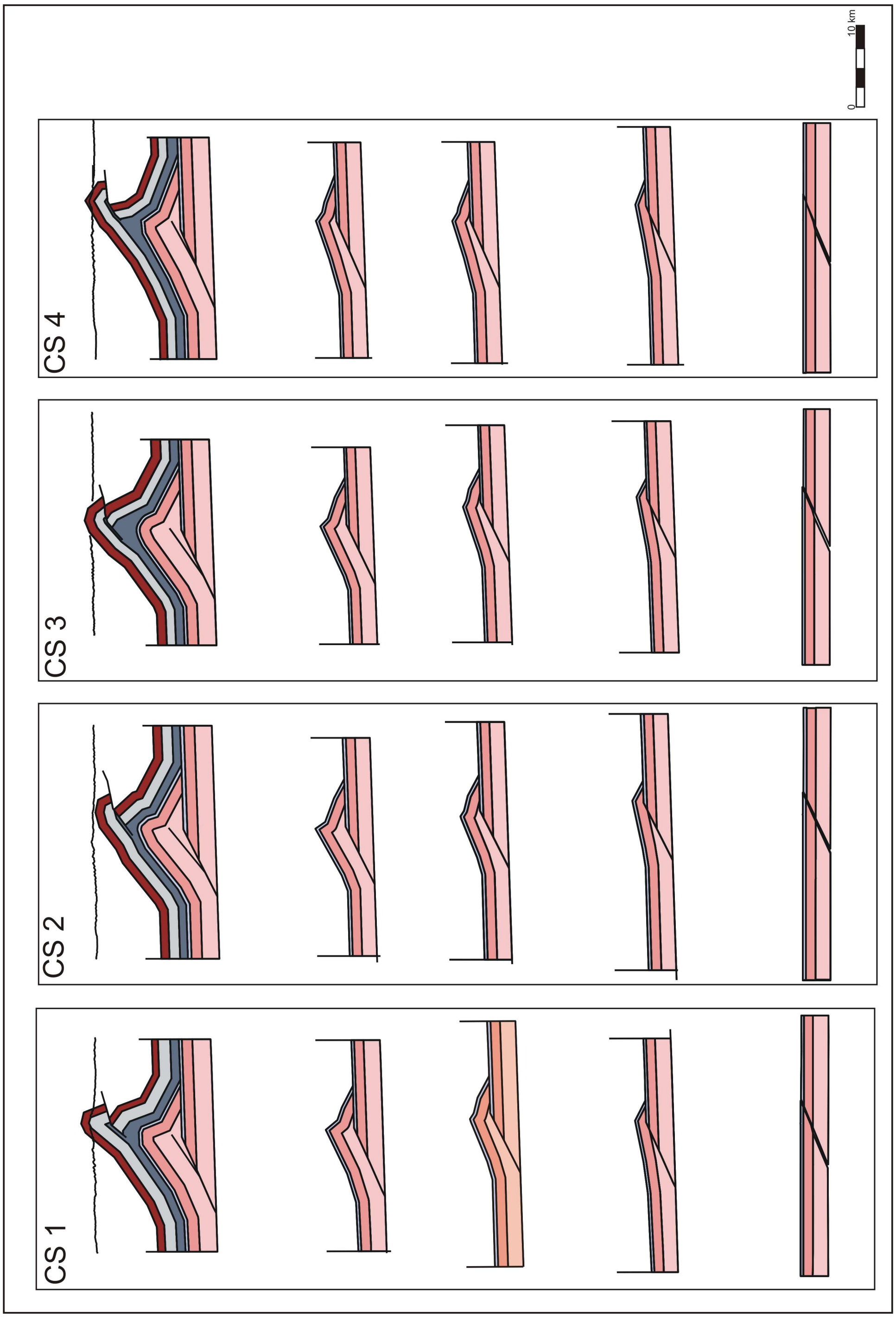

Figure 7.3: 2D restoration of cross section 1 through 4 in incremental steps. For explanation of formation units see Figure 7.2

To check the validity of each of these stages, a combination of the flexural slip algorithm (see chapter 4) used to balance the Icla/Huamampampa package and the Los Monos wedge in the Lower Structural Level. Area balance was used to balance the Kirusillas/Santa Rosa package. I restored each of the intermediate steps to the undeformed state, and then compared these to the single step line length restoration; an excellent match was observed between the two. Minor differences appear between the deformed and undeformed areas of the Kirusillas/Santa Rosa package in each step. The area was constrained assuming the same line length as that of the Icla/Huamampampa and Los Monos units, and the undeformed thickness for the Kirusillas/Santa Rosa package. The difference between areas is around 6% but it rises up to 10% in the deformation step 4.

In spite of the limitations presented by the method, I believe it support my geometrical interpretation of the geology of the Subsurface Anticline. Since the specific history of deformation will have a major impact in the control of the fracture distribution, the deformation evolution was performed in the 3D forward modeling (see below) analysis to assess fracture distribution.

7.4 Surface and Volume Construction

Once the validation of the interpretation was done in 2D, I integrated the present day geometry of the six cross sections in a tridimensional environment using 3D Move® (Figure 7.5). Then, the Kriging algorithm was used to interpolate information between the cross sections and create a 2.5D (see below) deterministic surface defined by a list of triangles (Moretti and Delos, 2006), which ties the tops of the Huamampampa Formation in each cross section. This was done both for the hangingwall and the footwall (Figure 7.6a). I also created a surface from the individual traces of the fault in each section, but in this case the geometry is much simpler than those of the formation tops and the Spline algorithm was used. This algorithm creates a simpler surface, allowing me to avoid erroneous point interaction (Bonora, personal communication), which generates spurious concentrations of strain (Figure 7.6b).

From the surfaces obtained for the hangingwall and footwall, two oriented grids (given by a rectangular mesh) were created, with a size of 1000 x 1000 and a strike of 16°, so it would coincide with the trend of the structure. These grids do not tie perfectly with the surface but the differences are negligible. The gridding process is done to facilitate restoration and strain analyses, due to the fact that fewer points are present in the grids, facilitating computational calculations.

The process to create surfaces defined above, represent what Moretti and Delos (2006) calls 2.5D surfaces, since they are represented in 3D but they have area and not volume. In order to perform strain analyses a volume is needed. To account for this I constructed a surface 400 m beneath the top of the Huamampampa (this value was used to define approximately regular cubes with similar side and thickness values). I used for this the function parallel folding in 3D Move, since I consider these folds as constant orthogonal thickness Class 1B according to Ramsay classification (1967). Finally, I created a 3D volume between both surfaces, defined by regular cubes that allowed me to perform strain analyses.

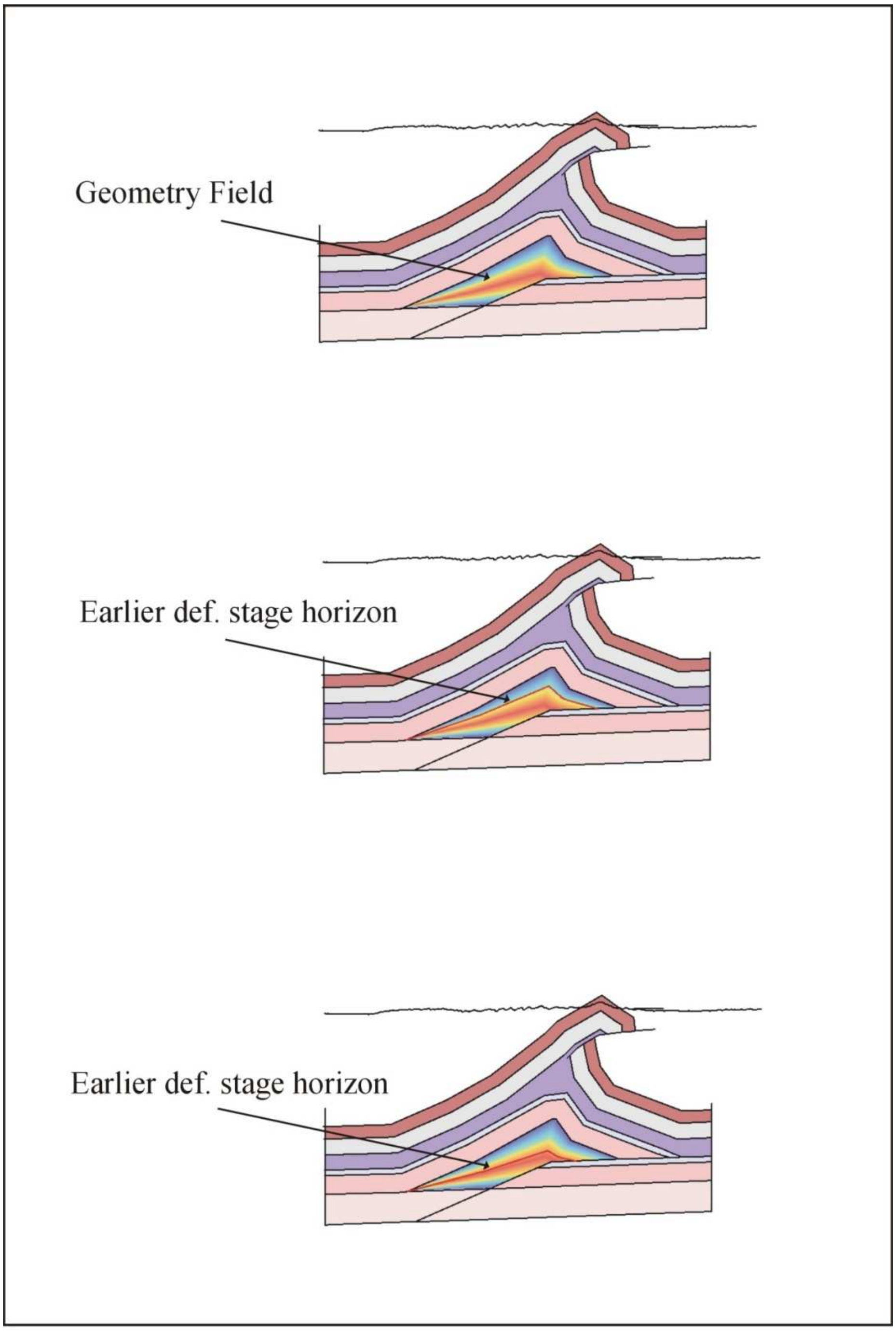

Figure 7.4: Geometry field defined for the Kisrusillas/Santa Rosa sedimentary package and used to define previous deformation stages in 2D. For explanation to formation units see Figure 7.2

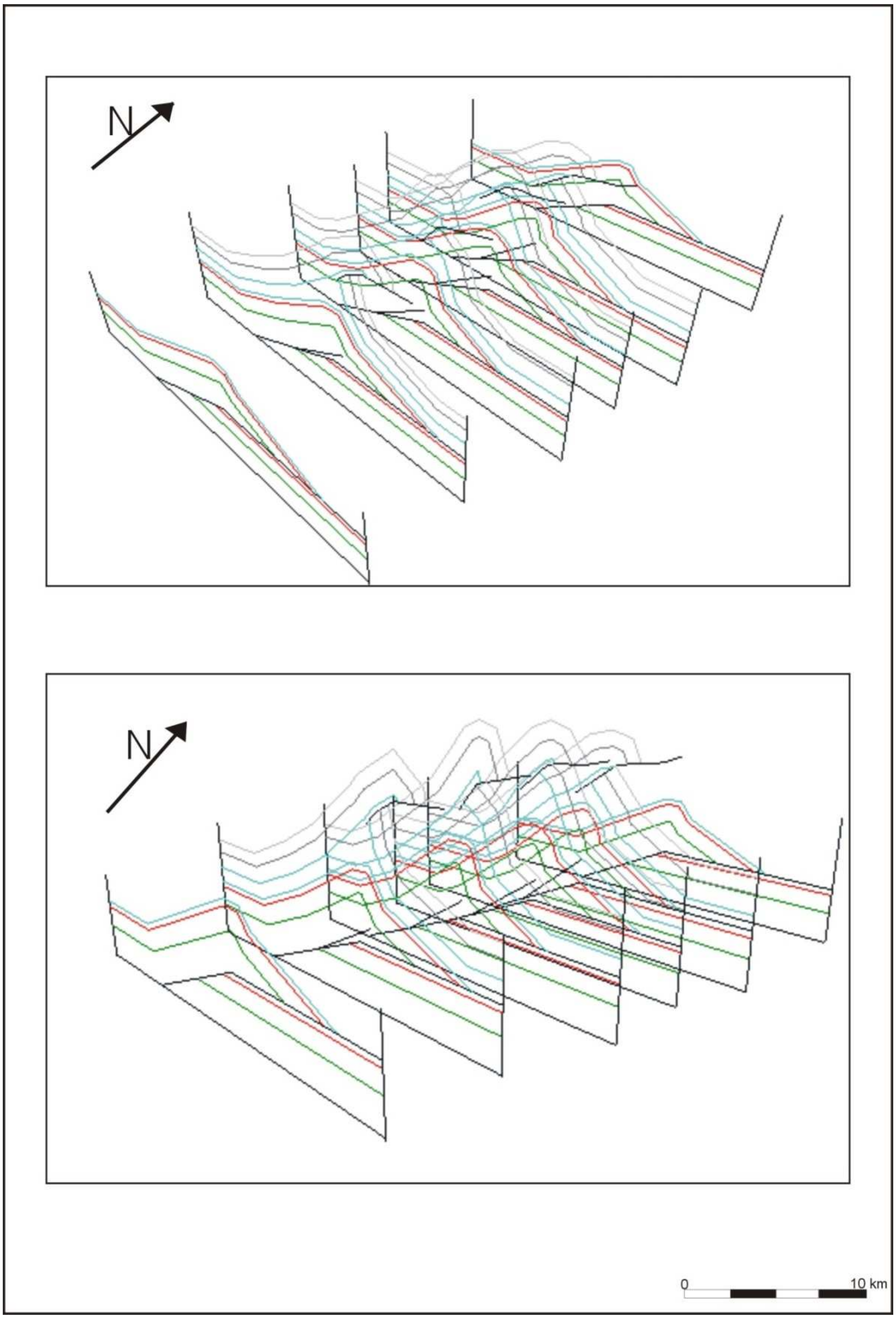

Figure 7.5: Integration of 2D cross section in a 3D environment. The cross sections correspond to those of Figure 7.1

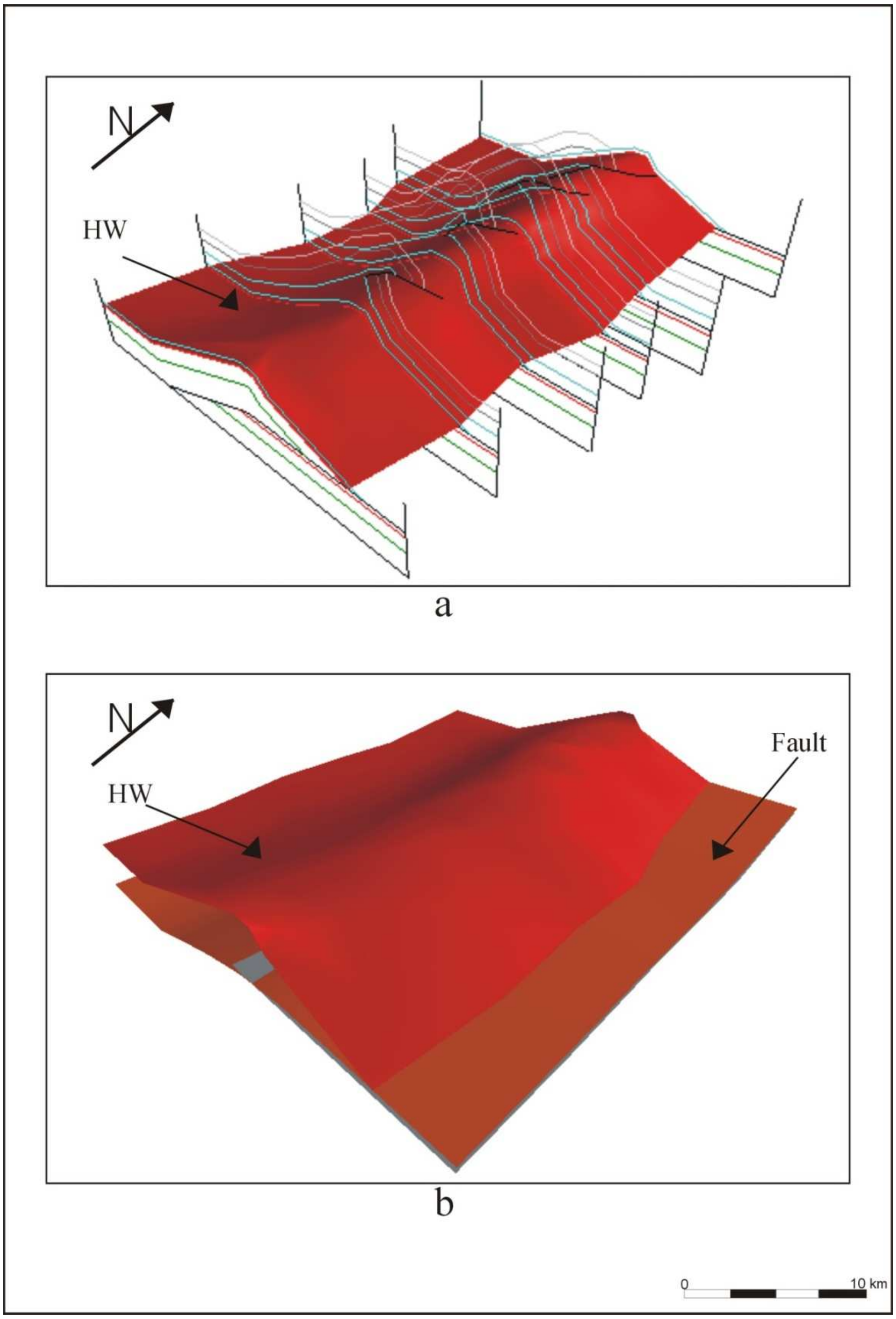

Figure 7.6: 2.5D surfaces created from 2D cross sections using Kriegging and Spline algorithm. a: Cross sections and Huamampampma top. b: Huamampampa top and fault.

7.4 FORWARD MODELING IN 2.5D AND 3D

The history of deformation will have a major impact in the distribution of strain and fracture analyses. As the strain recorded by many fracture sets is very small (e.g., Olson et al., 2009), subtle steps in the evolution of a fold may be as likely to be responsible for fracture as are large scale deformation steps. For these reason I performed a forward model of both a 2.5D surface and a 3D volume, departing from the undeformed state. Through the usage of the fault parallel flow algorithm (See chapter 4), I mimicked the shape of the present day geometric distribution. To better explain the deformation workflow I defined an *initial*, *intermediate* and *final step* of deformation.

The *initial step* in this process is given by a flat surface extrapolated from the undeformed footwall, in a direction perpendicular to the regional strike (azimuth 207°) (Figure 7.7). This surface constitutes the undeformed hangingwall. After gridding this surface, I created a volume between it and a surface beneath.

The *intermediate step* is given by the fault propagation fold deformation. To model this I created a fault to the west of that one associated to the fault bend folding process that is a propagation fault. Then, I modeled the deformation of both the flat surface and flat volume, by increasing the amount of shear. This created a gently dipping back limb and a steeply dipping forelimb. Figure 7.8 shows the modeled evolution of the deformation for the Huamampampa top.

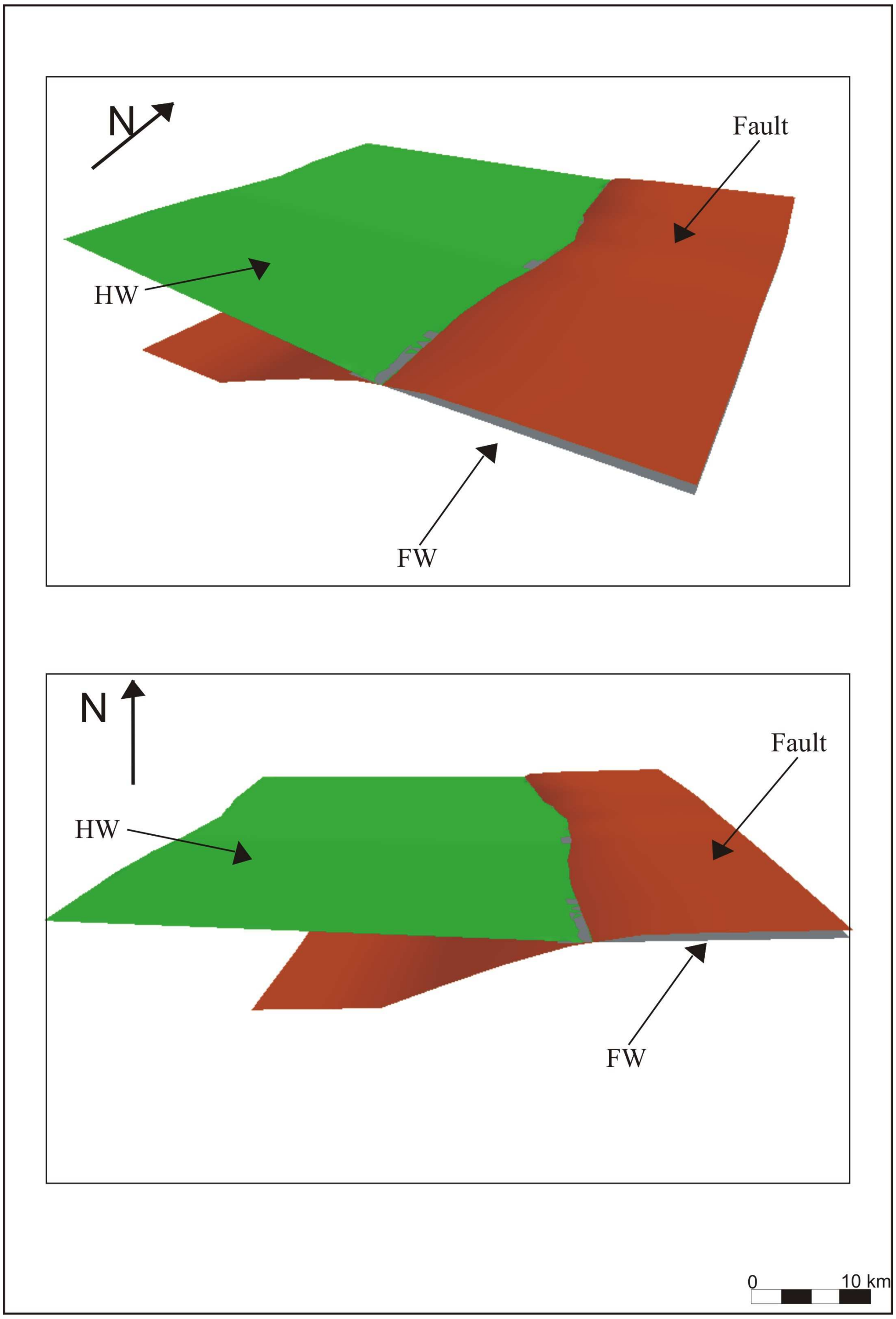

Figure 7.7: 2.5D fault surface and flat Huamampampa hangingwall (HW) extruded from the footwall (FW).

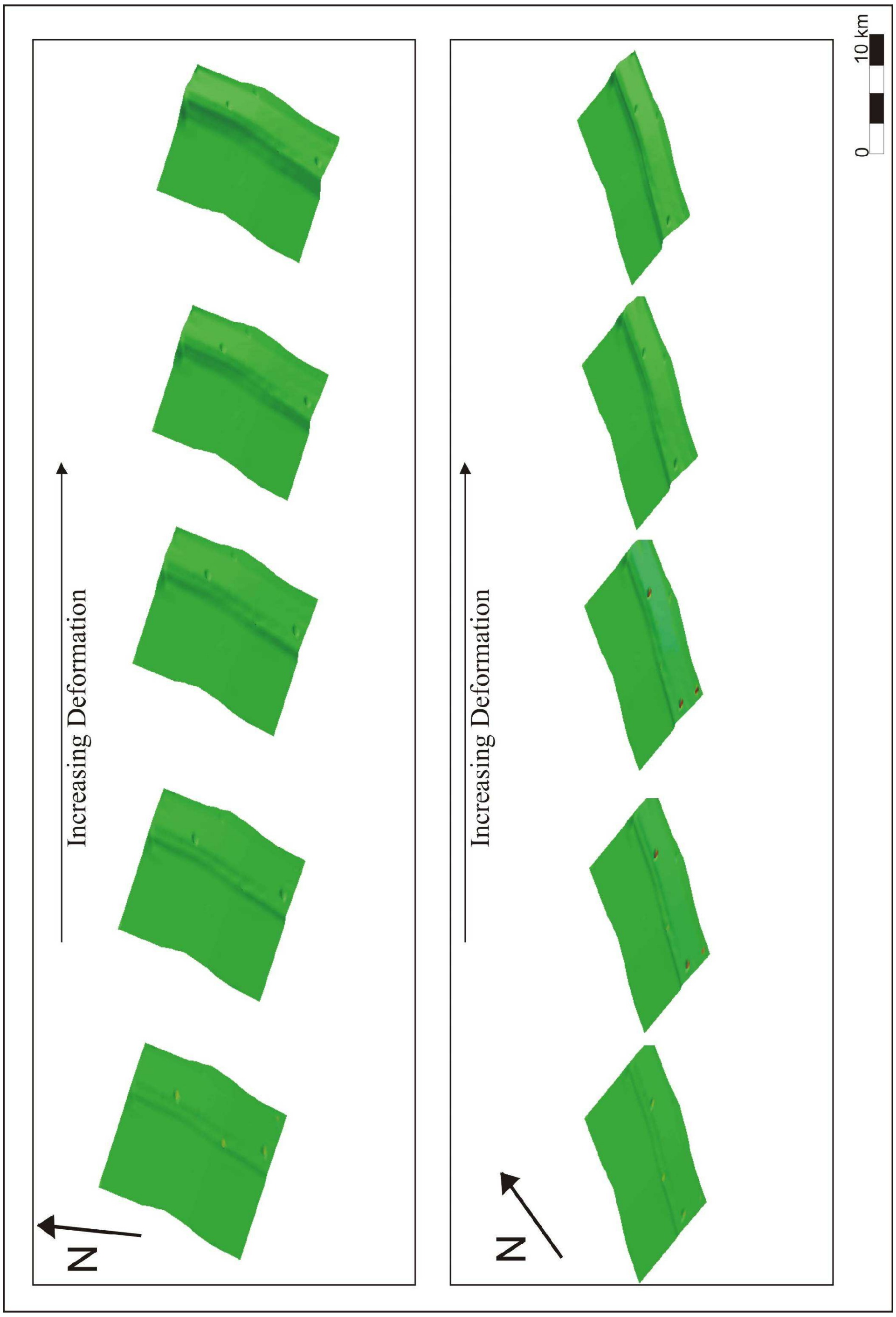

Figure 7.8: Two different views of the deformation sequence associated to the propagation fault for the Huamampampa top. Increasing deformation from 10° to 50° of shear, from left to right.

The *final step* in the deformation history is the displacement associated with the fault bend folding process. As I mentioned in Chapter 6 the amount of displacement is not constant along the fault, reaching a maximum in the center of the structure and diminishing as we move to the fault tips. To account for this I constructed an Allan map (Allan, 1989) between the present day geometry of the hangingwall for the Huamampampa top, the top at the footwall and the fault. From the intersections of these surfaces with the fault I identified two lines that allowed me to define “heave bands” that account for the change in displacement along the fault. Finally, I used these heave bands and the fault parallel flow algorithm to deform the *intermediate step* surface and volume. However, this time instead of adding shear, I added incremental amount of displacement in the direction of tectonic transport (azimuth 106°) (Figure 7.9).

As a way to support my interpretation, I compared the present day geometry of the Huamampampa top surface and volume, to those obtained through the forward modeling process, obtaining an accurate fit. I should mention that some minor differences (few tens of meters) appear in the hinge between the model and present day geometry. The modeled fold is less tight than the actual one. This could be either explained to minor errors related to the model or to a posterior deformation as that one interpreted by Starck et al (2002b).

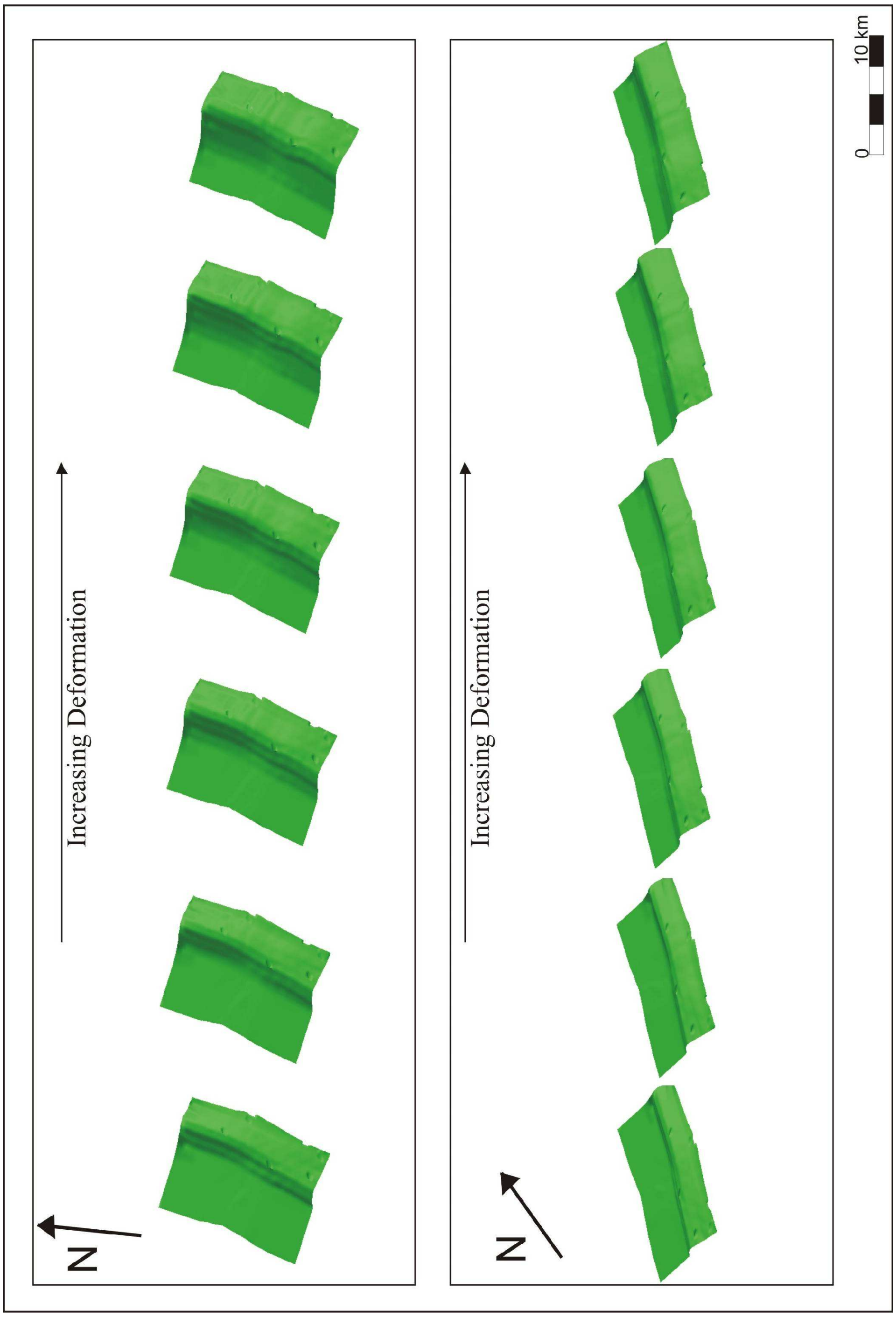

Figure 7.9: Two different views of the deformation sequence associated to the bending fault for the Huamampampa top. Increasing deformation from 0 to 6100 m of displacement, from left to right.

7.5 Static Analyses

The theory and basis of the curvature analyses was presented in chapter 4, here only the results of these studies applied on the 2.5D surface of the Huamampampa hangingwall are shown.

7.5.1 CURVATURE

Simple curvature analysis of the Huamampampa top (Figure 7.10) shows, as expected that the maximum values (red colors) are located along the hinge zone of the structure. The values appear to be homogeneously distributed along the strike of the structure, and decrease towards the nose of the anticlines. This is consistent with the presence of a broader hinge zone and gentler dipping limbs, associated to the absence of the propagation fault in the north and south plunge (see figure 7.1). According to the theory discussed in chapter 4 that relates curvature with fracture presence, the hinge zone should have high fracture intensity. A well trajectory into the hinge that cuts across fracture strike or where the fractures were closely spaced should intersect a large amount of fractures. Moreover, according to Stearns' (1968) model discussed in chapter 3, the type of fracture for this zone should parallel the fold axis. Such fractures are envisioned to be a consequence of outer arc extension during orthogonal flexure mechanisms. They are more abundant the tighter the structure and in lithologies where the extensional strain is accommodated by fracturing. Cohen (2002) analyzed fields similar to the one analyzed here, and reports an increment of the number of fractures parallel to the fold axis for wells drilled in fold hinges.

7.5.2 GAUSSIAN CURVATURE

Gaussian curvature analysis shows maximum values where the hinge is tightest (Figure 7.11) suggesting that the fracture intensity should be highest in that region. However, the pattern is different from one of simple curvature because even when the maximum Gaussian curvature values are located along the hinge, the highest values are related to small changes in the immediate vicinity of the cross sections. This is a consequence of the interpolation algorithms and not related with the shape of the overall structure. In other words, they appear to be artifacts. Because Gaussian curvature values reflect major and minor axis curvature I would have expected to find extreme values towards the noses as a consequence of the presence of higher curvature values in two directions in these parts of the fold. However, this is not the case and only patchy isolated extreme values appear along the structure.

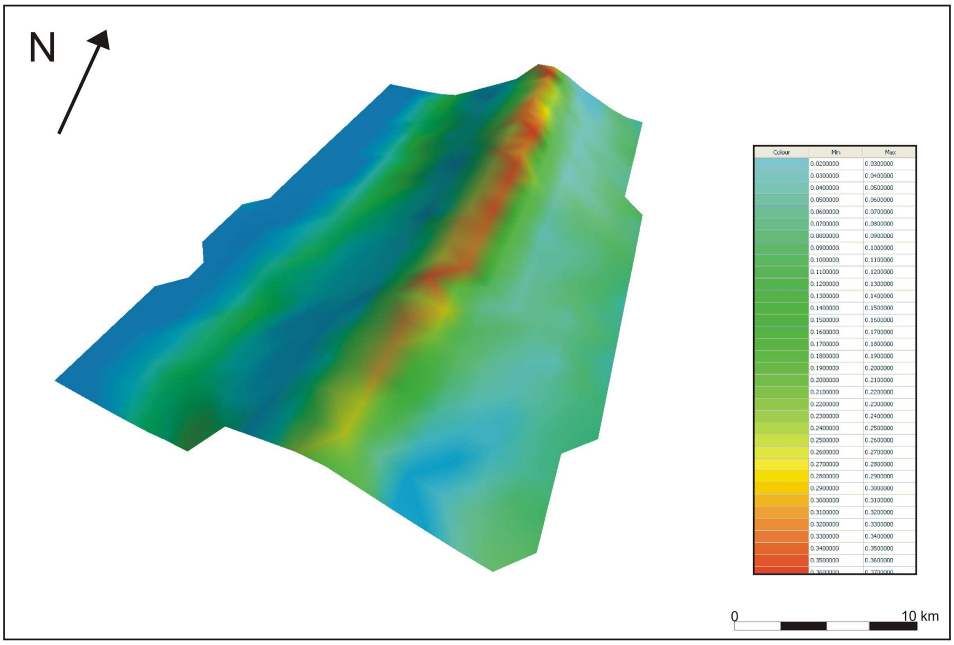

Figure 7.10: Curvature distribution for the Huamampampa top, calculated with 3D Move®. Red colors indicate highest curvature.

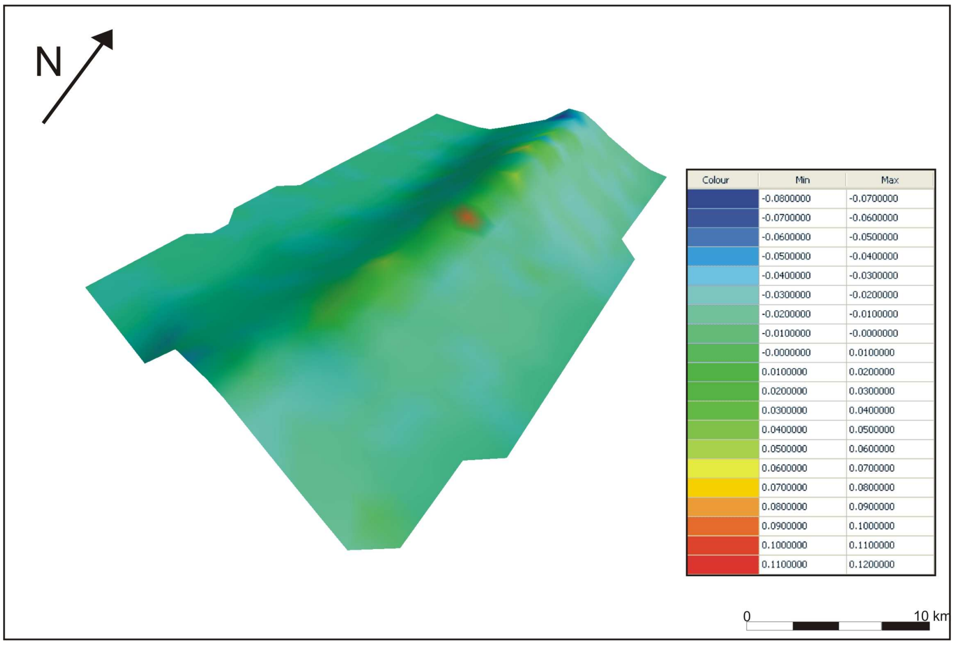

Figure 7.11: Gaussian curvature distribution for the Huamampampa top, calculated with 3D Move®. Red colors indicate highest curvature.

7.6 Kinematic Analyses

As was stated in Chapter 4, current and cumulative dilatation provide information on the magnitude of change in volume on a body and can be used as indicators of potential for fracture development and fracture density. In this section the workflow and results of the strain evolution are presented for the top of the Huamampampa Formation in the hangingwall.

7.6.1 STRAIN DISTRIBUTION

To represent the distribution of strain and its relation to the deformation path, I chose the cumulative strain ratio e1 to e3, since this would register the areas of more intense strain. I used multiple deformation steps to simulate fault propagation fold, going from an *initial* undeformed surface, to an *intermediate* deformed step by adding 10° increments of shear up to 50° (Figure 7.12a). Analogously, the effect of the fault bend fold was simulated in multiple steps of displacement, with an increment of 1000 m for each step up to a final value of 6100 m (Figure 7.12b). From this analysis it appears that as the fault propagation fold process proceeds, the strain is increasingly concentrated along the hinge. The transport of the hangingwall block along the fault bend increases the strain ratio towards the west, close to the crest area but not necessarily on the hinge.

The volumetric change through deformation was also analyzed (Figure 7.13) and similar results are obtained. The highest volumetric changes appear to be west of the hinge position.

Couples (1997) suggests that strain studies explain fracture presence that correlate to with Type 1 and 2 of Stearns' classification (see Chapter 3). These fractures are opening mode either perpendicular or parallel to the axis fold, which bisects two Mode II shear fractures. According to my analyses these fractures should be concentrated in the crest area but not exactly on the hinge. Once again, these results seem to match the analyses of Cohen (2002), Sanguinetti et al. (1998) and Araujo and Clivio (2001) for similar fields on the Devonian Subandean basin. They conclude that Type 1 and 2 of Stearn's model are located in a crest position close to the hinge.

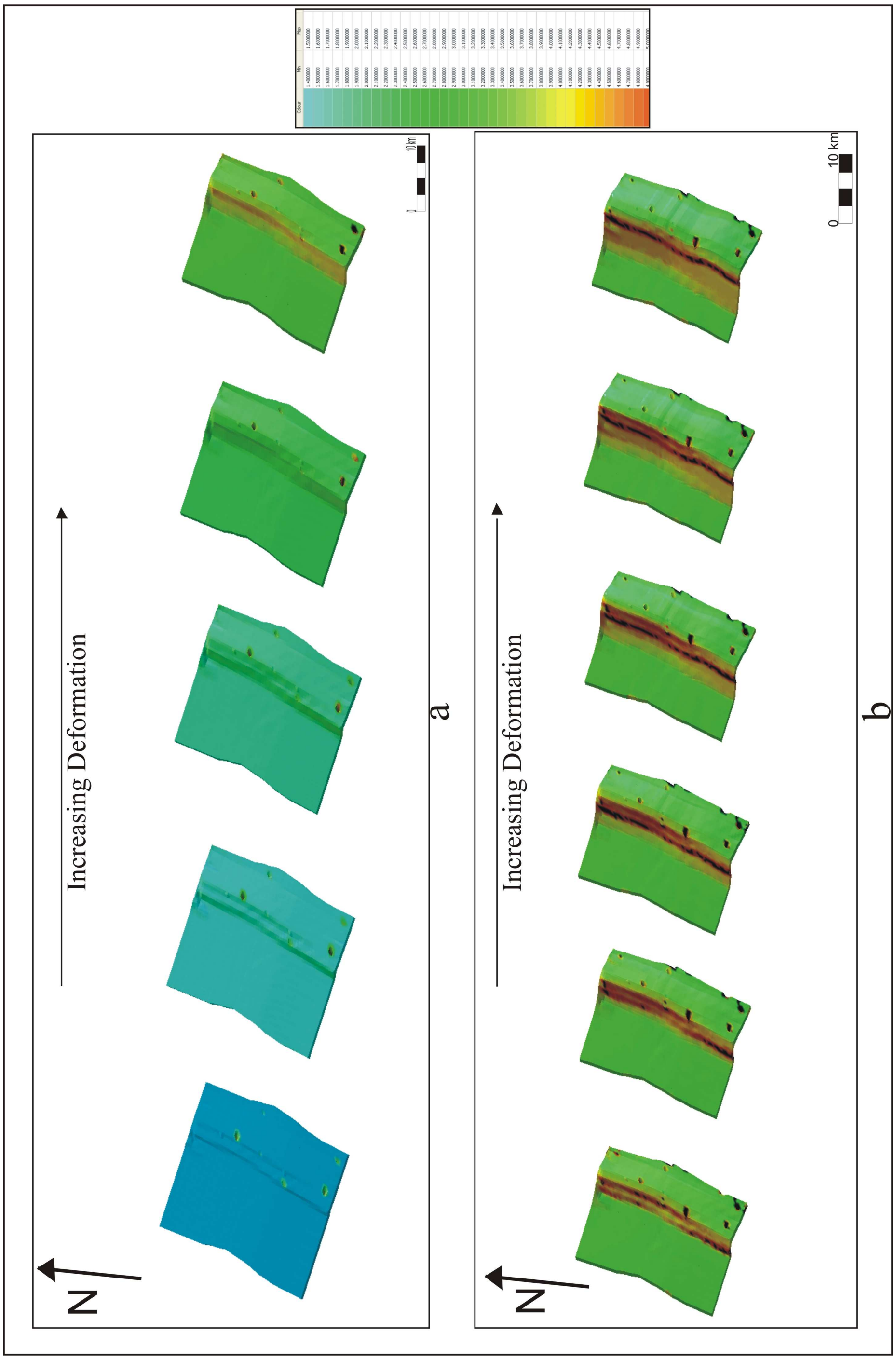

Figure 7.12: Strain distribution for the Huamampampa Formation top. Red colors indicate highest curvature. a: Strain through fault propagation folding. b: Strain through fault bend folding.

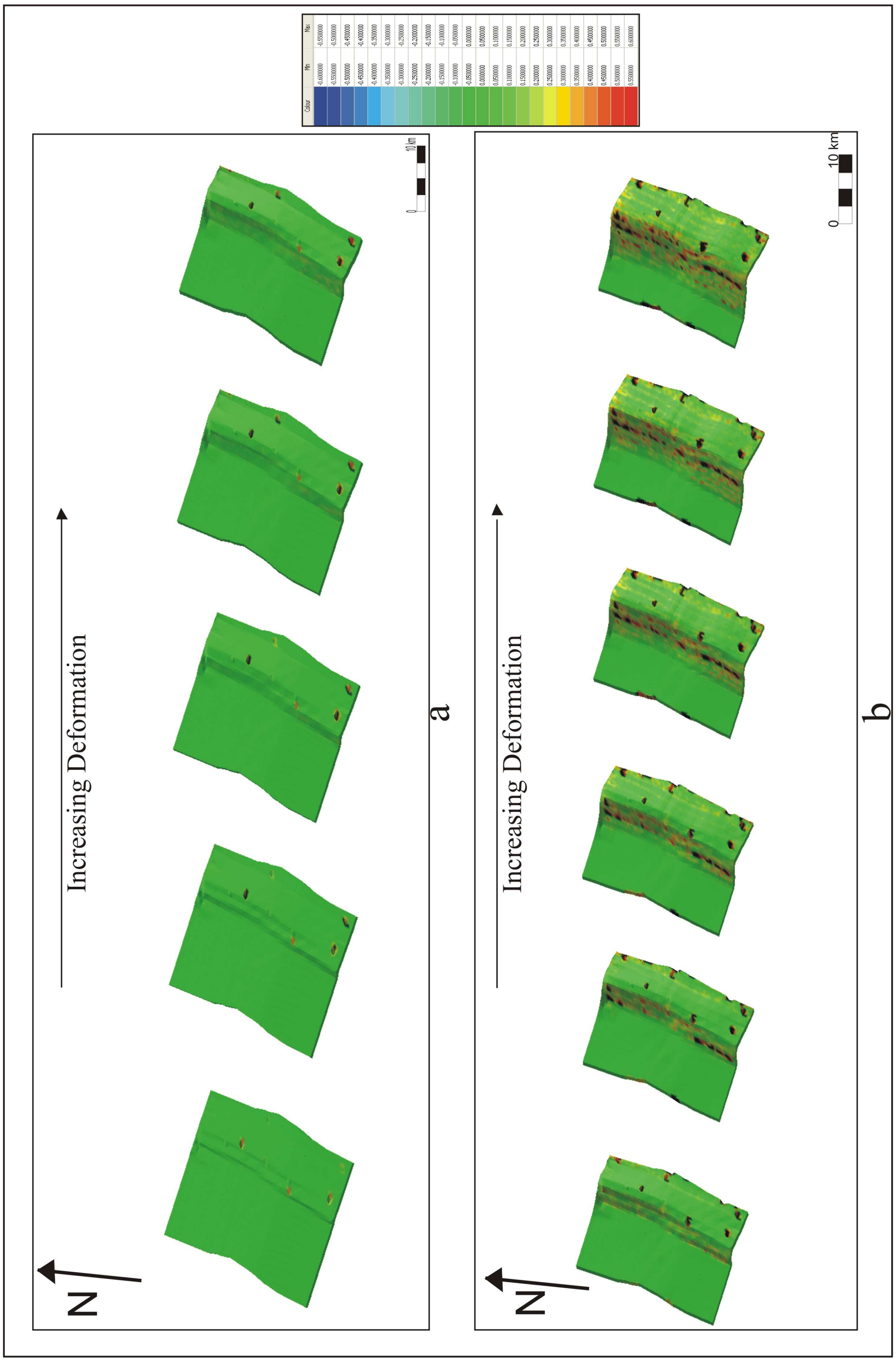

Figure 7.13: Absolute volumetric dilation distribution for the Huamampampa Formation top. Red colors indicate highest curvature. a: Strain through fault propagation folding. b: Strain through fault bend folding.

CHAPTER 8: MACROFRACTURE ANALYSES

8.1 Fractures in the Subandean Ranges

The Devonian outcrops in the Abra del Condor and Piedra Larga anticlines, allowed me to assess the fracture system exposed in these folds and to compare this outcrop observation to the analysis of the Devonian reservoir. I assessed fracture type, kinematics, crosscutting relations, orientation, and how fracture distribution is affected by stratigraphic and structural features. Most of the fractures observed in my study of the Abra del Condor fold are joints, which are opening-mode fractures having little or no mineralization (Pollard and Aydin, 1988). Some of the fractures contain trace amounts of quartz cement, but are otherwise open. I also found minor evidence of faults. Florez Niño et al. (2005) described veins (cement-filled fractures) in outcrops of the Santa Rosa Formation further to the east and outside the area of my study, but I found no veins in the Huamampampa Formation.

The Subandean Ranges contain tectonic related fractures (as discussed in chapter 3). To the best of my knowledge all analysis of the Subandes assume a synfolding origin for the fractures related to the Andean orogeny (Cohen, 2002; Sanders et al., 2004; Kozlowski et al., 2005; Moretti and Delos, 2006). My analysis of the Abra del Condor structure allowed me to address this issue and present a possible genesis and evolution for these fractures.

8.1.1 JOINTS

Two sets of fractures with a systematic orthogonal arrangement were identified in the field. Sets were defined based on their orientation and deformation mode. Information on fracture attributes is grouped into stations at various locations across the field area. Fractures were included in one of these sets based on common range of strike and dip. In addition, both sets share a number of characteristics which include: displacement perpendicular to the fracture walls (no clear evidence of shearing either in the field or thin section) almost complete absence of cement filling them (except for isolated fractures where quartz crystals were recognized with the aid of a hand lens), and an overall consistency in their orientation distribution with respect to the structure axis (Figure 8.1).

For the backlimb of Abra del Condor, these two sets can be recognized on a pavement (bed-parallel exposure) in the Upper Huamampampa. Here fractures have a high degree of alteration marked by a fill of light colored, porous carbonate that I interpret to be caliche. The exposures are also covered with lichen (Figure 8.2). These alteration processes and the absence of cement within these fractures, preclude me from measuring reliable aperture values. The low quality of these outcrops limited my analyses and impeded planned studies of fracture size distribution such as those described by Ortega et al. (2006).

A predominant Set I, trending perpendicular to the direction of the anticline axis, and a subordinate Set II perpendicular to Set I and parallel to the structural trend were defined (Figure 8.3).

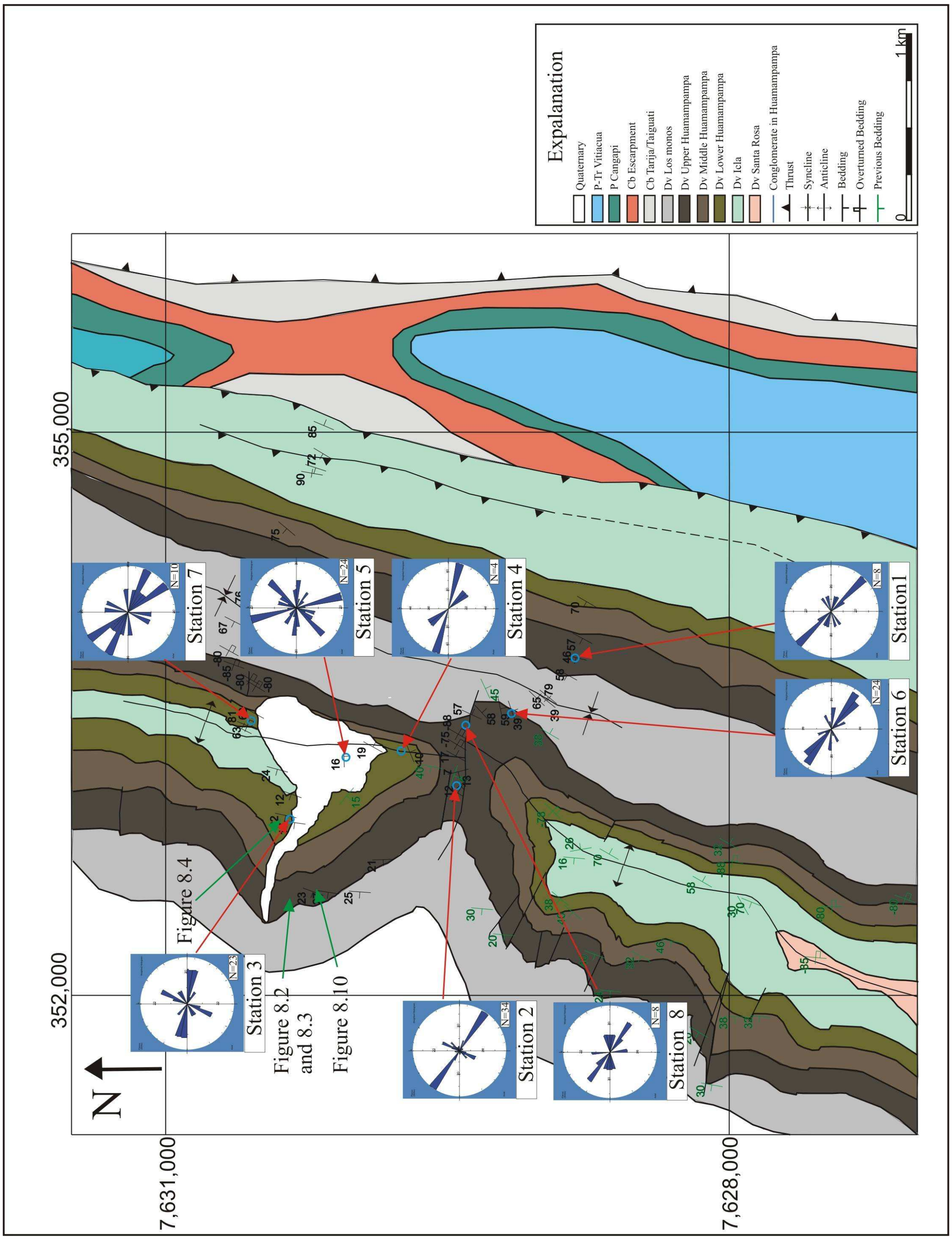

Figure 8.1: Geologic map of Abra del Condor showing station location and fracture distribution. For figure explanation see Figure 6.1 caption.

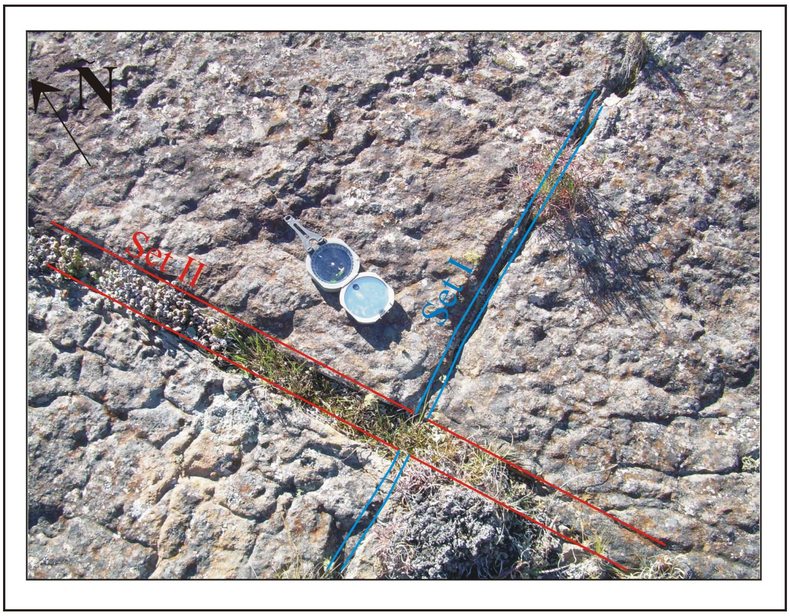

Figure 8.2: Both sets of fractures filled with caliche and covered with lichen. For location see Figure 8.1.

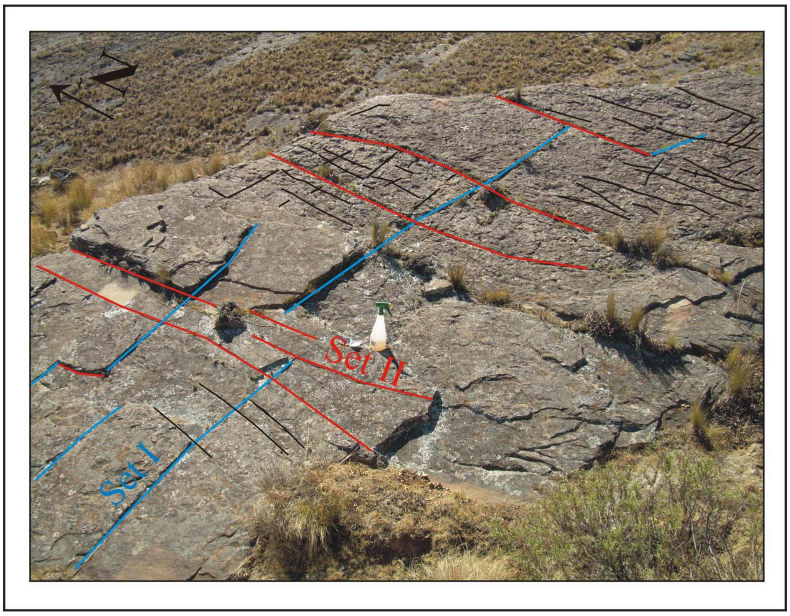

Figure 8.3: Fractures of Set I and Set II in the backlimb of the Abra del Condor anticline. For location see Figure 8.1. View toward E.

8.1.1.1 Set I

Set I includes planar and parallel fractures with lengths of about 5 m in the backlimb of the Abra del Condor anticline (see Figure 8.3). In vertical to overturned limbs it is harder to define fracture continuity. Fracture height is limited to individual sandstone beds. Individual fracture traces can range from 10 cm up to 60 cm. Fracture height is commonly limited by the presence of mechanical boundaries such as the tops and bases of sandstone beds (Figure 8.4). Multiple studies have addressed the relation between mechanical layer thickness and fracture spacing (Narr, 1991; Narr and Suppe, 1991; Bai and Pollard, 2000a). A proportional relation between bed thickness and spacing between fractures is common place. This seems to be true for massive sandstones in the backlimb of Abra del Condor (see Figure 8.4). However, stratified sandstone packages diverge from this axiom. A thick stratigraphic interval formed by thin individual bedsets, has a similar spacing than much thinner contiguous massive sandstones (see rectangle area in Figure 8.4).

There is a clear control of bedding attitude and amount of strain on the distribution of the fractures with respect to the axis trend. In the backlimb of the anticline, where the fold should exhibit low amounts of strain and bedding has an average strike of 190°, the average strike of fractures is 285° and the dip is 80° (Figure 8.5). To the east, those fractures present in the forelimb and in regions with complex deformation patterns fractures are rotated 20° clockwise, defining an average strike of 305° to 315° (see stations 1, 2, 6, 7 and 8 in Figure 8.1). However, the perpendicular distribution with respect to the structure axis does not change substantially where bedding has an average azimuth of 25° to 40° (Figure 8.6). Further to the east and in the Piedra Larga anticline backthrust the same pattern is found (Figure 8.7).

My description of fracture patterns differs from that of Florez Niño et al. (2005), who defined a set of opening-mode fractures with a distribution oblique to the structural axis in the Abra del Condor fold. Based on abutting relations, they interpret these oblique fractures as splay or tail joints, associated with strike slip shearing and faults with an oblique sense of shear. However, I did not recognize a clear relation of fractures to the other faults in the Huamampampa outcrops of the Abra del Conor and Piedra Larga anticlines. In addition, almost no measurements of strike and dip are presented in their study and I believe their oblique fractures can be interpreted as part of Set I; since the degree of obliquity with respect to the perpendicular of bedding strike is less than 10°. I do agree in their assessment that this small diversion from strict perpendicularity with respect to the fold axis could be related to local rotation of the stress field or rock rotation. This could also explain the presence of small offset faults I recognized in these highly deformed regions and described below.

In order to assess the relative timing relation of set I with respect to folding, I applied stereographic rotation to remove bedding dip using the software Stereowin. The plunge of the fold was not considered to remove the effect of strata since plunge is less than 6° (see Chapter 6). From this, I was able to determine that fractures poles become closer upon unfolding (Figure 8.8). The strike of the fractures did not substantially change; but minor rotations diminished the dispersion of the data (Figure 8.9).

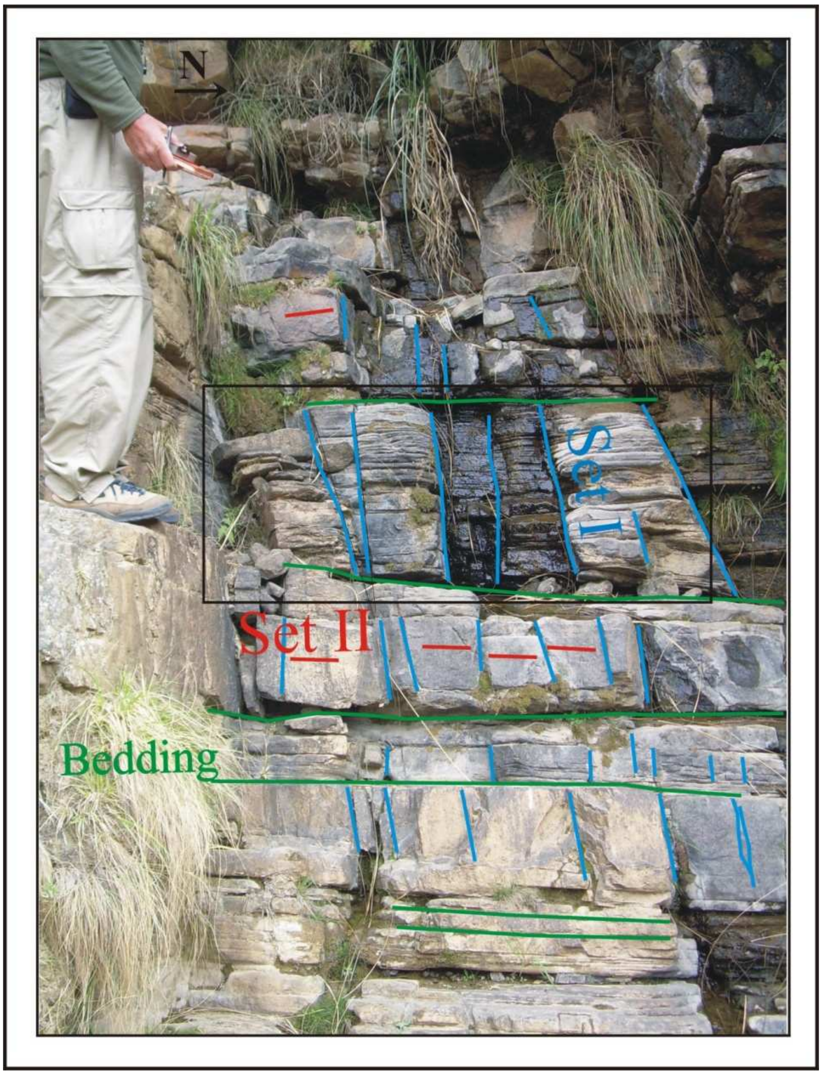

Figure 8.4: For both fracture sets (Set I and Set II), there is a systematic relation between fracture spacing and bed thickness in massive sandstones. Fracture spacing is similar to or slightly less than mechanical layer thickness. Sandstones having thin bed stratification (beds less than 10 cm thick) do not seem to follow this axiom (see rectangle area). Instead, spacing is similar to massive sandstones even when the whole bed is much thicker. See Figure 8.1 for location. View to the W direction.

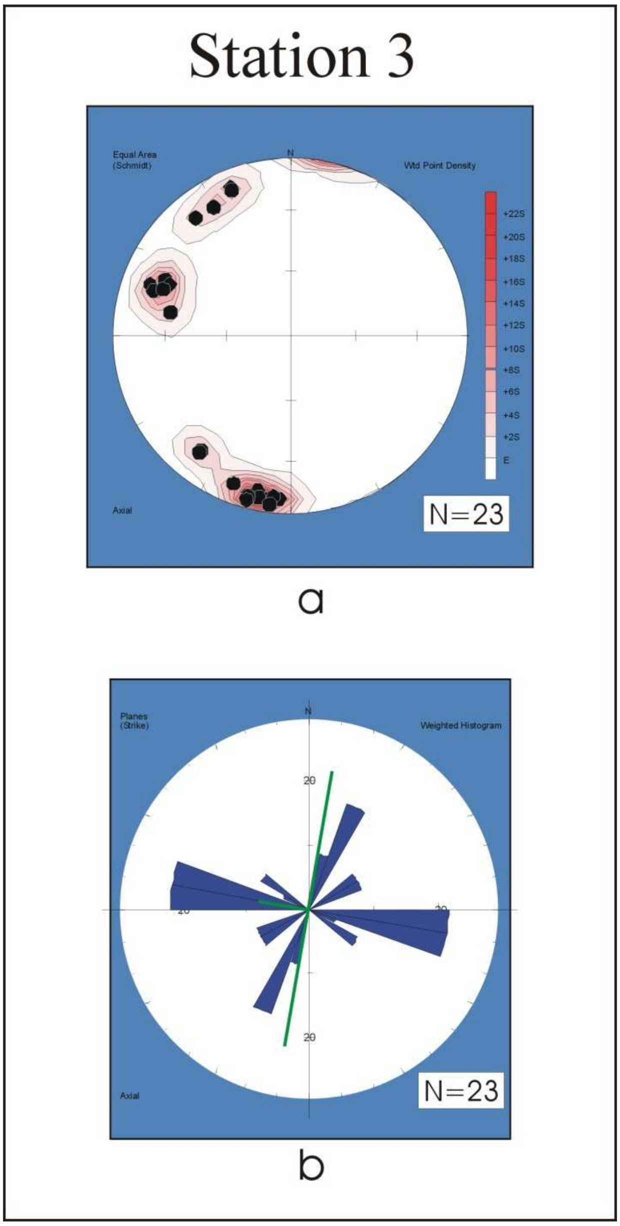

Figure 8.5: Fracture distribution for backlimb Station 3 marked by low strain (see figure 8.1 for location). a. Shows fracture distribution in a Schmidt equal area low hemisphere projection (see text for further explanation). b. Fracture distribution in rose diagram, bedding attitude is also represented (green).

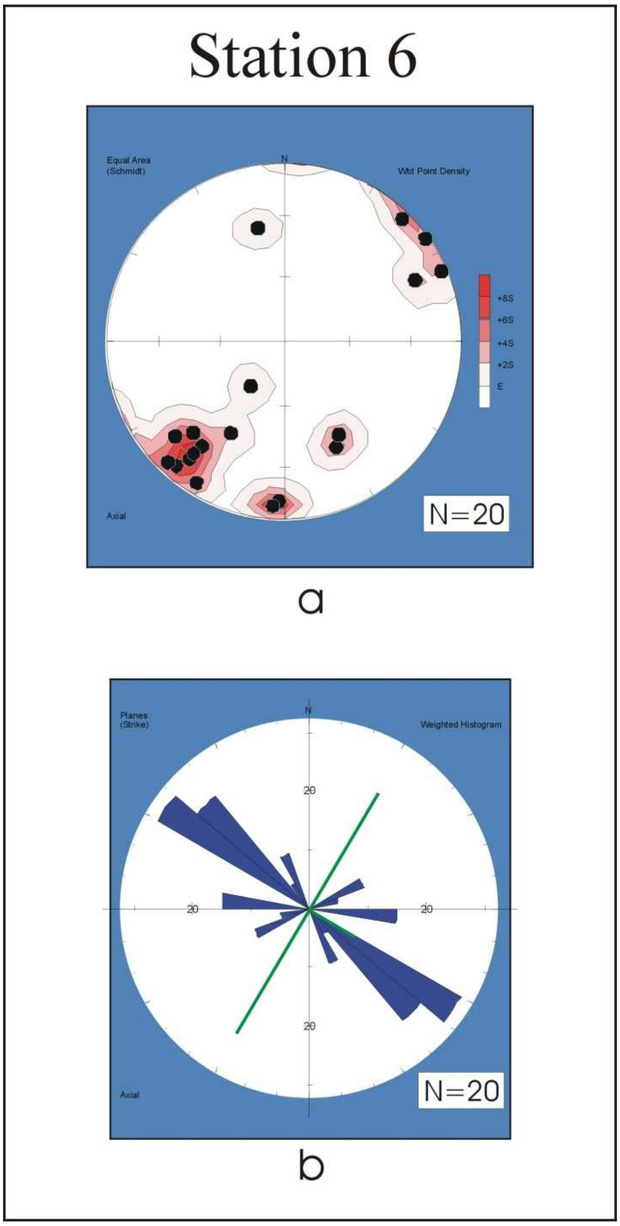

Figure 8.6: Fracture distribution for forelimb Station 6 marked by high strain (see figure 8.1 for location). a. Shows fracture distribution in a Schmidt equal area low hemisphere projection (see text for further explanation). b. Fracture distribution in rose diagram, bedding attitude is also represented (green).

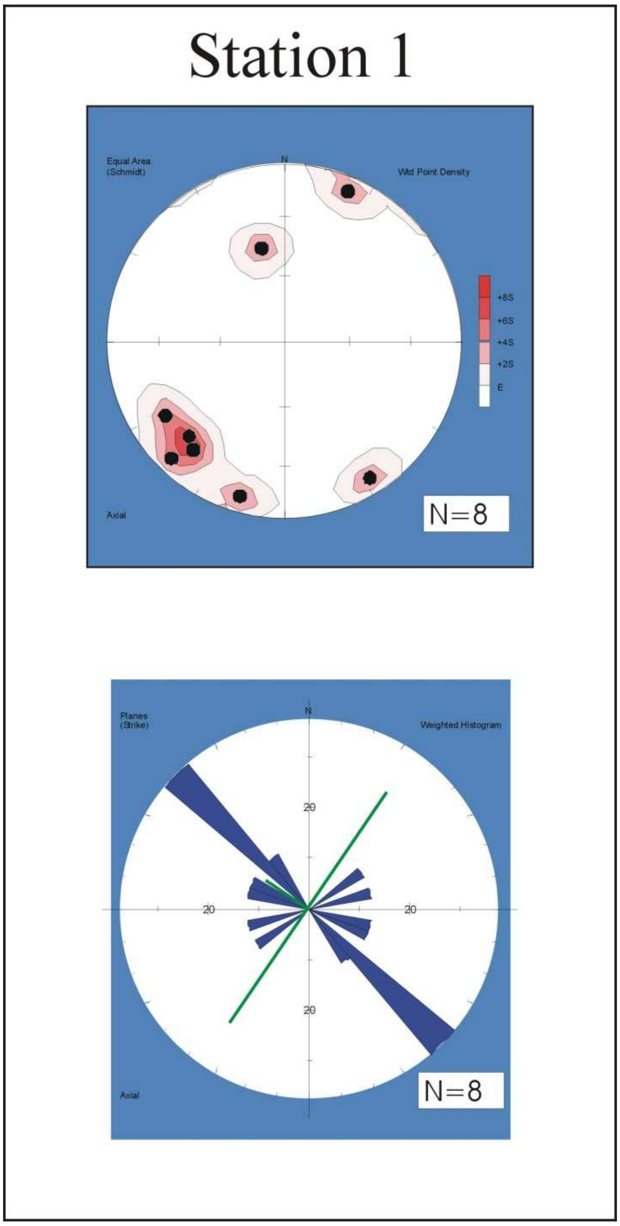

Figure 8.7: Fracture distribution for Piedra Larga backlimb Station 1 (see figure 8.1 for location). a. Shows fracture distribution in a Schmidt equal area low hemisphere projection (see text for further explanation). b. Fracture distribution in rose diagram, bedding attitude is also represented (green).

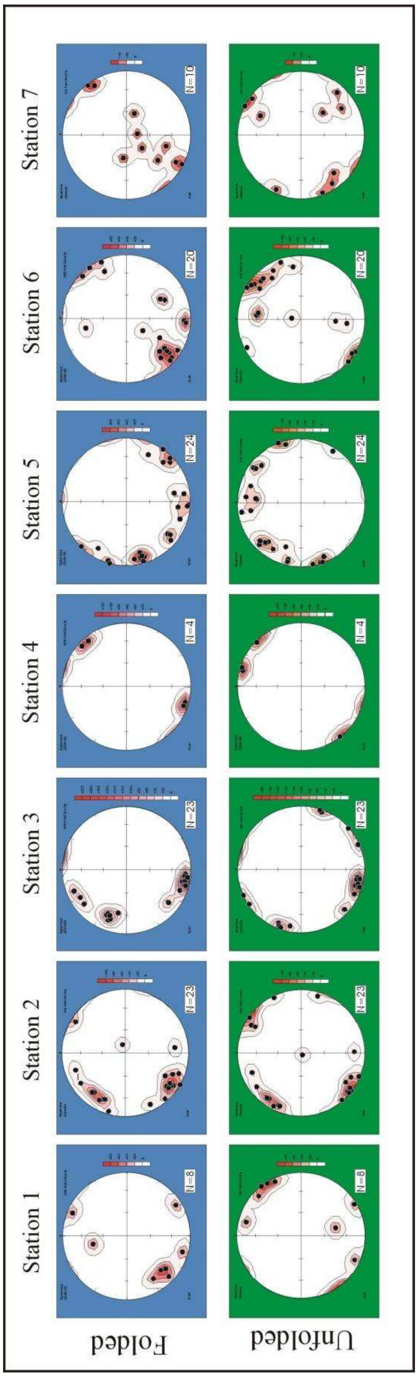

Figure 8.8: Lower hemisphere equal area stereographic projection showing fracture attitude folded and unfolded. Locations correspond to Figure 8.1.

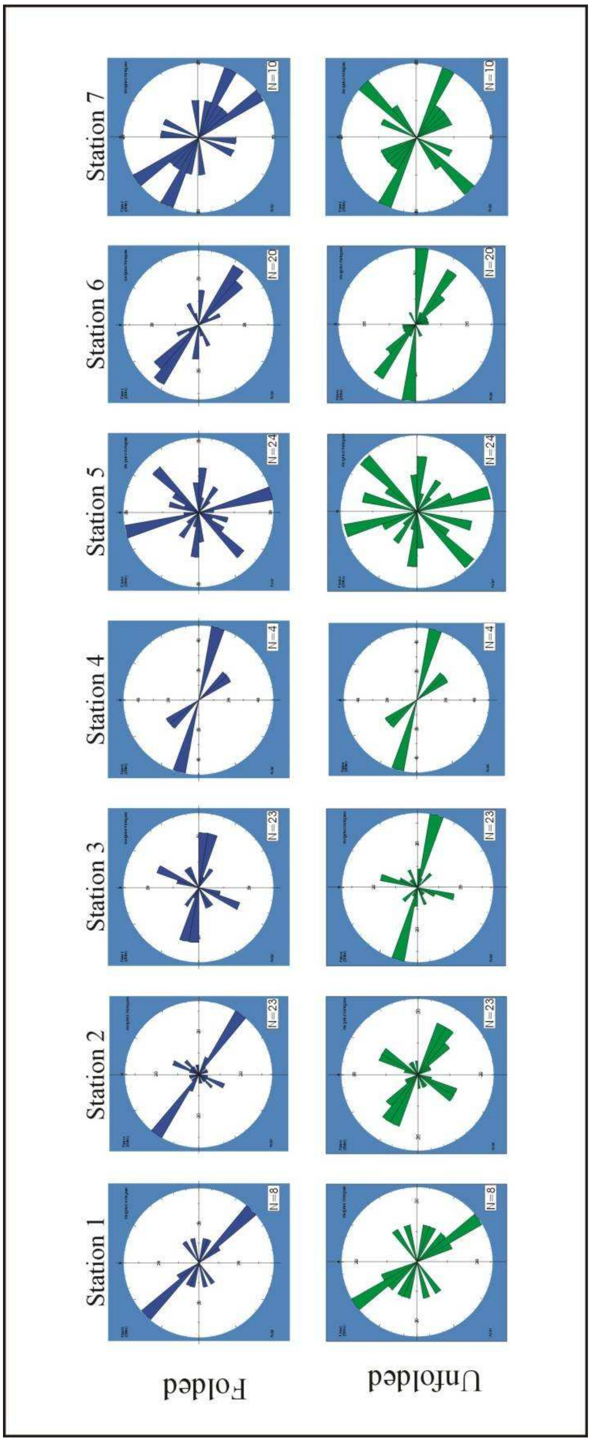

Figure 8.9: Rose diagrams showing fracture orientation in folded and unfolded state. Locations correspond to Figure 8.1.

8.1.1.2 Set II

Set II is orthogonal to Set I (see Figure 8.3) and crosscutting relation between the two is variable according to location. While in some outcrops mutual crosscutting relations are identified (see Figure 8.2 and 8.3), in some other localities Set II abut Set I (see Figure 8.10). I defined this set as subsidiary because the number of fractures that define it are fewer than those of set I. It is comprised of planar fractures with lengths up to 2 m (see Figure 8.3) although fractures in this set are generally much shorter (Figure 8.10). In the backlimb of the Abra del Condor anticline this set has an average strike of 22° and average dip of 60°. The distribution of this set is less clear than that of set I. It is straightforward to identify the members of this set in the gently dipping beds of the backlimb, but it is not easy to define fractures of this set in other regions of the fold. Even where there seems to be an orthogonal arrangement in some locations along the forelimb, the dispersion of fracture strike makes it hard to unequivocally identify this set. The fewer measurements of this set in the steep forelimb could be explained as a consequence of the absence of pavements, where only vertical outcrops are present (Figure 8.11) and thus a consequence of sampling bias rather than the true distribution of these fractures.

Upon rotation of bedding dip, Set II has similar results as those of Set I. Dispersion of fractures poles diminishes and for these fractures dip values become close to 90°. No major strike rotation was registered, (see Figure 8.8 and 8.9).

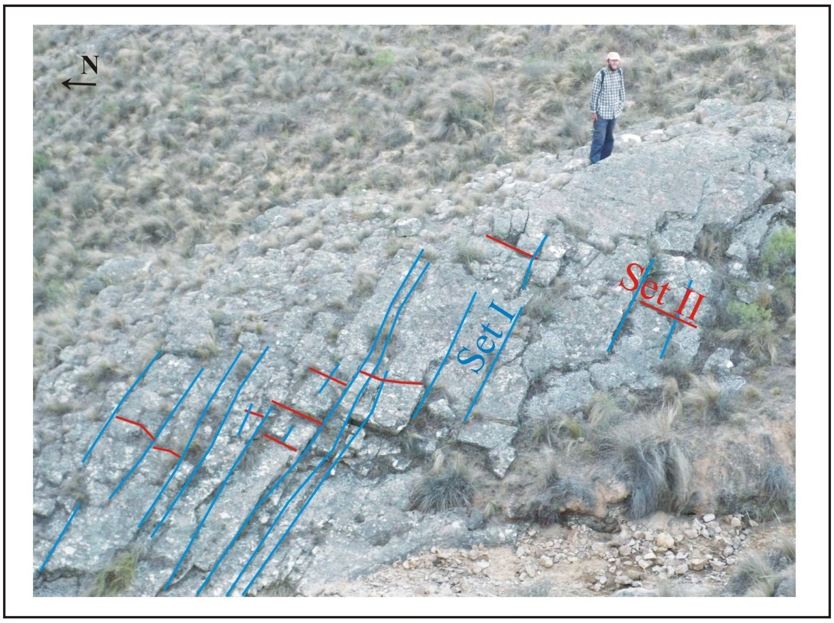

Figure 8.10: Set I and Set II fractures in pavement. Notice person for scale, for location see Figure 8.1. Set I, blue traces on bedding surface; set II, red traces. Note that set II appears to abut set I, suggesting that set II is younger. E view direction.

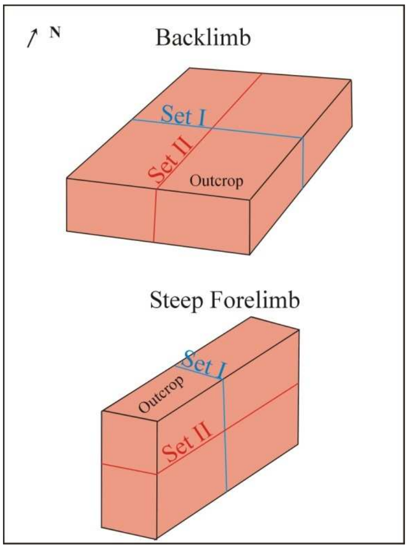

Figure 8.11: Fracture distribution in backlimb and forelimb outcrops. The tabular body represents part of a bed; the large surface is the bedding plane. The absence of Set II fractures in the forelimb could be related to sampling artifacts (absence of pavements).

8.1.2 FAULTS

Florez Niño et al (2005) and Antonellini (1998) described minor faults, with offsets ranging from 10 meters to a few centimeters in Suabandean Ranges outcrops. The interpreted these faults to be a consequence of shearing along joints in zones of high strain. In my analyzes of the Huamampampa Formation performed in the same zone as Florez Niño et al., I recognized at the outcrop scale the WNW-ESE strike slip intermediate faults defined by Florez Niño et al. (2005) and what they defined as small faults and sheared joints. In my study I focused only on the later. For these, I observed a small number of centimeter-size faults with clear evidence of shearing. These contrast with joints that are purely opening mode joints.

In the field I recorded fault strike and dip, as well as *striae* trend and plunge, and sense of displacement. Then, using the software FaultKinWin, I created P-T axis scatter graphics and from this beach-ball graphics, in order to assess fault type, orientation, and their relation to joints. In beach ball graphics the shaded region represents the T quadrant; when only one fault is present for a station the software defines the fault plane solution with the P and T axis, if more than one fault is present for a station, the program uses the moment tensor sum to determine average P and T axes (FaultKinWin tutorial, 2001)

Figure 8.12 shows the location of the measured faults, and rose diagrams of the fault orientation. In order to assess the relation between fault orientation and type of fault, I grouped faults in each station according to their type of displacement (e.g. normal, thrust, strike slip). Figure 8.13 shows the lower hemisphere projection of the faults on a Schmidt equal area stereonet and the fault plane solution for each station.

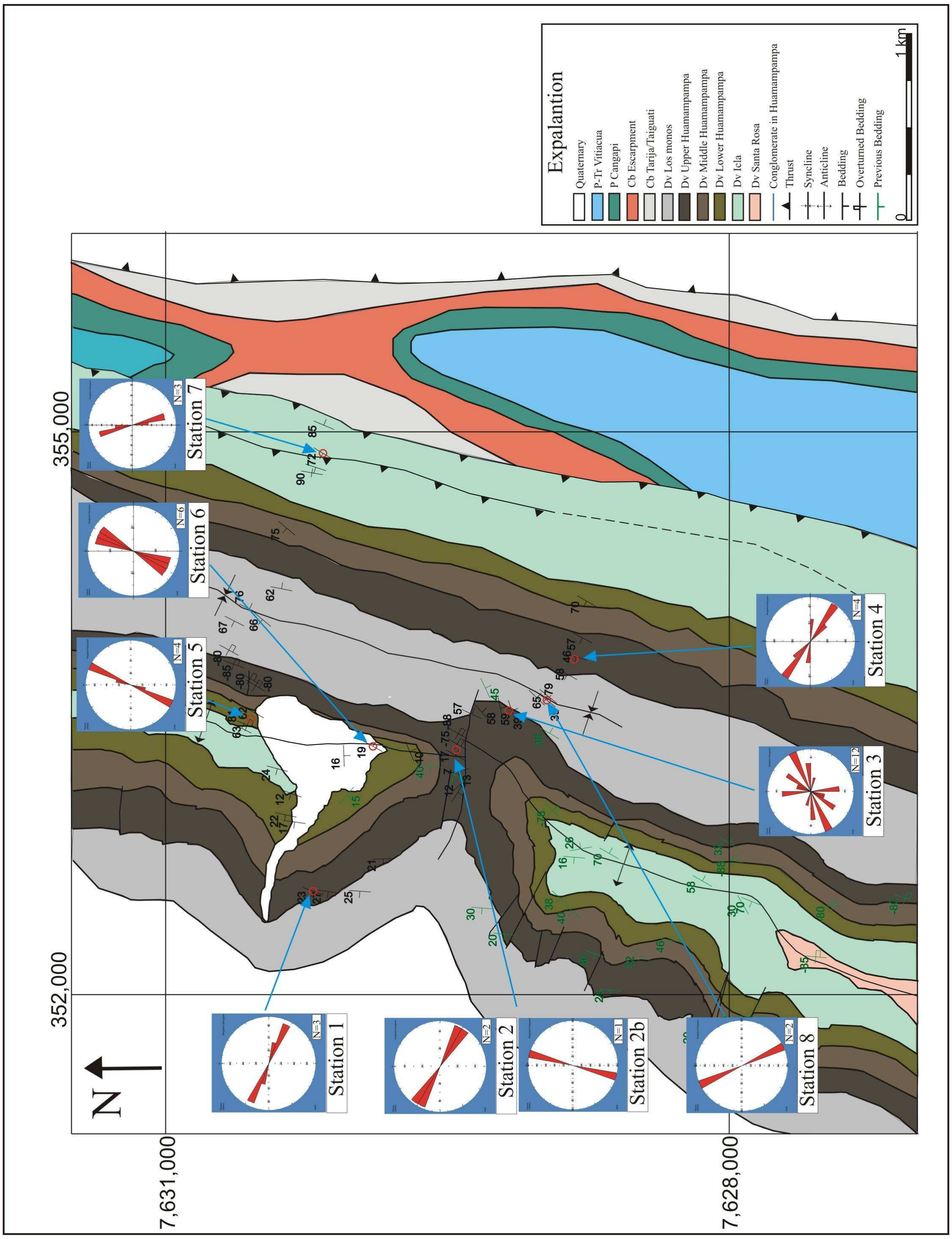

Figure 8.12: Geologic map of Abra del Condor showing station location and fault distribution.

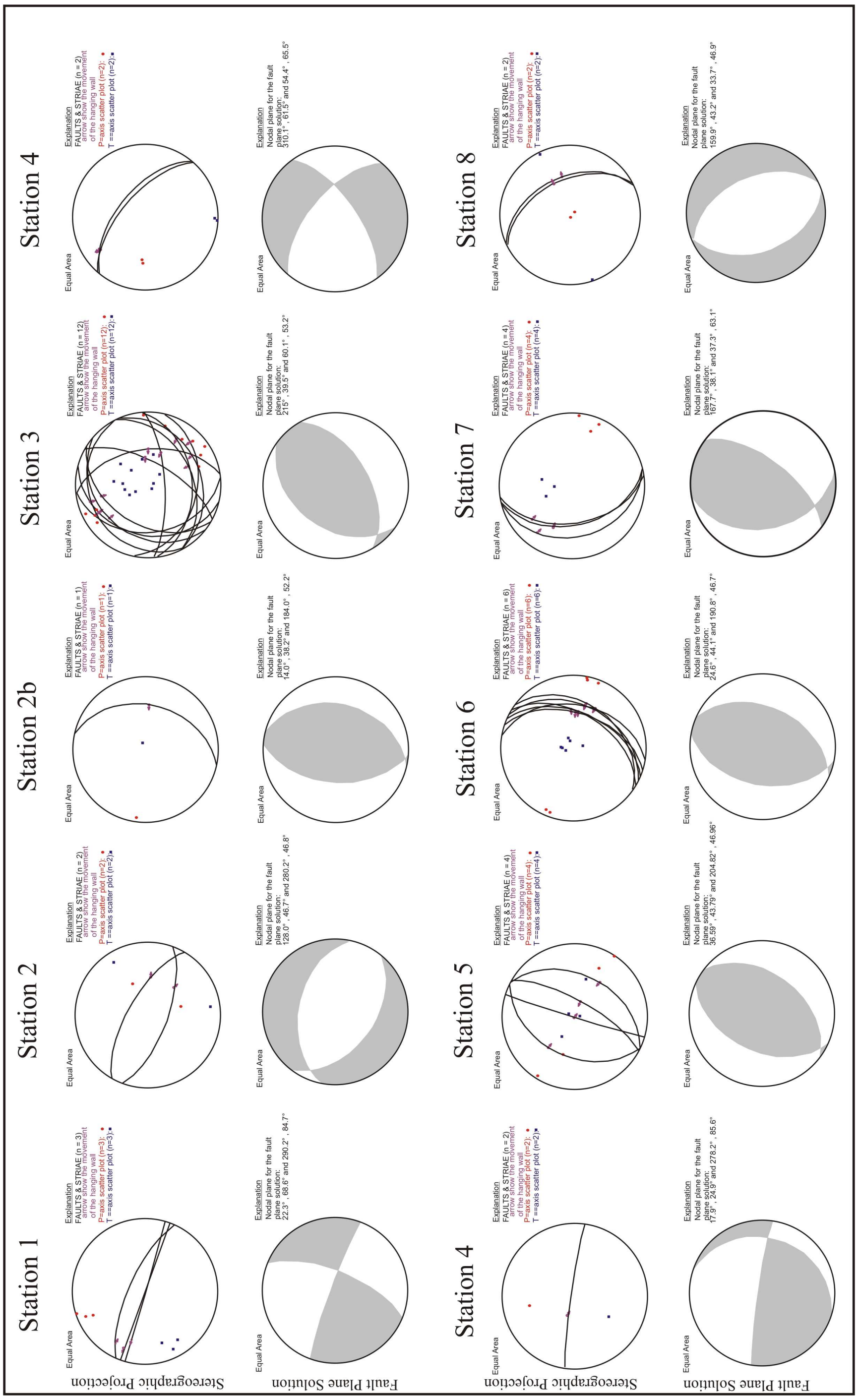

Figure 8.13: Low hemisphere Schmidt equal area stereographic projection showing fault and striae orientation; fault plane solution for fault kinematics.

Figure 8.14 shows the stereographic projection and plane solution distribution in the geologic map. From this I concluded that thrusts have an orientation that almost parallels the orientation of Set II, with an average azimuth of 25°. In addition, I unfold the bedding using the same methodology described for joints, in order to evaluate the distribution of the minor thrusts prior to folding. From this test I observed that most of the thrusts did not change their strike substantially but they rotate towards a horizontal distribution (Figure 8.15), which is consistent with the fact that thrusts have low cut off angles with respect to bedding. This evidence allowed me to interpret these thrusts as a consequence of shortening during fold development. Stations 3 and 7 have thrusts that diverge from the characteristics presented above. For station 3 larger numbers of faults, some dispersion of the strike and a clockwise rotation of the fault plane attitudes are apparent (Figure 8.16). This could be related to the presence of a larger shear strain in this area that rotated the fracture strike and developed a larger number of fractures. Upon unfolding of bedding, Station 7 shows the faults attain a vertical position (Figure 8.17), and parallel joint Set II. From this I inferred that this fault may have been a joint from Set II that was rotated and later reactivated as a thrust.

Close to purely normal sense of slip faults were identified in station 8. These have a strike that is oblique to the N-S direction. However, upon unfolding of bedding, the strike becomes closer to a N-S orientation and the dip becomes close to a 90° (Figure 8.18). From this, I infer that normal faults developed prior to or in early stages of folding.

Finally, strike slip is the principal sense of displacement observed at stations 1, 2 and 4 (see figure 8.13). The faults in these zones are almost perfectly parallel to those of joint Set I. Upon unfolding of bedding the changes in strike and dip of the fault planes are minor (Figure 8.19).

These could easily be interpreted as joints of Set I reactivated as a consequence of shear strain. However, the fact that both left-lateral and right-lateral sense of slip were observed in the field, suggests that not all of them can be slip reactivated Set I joints. A possible explanation for the presence of both senses of slip could be related to the explanation of Couples et al. (1997) for flexural slip deformation mechanisms, where active slip horizons, along the margins of areally limited bedding parallel slip events follow an inchworm-fashion displacement (Chapter 3). This interpretation is partly in agreement with that of Florez Niño et al. (2005). However, I found no evidence that the inversion in sense of strike slip was a consequence of shearing along splay joints.

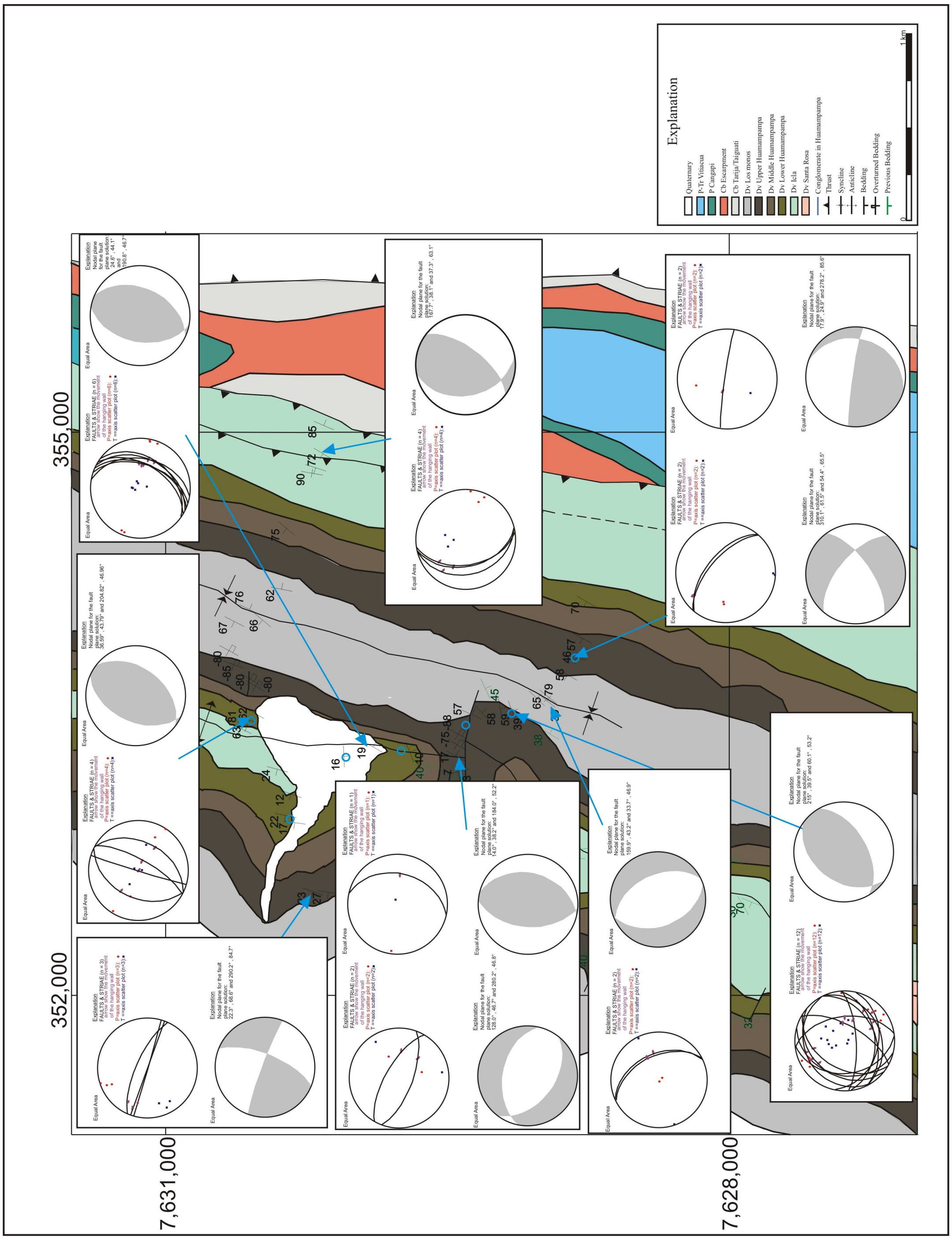

Figure 8.14: Geologic map of Abra del Condor showing station location, fault stereographic projection and fault plane solution distribution.

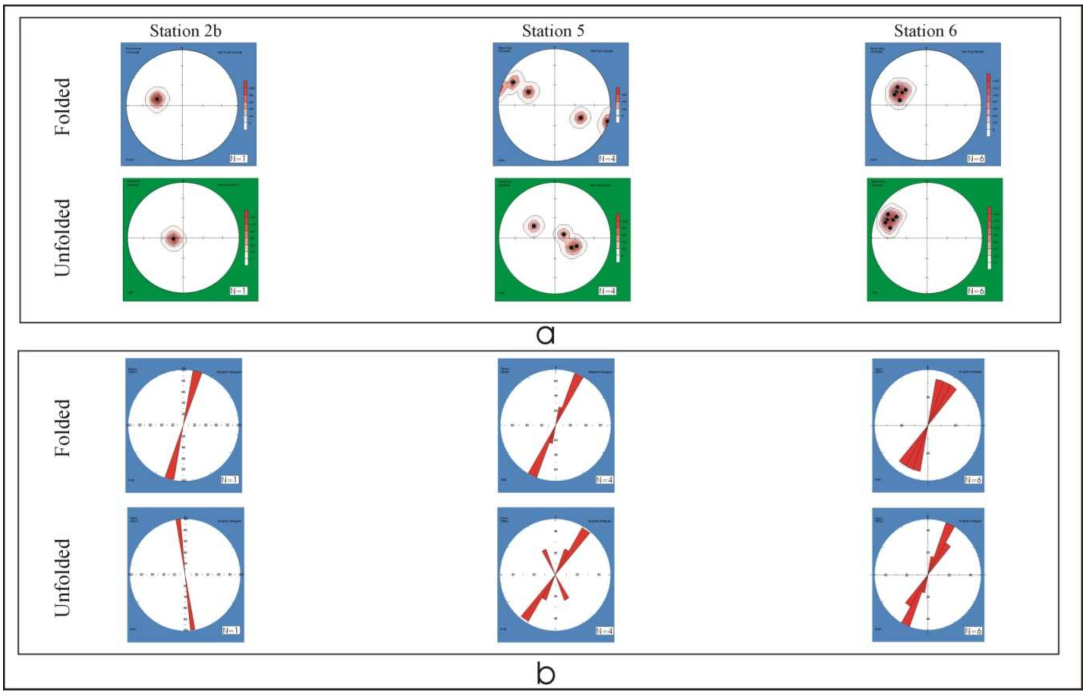

Figure 8.15: Minor thrust distribution in Abra del Condor, for location see Figure 8.12. a. Low hemisphere stereographic projection for thrusts folded and unfolded. b. Rose diagram for folded and unfolded thrust.

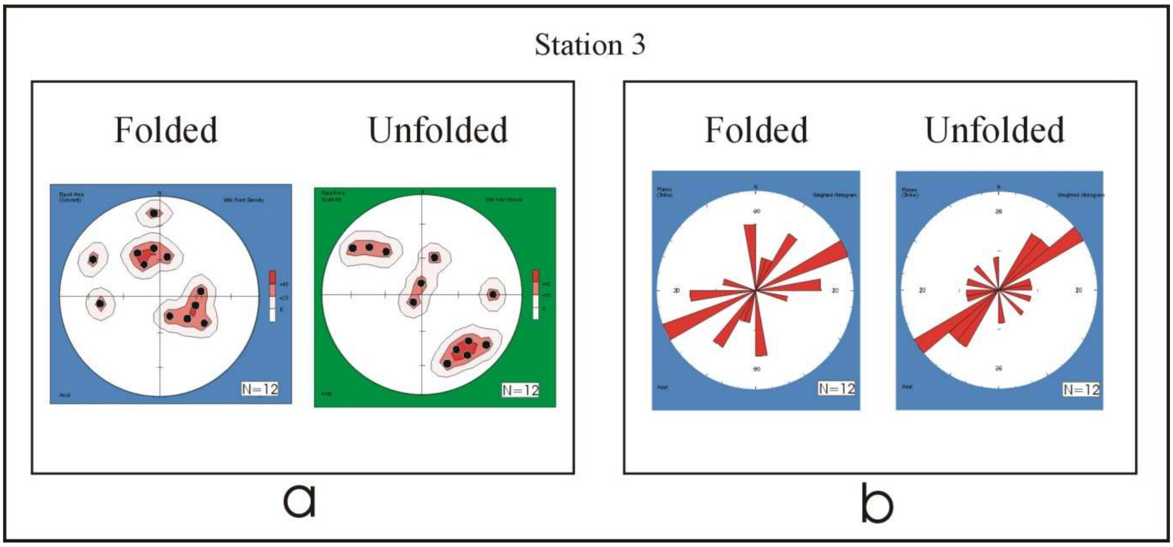

Figure 8.16: Station 3 thrust distribution, for location see Figure 8.12. a. Lower hemisphere stereographic projection for thrusts folded and unfolded. b. Rose diagram for folded and unfolded thrust.

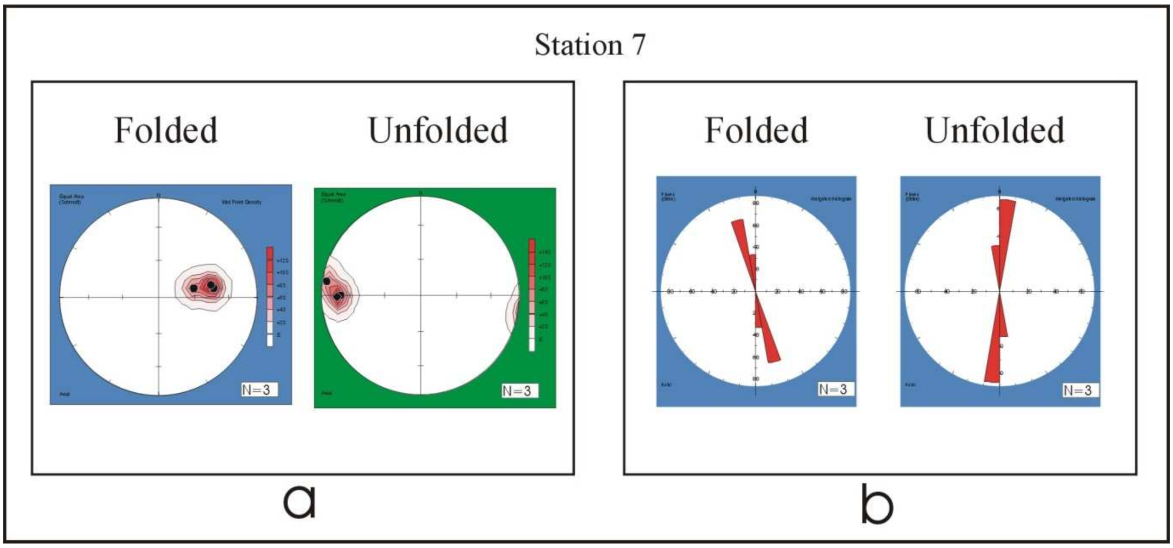

Figure 8.17: Station 7 thrust distribution, for location see Figure 8.12. a. Lower hemisphere stereographic projection for thrusts folded and unfolded. b. Rose diagram for folded and unfolded thrust.

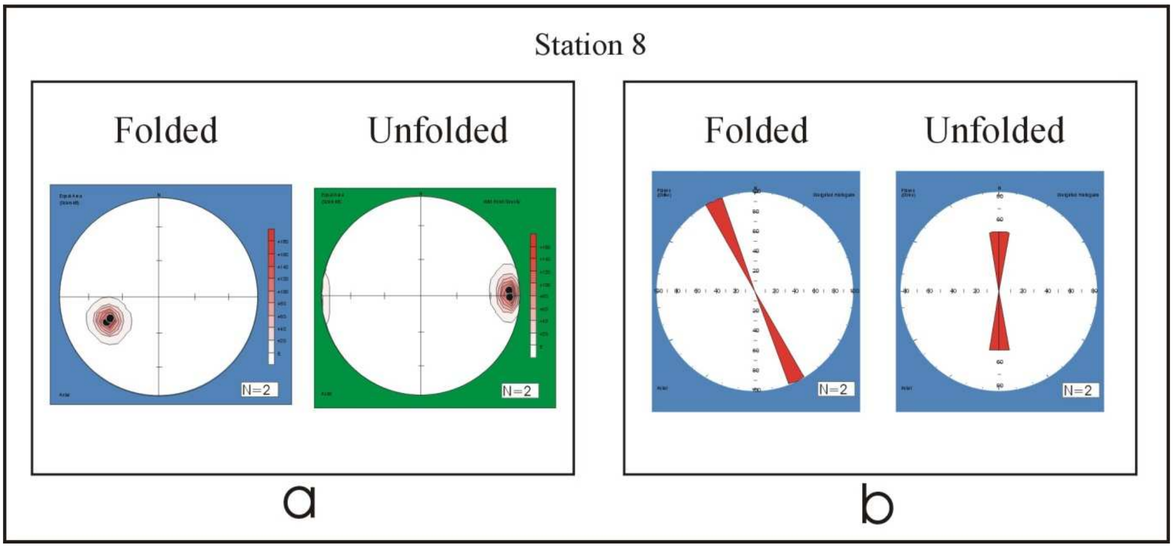

Figure 8.18: Station 8 normal fault distribution, for location see Figure 8.12. a. Lower hemisphere stereographic projection for normal faults folded and unfolded. b. Rose diagram for folded and unfolded normal faults.

8.2 Fracture Relations to Structural and Stratigraphic Features

One of the major objectives of my field work was to assess changes in overall fracture distribution with respect to structural and stratigraphic macro-features. However, the quality of the outcrops precludes a quantitative analyses of fracture distribution using scanlines. A brief qualitative assessment of fracture distribution with respect to lithology, structural position along the fold, and degree of deformation is presented below.

Lithology as a major control of fracture intensity has been described by Hanks et al. (1997) and Ericsson et al. (1998). A quantitative evaluation of primary composition and diagenesis control, on microfracture abundance is presented in chapter 9, 10 and 13. In the field I was able to observe that for backlimb positions, the quartz rich (“cleaner”), extremely hard sandstones of the Lower Huamampampa (station 3 in figure 8.1), qualitatively have a larger number of fractures than those more friable and mica rich sandstones of the Upper Huamampampa. This suggests that there is some control of lithology in fracture distribution. A similar pattern was observed in the forelimb of the structure. Similar numbers of fractures were found for identical stratigraphic positions both for the back limb and the forelimb, so structural position is apparently not a major control on macrofracture abundance. Having said this, very few fractures were observed in vertical to overturned beds. Hinge zone outcrops were limited; but where outcrops were good a similar number of fractures was found as in other structural domains (see stations 4 and 5 in figure 8.1).

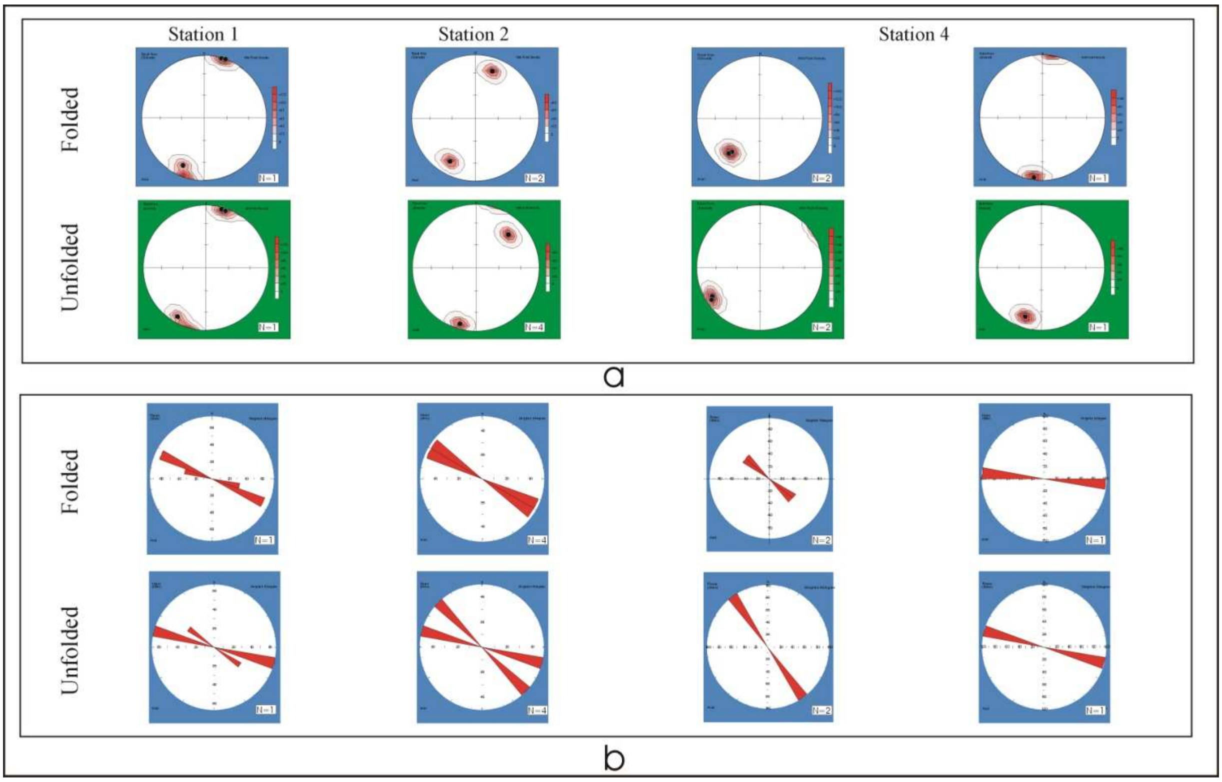

Figure 8.19: Strike slip fault distribution in Abra del Condor, for location see Figure 8.12. a. Low hemisphere stereographic projection for thrusts folded and unfolded. b. Rose diagram for folded and unfolded thrust.

On the other hand perhaps the poor outcrop in fold hinges is a sign that the rocks are more highly fractured. Notably at station 4 where a hinge structural position is exposed, the observed fracture pattern has greater complexity than described for other stations. The main orientation of fractures is close to N-S, but there are also fractures that are perpendicular and oblique to the dominant trend. Complex fracture patterns in the hinge could be related to superimposed fractures from Set I and II, developed during early stages of folding, coupled with fractures associated to orthogonal flexure and hierarchical shearing that involves new layers in the deformation as the fold develops (Couples et al., 1997).

The amount of shear strain deformation was proposed by Florez Niño et al. (2005) as the major control in fracture presence and distribution. My interpretation of the Abra del Condor anticline suggests that higher amounts of shear strain produced a rotation of both bedding and fractures. In the outcrops I studied there does not seem to be an increment of joint intensity for zones with higher strain, but there is a clear relation between the presence of faults and higher amounts of strain. Evidence of this is given by the almost complete absence of faults in low deformation zones such as the backlimb (Figure 8.12). In addition to this, Florez Niño et al. (2005) proposed that there was an increment of fracture intensity close to strike slip faults with meter-scale offsets.

8.3 Origin and Evolution of the Fracture System

Many studies have addressed the presence of orthogonal joints sets in outcrops and their relation to folding processes (Rives et al., 1992; Bai and Pollard, 2000b; Bai et al., 2002; Hennings et al., 2000; Bellahsen et al., 2006; Bergbauer and Pollard, 2004). From these, multiple theories based on timing relations between the fracture sets, loading-unloading conditions, and stress field rotation have been proposed. In the Abra del Condor anticline Set I and Set II have zones with mutual crosscutting relations and zones where Set II abut Set I. In addition, smaller pole dispersion, and dip close to 90° upon unfolding of bedding was also recognized. For these reasons, I interpret these two sets as contemporaneous and generated during the early stages of folding. This statement is based on similar studies and conclusions in other naturally fractured anticlines in the world (Jamison 1997, Bergbauer and Pollard, 2004). In my interpretation Set I would correspond to fractures developed parallel to the maximum compression direction, and Set II could be associated either with local increments of strain associated to curvature, or with an internal rotation of stress as that defined by Bai and Pollard (2000a) when fractures get close to a saturation stage. The later is present when fractures reach such a close spacing that no more fractures can infill even with increasing strain (Bai et al., 2002).

Folding caused the superposition of late fractures on early joints in hinge regions. Later, the systematic arrangement given by Set I and Set II was rotated and sheared as a consequence of shear strain associated with local stress rotation, or block rotation during folding. This favored the development of what I define as sheared joints of Set I, the dextral strike slip faults.

Fractures with sinistral sense of shear are explained as due to flexural slip processes such as those defined by Couples et al. (1997). Finally, I interpreted thrust faults oriented perpendicular to the tectonic transport direction as forming during the early stages of folding.

CHAPTER 9: MICROFRACTURE ANALYSIS

Microfractures are defined as those fractures visible only under magnification (Laubach, 1997). The study of microfractures is required for a complete fracture description. Moreover, microfractures can be extremely helpful to overcome the absence of information on large fractures when analyzing fracture distribution in subsurface core samples, or as complementary information when working in fractured outcrops. Microfractures are useful for subsurface studies due to the fact that in many sandstones microfractures are much more abundant than genetically related macrofractures; allowing sampling of a population large enough for evaluating sets, preferred orientation, or size distribution even in small volumes of rock (Laubach, 1989; Laubach and Milliken, 1996; Hooker et al., 2009).

Microfractures have a variety of morphologies, sizes and patterns. The pattern of cementation in microfractures occurs in a spectrum between fractures filled with secondary minerals, to open and barren. Nonmineralized microfractures should be carefully analyzed, since these could be just the result of drilling and coring processes in subsurface samples (Kranz, 1983); or the result of sample preparation and handling for both in core and outcrop rocks. Laubach (1997) states that microfractures that contain authigenic mineral precipitates such as quartz are indisputable subsurface features. Within natural subsurface fractures, he makes further divisions (better described below) into transgranular (Category I), compaction (Category II) and inherited (Category III). Transgranular fractures that share a common orientation with larger fractures are of interest for further analyses, since they may be genetically related to large postdepositional fractures (or macrofractures) and can be used as a proxy to help infer macrofracture parameters such as intensity (Marrett et al., 1999) and orientation (Laubach, 1989; 1997).

In my thesis, I studied microfracture distribution as a surrogate of macrofractures, in core and outcrop samples with three final goals: 1. quantitatively assessing changes in fracture distribution, related to structural and lithologic features; 2. constraining the results of fracture prediction, obtained through structural modeling (presented in Chapter 7); and 3. assessing aggregate properties of fracture populations such as porosity and permeability.

I analyzed nine subsurface core samples, obtained from multiple hydrocarbon fields in the Devonian basin. The subsurface samples will be referred hereafter as H and N°. In addition, I collected six outcrop samples and analyzed them in the lab; Figure 9.1 shows the location of these samples along the Abra del Condor anticline.

I found quartz filled transgranular fractures in these samples. These proved useful for understanding the overall fracture history and patterns in these rocks. Through the study of these microfractures I was able to assess patterns such as orientation, size distribution and spacing. This allowed me to make comparisons with macrofractures observed in outcrop, and to assess structural, stratigraphic and diagenetic controls on fracture distribution.

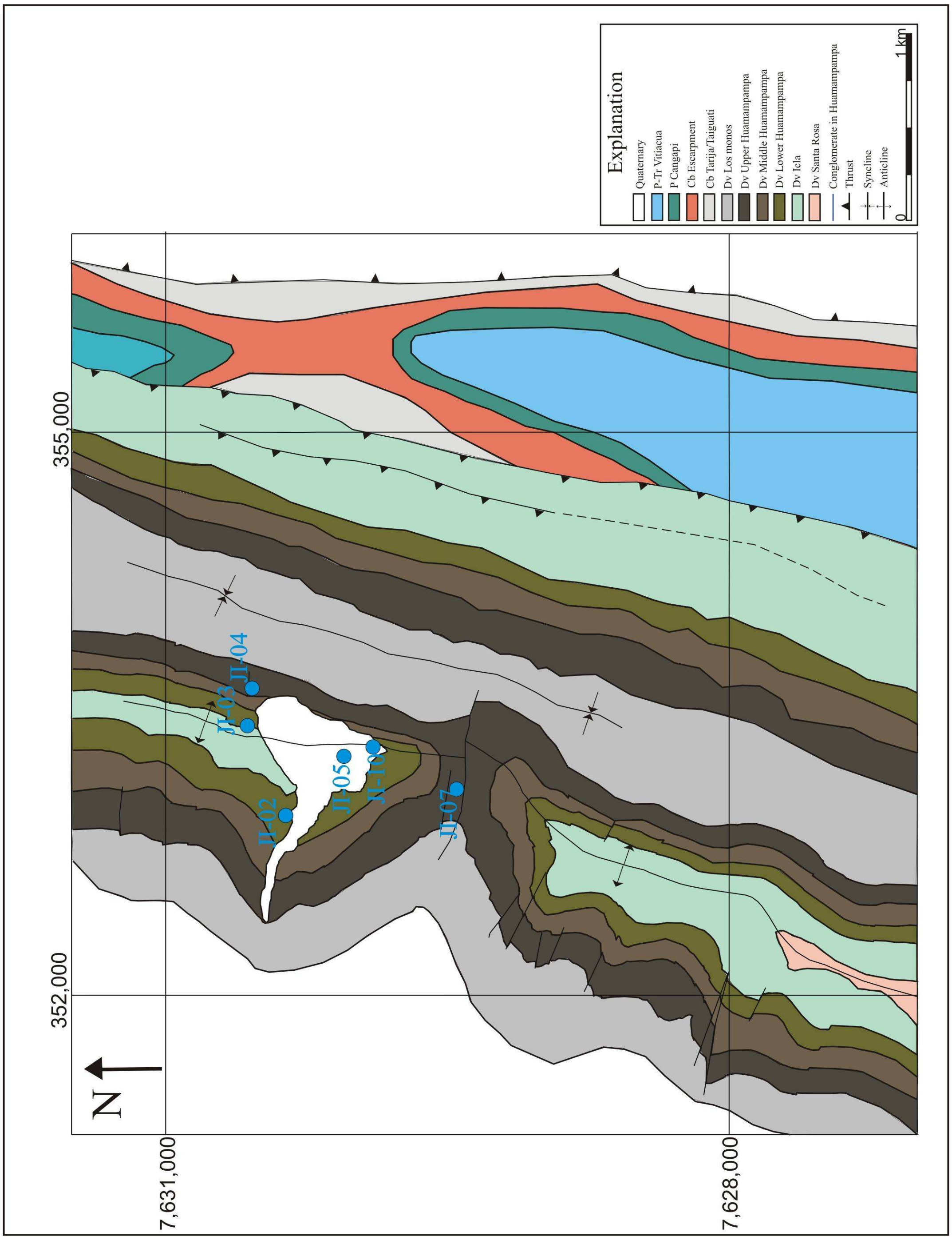

Figure 9.1: Sample locations along the Abra del Condor anticline. For explanation see Figure 6.1 caption.

9.1 Sampling

Microfracture properties were assessed along 1-dimensional lines (scanlines) defined perpendicular to the principal macrofracture orientation, and following the methodology described by Marrett (1996) (Chapter 5). Multiple contiguous thin sections are needed to thoroughly analyze microfractures to obtain good statistic. Continuous scanlines are needed to avoid gaps in data coverage, and correctly assess fractures properties such as aperture, strain and spacing (Gomez and Laubach, 2006).

In order to obtain multiple-contiguous thins sections, the methodology described by Gomez and Laubach (2006) was followed. Continuity was preserved between rock chips, by preventing the trim saw from cutting entirely across the slab (Figure 9.2). Then the sample was gently broken and thin sections parallel to bedding were made from individual chips. This was done both for outcrop and subsurface samples. In order to maximize the usage of the available rock, 25x50 mm (1x 2 inches) or 50x75 mm (2x3 inches) thin sections were made (Figure 9.3).

Figure 9.2: Contiguous thin section preparation, showing how rocks are trimmed up to a thickness, and then gently broken to avoid missing data. Sample is from outcrop sample JI-04. Orientation of the thin section traverse is NNE-SSW.

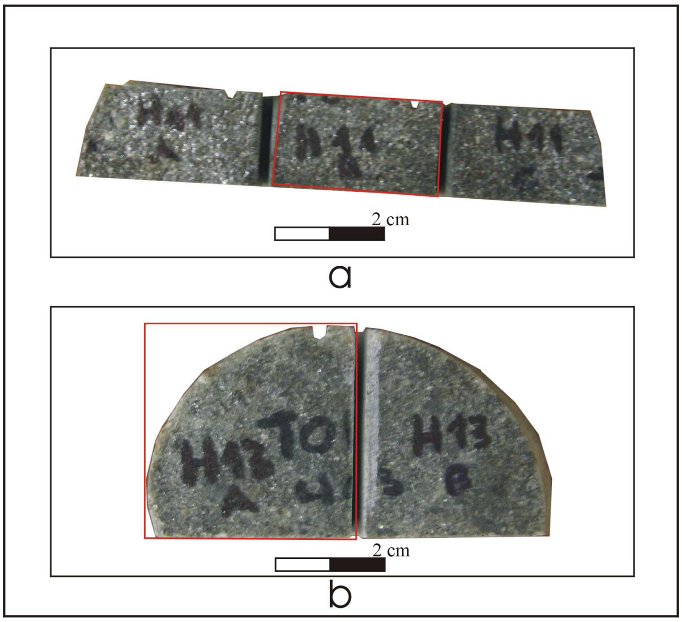

Figure 9.3: Contiguous thin section preparation. a. 25x50 mm thin section b. 50x75mm thin section. Sample is from subsurface samples H11 and H13. Both these samples come from unoriented core so section traverse orientation is unknown.

9.2 SEM-CL Acquisition

SEM-CL microscopy identifies subtle differences in mineralogical structure and chemistry (Pagel et al., 2000) permitting observation of quartz-sealed microfractures, which constitute the most common microstructure in the Devonian sandstone samples I studied. The major advantage of SEM-CL microscopy is that fractures that are invisible in transmitted light microscopy owing to optical continuity between the quartzose rock mass and quartz cement can be identified. SEM-based CL reveals more features than petrographic microscopy or cold-cathode CL microscopy (Milliken and Laubach, 2000).

Prior to imaging, thin sections need to be cleaned and carbon-coated, to avoid charging during electron bombardment. I acquired images along a predefined scanline, at 150x magnification. At this magnification each image presents an area of 0.45 mm^2 and a width of 0.77 mm. Contiguous images have an overlap of 7%. Mosaics of individual images along the whole thin section length were assembled using Photoshop® (Figure 9.4). The number of images in each mosaic varies from 30 to 60, according to the width of the mounted rock slice.

Most of the CL images I acquired are panchromatic (grey scale) images. I also acquired color CL images along the largest sampled fractures, in order to analyze cement patterns and porosity preservation. To do this, individual images are acquired using blue, green and red filters; then, the three images are stitched together in Photoshop® to obtain an RGB colored picture (Figure 9.5). Color images enhance interpretation, and have proven to be extremely useful in studies of fracture aperture history (Laubach and Ward, 2006). Color CL images were only used in my thesis to analyze those features from which I needed information on textural detail not apparent in panchromatic images. However, color imaging along the whole thin section is prohibitive because using the filter system the amount of time needed triplicates that of panchromatic imaging. In addition, with the instrument set up available to me, SEM automation software cannot be used for acquiring these images; manual input of a SEM-operator is needed, which implies higher costs.

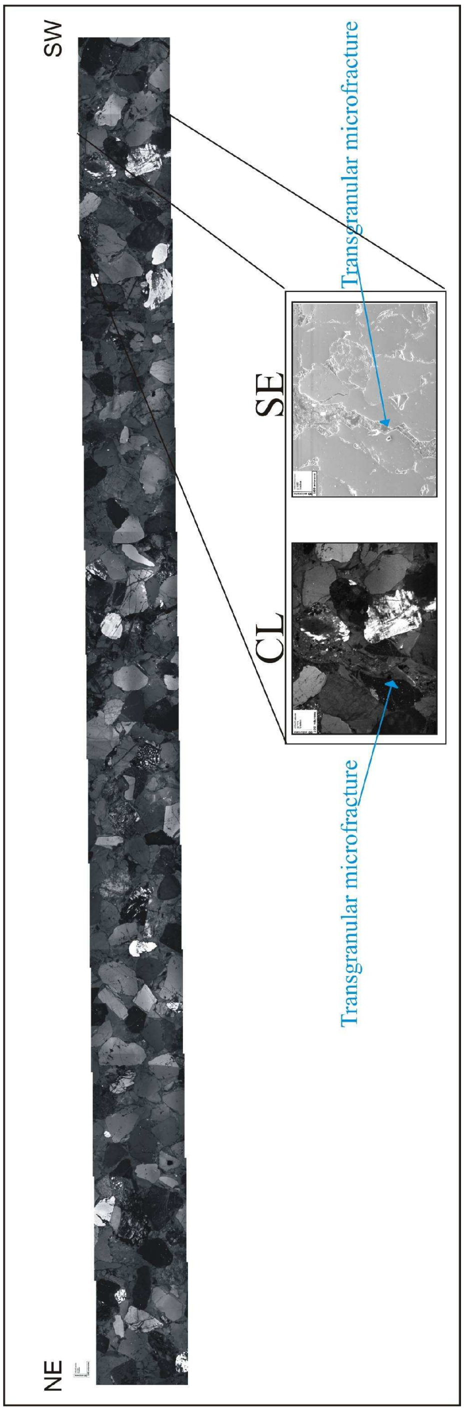

Figure 9.4: Sample H6 bed parallel image mosaic. Below one of the images that compose the mosaic obtained with cathdodoluminescence (CL) and secondary electron (SE) microscopy. Notice scale bars of 100 microns in all the pictures. The image mosaic presents a NE-SW orientation.

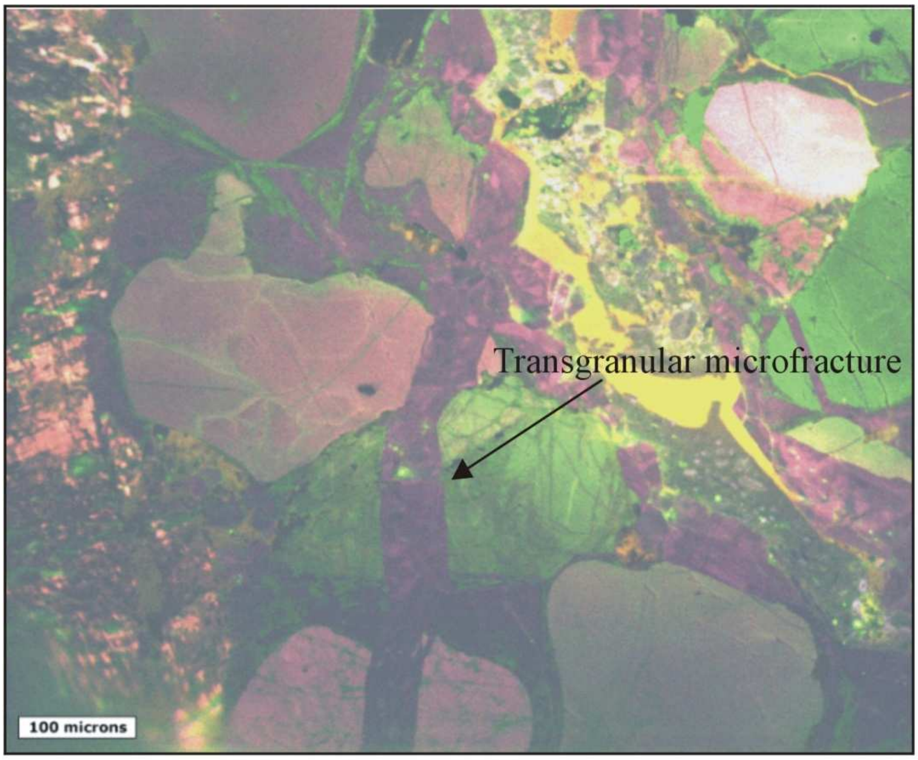

Figure 9.5: Color SEM-CL image of sample H13 (the real orientation of the sample is unknown). Notice 100 micron scale bar on the left of the image.

9.3 Microfracture Interpretation

Microfracture interpretation and mapping was done using Didger3® and following the methodology described by Gomez and Laubach (2006). I imported and calibrated the image mosaics into Didger3® to obtain coordinate information for fracture interpretation. Each fracture is recorded as a closed polygon given by four points, where the first and third point represent the fracture tips and the second and fourth the aperture (Figure 9.6).

I assigned an identification (ID) to each of the fractures based on the classification of Laubach (1997), differentiating among: Category I-Transgranular microfractures given by planar lens shaped fractures, with straight traces that cut through grain boundaries and cement (Figure 9.7a); Category II-Crushed grains microfractures with moderate to strong curve traces, and related to stress concentration at grain contact (Figure 9.7b); and Category III-Inherited microfractures given by wide fractures that end abruptly with blunt terminations at grain contacts (Figure 9.7c). Subsequently, in order to simplify my interpretation I grouped both Category II and III microfractures as intragranular (i), and left Category I as transgranular (t). I used an additional ID (t-) for those fractures considered as transgranular but with some degree of uncertainty.

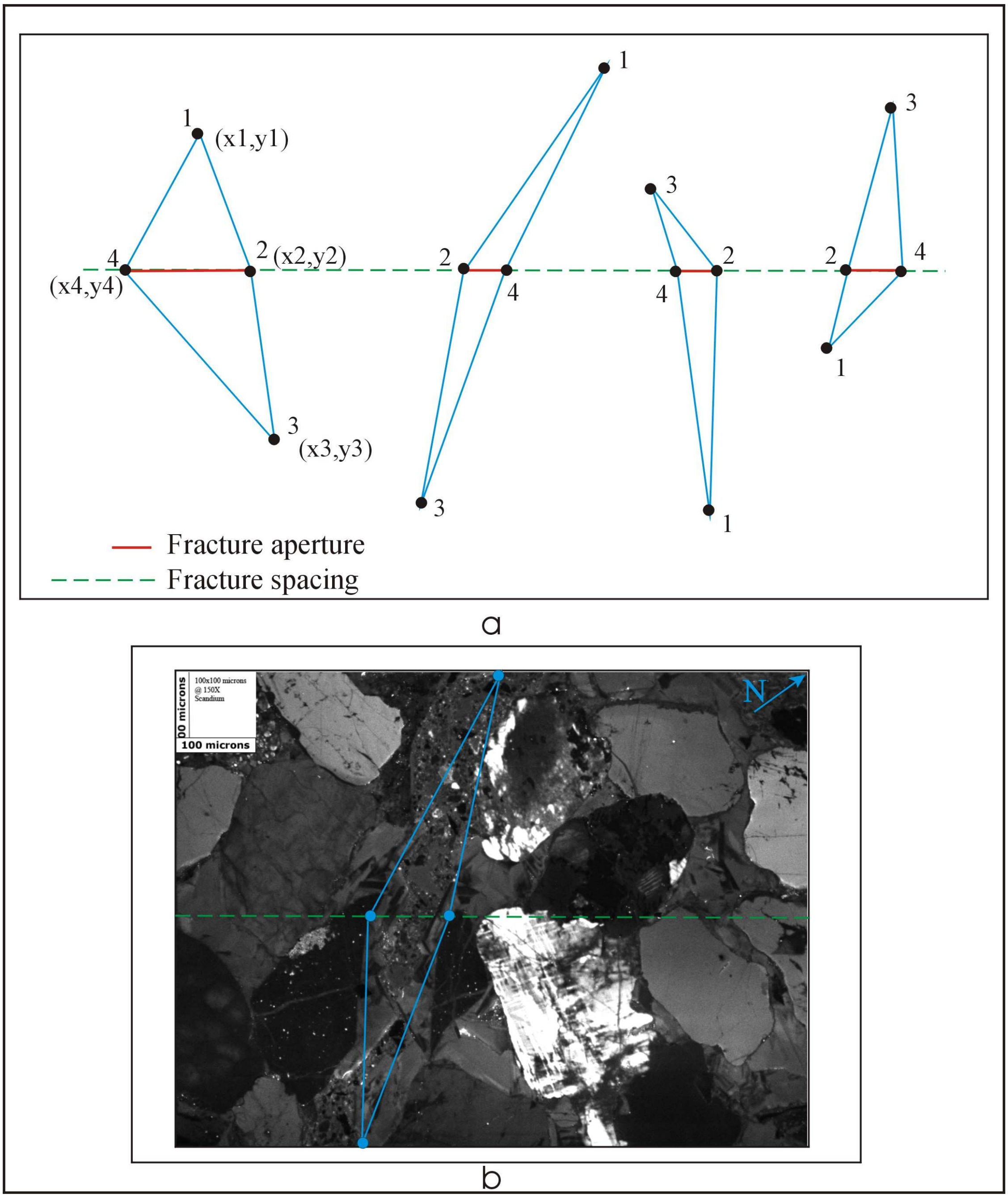

Figure 9.6: Microfracture interpretation. a. Polygon represent fracture interpretation, aperture and spacing can be obtained from the distance between vertices (From Gomez and Laubach, 2006). b. Opening mode fracture and interpretation in sample H6.

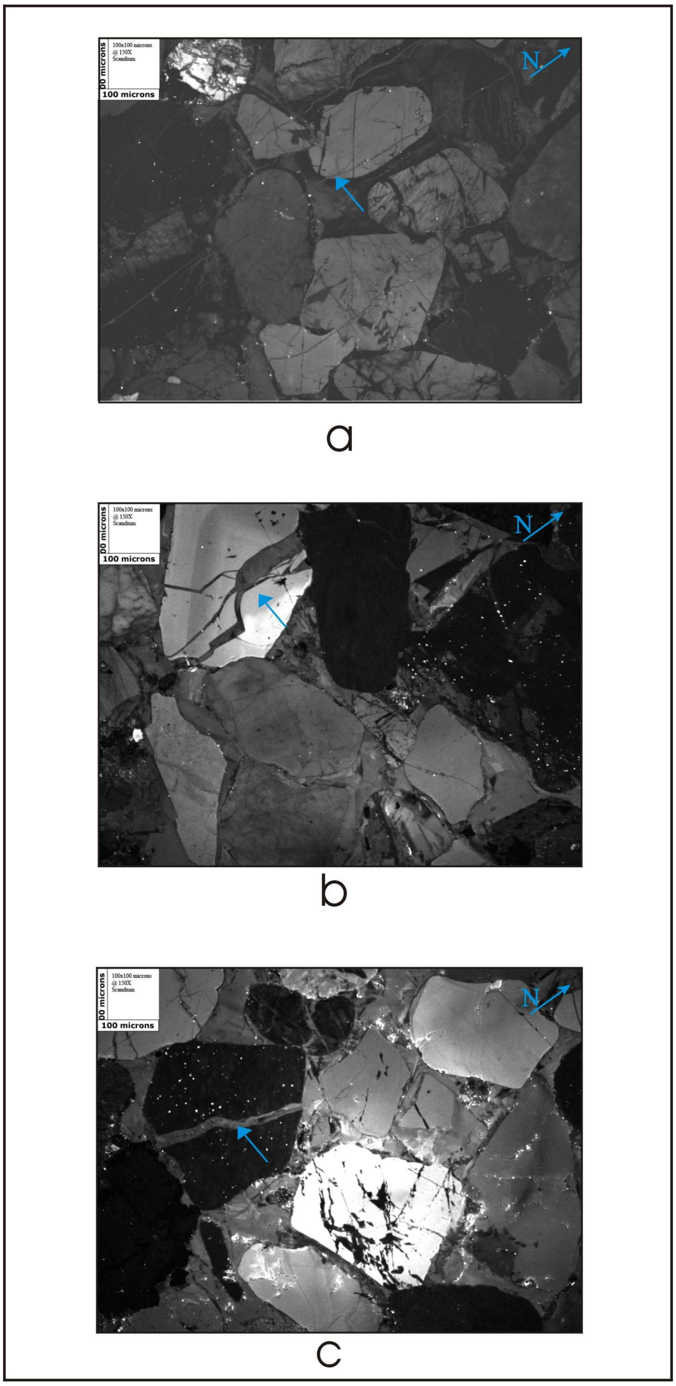

Figure 9.7: Microfracture classification. a. Category I-Transgranular microfractures in sample JI-04. b. Category II-Crushed grain microfracture in sample H6. c. Category III-Inherited microfractures in sample H6.

In 15 samples, a total of 2923 fractures were interpreted along 1298 mm of scanline. From this only 552 are transgranular t or t- fractures, around 19% of the total fracture population. Even when I interpreted all of the fractures present in the studied samples, I performed properties distribution analyses (described below) only on the transgranular ones, since these are the ones most likely associated with postdepositional processes *and* genetically related to a macrofracture population. Table 9.1 shows the number of transgranular fractures for each sample, the length of the scanline and the number of fractures normalized per meter.

Most of the natural transgranular microfractures in these Devonian sandstones of the Subandean Ranges are related to opening mode mechanisms (Figure 9.8). Some minor examples of fractures related to purely shearing processes and shearing along preexisting opening mode fractures were also recognized (Figure 9.9). The term joint is avoided in this part of the thesis since some amount of cement is always present within the fractures; thus I unequivocally attribute these fractures to natural subsurface mechanisms.

The data obtained from my interpretation was exported into GoMezure^{TM} spreadsheet (a set of Excel macros for data reduction; Gomez and Laubach, 2006) to characterize the transgranular microfracture population by quantifying their associated strain, strike, aperture and spacing distribution. In order to quantify these properties and to assess the relation between fracture properties and sample environment, I subdivided the samples into outcrop and subsurface; and according to their structural position into backlimb, hinge and forelimb samples.

Sample	**Scanline length (mm)**	**N of fractures**	**Fractures/m**
H1A	82.08	25	304.58
H1B	40.32	10	248.02
H4A	36.26	8	220.63
H4B	47.45	9	189.67
H6	81.47	45	552.35
H7A	40.78	37	907.31
H7B	46.73	53	1134.18
H8A	47.15	7	148.46
H8B	62.91	6	95.37
H9	83.62	7	83.71
H11A	47.48	4	82.24
H11B	72.85	13	178.44
H12	46.29	4	86.41
H13A	62.74	29	462.23
H13B	34.8	33	948.28
JI_02	69.11	8	115.76
JI_03	97.71	18	184.22
JI_04	139.96	207	1478.99
JI_05	32..11	3	93.42
JI_07	67.65	4	59.13
JI_10	91.13	5	54.87

Table 9.1: Scanline length, number of fractures registered for each sample and number of fracture normalized per meter. Samples that appear twice are for two orthogonal scanlines.

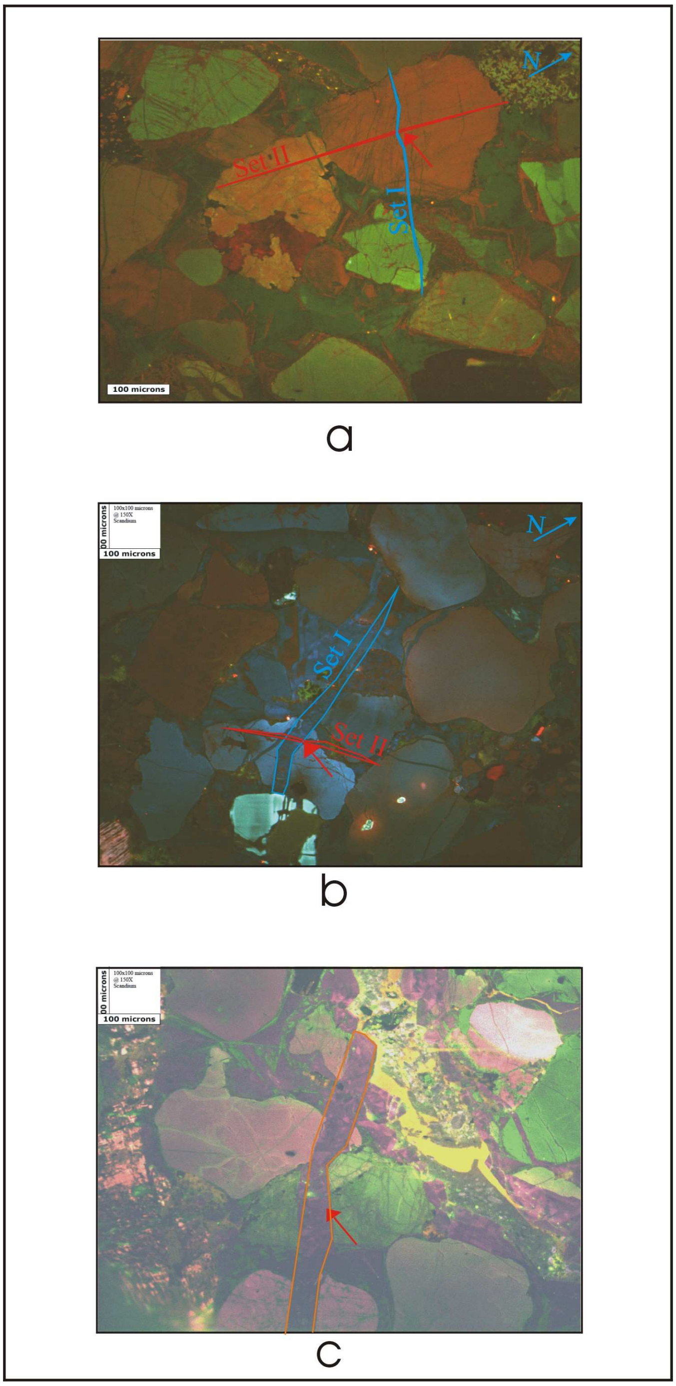

Figure 9.8: Opening mode microfracture. a. Mutual crosscutting between opening mode fractures of Set I and Set II in sample JI-04. b. Mutual crosscutting between opening mode fractures of Set I and Set II in sample H6. c. Opening mode microfractures in sample H13, orientation is unknown.

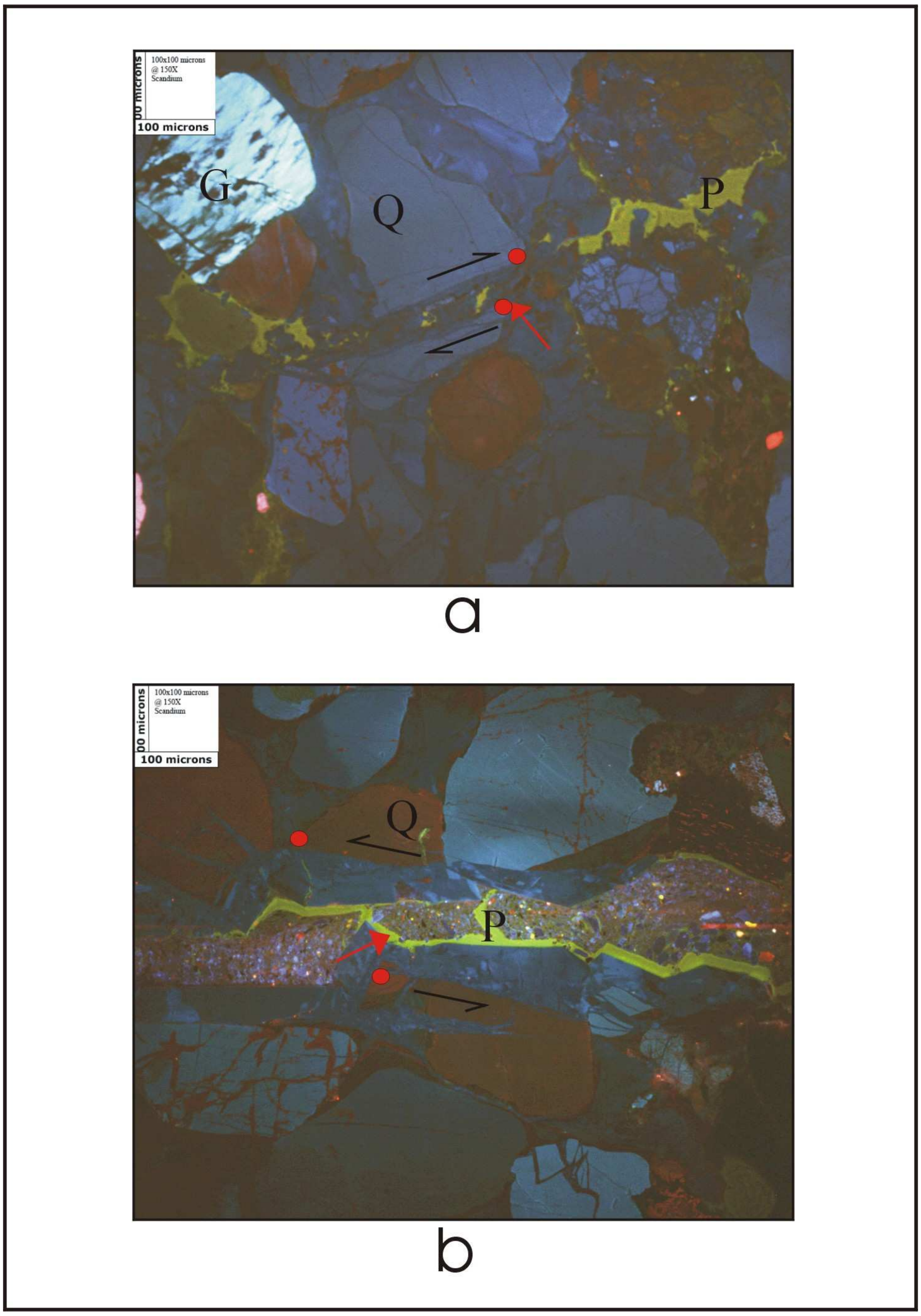

Figure 9.9: Opening mode microfracture with a shear component. a. Shear in microfracture of sample H6. b. Shear in microfractures of H13. Direction and sense of shear is unknown. The red dots are the offset points. Q (quartz), P (porosity) and G (grains).

9.4 Microfracture Related Strain Distribution

Imaging and measurement of fracture properties along a scanline represents a one dimensional sampling from a topological point of view. Therefore, the fracture related strain I analyzed in my thesis is a linear strain (Marrett, 1996) and is calculated as an extension of the material, defined as

$$e_n = \frac{l\text{-}L}{L}$$

Where l-L is the final length of the line and L the initial length. We can consider the difference l-L as the amount of opening. Therefore, we redefine the linear strain as the sum of the sampled fractures' kinematic aperture, divided by the length of the scanline without the fractures

$$e_n = \frac{\Sigma a}{L_l}$$

Where a represents the kinematic aperture and L_l is the length of the scanline minus the sum of the apertures.

In my thesis, I used linear strain magnitude as a measure of rock strain. Where higher strain magnitudes were detected larger deformation was interpreted. It is important to bear in mind that strain magnitude is not always directly proportional to fracture abundance, since a smaller number of fractures with larger apertures would give similar strain values as those of a larger number of fractures with smaller apertures. However, in my thesis I used the magnitude of fracture opening strain as a valid measurement of deformation independent of the number of fractures intercepted, since overall deformation is independent of the way it is solved (e.g. more abundant narrow fractures or fewer wider fractures). This will not affect two of my goals for microfracture analyses: fracture opening strain related to structural and lithologic features; and comparison with the results of structural modeling. Having said this, the distribution of linear strain, coupled with the cementation of these fractures, will have an enormous impact on other aggregate properties of fracture such as permeability (see Chapter 12).

When all the representative samples are considered as a whole the minimum fracture related strain value is 1.56 E-04 and the maximum is 8.26 E-03 with an average value of 2.1 E-03, this shows overall low strain values, comparable in magnitude to those described by Hooker, et al. (2009) and smaller than the ones defined by Gomez and Laubach (2006).

9.4.1 OUTCROP SAMPLES

To assess relations between strain magnitude and sample environment, I subdivided the samples into outcrop and subsurface. Within the outcrop samples the maximum strain is 3.9E-03, the minimum 1.58 E-04 and the average 9.27 E-04. I did further subdivisions between backlimb, crest and forelimb samples, based on bedding attitude and overall location along the structure. Table 9.2 presents the scanline length, and the strain magnitude for each sample.

9.4.1.1Backlimb samples

JI-02 and JI-07 are backlimb samples (see Figure 9.1 for location), since they have gently dip to the WNW. The scanlines in these two samples were aligned in a direction NNW-SSE in order to sample fractures of Set I and Set II (defined in Chapter

8). The amount of strain and fracture intensity in these samples is extremely low and values do not differ significantly from one another (see table 9.2). It seems that low amounts of deformation related to their backlimb location prevail as the main control on fracture related strain.

9.4.1.2 Crest samples

Contrary to what I would have expected, and to the fold-related fracture theory underpinning models presented in Chapters 3 and 4, samples JI-05 and JI-10 from crest positions, have fracture intensity and strain values as low as those of the backlimb (see table 9.2). In order to assess whether different fractures sets are present, and whether more intense fracturing occurs along the crest position, perpendicular scanlines were defined for these samples. A NNE-SSW direction was defined for sample JI-05 and ESE-WNW for sample JI-10. Once again the amount of strain is similar for both samples.

9.4.1.3 Forelimb samples

Samples JI-03 and JI-04 were obtained from the forelimb of the Abra del Condor anticline. The forelimb has steep to overturned bedding. The contrast of strain and fracture intensity in these two samples is significant, being one order of magnitude larger for sample JI-04 (see table 9.2). The fact that these two samples were obtained in beds with very similar attitude, and scanlines on them were defined with a difference in orientation smaller than 5°, indicates that structural position is not the main control on fracture distribution. Something else must be controlling fracture intensity and strain. The presence of a strike slip fault next to sample JI-04, in addition to the difference present on fracture orientation (see below) between the two, suggests that proximity to the fault controls the amount of strain in the hand sample. Similar observations were made by Florez Niño et al. (2005) in the macroscale, who observed higher fracture numbers near faults.

Sample	Structural Position	Scnaline Length (mm)	Strain
JI_02	Back Limb	69.11	2.09E-04
JI_07	Back Limb	67.65	2.54E-04
JI_05	Hinge	32..11	5.04E-04
JI_10	Hinge	91.13	1.57E-04
JI_03	Forelimb	97.71	5.31E-04
JI_04	Forelimb	139.96	3.91E-03

Table 9.2: Outcrop sample strain magnitude distribution, showing structural position and scanline length

9.4.2 SUBSURFACE SAMPLES

Even though the subsurface samples studied in my thesis come from multiple fields in the Devonian basin of the Subandes, they are considered here together. Since as it was stated in Chapters 2, 6 and 7 the Lower Structural Level which contains the analyzed Devonian sandstones, presents a high degree of similarity over different structural axis of the eastern Subandean Ranges. Moreover, fracture predictions performed on different hydrocarbon fields of the Devonian basin, discovered similar fracture distributions (Cohen, 2002; Araujo and Clivio, 2001; Sanguinetti et al., 1998). Figure 9.10 is a geologic map that includes the gas and condensate fields from which samples were obtained.

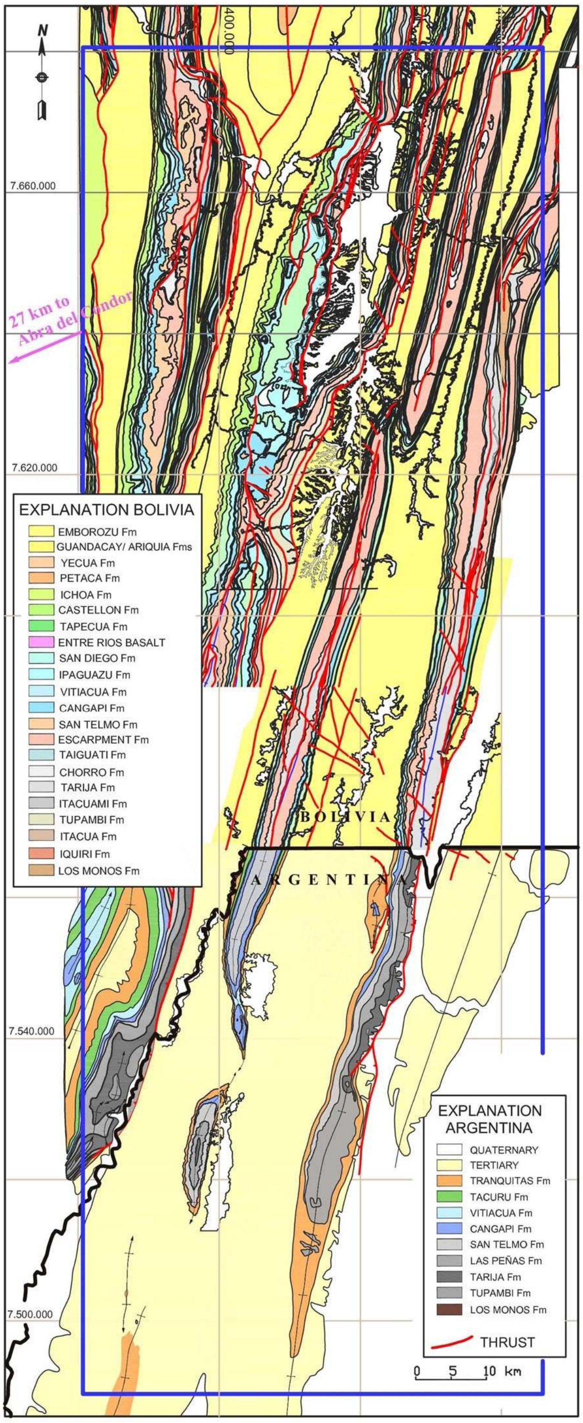

Figure 9.10: Geologic map of Argentinean and Bolivian Subandean region. The blue rectangle shows the area where subsurface samples where obtained.

When analyzed as a whole, subsurface samples record a maximum strain of 8.26 E-03, a minimum value of 1.68 E-04 and an average value of 2.58 E-03. This shows higher values of fracture related strain in subsurface samples with respect to the outcrop analog.

The subdivision of samples into backlimb, crest and forelimb domains was based on the attitude of bedding obtained from microresistivity and dipmeter logs, and from seismic structural maps. The use of structural maps allows me to assign a sample to a particular domain, since classification based on attitude data alone can be influenced by local anomalies in the overall structure. Table 9.3 shows the scanline length and the strain magnitude for each sample.

As I stated in Chapter 5, for those cores were orientation was known, and macrofracture orientation information was available, I performed a single scanline perpendicular to the principal fracture set. Since most of the subsurface core samples were not oriented, two scanlines perpendicular to each other were used to avoid undersampling a particular fracture orientation.

9.4.2.1 Backlimb samples

Samples H4, H8 and H9 are located along the backlimb of the Lower Structural Level, since beds here have dip values around 30° to the west. It can be observed in Table 9.3 that the amount of strain registered in these samples is low but larger than that of the backlimb outcrop samples. In addition, strain increases from sample H9 to H4 to H8. Since all these correspond to backlimb structural positions differences in strain cannot be explained as a consequence of structural location (unless they reflect stain variation within backlimbs). Therefore, I argue that differences in fracture related strain must be a consequence of some other property (see Chapter 13).

9.4.2.2 Crest samples

Samples H6, H13, H1 and H12 come from the crest position of several anticlines. They have dip values around 20° or lower, predominantly to the west. For sample H6 orientation of the core is known and microresistivity logs are available. A scanline perpendicular to the principal fracture strike obtained from logs was defined. In samples H13 and H1 two perpendicular scanlines were measured. The amount of strain in these samples, largest amount of strain of all the samples I analyzed (see table 9.3), is one order of magnitude larger than those of the backlimb. Is interesting to notice that contrary to what I observed for outcrop samples, in subsurface samples there is an increase in fracture related strain as we move from the backlimb to crest areas. Sample H12 is the exception to this pattern since even when two orthogonal scanlines were analyzed few fractures were found in one, and none in the other (see Table 9.1). The strain magnitude is as low as those of the backlimb (see Table 9.3).

Sample H11 also is from a crest region, but it was not included for comparison within the rest of hinge-related samples because even when it is part of the same reservoir, the deformation history is different from the rest of the samples.

9.4.2.3 Forelimb samples

The forelimbs of the subsurface anticlines associated with hydrocarbon production are very steep (Chapter 6). Because of this seismic resolution is extremely low in these structural domains, impeding definition of limb position and extent. To the best of my knowledge no well has had the forelimb as a hydrocarbon target. Moreover, most wells have objectives located close to the hinge but sufficiently far from the forelimb to avoid missing the structure or falling below the gas water contact. This explains why I have only one subsurface sample that according to my interpretation belongs to the forelimb; these areas of the structure are rarely penetrated. Sample H7 has dip values above 30° to the east, allowing interpretation of it as part of the forelimb but extremely close to the fold axis. It has a fracture related strain magnitude of 7.11 E-03 comparable to the largest values observed in the crest area. However, since this sample comes from a different geologic formation care should be taken when comparing it to the other samples.

Sample	Structural Position	Scanline Length (mm)	Strain
H4	Back Limb	36.26	7.17E-04
H4	Back Limb	47.45	6.90E-04
H8	Back Limb/Hinge	47.15	4.45E-03
H8	Back Limb/Hinge	62.91	6.46E-04
H9	Back Limb	83.62	1.68E-04
H6	Hinge	81.47	8.26E-03
H1	Hinge	82.08	1.17E-03
H1	Hinge	40.32	8.32E-04
H13	Hinge	62.74	1.76E-03
H13	Hinge	34.8	6.67E-03
H11	Hinge	47.48	2.64E-04
H11	Hinge	72.85	6.78E-04
H12	Hinge	46.29	3.54E-04
H7	Forelimb	40.78	4.23E-03
H7	Forelimb	46.73	7.11E-03

Table 9.3: Subsurface sample strain magnitude distribution, showing structural position and scanline length.

9.5 Microfracture Orientation Distribution

The strike of microfractures was studied in thin sections cut parallel to bedding. For those cores for which I knew the orientation as well as for all of the samples collected in the field, the actual distribution for the strikes of the fractures with respect to north was obtained. For samples where the absence of orientation information precluded obtaining the true orientation, microfractures strikes were oriented respect to an arbitrary north (arbitrary sample reference direction).

I performed an orientation analysis for microfractures based on strike distribution, weighted by fracture length in order to account for curved fractures (Gomez and Laubach, 2006). Length weighting assumes that the longer fractures are more representative of regional trends rather than grain-scale effects that can cause strike dispersion. Rose diagrams obtained from GoMezure^{TM} are calculated using circular statistics. Then using sample orientation (when present) I rotated the rose diagram a fixed angle to plot it correctly with respect to north.

In the case of field samples, microfracture orientation was compared to the macrofracture data obtained on large fractures in outcrops to assess the relation of these two features. For the two subsurface cores that were oriented with the microresistivity logs, the true orientation of microfractures was determined; and was compared to macrofracture strike and dip. For the rest of the subsurface core, microfractures orientation is unknown. Microfractures data was rotated to compare their distribution to samples that share similar features. The objective was to permit delineation of microfracture preferred orientation.

Finally, I should mention that there is an inherent bias to sample fractures that are aligned perpendicular to the direction of the scanline, and undersample fractures that run in different orientations. This could be avoided working with two dimensional image mosaics. However, due to timing and cost issues this was not viable in the scope of my thesis. In addition, assessing fracture properties, such as porosity and permeability, is easier when working with one-dimensional sampling (Marrett, 1996).

9.5.1 OUTCROP SAMPLE FRACTURE ORIENTATION

9.5.1.1 Backlimb samples

Scanlines in samples JI-02 and JI-07 were aligned in a direction NNW-SSE. Figure 9.11 shows the relation between the macrofractures in the field and the microfractures examined in the lab. Sample JI-02 has two orthogonal sets; a predominant one perpendicular to the fold axis and a subordinate parallel to the structural trend. Sample JI-07 also shows two sets almost perpendicular, in this case with similar intensity. However, there is some amount (28 degrees counterclockwise) of rotation with respect to macrofractures found in the field.

9.5.1.2 Crest samples

Sample JI-05 has two orthogonal sets and an overall good agreement with the data obtained on large fractures in the field (Figure 9.12). In sample JI-10 the direction of the scanline defined parallel to the dip direction favors the sampling of those fractures parallel to the bedding strike in detriment of those that are perpendicular. Figure 9.13 shows a predominance of fractures oriented N-S and an almost complete absence of fractures perpendicular to the structural trend.

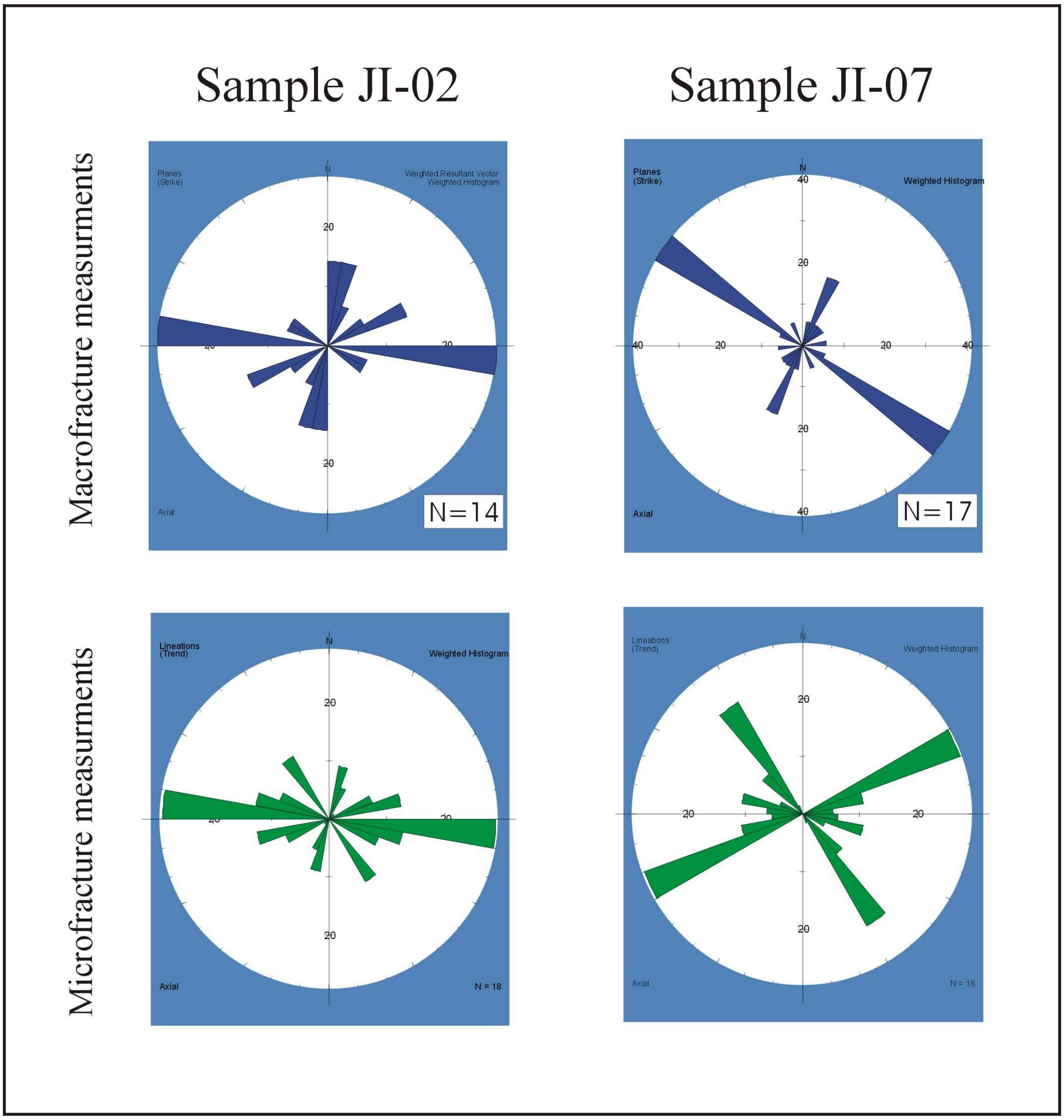

Figure 9.11: Fracture distribution obtained in the field (macrofracture measurements) and the lab (microfracture measurements). In all cases two mutually orthogonal fracture sets can be recognized. Notice that measurements are weighted by abundance for field samples and by length of segments for lab measurements. For the later the n value does not have any particular meaning and therefore are not presented here. Unweighted rose diagrams and a table of fracture measurements are included in Appendix B.

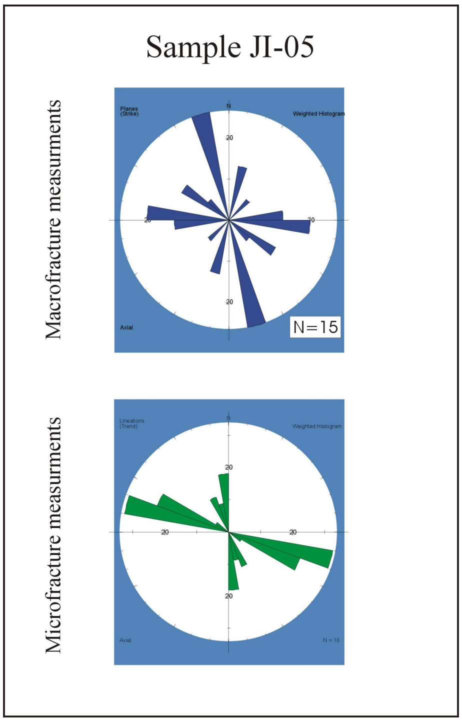

Figure 9.12: Fracture distribution obtained in the field (macrofracture measurements) and in the lab (microfracture measurements). Unweighted rose diagrams and a table of fracture measurements are included in Appendix B.

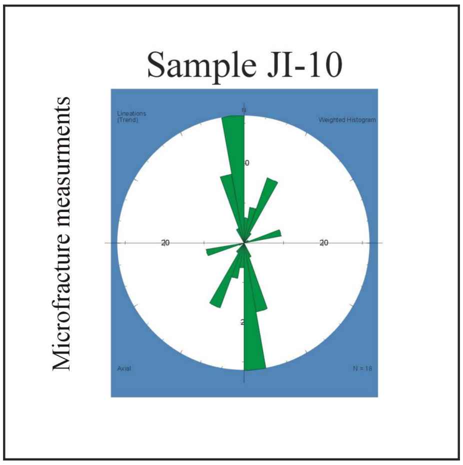

Figure 9.13: Microfracture distribution obtained in the lab for sample JI-10. No macrofractures were observed in the field. Unweighted rose diagrams and a table of fracture measurements are included in Appendix B.

9.5.1.3 Forelimb samples

For samples JI-03 and JI-04, the sampled microfractures have a different distribution than the fractures observed in the field. Sample JI-03 has a predominant fracture orientation that parallels those of Set I. In addition, the distribution of microfractures in thin section shows a similarity with those measured in the field (Figure 9.14). Sample JI-04 on the other hand, presents microfractures that parallel Set II (Figure 9.15). The number of fractures and fracture related strain is much larger than that of JI-03. No macrofracture were observed near sample JI-04 in the field.

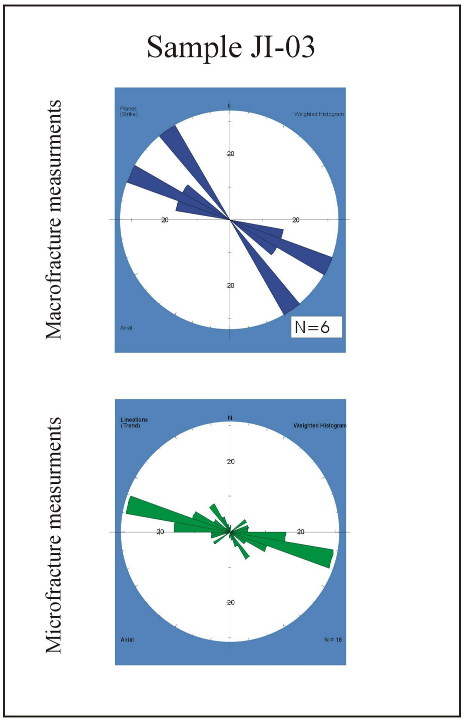

Figure 9.14: Fracture distribution obtained in the field (macrofracture measurements) and in the lab (microfracture measurements). Unweighted rose diagrams and a table of fracture measurements are included in Appendix B.

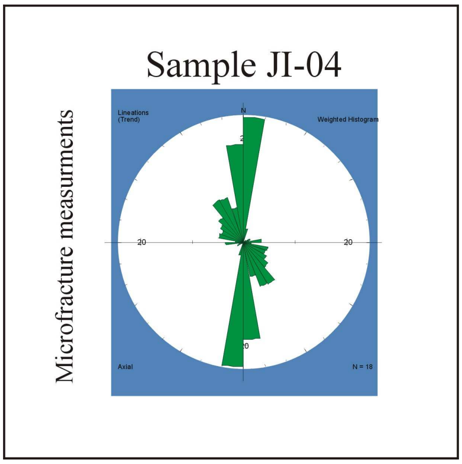

Figure 9.15: Microfracture distribution obtained in the lab for sample JI-04. Unweighted rose diagrams and a table of fracture measurements are included in Appendix B.

9.5.2 SUBSURFACE SAMPLE FRACTURE ORIENTATION

For subsurface samples I analyzed microfracture orientation in all of the cores. However, most of the fractures were oriented to an arbitrary north. Therefore, orientation analyses presented here include only those samples where more than 15 fractures were measured.

9.5.2.1 Backlimb samples

Sample H8 presents a bimodal distribution given by two orthogonal sets oriented perpendicular and parallel to the fold axis (Figure 9.16). Even though there is a large dispersion of the data, Set I (predominant) and Set II (subordinate) can be recognized. When compared with fracture strike data obtained from the microresistivity log a good match is observed between microfractures of Set I sampled with SEM-CL and macrofractures registered with well logs (Figure 9.17).

9.5.2.2 Crest samples

Sample H6 shows some dispersion of strike data but the pattern of sampled microfractures can be unequivocally assigned to Set I, defined in Chapter 8. Comparison between microfractures obtained in the lab and macrofractures from microresistivity log, shows an excellent match (Figure 9.18). This reinforces the hypothesis that transgranular microfractures are genetically related to macrofractures, and can be used as a proxy to define properties such as orientation or intensity; and to assess aggregate properties of fracture population based on their distribution.

Finally, in samples H1, H13 and H7 from crest and forelimb positions (see above), two orthogonal scanlines were defined. In each sample, fracture orientations obtained from one of the scanlines were rotated 90°, to orient all the fractures to the same arbitrary north. Rose diagrams weighted by length, and including fractures sampled in both scanlines, were assembled for each sample, and then rotated an arbitrary angle to make them coincide with the arrangement obtained in other subsurface samples and in the field (Figure 9.19). These samples demonstrate that patterns of preferred orientation can be extracted from samples in this area.

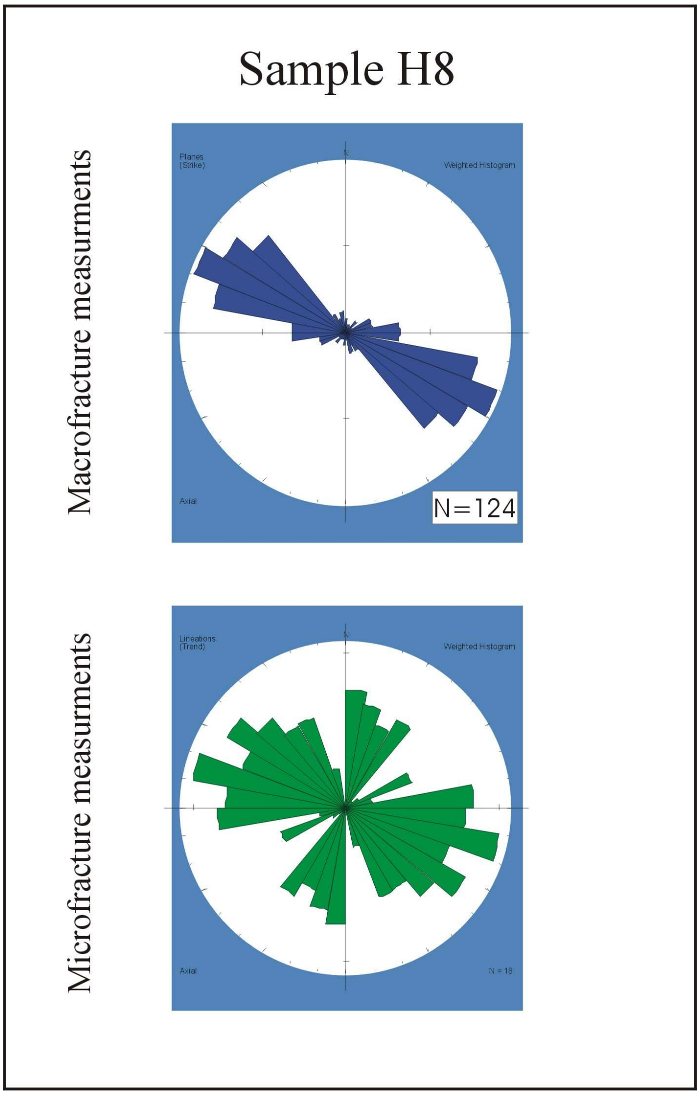

Figure 9.16: Fracture distribution obtained from microresistivity logs (macrofracture measurements) and in the lab (microfracture measurements). Unweighted rose diagrams and a table of fracture measurements are included in Appendix B.

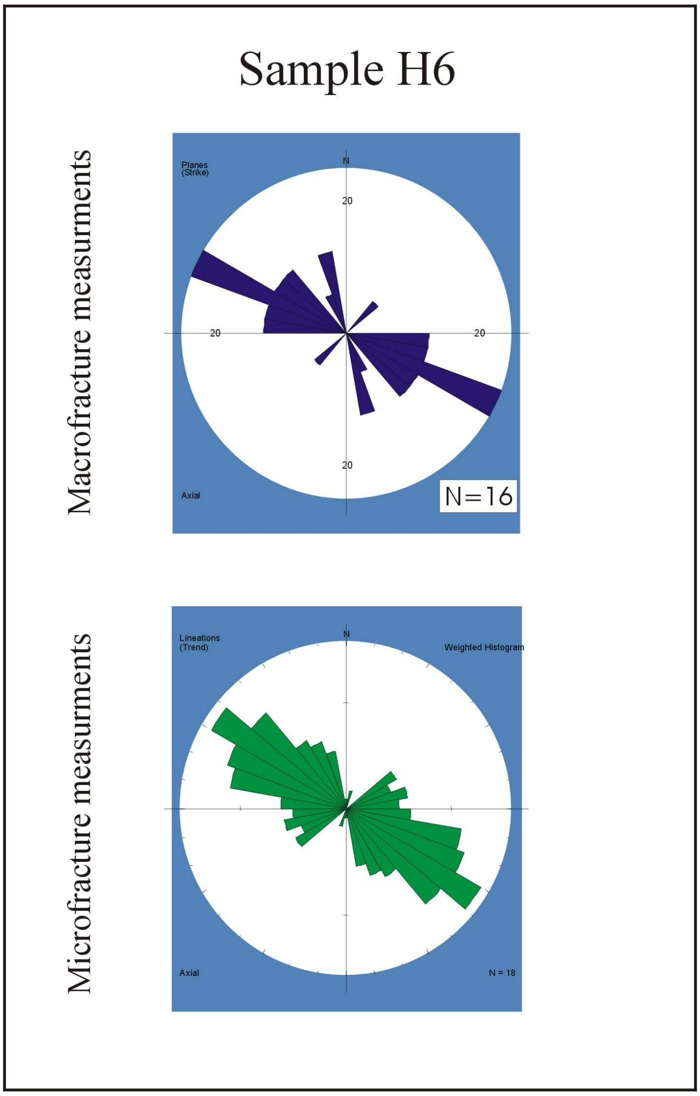

Figure 9.17: Fracture distribution obtained from microresistivity logs (macrofracture measurements) and in the lab (microfracture measurements). Unweighted rose diagrams and a table of fracture measurements are included in Appendix B.

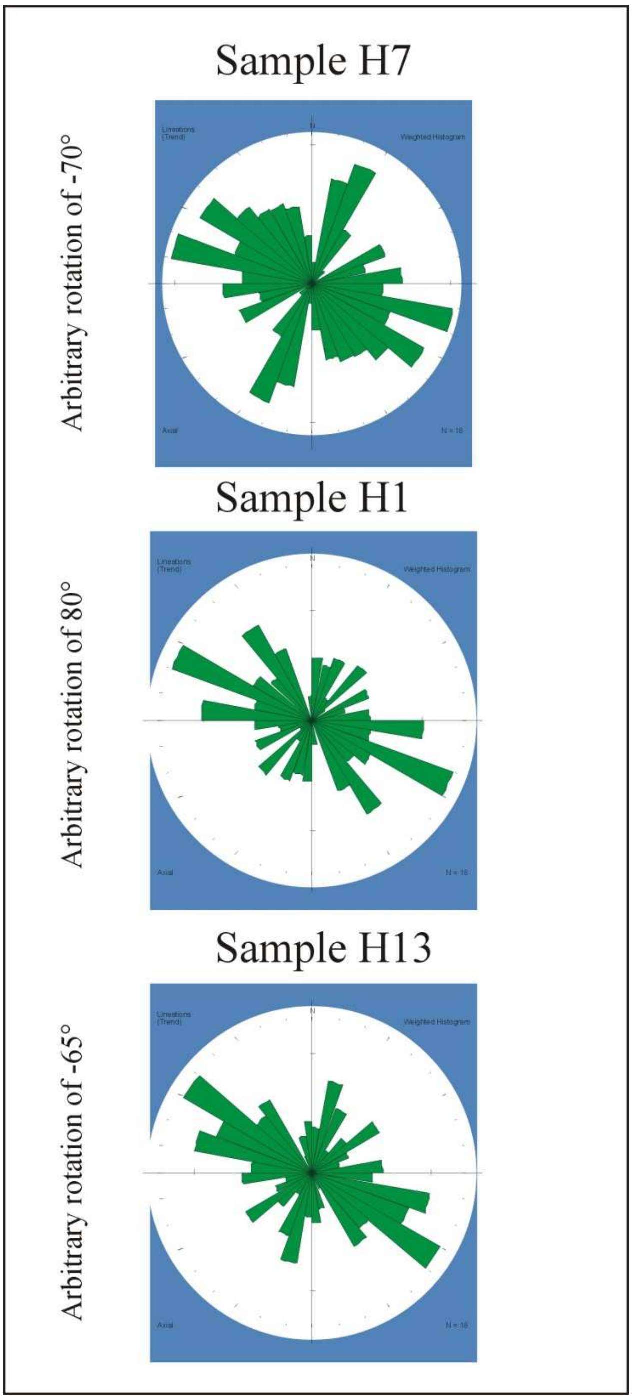

Figure 9.18: Microfracture distribution obtained in the lab and arbitrarily rotated to make it coincide with fracture distribution observed in other samples.

9.6 Microfracture Size Distribution Assessed by Aperture

Size distribution, spatial arrangement, and fracture abundance are some of the primary features of fractures that should be characterized in order to understand the overall fracture system. Many different measurements of fracture distribution can be used to quantify fracture abundance, and how these are arranged in space (e.g. fracture density, frequency, spacing and intensity) (Ortega et al., 2006). However, if these measurements are not constrained to a particular fracture size they become meaningless. This can be easily understood when we analyze fracture intensity or spacing at different scales of observation, such as fractures sampled in outcrop, and microfractures from the same rock studied in the lab with the microscope. The fracture intensity measured at these two scales can be completely different. Where a wide range of fracture sizes is present, a measure of fracture intensity is needed that takes fracture size into account. In my thesis I used cumulative frequency distribution of fracture aperture to characterize fracture distribution, following the methodology described by Ortega et al. (2006) and employed in other fracture studies such as Gomez and Laubach (2006), Gillespie et al. (2001) and Hooker et al. (2009). Cumulative-frequency of fracture-size distribution allows me to unequivocally assess fracture intensity or spacing, since fracture abundance is strictly related to a particular fracture size (Ortega et al., 2006). I use *kinematic aperture* (hereafter, aperture), or the distance fracture walls have moved apart irrespective of mineral fill, following Marrett et al. (1999).

The cumulative frequency of fractures is defined as the cumulative number (N) of fractures normalized by the length of the scanline (L), and is a measurement of the number of fractures of a certain size or larger per unit length of a scanline (Marrett et al., 1999; Ortega et al., 2006). The advantage of working with cumulative-frequency of fracture-size distribution is that it allowed me to define fracture intensity objectively, and by means of this to compare fracture distribution for different samples, over a range of scales, to assess the control imposed by tectonic and lithological features on fracture intensity arrangement.

Kinematic aperture of each fracture was defined in GoMezure^{TM} using the x and y points of vertex 2 and 4 (see Figure 9.6). If the fracture is not perpendicular to the direction of the scanline the aperture defined is an apparent aperture. However, GoMezure^{TM} takes into account the scanline orientation and calculates the full aperture of fractures (Gomez and Laubach, 2006).

In order to assess which distribution (e.g. power-law, log-normal, negative exponential) best fit aperture size arrangement of microfractures, I plotted the cumulative frequency number against the aperture values of the fractures. Through the square of the correlation coefficient (R^2), I defined the best fit for fracture distribution.

Power laws have been widely used to describe size distribution of opening mode fractures (Marrett et al., 1999; Ortega and Marrett, 2000; Ortega et al., 2006; Gillespie et al., 1993; Gillespie et al., 2001; Gomez and Laubach 2006; Laubach and Ward, 2006; Clark et al, 1995). By means of these distributions, predictions could be made about the frequency of fractures of different sizes. However, most of these studies are focused on cemented filled fractures (veins) and not on partially filled, joint-type fractures such as the ones I analyzed in my thesis.

Gillespie et al. (2001) performed studies of size distribution for joints, by surveying the length of these fracture type in Ireland and studying their distribution with the log-interval method (frequency histograms with the length divided into logarithmic class intervals), but they did not measure aperture. These authors argue that joint type fractures follow log-normal length distribution, due to the fact that joints in the studied outcrops abut each other, and the length is controlled by the orientation and spacing of pre-existing joints; restricting them to a narrow range of scales. Hooker et al. (2009) studied size distribution of joints (open fractures with negligible cement) but they surveyed aperture instead of length since the data was from horizontal core. They propose that in low strain zones, aperture distribution of joints may follow a power law for certain ranges of the scale. However, log-normal distributions were also found in the smallest ranges of the studied scale, and explained by the absence of fracture linkage or coalescence during the initiation of the fracture nucleation. By means of this, they define a log-normal distribution up to a threshold size from which a power law kicks in to represent the distribution of the largest fractures.

Although I performed size distribution analyses in all of the available samples, I only present the results of those where at least ~15 microfractures were measured. A distribution defined on a smaller number of elements would lack reliability. All size measurements and the GoMezure files are included in Appendix B. In addition, I assessed the distribution of fractures according to their orientation. Where only one predominant set was present (e.g. sample JI-04 above) I analyzed fractures as a whole. However, most of the samples have a bimodal orientation distribution and I did two analyses: one considering all the fractures together and another one with fractures divided by set. Finally, I did a size distribution analyses by imposing a size threshold above which I eliminated larger fractures from the analysis. My premise is that where the two orientations of fractures in orthogonal sets are genetically related (see Chapter 8), they should be analyzed together because any self organization would be affected by the development of both sets. On the other hand, if these two set were not contemporaneous, they should be analyzed separately since they were responses to different deformation processes. Further complications can be added to the problem. Bergbauer and Pollard (2004) argue that first-generation fractures will have an impact on all fractures formed later.

9.6.1 OUTCROP SAMPLE SCALING RESULTS

The number of fractures in outcrop samples is extremely low. For scaling analysis a minimum sample size of 200 fractures is preferred (Marrett et al., 1999). This allowed me to only perform distribution analyses on the two samples of the forelimb.

9.6.1.1 Forelimb samples

In sample JI-04 a unimodal distribution of fracture orientation was present parallel to what I defined as Set II. Figure 9.19 shows that fracture size arrangement is well fitted both by a log-normal distribution and a negative exponential distribution with practically equal R^2 values. It is interesting to notice that no fractures with a size larger than 0.015 mm are present in the sample.

Microfracture orientation distribution on sample JI-03 has only one predominant set that parallels the distribution of Set I (see above). Therefore, I treated all of the fractures as one group. Figure 9.20 shows these fractures have a fairly good power law size distribution. However when we removed the fractures with a size larger than 0.015 mm (a value I chose as a size threshold based on the threshold size defined by Hooker et al., 2009), we see that a power law (red line), a negative exponential (black line) or a log-normal distribution could represent the data equally well, based on the R^2 values obtained (Figure 9.20).

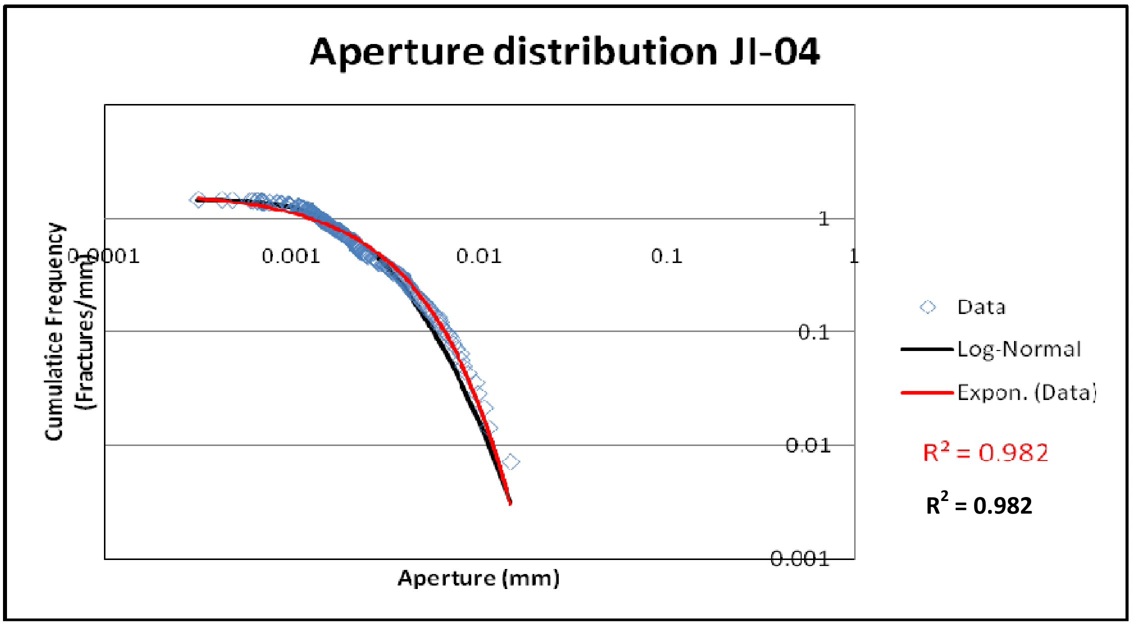

Figure 9.19: Fracture aperture distribution for sample JI-04. Data could be fitted both by a log-normal or an exponential distribution.

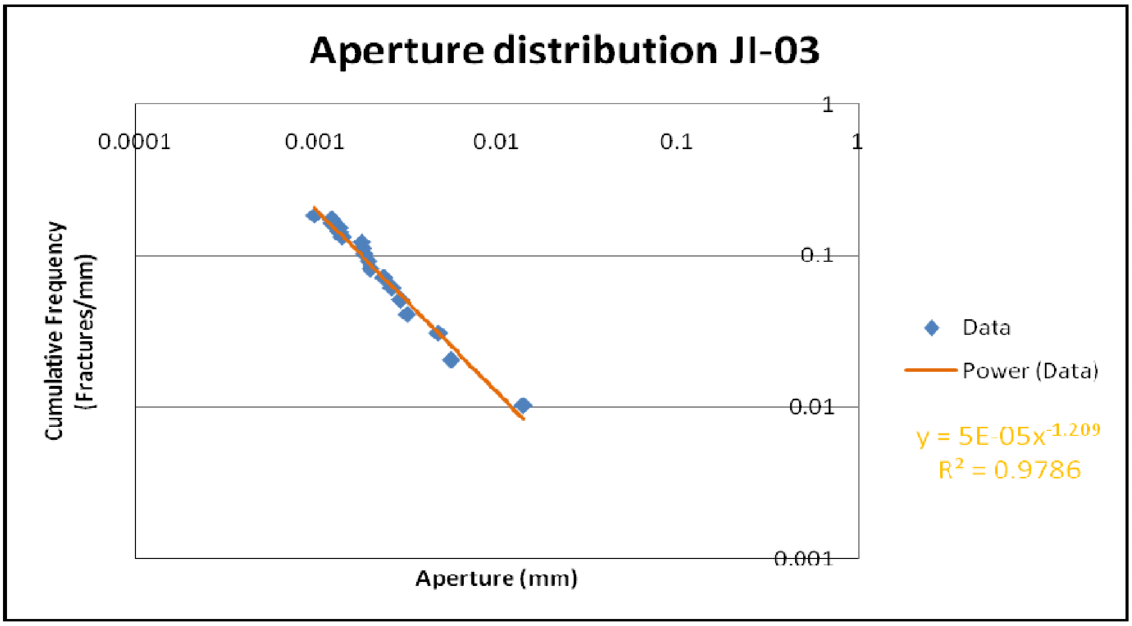

Figure 9.20: Fracture aperture distribution for sample JI-03. Data could be fitted by a power law.

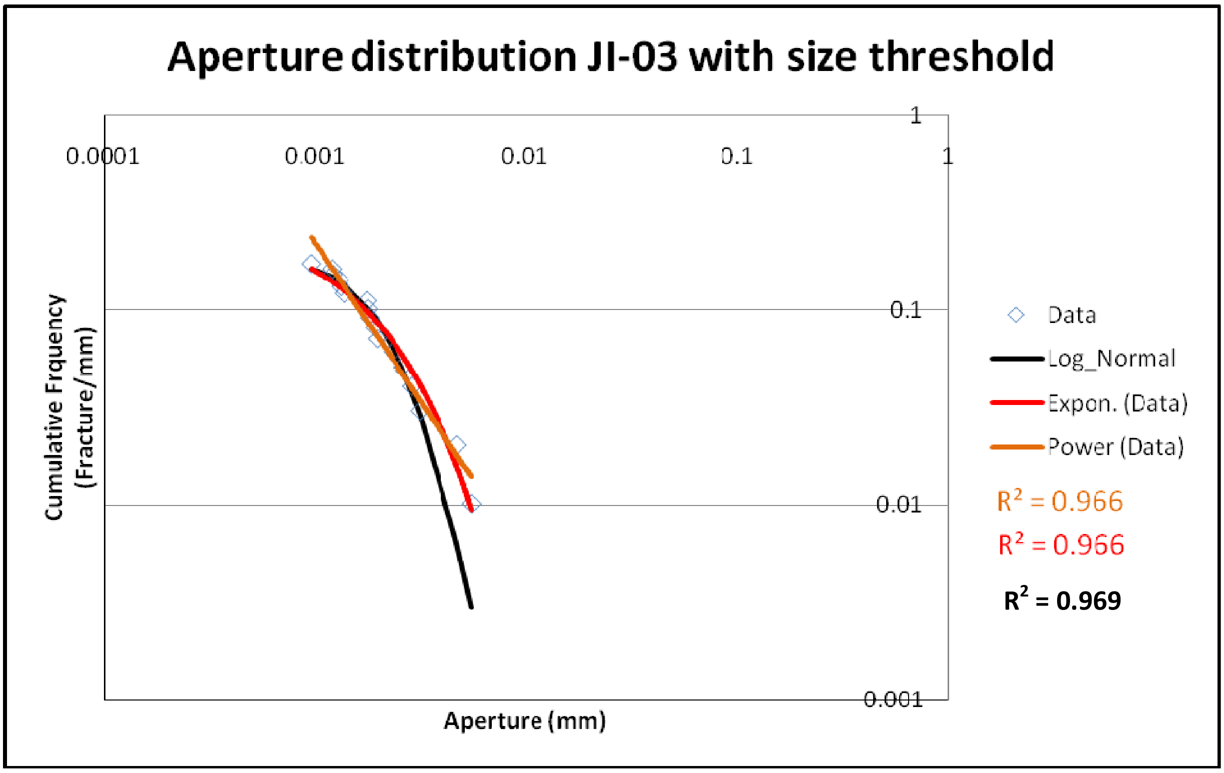

Figure 9.21: Fracture aperture distribution for sample JI-03 with a size threshold. Data could be fitted equally well by a log-normal, an exponential distribution, and a power law.

9.6.2 SUBSURFACE SAMPLE SCALING RESULTS

Most of the subsurface samples were not oriented with respect to north. Therefore for size scaling, I conducted two scanlines perpendicular to each other. Below I present the size distribution for the scanlines analyzed individually and collectively.

9.6.2.1 Backlimb samples

In sample H8, I performed two orthogonal scanlines. Figure 9.22 shows the distribution of fractures intersected in each scanline, which were interpreted as Set I and Set II. It can be observed that the fractures of both sets could be defined by fair power law dsitributions. However, few fractures were sampled in each scanline making the results uncertain. When the fractures were analyzed as a whole a power law distribution fits the data with an R^2 value of 0.96 (Figure 9.23). Then, when I removed those fractures above a threshold size (0.015 mm) a negative exponential equation better fits the aperture arrangement; a log-normal distribution also fits the data (Figure 9.24).

9.6.2.2 Crest samples

Fractures in sample H1 were arbitrarily rotated to make them coincide with the Sets I and II as defined in the field and from other samples. In spite of the orientation uncertainty in this, two orthogonal fracture sets are present, which were analyzed separately and together. Figure 9.25 shows the aperture distribution for each set and the power law equation fitted to them. Figure 9.26 shows the two sets analyzed together; it can be seen that a power law describes this distribution fairly well. However, when the fractures above a size threshold of 0.01 mm are removed a log-normal distribution is a better match for the fracture arrangement (Figure 9.27). We should mention, however that negative exponential, logarithmic and normal distribution all have R^2 values above 0.96.

Sample H13 is similar to H1, since fractures were arbitrarily rotated to make them coincide with the pre-defined sets. It is interesting to notice that in this sample the distribution of each set cannot be characterized with a statistical distribution. The fractures of Set II are poorly fitted by a power law, and those of Set I have a fair to poor R^2 value for either a negative exponential or power law distributions. A log-normal distribution has a better fit (Figure 9.28). When the two sets are combined a poor power law distribution is apparent as shown in Figure 9.29. Finally, when fractures above the size threshold (0.015 mm) are removed, the best fit is obtained with a log-normal distribution (Figure 9.30).

In sample H6 the orientation of the core was known, and one single scanline perpendicular to macrofracture orientation was defined. The same pattern found in the other samples was observed. Fractures have a good power law distribution with a R^2 value of 0.96 (Figure 9.31). When a size threshold of 0.015 mm is applied, the fractures are better characterized with a negative exponential distribution or even a log-normal distribution (Figure 9.32).

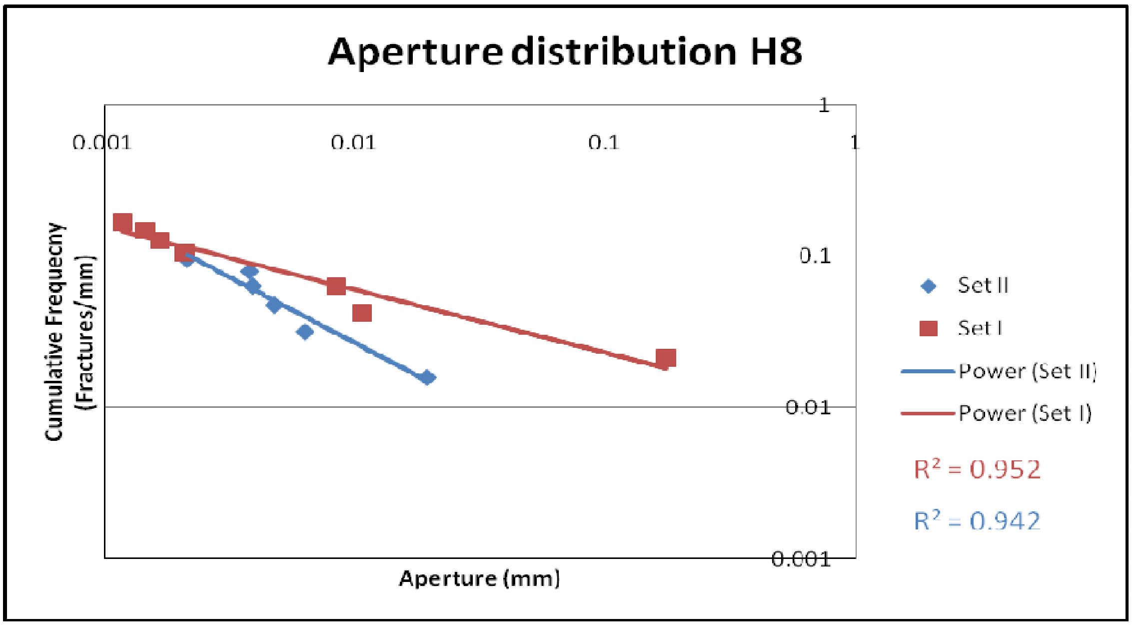

Figure 9.22: Fracture aperture distribution for sample H8. Both sets could be fitted by a fair to poor power law.

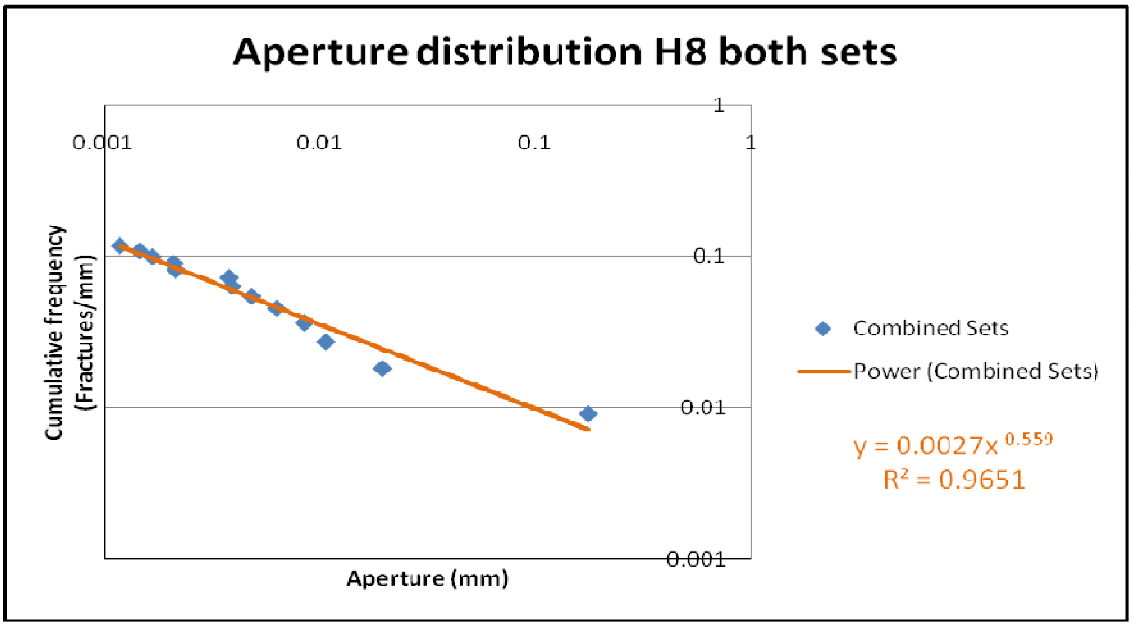

Figure 9.23: Fracture aperture distribution for sample H8 both sets together. Both sets combined could be fitted by a fair power law.

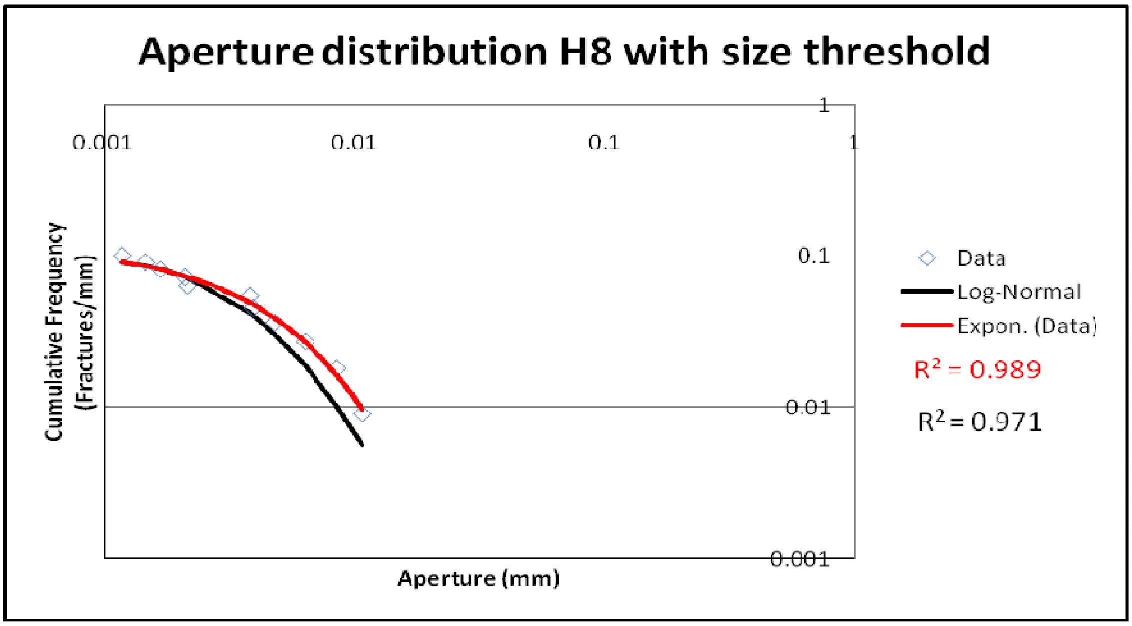

Figure 9.24: Fracture aperture distribution for sample H8 with a size threshold. Data can be fitted by an exponential or a log-normal distribution.

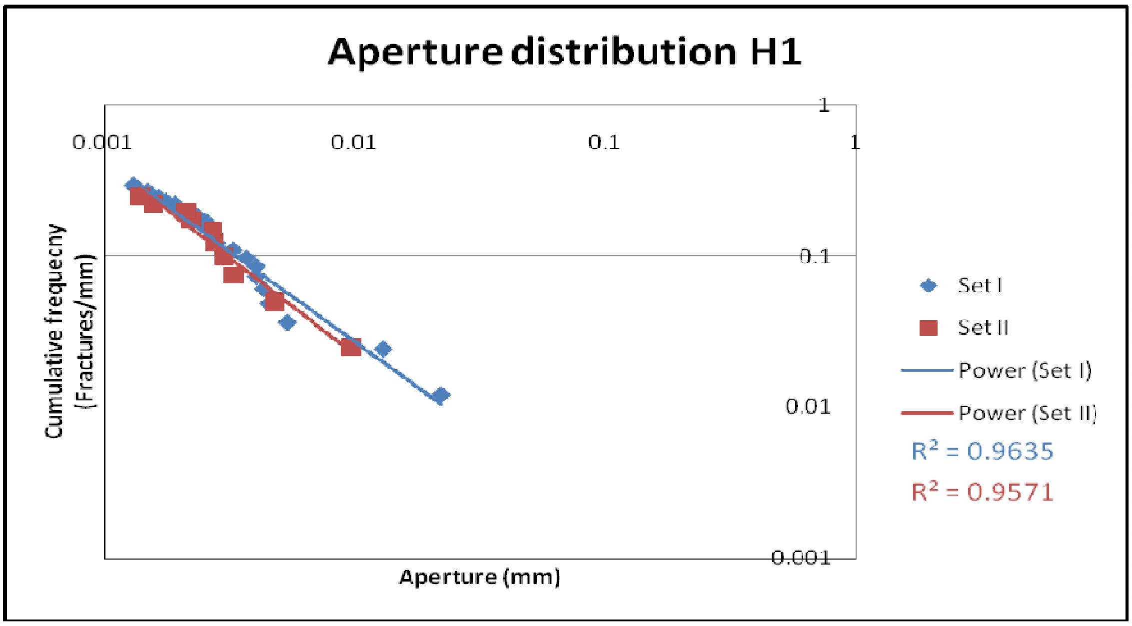

Figure 9.25: Fracture aperture distribution for sample H1. The data of the two orthogonal fracture sets interpreted here as Set I and Set II, can be fitted by a power law distribution.

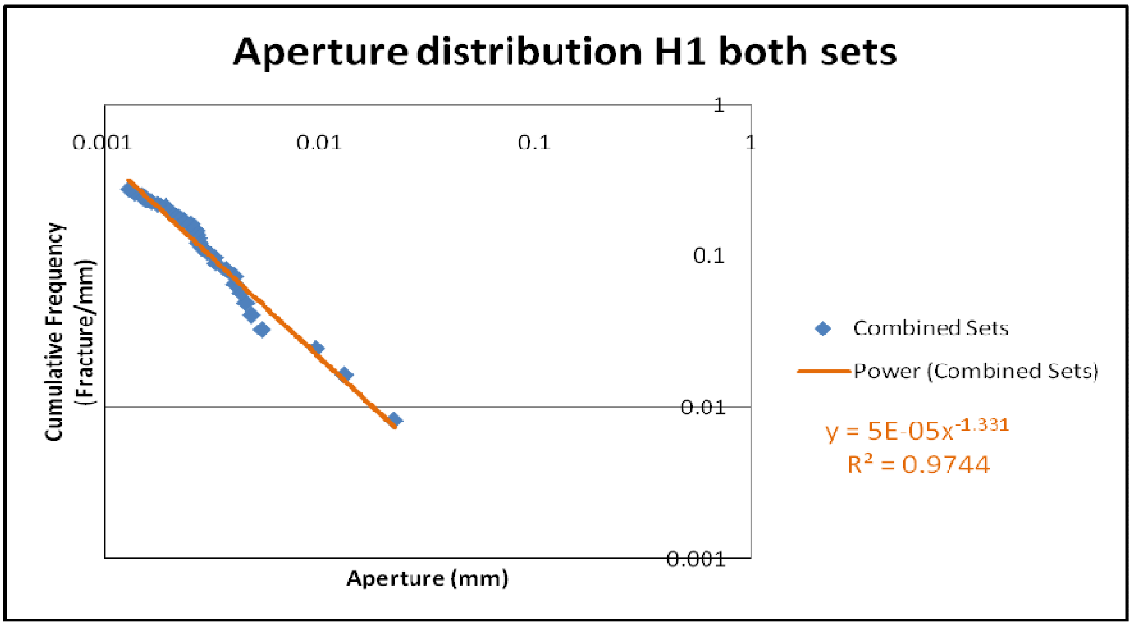

Figure 9.26: Fracture aperture distribution for sample H1 both sets combined. The data could be fitted by a power law distribution.

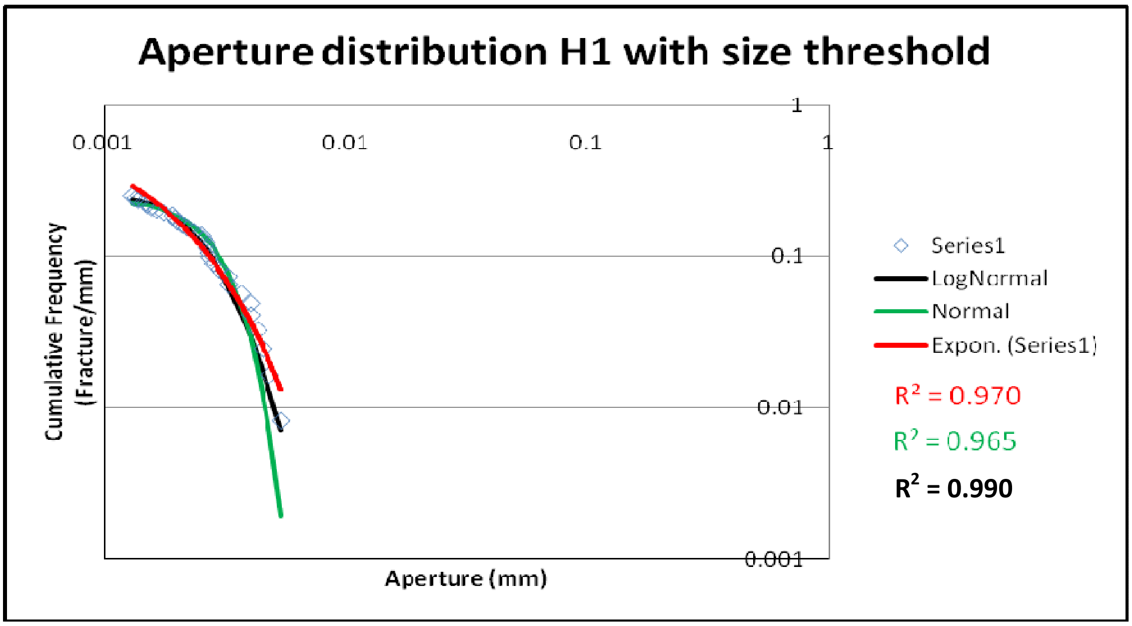

Figure 9.27: Fracture aperture distribution for sample H1 both sets combined with size threshold. The data could be fitted almost perfectly by a log-normal distribution; normal and exponential distribution also shows good fit.

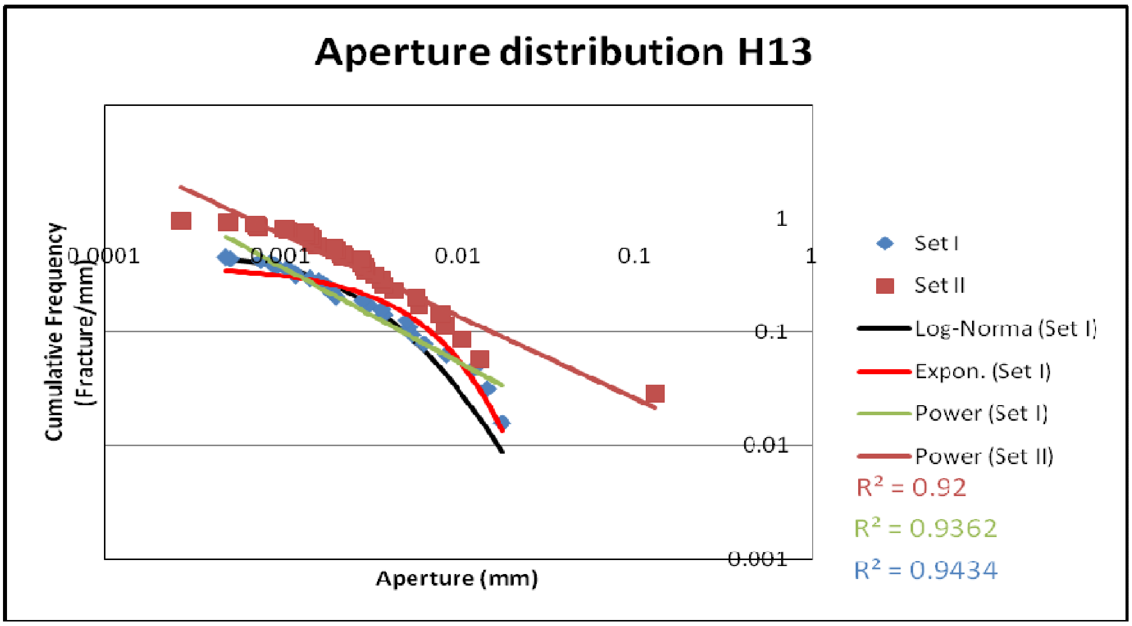

Figure 9.28: Fracture aperture distribution for sample H3 both sets. The data of Set II could be fitted by a poor power law. Set I data present poor R2 values for power law and exponential distribution and a much better fit with a log-normal distribution.

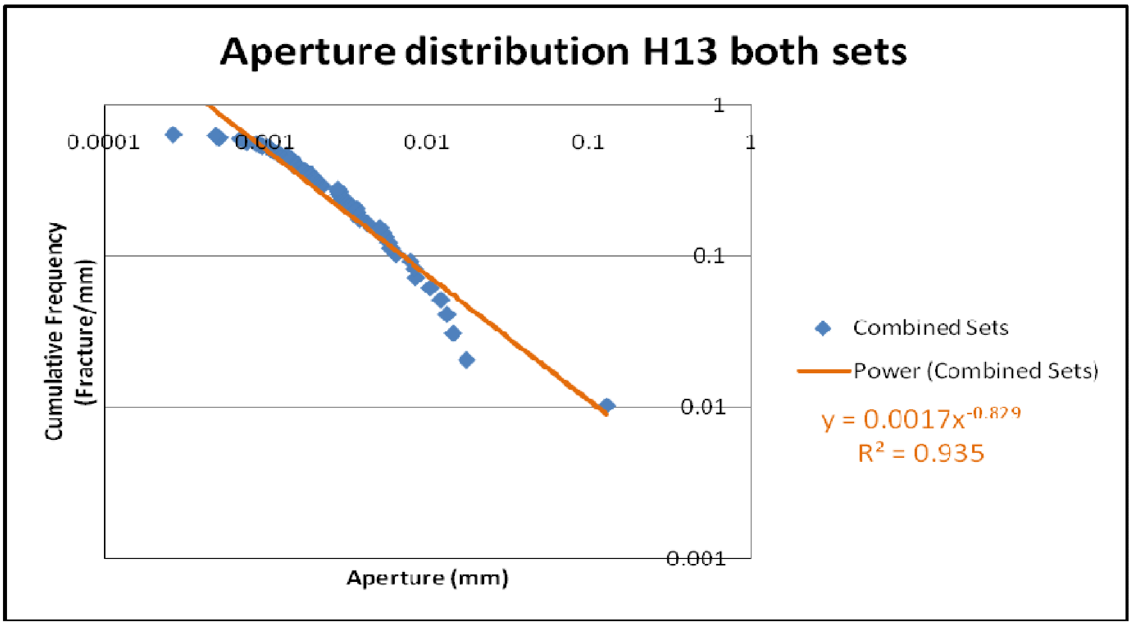

Figure 9.29: Fracture aperture distribution for sample H13 both sets combined. The data could be fitted by a poor power law distribution.

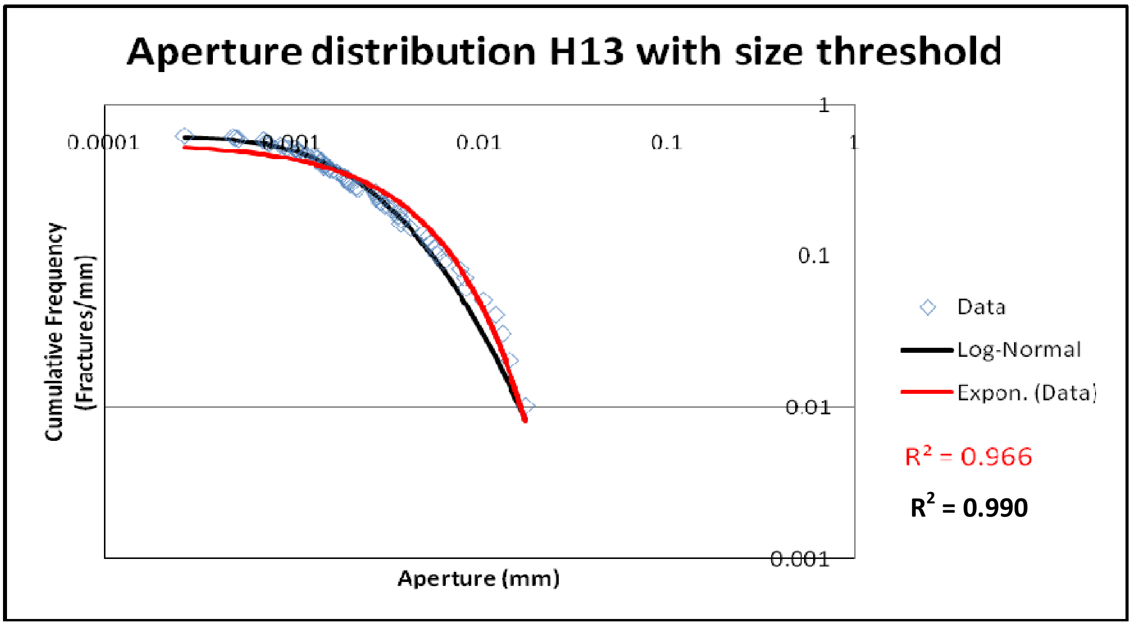

Figure 9.30: Fracture aperture distribution for sample H13 both sets combined with size threshold. The data could be fitted almost perfectly by a log-normal distribution; an exponential distribution also shows good fit.

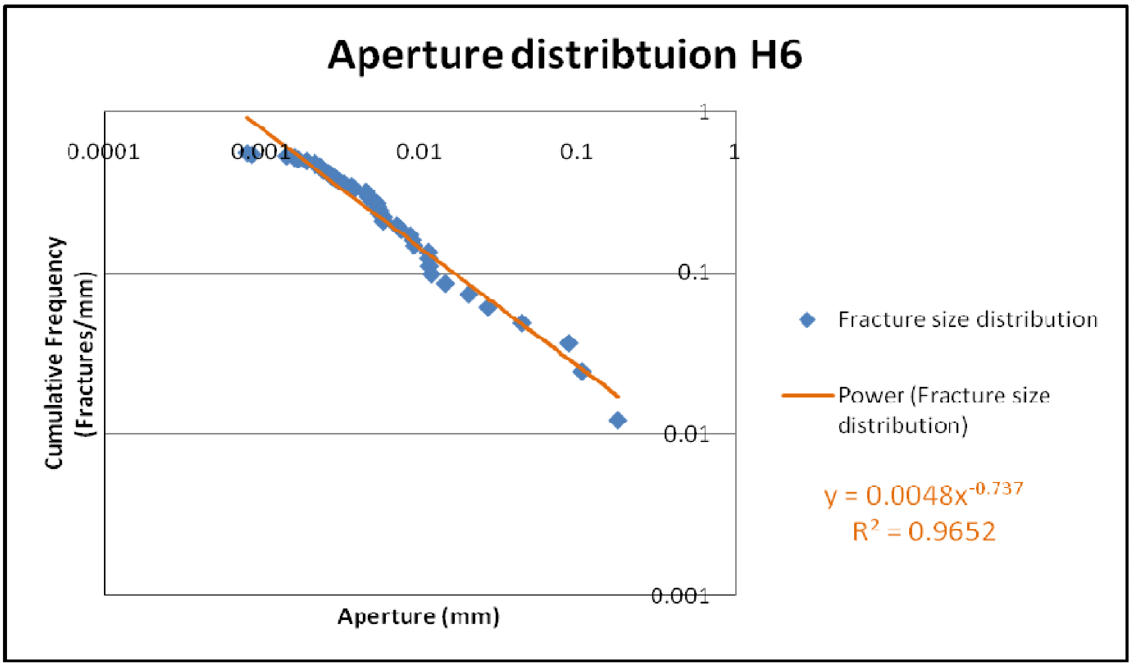

Figure 9.31: Fracture aperture distribution for sample H6. The data is fitted by a power law.

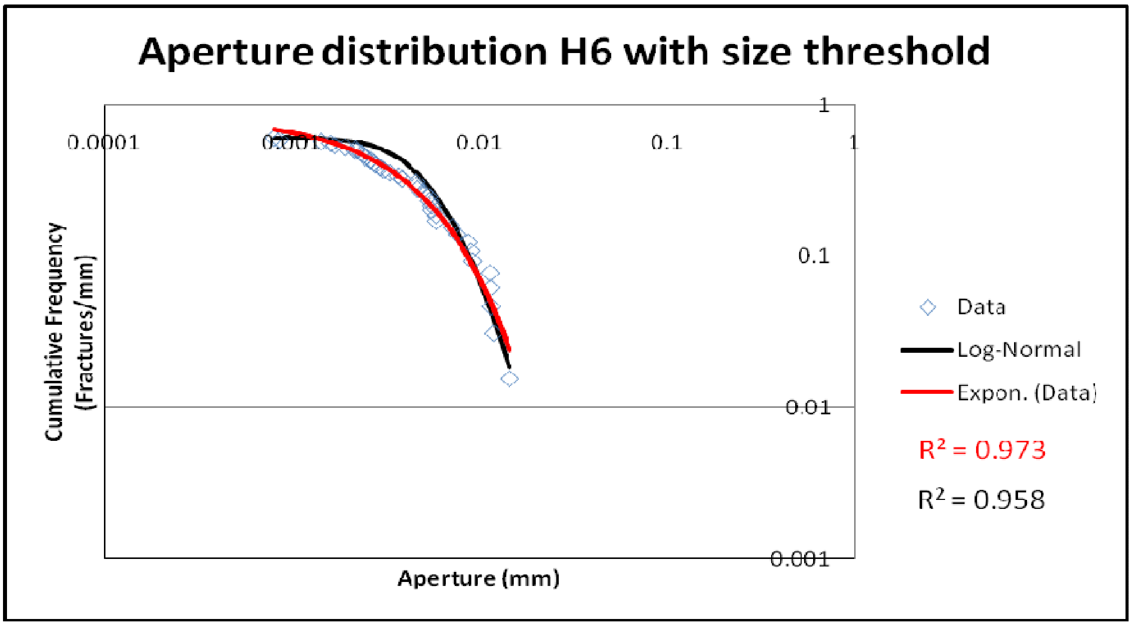

Figure 9.32: Fracture aperture distribution for sample H6 with size threshold. The data could be fitted by an exponential distribution; a log-normal distribution also shows good fit.

9.6.2.3 Forelimb samples

In sample H7, an arbitrary rotation of fractures was performed and the fractures sampled on the two orthogonal scanlines were ascribed as possible Set I and Set II elements. When studied separately the fractures of Set II are better represented by a log-normal distribution, while those of Set I are best represented by a power law distribution (Figure 9.33). When the fractures were analyzed as a group a power law distribution is apparent (Figure 9.34). Finally, Figure 9.35 shows that if the fracture above the size threshold (0.015 mm), are excluded the best fitting distribution is log-normal.

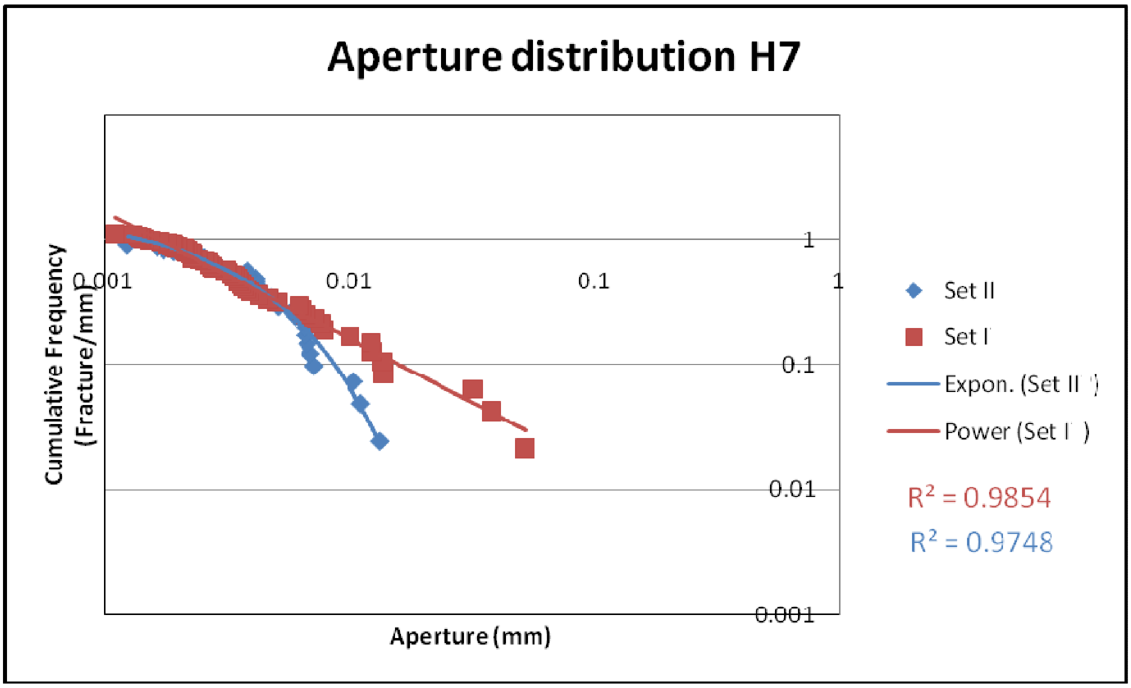

Figure 9.33: Fracture aperture distribution for sample H7. Set II is better fitted by a power law, while Set II shows a better exponential fit.

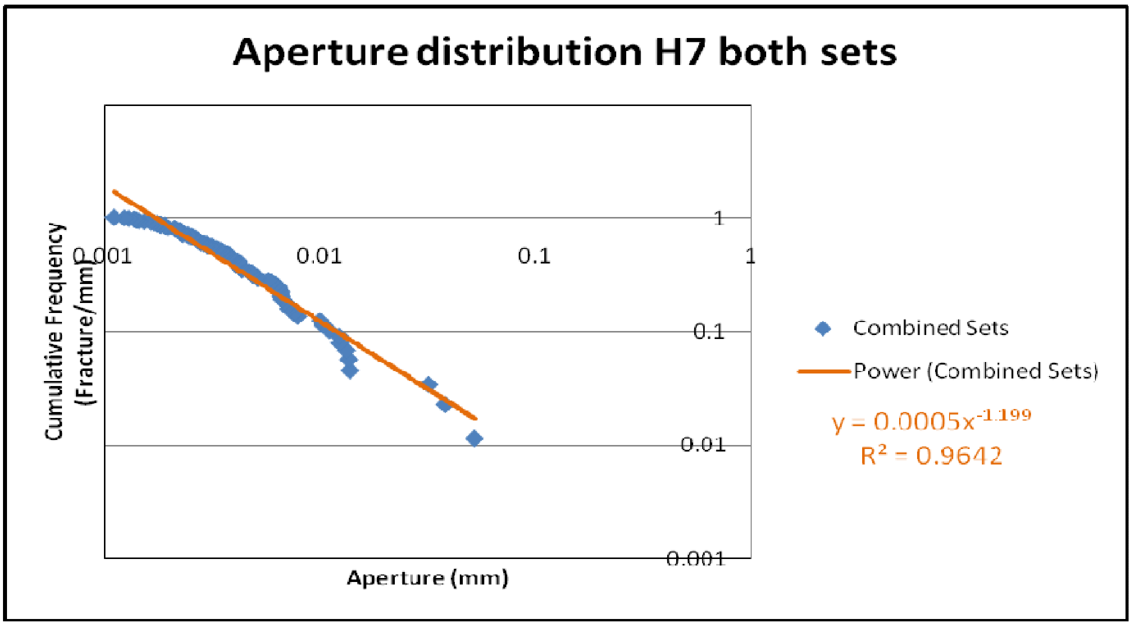

Figure 9.34: Fracture aperture distribution for sample H7 both sets combined. The data could be fitted by a poor power law distribution.

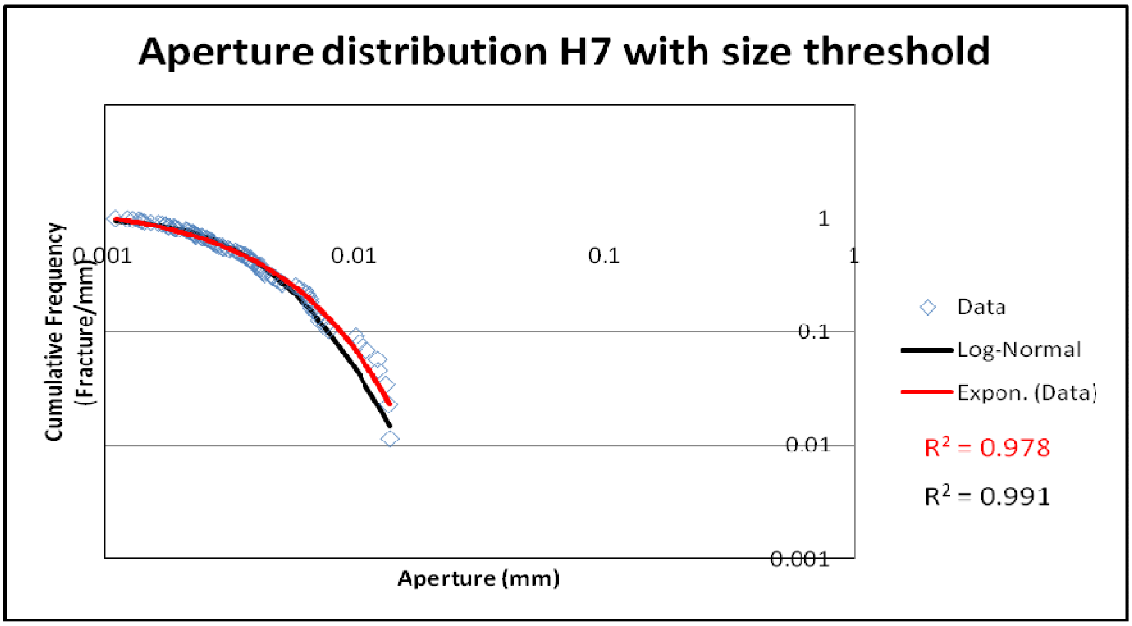

Figure 9.35: Fracture aperture distribution for sample H7 both sets combined with size threshold. The data could be fitted almost perfectly by a log-normal distribution; an exponential distribution also shows a good fit.

9.7 Spacing Distribution of Fractures

Spacing is perhaps the most used feature studied to asses fracture distribution along a scanline. Most common arrangements of spacing between fractures are given by negative exponential (Pineau, 1985) and log-normal distributions (Narr and Suppe, 1991; Gillespie et al., 1993; Rives et al., 1992). I obtained spacing data from the analyses performed in GoMezure^{TM}, in which the distance between vertices located on the scanline is employed to define the spacing between consecutive fractures (see Figure 9.6). I assessed the spacing between fractures in two different ways: The first method involved a similar methodology to the one described for fracture size distribution. In this case the spacing values for fractures were plotted against the cumulative frequency of spacing, obtained by dividing the cumulative number of the spacing values by the total length of the scanline. Then, I fit equations to assess which distribution best describes the spacing arrangements. The second one was done applying the correlation counting technique (Marrett et al., in review), described below. This allowed me to define the spacing sequence of fractures.

The main difference from size distribution analyses is that fracture sets were studied separately, since independent of the interpreted fracture origin, it would not make any sense to assess the spacing between fractures that are not parallel and definable with a single scanline.

Figures 9.36 through 9.46 represent the cumulative frequency distribution of spacing against spacing sizes. All of the samples I studied are best defined either by a log-normal or a negative exponential distribution; this would mean that fractures should be periodically spaced with a particular value that represents the most common spacing between fractures. Table 9.4 is the R^2 value for both distributions in each of the samples studied.

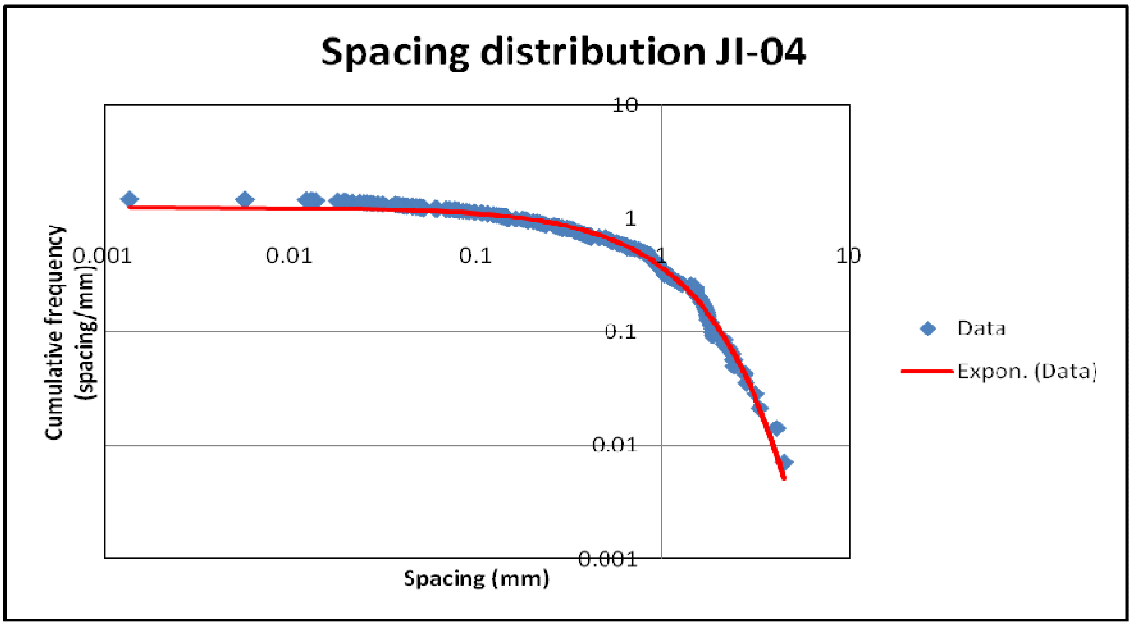

Figure 9.36: Fracture spacing distribution for sample JI-04. The data could be fitted almost perfectly by an exponential distribution.

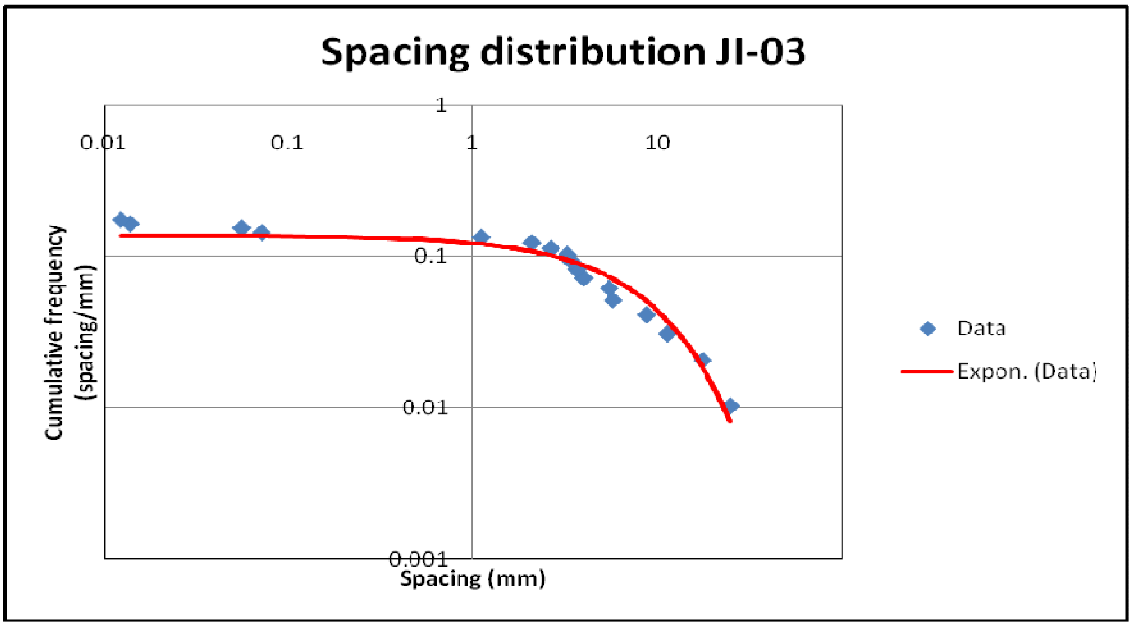

Figure 9.37: Fracture spacing distribution for sample JI-03. The data could be fitted by an exponential distribution.

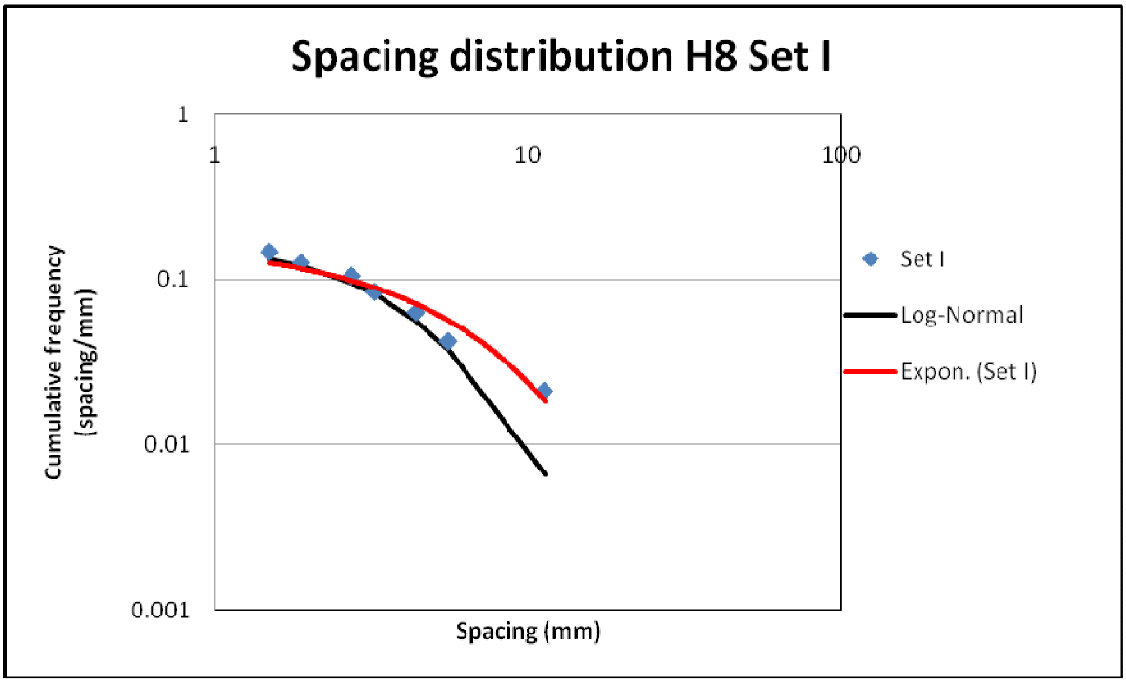

Figure 9.38: Fracture spacing distribution for H8 Set I. The data could be fitted by an exponential or a log-normal distribution.

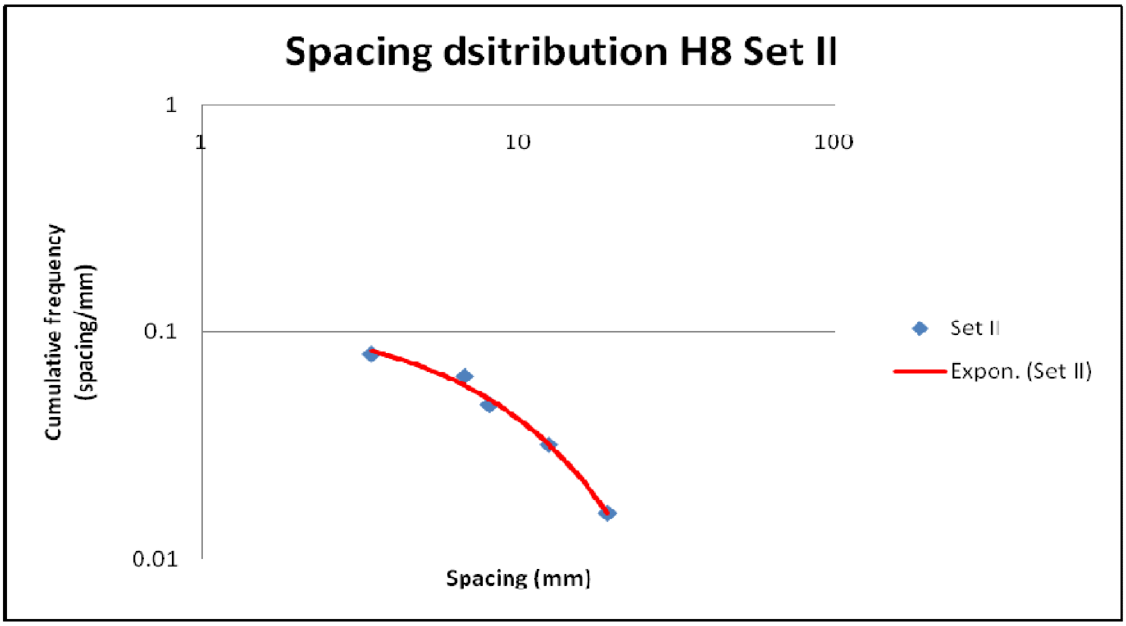

Figure 9.39: Fracture spacing distribution for H8 Set II. The data could be fitted by an exponential distribution.

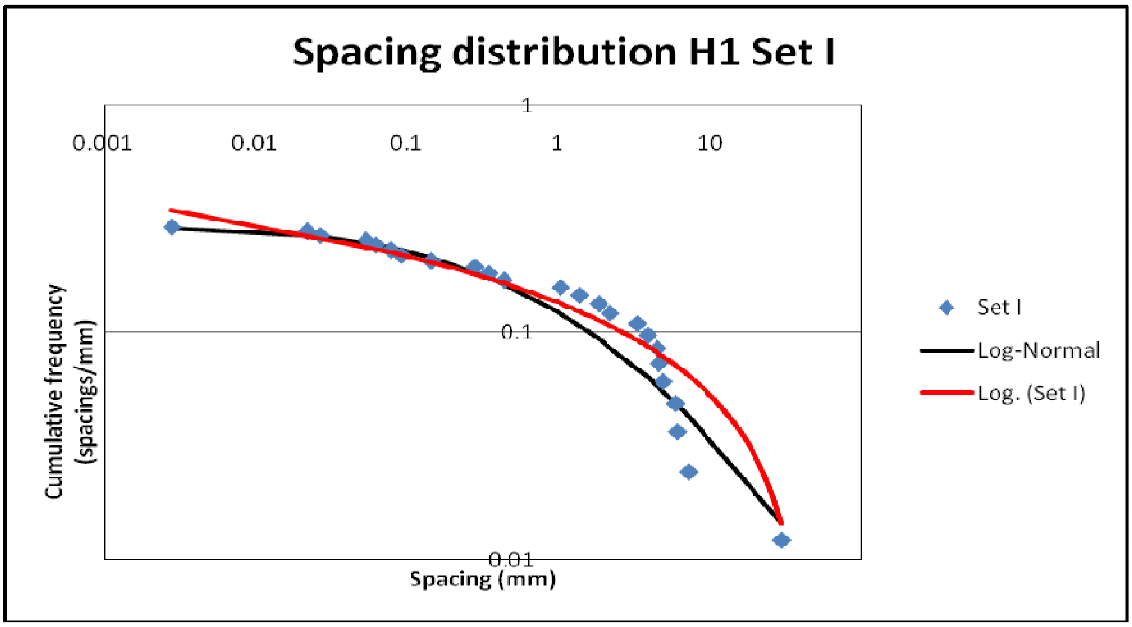

Figure 9.40: Fracture spacing distribution for H1 Set I. The data could be fitted by an exponential or log-normal distribution.

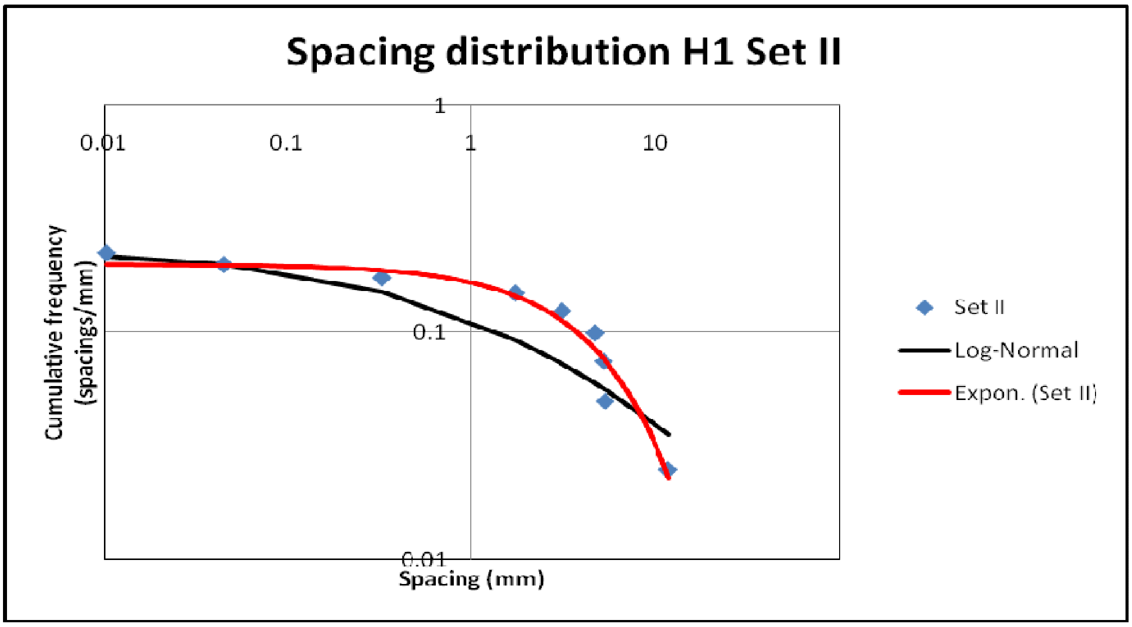

Figure 9.41: Fracture spacing distribution for H1 Set II. The data could be fitted by an exponential or log-normal distribution.

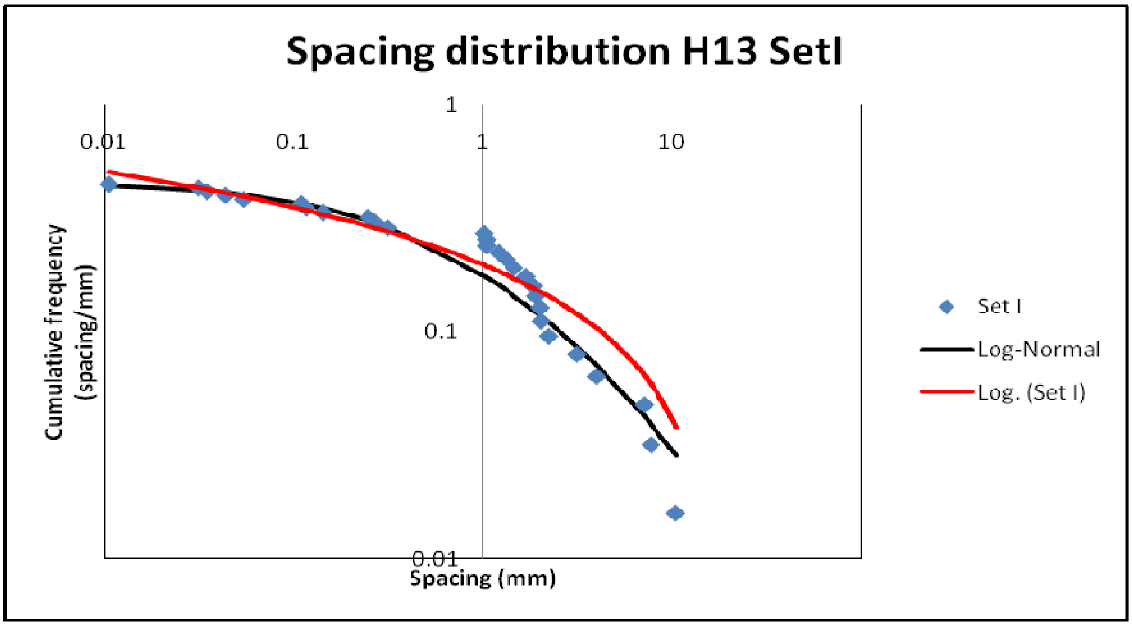

Figure 9.42: Fracture spacing distribution for H13 Set I. The data could be fitted by an exponential or log-normal distribution.

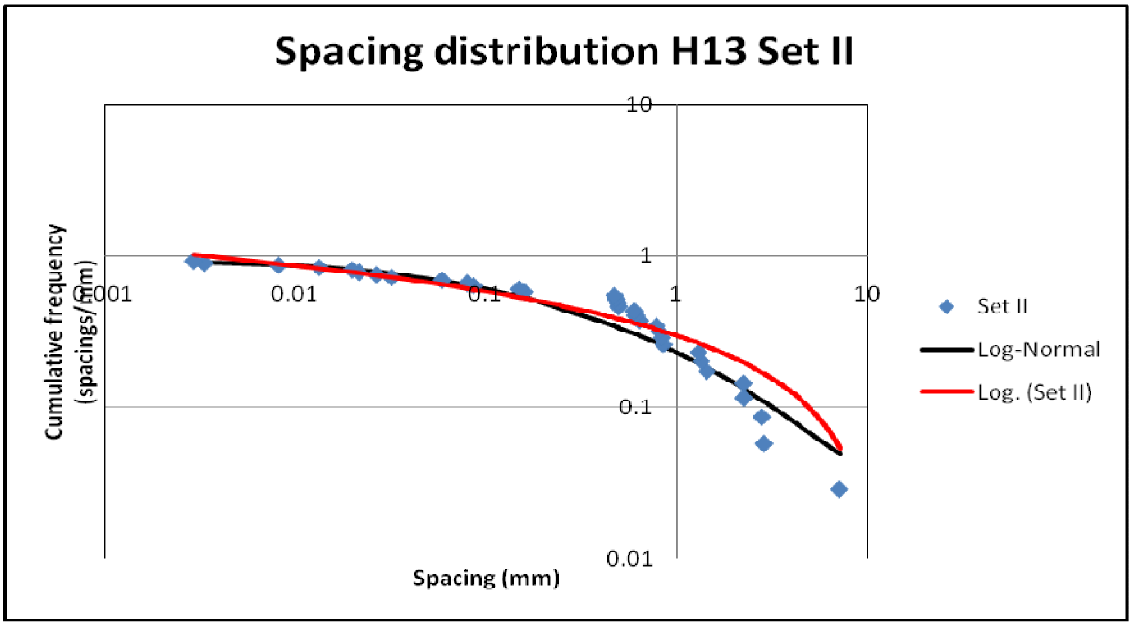

Figure 9.43: Fracture spacing distribution for H13 Set II. The data could be fitted by an exponential or log-normal distribution.

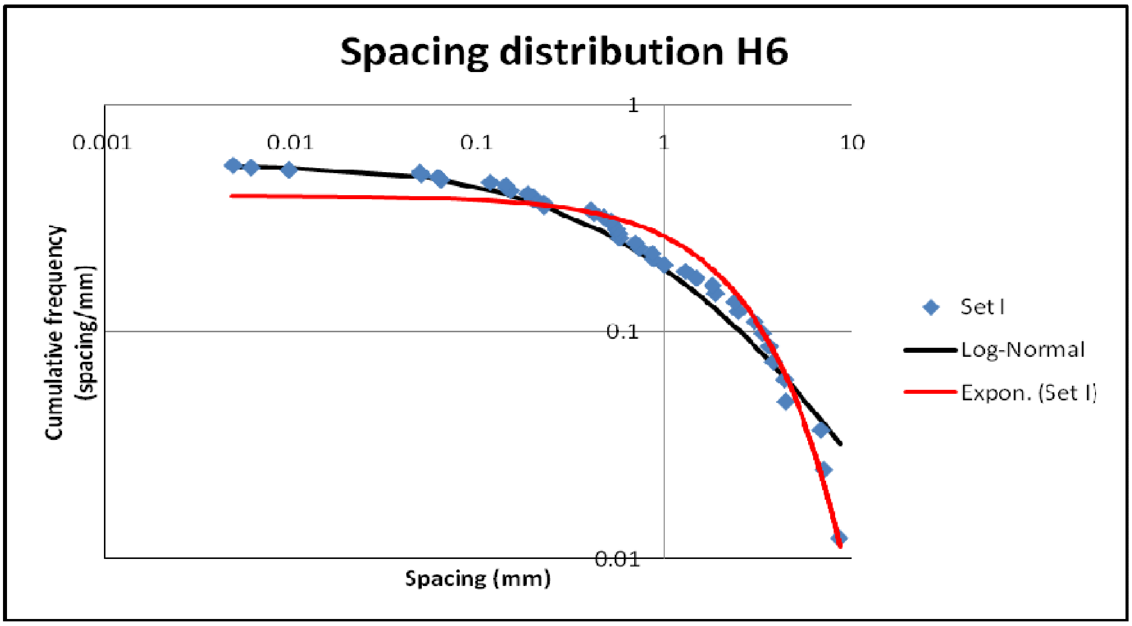

Figure 9.44: Fracture spacing distribution for H6. The data could be fitted by an exponential or log-normal distribution.

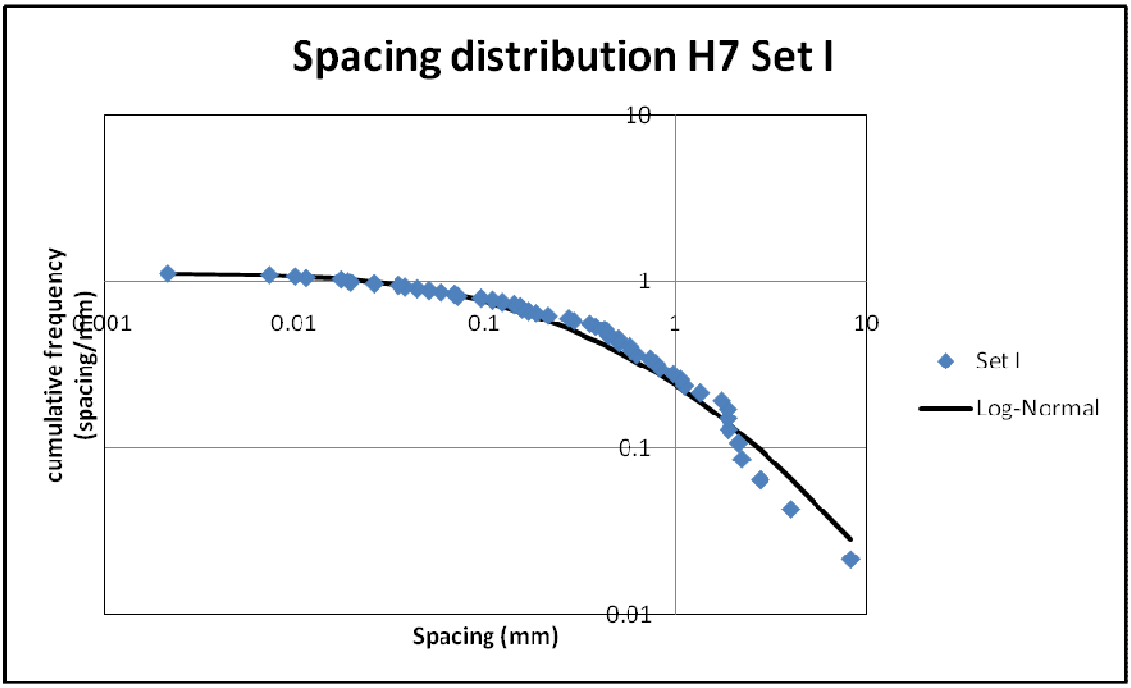

Figure 9.45: Fracture spacing distribution for H7 Set I. The data could be fitted almost perfectly by a log-normal distribution.

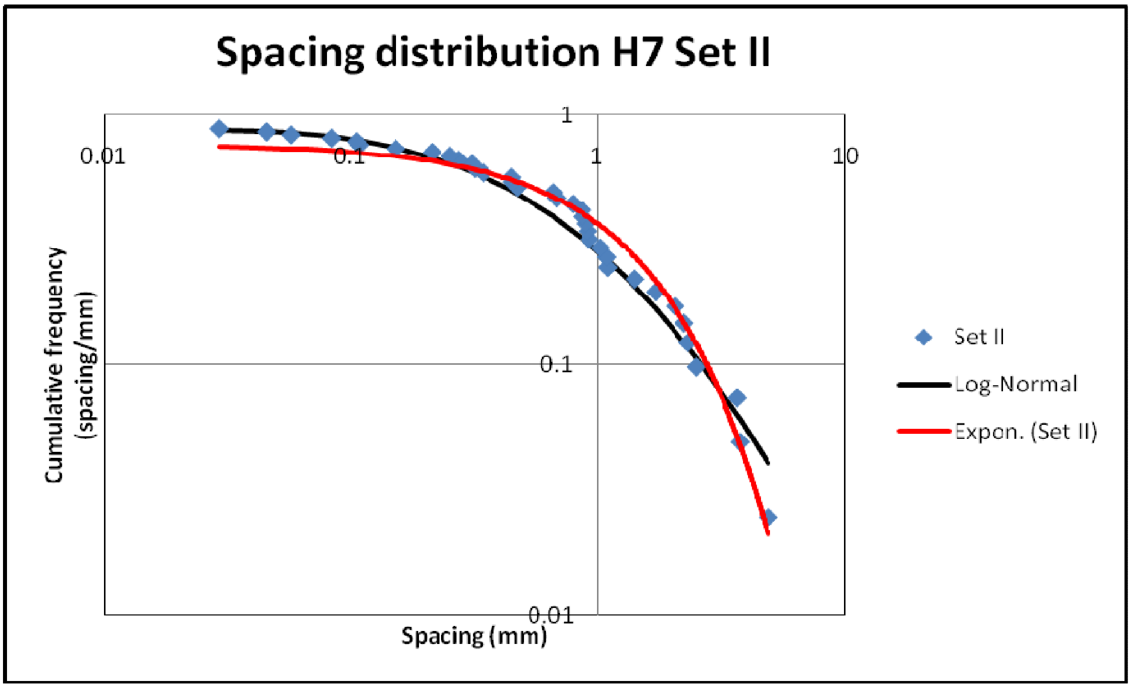

Figure 9.46: Fracture spacing distribution for H7 Set II. The data could be fitted by an exponential or log-normal distribution.

Sample	Log-Normal distribution R^2 value	Exponential distribution R^2 value
JI-04	0.982	**0.990**
JI-03	0.856	**0.951**
H8 Set I	**0.988**	0.943
H8 Set II	0.986	**0.992**
H1 Set I	**0.958**	0.945
H1 Set II	0.868	**0.944**
H13 Set I	**0.942**	0.937
H13 Set II	**0.944**	0.934
H6	**0.988**	0.955
H7 Set I	**0.988**	0.819
H7 Set II	**0.982**	0.974

Table 9.4: Squares correlation coefficient (R^2) for log-normal and exponential distributions in each of the studied spacing arrangements.

9.8 Correlation Counting Technique

This methodology is defined in the work of Marrett et al. (in preparation) and Marrett (in preparation). The advantage of this technique is that it accounts for the sequence of fracture spacings and assesses potential relationships between fracture spacing and size. However, the later was not analyzed in my thesis and will not be further explained. The distance, not only between consecutive fractures, but for all of the possible fracture pairs that can be created with a number of fractures N distributed on a scanline of length L, is assessed in order to account for sequences of fracture spacings.

The analysis of fracture spacing can diagnose the extent to which fractures are clustered in space; compared to random distribution. Fractures can be more clustered (positive correlation $C>1$) or more regularly spaced (negative correlation $C<1$). The method assesses the number of fracture pairs n_i, that are separated by a distance equal or less than λ_i (the length scale considered in a logarithmic distribution), and greater than λ_{i-1}. In order to give statistical validity to the results, the spatial correlation is normalized by the number of fractures pairs obtained in a random distribution n_{random} for the same number of fractures N along a scanline for the same length L.

$$C_i = \frac{n_i}{n_{random}}$$

Where

$$n_{random} = \frac{N\,(N-1)}{2}\,\frac{\lambda_i - \lambda_{i-1}}{L}\left[2 - 2\frac{\lambda_i}{L} + \frac{\lambda_i - \lambda_{i-1}}{L}\right]$$

The correlation between fractures and one hundred randomized versions of the same scanline were created using the Java version of the correlation count software created by Marrett (2006).

Only the three samples with the largest amount of surveyed fractures were considered (N>45), since smaller populations loses meaning in this analysis. For sample JI-04, some clustering of the microfractures occurs between the scale of 0.1 and 0.5 mm. Above a spacing of 05 mm, the arrangement cannot be differentiated from random distribution (Figure 9.47). Sample H6 and H7 show similar distribution with fractures spacing showing a clear positive correlation (C>1), meaning that more clusters are present than in a random arrangement (Figure 9.48 and 9.49). Both samples show larger amounts of fracture pairs with spacing in the range of 0.1 to 0.2 mm than those with spacing in the range of 10 mm. Although a power law equation could be fitted to the spacing distribution, the data set is too sparse for this to be meaningful.

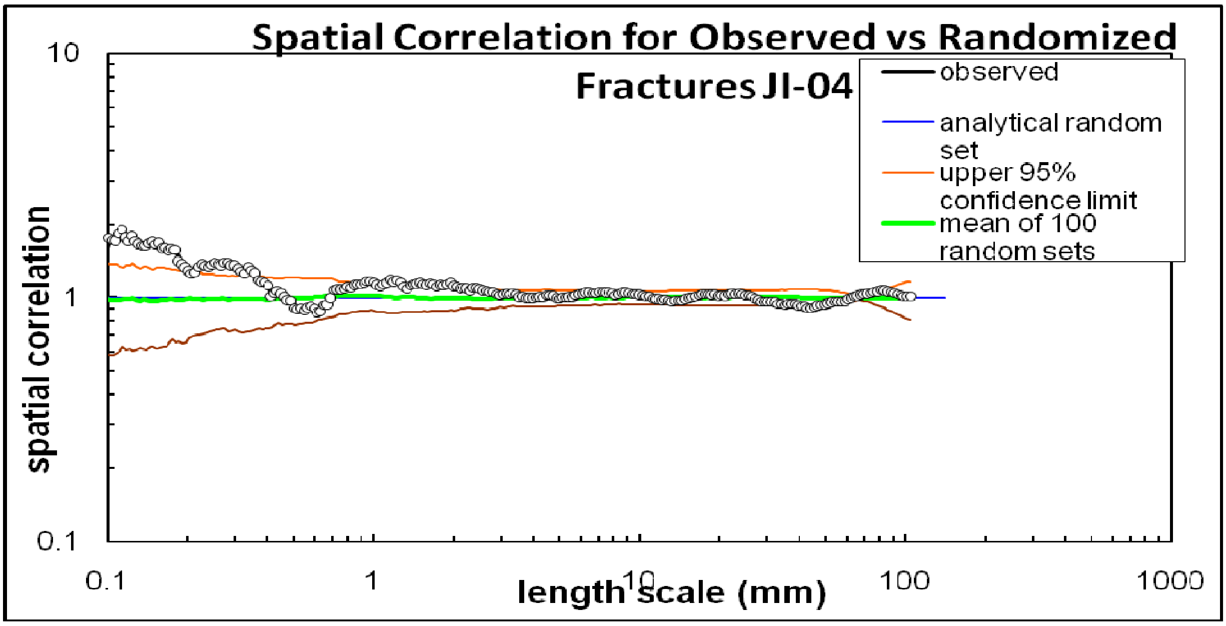

Figure 9.47: Spatial correlation for sample JI-04. See text for explanation.

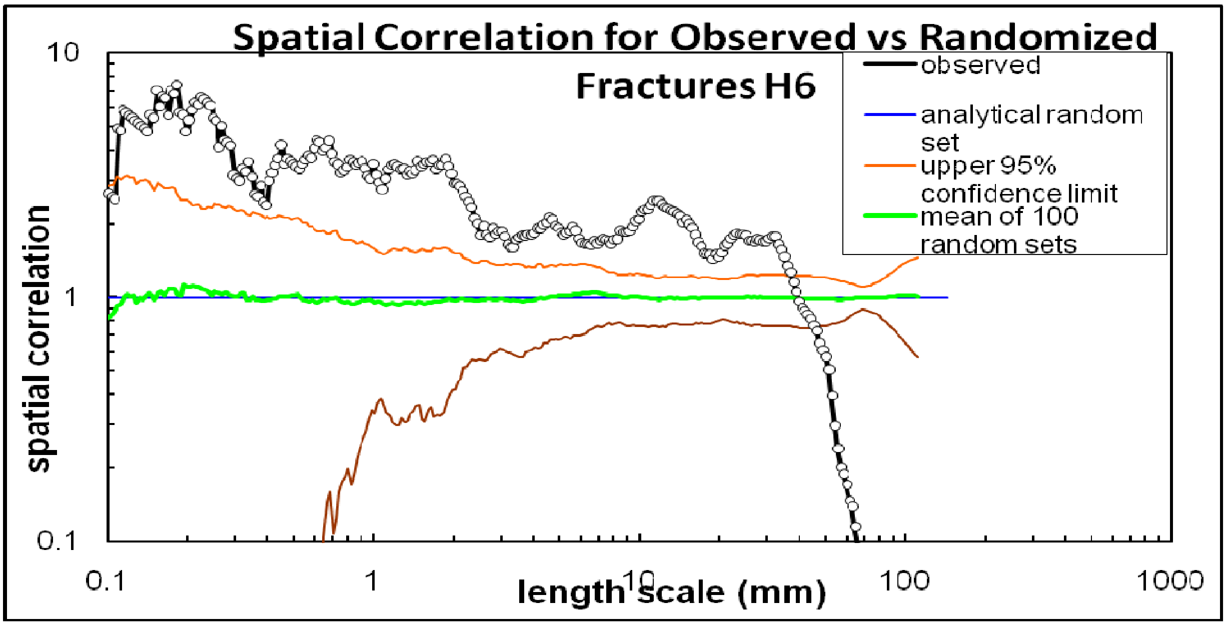

Figure 9.48: Spatial correlation for sample H6. See text for explanation.

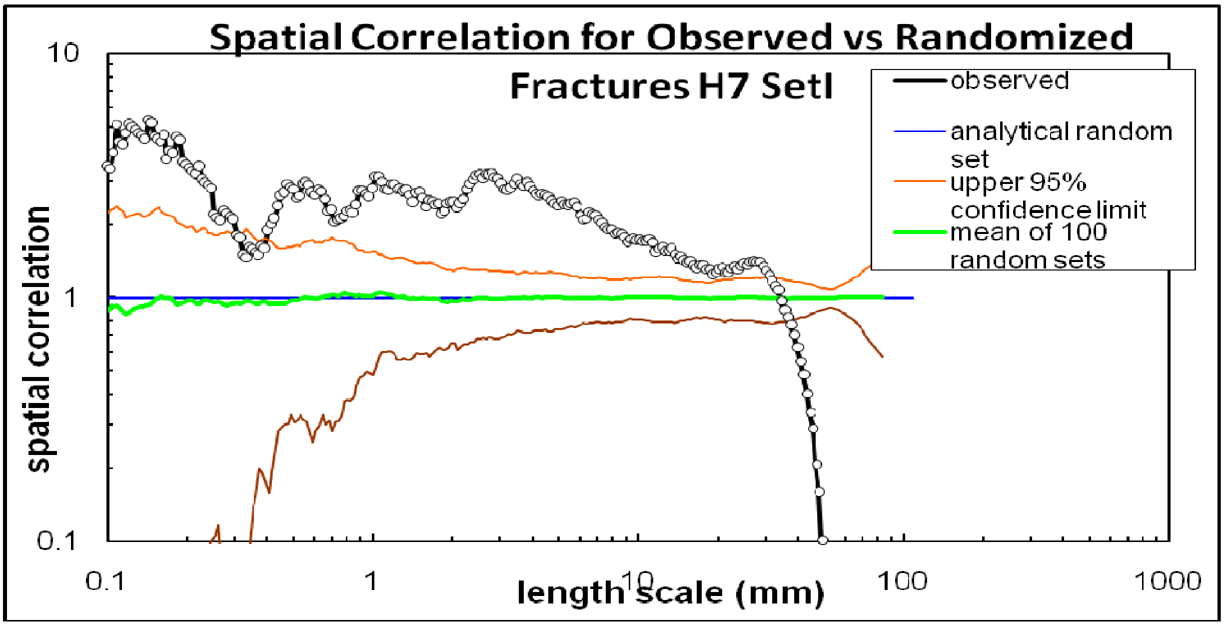

Figure 9.49: Spatial correlation for sample H7 SetI. See text for explanation.

CHAPTER 10: PETROGRAPHY

In order to assess variation of depositional lithology and diagenetic effects on the studied rocks and to analyze the influence exerted by these features in fracture patterns, I measured framework grain content, cement and porosity for all the studied samples. This was done by point counting elements, with a petrographic microscope. I counted three hundred points for each of the samples; Appendix D presents the charts with the point counting data for each sample. Although the Devonian sandstones of the Subandean Ranges are usually defined as quartzarenites, according to Folk's classification (1980) (Figure 10.1a) the studied rocks are mostly near the boundary between sub-litharenites and feldspathic litharenite, for their quartz contents are less than 95% (Figure 10.1b).

10.1 Principal Components

10.1.1 QUARTZ

Normalized quartz composition ranges from 62% to 42% both for outcrop and subsurface samples, and the average value is 52%. However, most subsurface samples usually have larger amounts of quartz, than the samples collected in the field. Monocrystalline anhedral quartz with undulose, normal and patchy extinction constitutes the most common grain. The samples are generally well sorted, with subangular to subrounded shaped grains (Figure 10.2). However, differences are evident in grain size and in packing arrangement. Many samples have quartz grains tightly packed together with concave-convex contacts between them as a predominant feature (Figure 10.3). Some samples have smaller grains immersed in a matrix of altered clay or pseudomatrix derived from deformed lithics (Figure 10.4). Interpenetrating contacts associated with compaction and dissolution are also present. I identified large amounts of quartz overgrowth cement in optical continuity with the quartz grains, this made it extremely difficult to correctly assess which points correspond to quartz grains and which to cement. Polycrystalline quartz is also present but is less abundant ranging from 9% to 1.7%, and with an average of 3.7%.

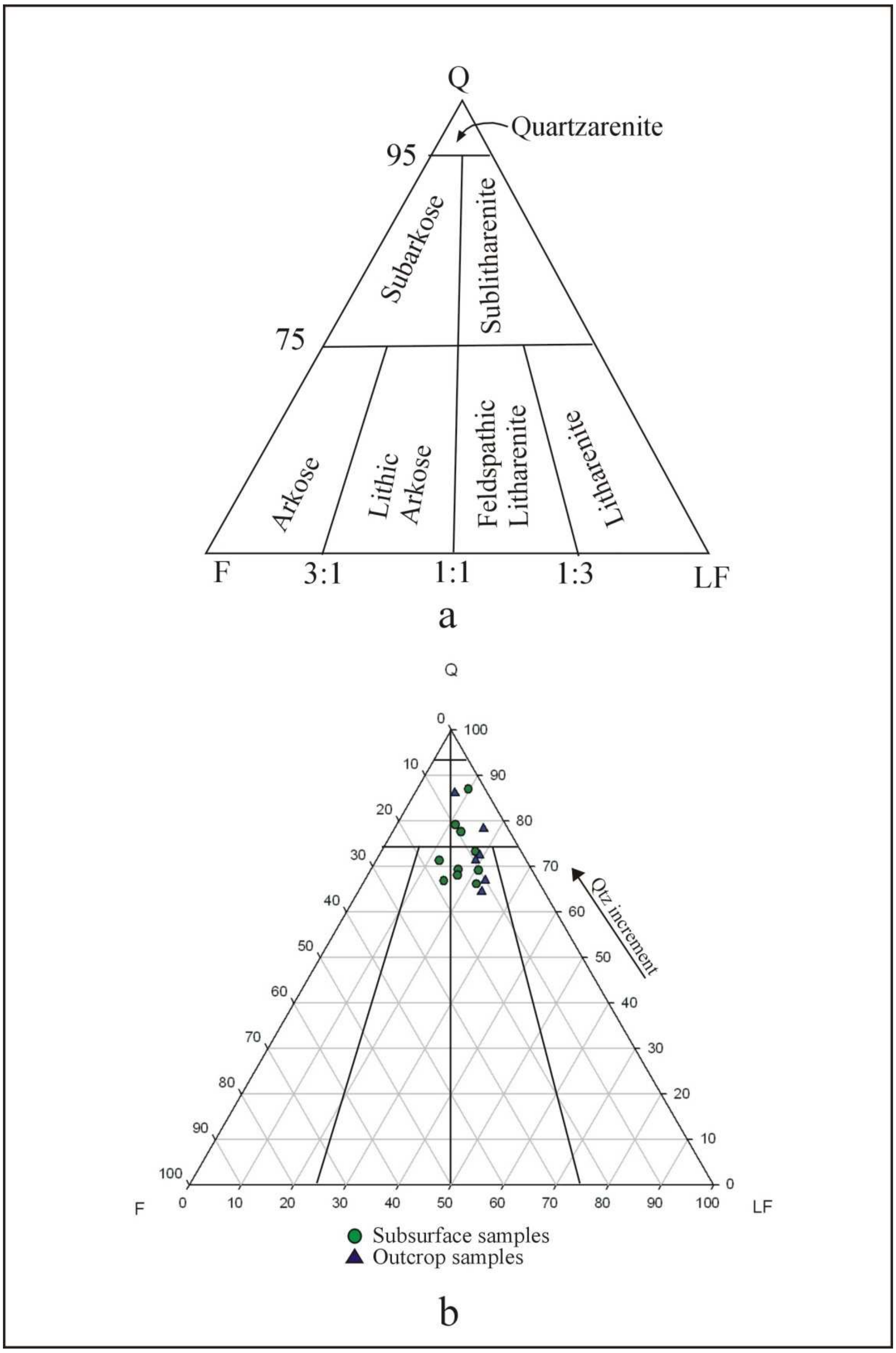

Figure 10.1: a. Folk's rock classification (modified from Folk 1980). b. Rock classification of Devonian sandstones in the Subandean Ranges.

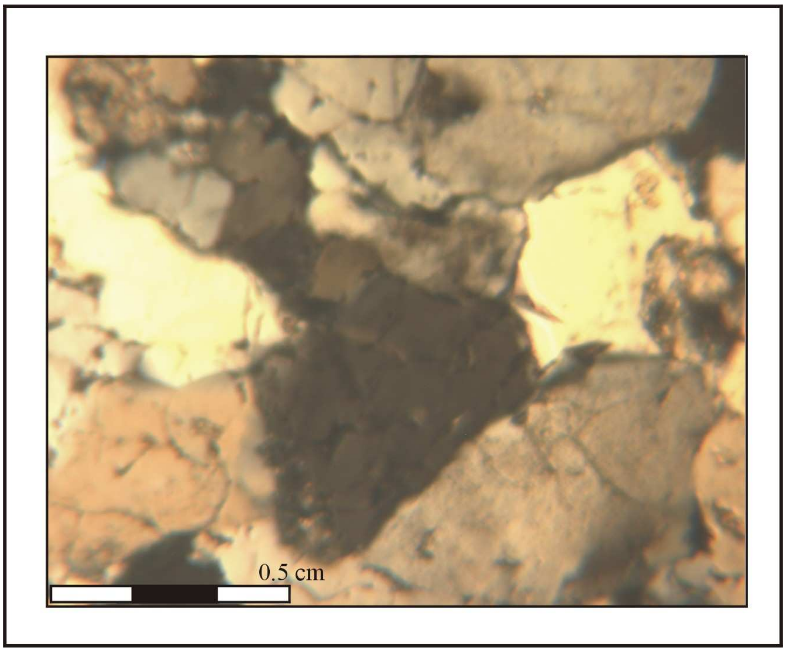

Figure 10.2: Petrographic image from sample H6, showing well sorted, anhedral quartz grains.

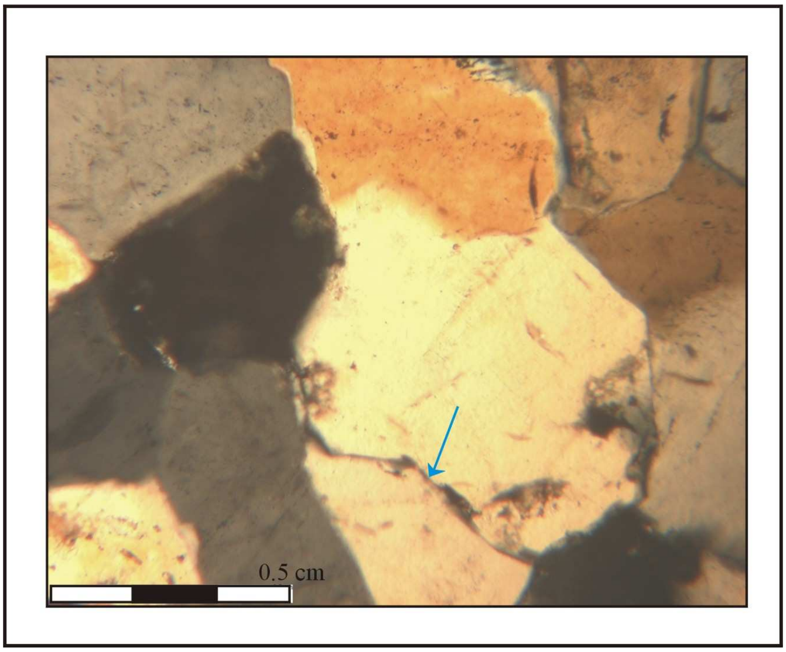

Figure 10.3: Petrographic image from sample JI-04, showing tightly packed quartz with concave-convex contacts.

10.1.2 FELDSPAR

Feldspar includes microcline, orthoclase and plagioclase. The first two combined range from 8.3% to 1.5% with an average of 4.2%; present as subhedral crystals and subrounded grains. Plagioclase is present in minor proportion ranging from 4.7% to 0.7% with an average of 2.5%. A small amount of cement overgrowth was found surrounding detrital feldspar. The presence of patchy (chessboard) extinction indicates albitization (Figure 10.4). The later is coupled with patches of vacuolization on the grain surfaces. Alteration marked by sericitization and small amount of dissolution that generate secondary porosity, was also recognized in the feldspars (Figure 10.5). For those samples where carbonate cement was found (see below), calcite replacement of plagioclase was observed (Figure 10.6)

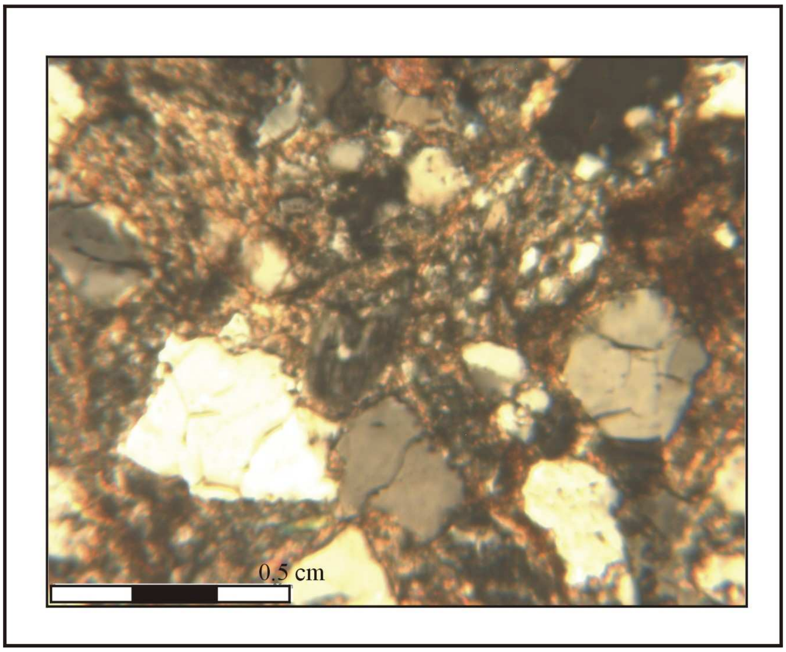

Figure 10.4: Quartz grains immersed in matrix and pseudomatrix in sample H9.

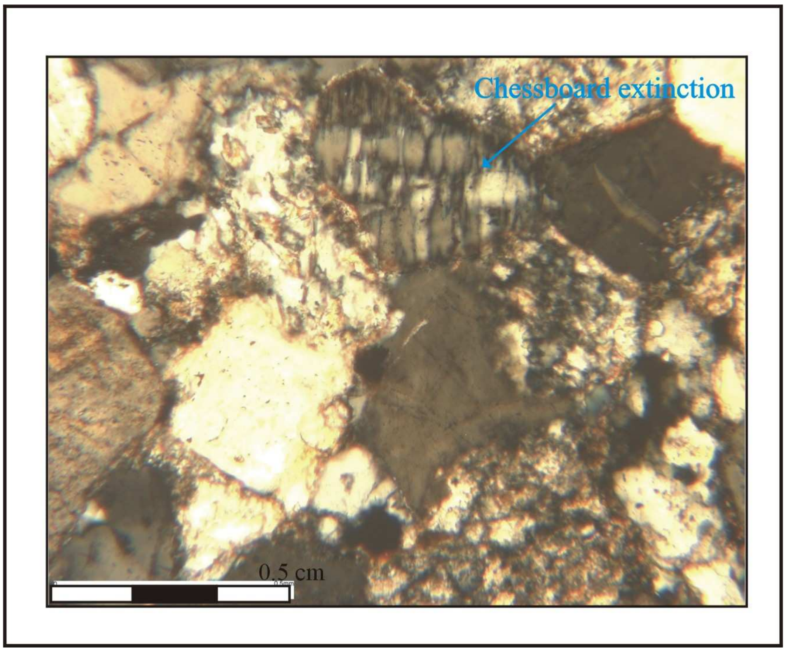

Figure 10.5: Chessboard extinction in sample H1, showing albitization of feldspar.

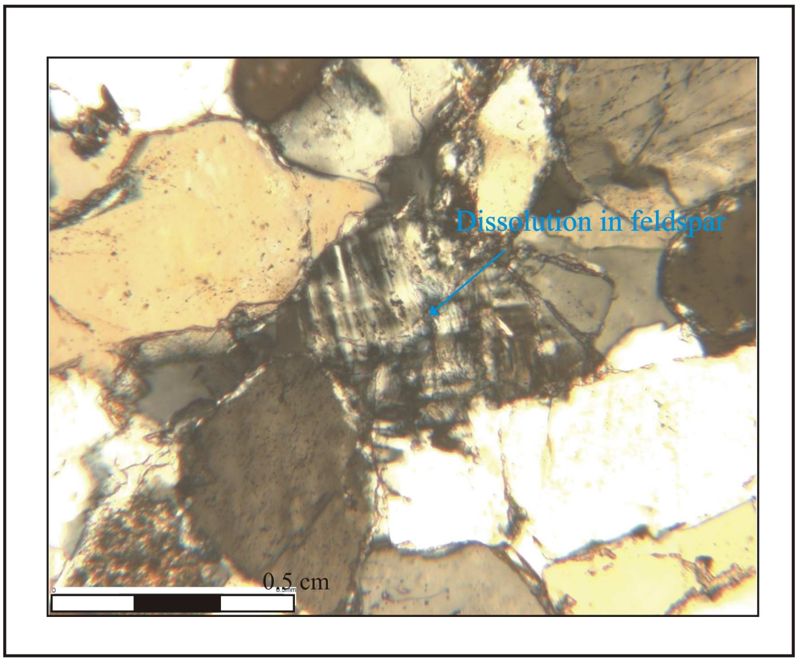

Figure 10.6: Small amount of dissolution of feldspar in sample H6.

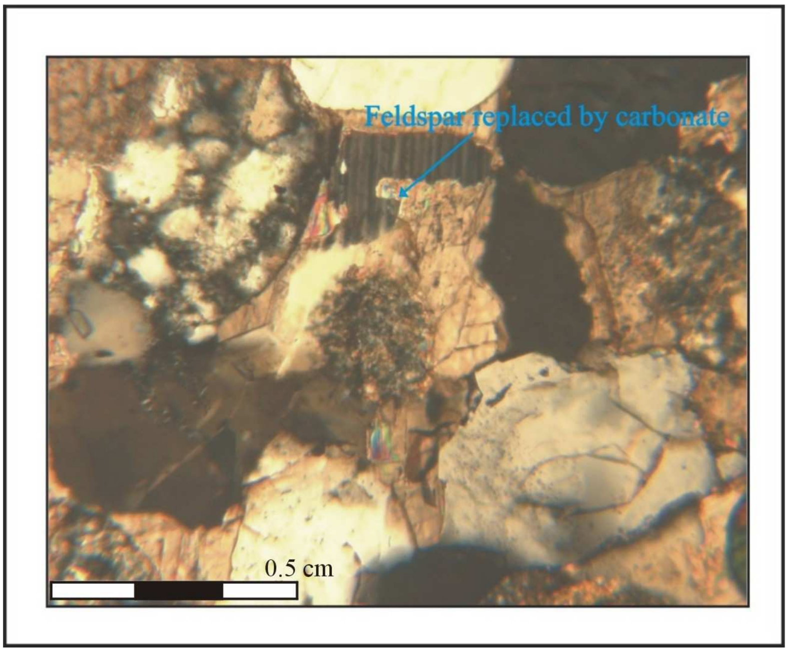

Figure 10.7: Feldspar replaced by carbonate in sample H11.

10.1.3 LITHIC FRAGMENTS

Lithic fragments constitute a major portion of the principal components of samples, ranging from 27% to 6.6%, with an average 13%. Metamorphic lithics are the most common features, ranging from 16% to 2%. They are characterized by abundant micaceous minerals (Figure 10.8). These fragments have an enormous impact on deformation and strain resolution of sandstones because they are highly ductile accommodating strain without producing any fractures (Figure 10.9). Plutonic lithics in the studied samples are mostly composite coarse grains of quartz and feldspar, but they are not present in all of the thin sections. Sedimentary lithics are mainly claystone clasts and in minor proportion by siltstones or clay siltstone and chert as trace components. The average content of sedimentary fragments is 3.2%. Volcanic felsitic lithics (VRF) formed by feldspar and quartz constitute the minor portion of the lithic fragment population.

Small to large amounts of pseudomatrix was recognized for some of the samples. These are associated with ductile behavior of mica rich metamorphic fragments and clay and silt rich clasts, that were squeezed between rigid quartz and feldspar grains during compaction (see Figure 10.9). Pseudomatrix was included within the lithic portion of the rock to perform sandstone classification.

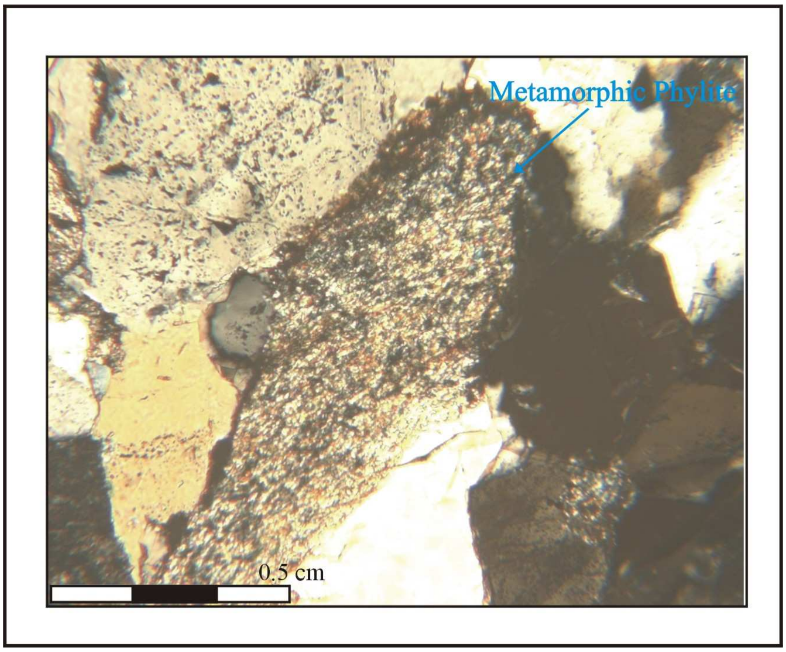

Figure 10.8: Metamorphic phyllite fragment in sample H13.

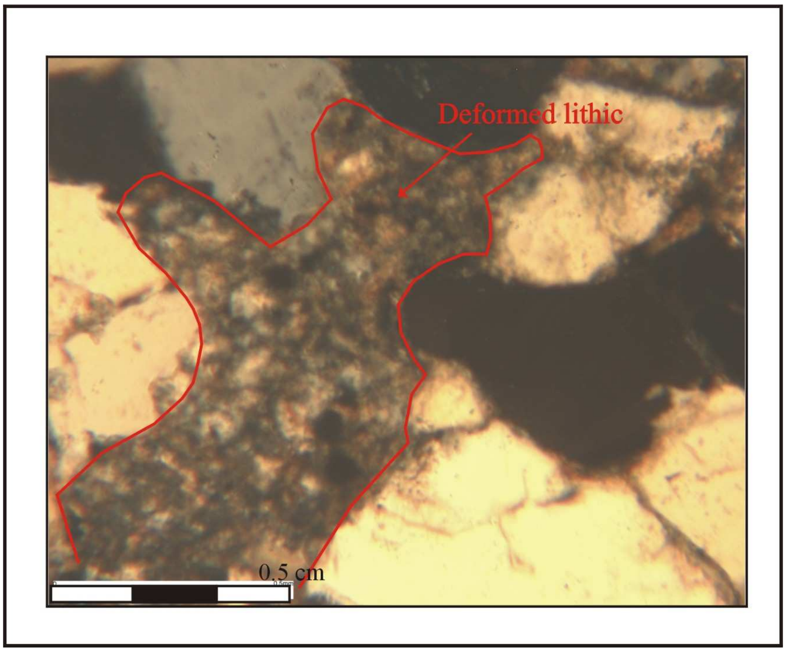

Figure 10.9: Pseudomatrix given by a lithic fragment squeezed between more rigid quartz grains in sample H13.

10.2 Rock Mass Cement

10.2.1 QUARTZ CEMENT

The vast majority of cement in the samples I analyzed is authigenic quartz overgrowth around detrital grains. Differentiating between quartz grains and cement in optical continuity with the grain is challenging. Quartz cement ranged from 21% to 10% with an average value of 15%. Quartz cementation has a major control in many of the properties that define the reservoir quality because not only plays a major role in porosity and permeability reduction (Bjørlykke and Egeberg, 1993), but also affects the mechanical properties of the rock (Rijken, 2005).

10.2.2 CARBONATE CEMENT

In addition to quartz cement, some of the studied rocks have patches of carbonate cement, primarily calcite (Figure 10.10). These carbonate cement patches were deposited before quartz cementation, since the later was observed overlapping them (Figure 10.11). In the samples where carbonate cement was recognized the values ranged from 3.3% to 0.5% with an average of 1.9%. In some samples, carbonate cement was dissolved leaving pyrite traces behind.

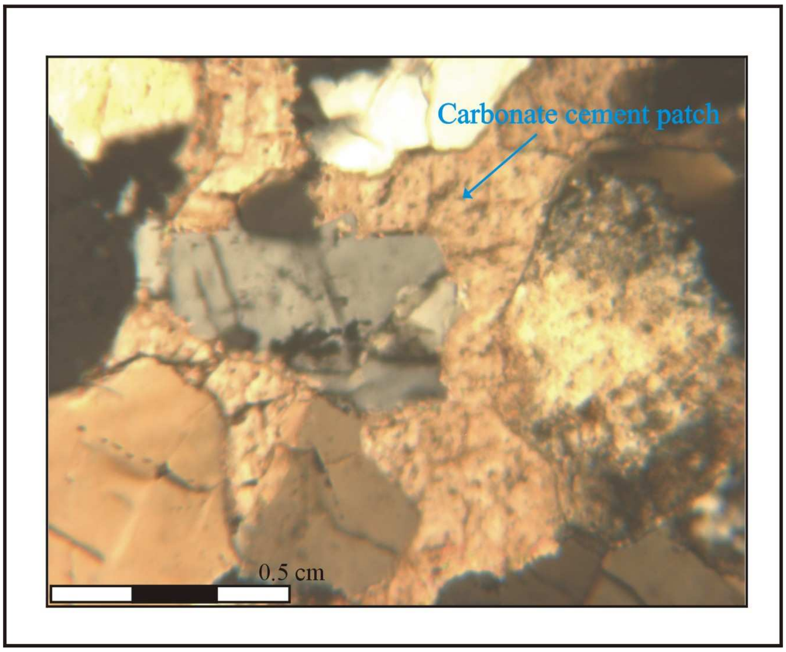

Figure 10.10: Carbonate cement patch in sample H12.

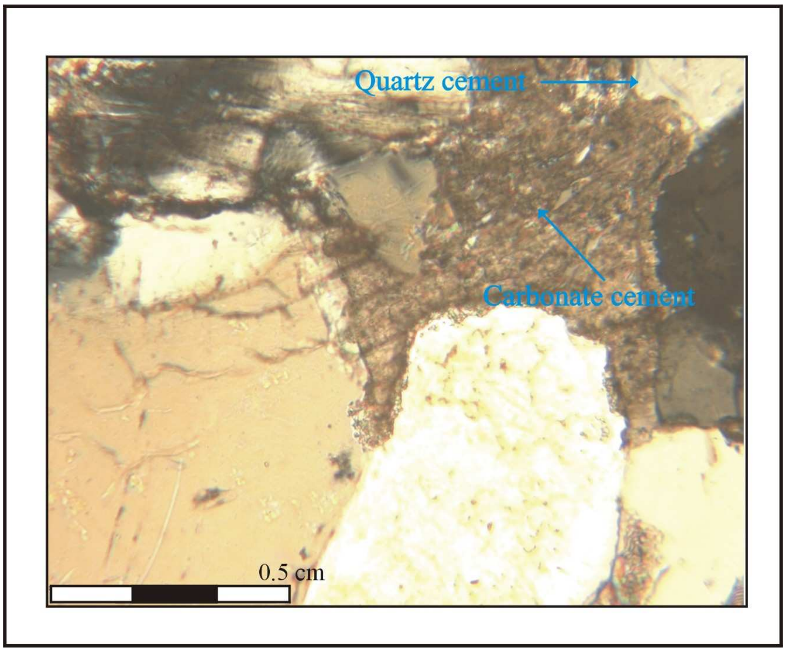

Figure 10.11: Carbonate cement and quartz cement on top of it in sample H13.

10.3 Rock Porosity

Porosity in these samples is extremely low. Primary porosity ranges from 0 to 2.1%. These values are in agreement with data presented by Kozlowski et al. (2005), Cohen (2002) and Moretti et al. (2002). Secondary porosity associated to dissolution reaches 6% in one of the samples (see Appendix C), but is extremely low for the rest, with values ranging from 0 to 1.3%. Finally, porosity associated with fractures ranges from 0 to 0.67%. This is in agreement to the values defined from logs by Cohen and Ollier (2002). One of the samples however, has a fracture porosity of 2.3% .

CHAPTER 11: ROCK MECHANICS

Fracture mechanics is the study of the propagation of cracks in a body. It is used to characterize and analyze the number, length and aperture of fractures. A variety of combinations of load and flaw geometry, as well as materials parameters govern the fracture process (Schmidt and Rossmanith, 1983). Linear elastic fracture mechanics is directly related with the Griffith crack theory (explained in Chapter 3), and has been used in numerous studies to assess fracture initiation and propagation (Segall, 1984; Atkinson, 1987; Olson, 1993). I evaluated some of the mechanical properties that govern fracture mechanics for the subsurface sandstones of the Subandean Ranges. I measured Young's modulus and subcritical crack index values, in order to assess variation of properties for the subsurface samples, and to establish possible correlation between these properties and fracture arrangement.

11.1 Young's Modulus

Young's modulus is one of the two elastic properties needed to define the elastic behavior of an isotropic material; the other is Poisson's ratio (Twiss and Moores, 1992). In order to obtain Young's modulus (E) values I cut samples into slabs of 1.65 mm thick, 25.8 mm wide and 76.2 mm long (0.065 x 1.015 x 3 inches) (Figure 11.1). These were polished to obtain planar, clean surfaces and oven dried to eliminate any residual oil from sample preparation. A torsion beam apparatus was employed to define the value of the Young's modulus (E), where the sample was located on two rollers and a load W was applied at four points (Figure 11.2 a and b). The load was incremented at a constant velocity, and measurements of load and displacement against time were registered both for loading and unloading conditions (Figure 11.3). A template spreadsheet in Excel that employs equations for four point loading, defined in Jaeger and Cook (page 131, 2007) was used to define the Young's modulus values.

Fifteen measurements were done for five subsurface samples. In some of the samples either the amount of core available or the presence of macrofractures made it impossible to cut the slabs necessary for this test. The distribution of Young's modulus does not change substantially among different samples and different slabs of the same sample. Figure 11.4 is a histogram showing the distribution of values. The average value for all of the measurements is 12.28 GPa. No further analyses considering structural position of samples (see Chapter 9) was conducted, due to the small number of samples tested and the obvious absence of correlation between structural position and Young's modulus.

In order to assess a relation between Young's modulus and fracture distribution, I did bivariate analysis. First I defined an average Young's modulus value, calculated as the arithmetic mean, for each of the samples I tested. These values were then plotted against the fracture related strain associated with Set I (Figure 11.5), and Set II (Figure 11.6). I defined the dependent variable as the fracture related strain magnitude (y axis in the graph), and the independent one as the Young's modulus (x axis in chart). Finally, I applied a linear regression to correlate these two values. The square of the correlation coefficient R, was employed to define the accuracy of the regression. There is no clear relation between fracture related strain and Young's modulus for Set I since $R^2 = 0.3469$. For Set II on the other hand, $R^2 = 0.876$ suggesting some type of correlation between these variables. However, the values obtained for the regression lines vary due to the causative geological process and the variation of deviation from the regression line due to randomness. Therefore, the significance of the regression line depends on the ratio of these variances (Swan and Sandilans, 1995). In order to assess the validity of the regression line, I followed the methodology described by Swan and Sandilans (1995) and performed the F test to reject or accept a null (no correlation between the two variables) hypothesis. According to the F value obtained using the regression function in Excel® and comparing it to the 95% confidence, F value obtained from charts (Swan and Sandilans, 1995), I was able to accept or reject the null hypothesis. Table 11.1 and 11.2 show the R^2 and F values obtained when correlating Young's modulus and fracture related strain in Excel®. From charts the critic F value obtained for Set I is 10.13 and for Set II is 18.51. Both values are smaller than the F value calculated; hence the null hypothesis (e.g. no correlation) cannot be rejected and no correlation is defined between these two variables. I should mention that the number of measurements is small and this may explain why correlations are weak.

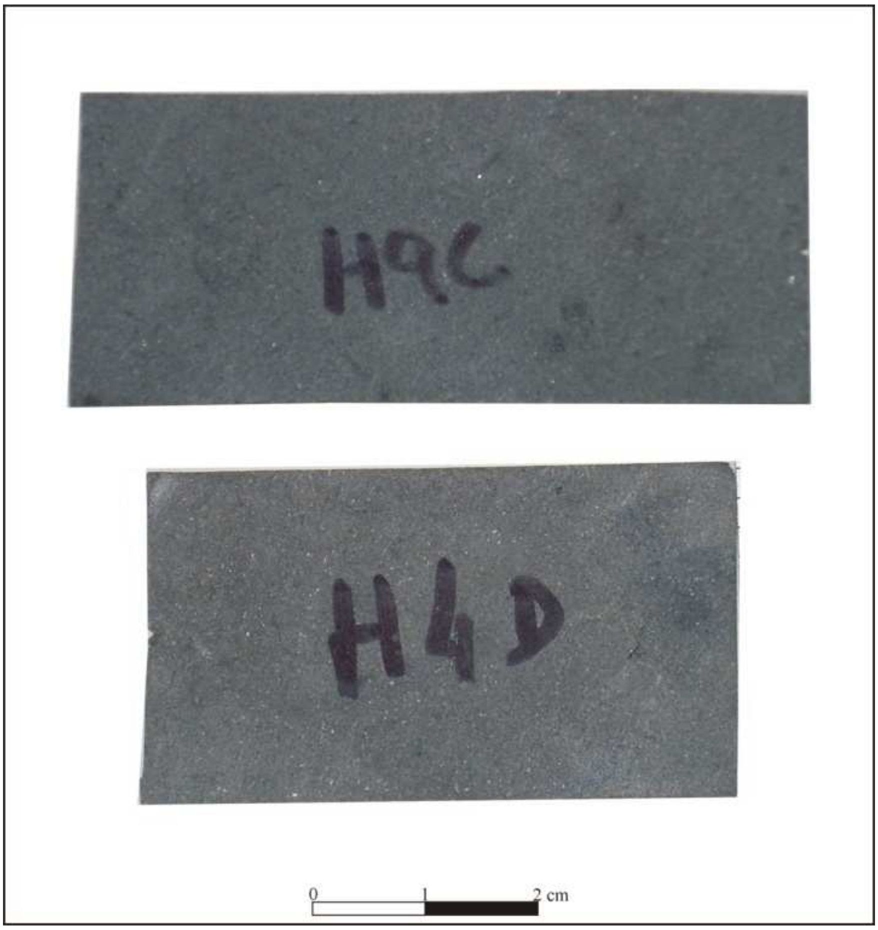

Figure 11.1: Slabs for samples H9 and H4 used for Young’s modulus tests.

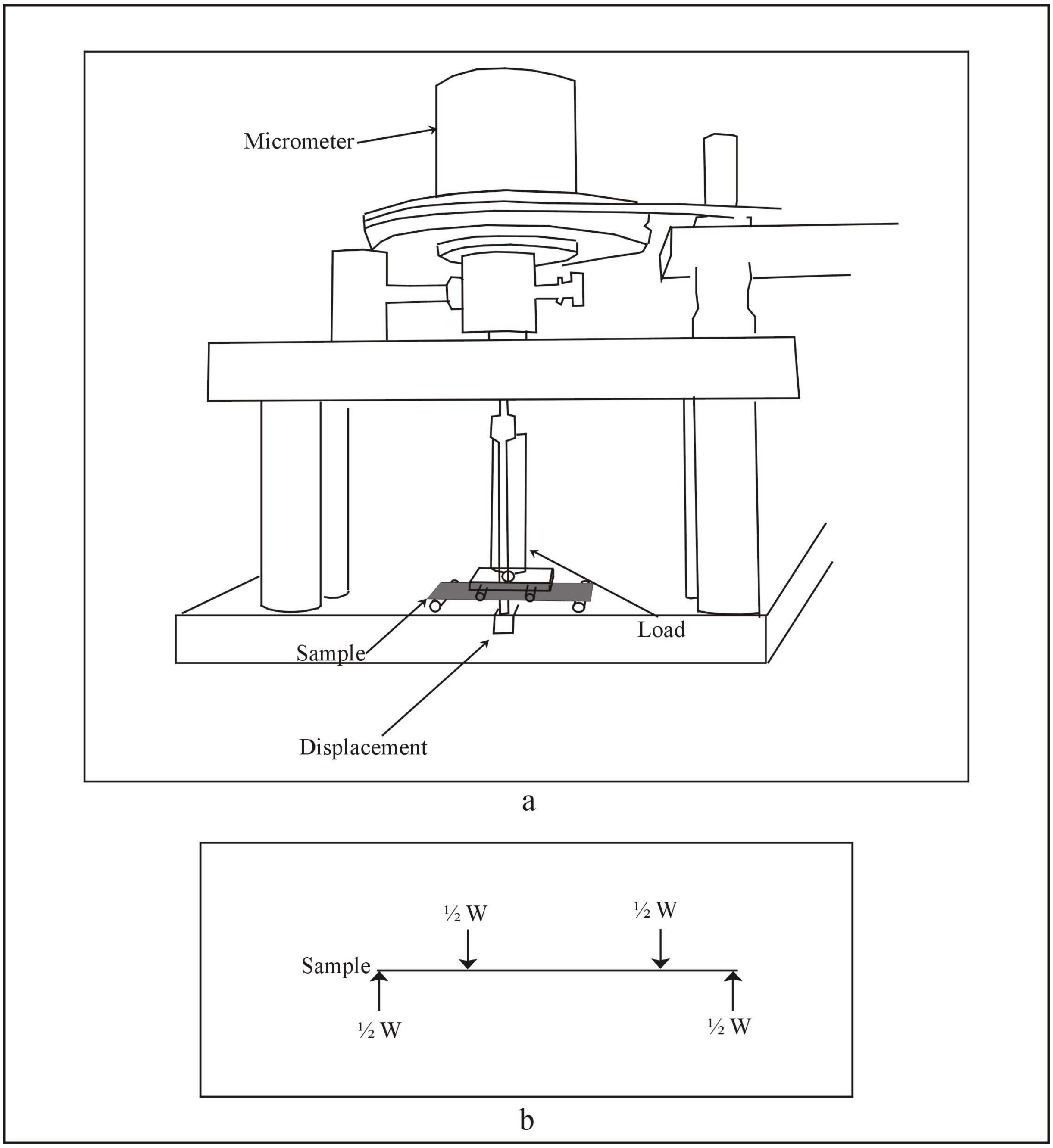

Figure 11.2: a. Scheme of the double torsion beam apparatus used to measure young’s modulus values. b. Four point loading of the sample (from Jaeger and Cook, 2007).

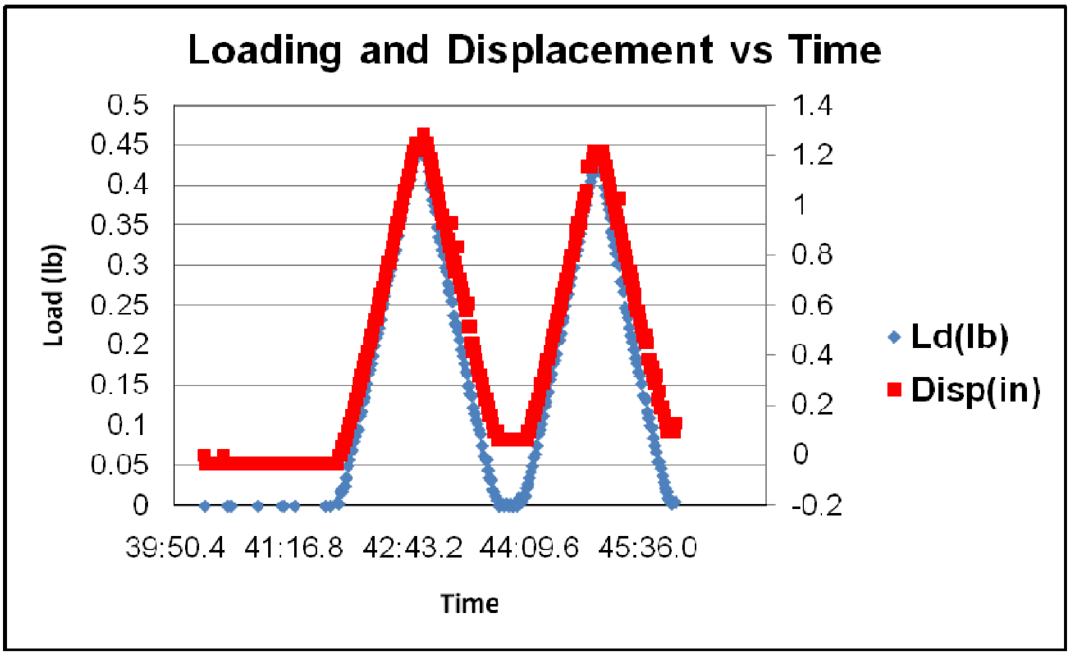

Figure 11.3: Loading and displacement measurement against time for sample H1.

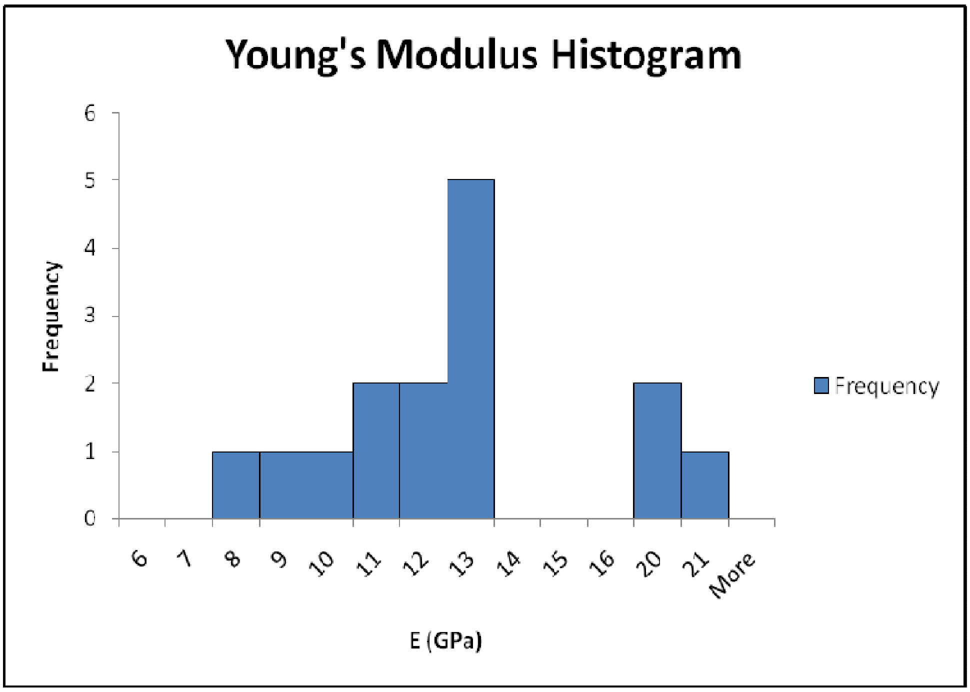

Figure 11.4: Histogram showing distribution of Young's modulus measurements.

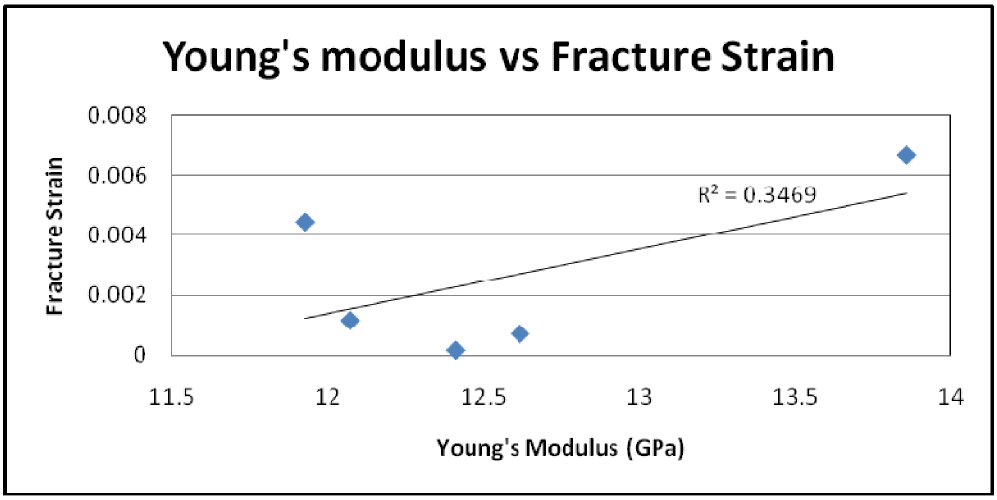

Figure 11.5: Scatter plot and lineal regression for fracture related strain of Set I and Young's modulus.

Regression Statistics	
Multiple R	0.588988
R Square	0.346906
Adjusted R Square	0.129209
Standard Error	0.00262
Observations	5

ANOVA

	df	*SS*	*MS*	*F*	*Significance F*
Regression	1	1.09E-05	1.09377E-05	1.593523	0.296031439
Residual	3	2.06E-05	6.86385E-06		
Total	4	3.15E-05			

Table 11.1: Output of regression analysis for fracture related strain of Set I and Young's modulus. F value does not allow rejection of the null hypothesis. Therefore, no relation can be defined between the two variables.

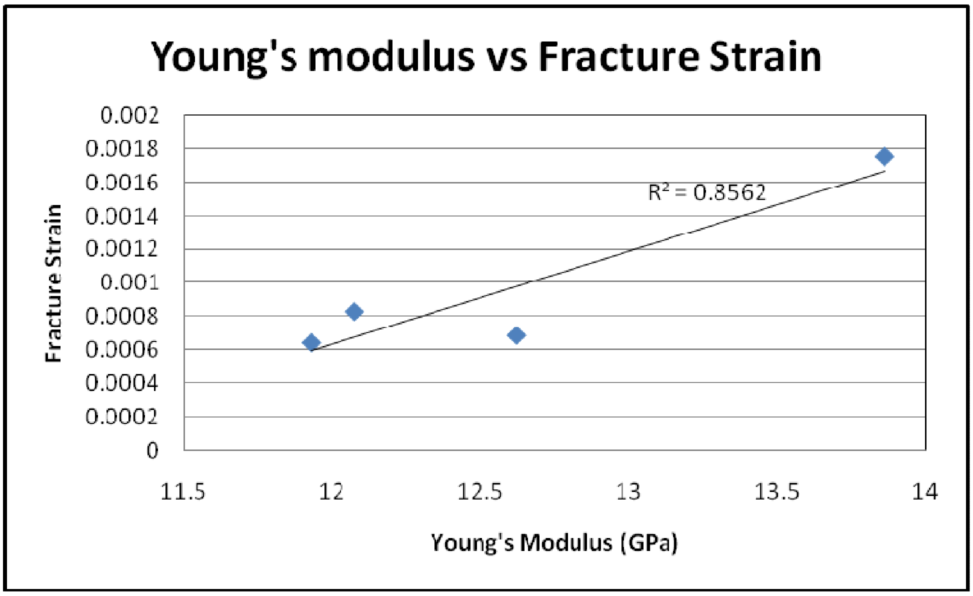

Figure 11.6: Scatter plot and lineal regression for fracture related strain of Set II and Young’s modulus.

Regression Statistics	
Multiple R	0.92528519
R Square	0.85615268
Adjusted R Square	0.78422902
Standard Error	0.00024301
Observations	4

ANOVA

	df	*SS*	*MS*	*F*	*Significance F*
Regression	1	7.02966E-07	7.02966E-07	11.9036306	0.074714812
Residual	2	1.1811E-07	5.90548E-08		
Total	3	8.21076E-07			

Table 11.2: Output of regression analysis for fracture related strain of Set II and Young’s modulus. F value does not allow rejection of the null hypothesis. Therefore, no relation can be defined between the two variables.

11.2 Subcritical Crack Index

Fractures can propagate either by critical or subcritical growth mechanisms. In critical growth mechanisms, fractures grow rapidly when the critical strength or critical fracture toughness (K_{Ic}) of the material is exceeded. Where K_{Ic} is given by equation 11.1 (Pollard and Aydin, 1988).

$$K_{ic} = \sigma_{ic} \sqrt{\pi a} \quad \text{(Eq. 11.1)}$$

With the half length of the fracture, a, and the net critical driving stress, σ_{ic}. Under critical conditions fracture propagation is unstable and occurs at velocities comparable to the elastic wave speed of the material (Irwin 1958, in Atkinson and Meredith 1987). Multiple studies (Pollard and Segall, 1987; Gross, 1993; Becker and Gross, 1996) state that in critical crack growth, fractures reach macroscopic dimensions without simultaneous propagation of neighbor fractures because a stress shadow forms, and impedes the development of further fractures. As a result, fractures show periodic spacing related to the size of the stress shadow, governed in part by the mechanical layer thickness of the bed (Cladouhos and Marrett, 1996; Marrett in preparation).

In subcritical crack growth propagation velocities are many orders of magnitude slower than in critical growth (Atkinson and Meredith, 1987). This type of mechanism can occur when rocks are affected by long term loading as typical in subsurface. Subcritical fractures propagate even when stress intensities are below critical values $K_I < K_{Ic}$ (Atkinson and Meredith, 1987). Subcritical crack growth favors fracture interaction, with small fracture linkage and coalescence to form larger fractures. This behavior can lead to chaotic and fractal geometries without a characteristic length scale (Marrett in preparation).

Propagation velocity in subcritical crack growth can be quantified by a power-law relation given by equation 11.2 (Pietka and Wiederhorn, 1978 in Rijken, 2005)

$$v = V^* \left(\frac{K_I}{K_0}\right)^n \quad \text{(Eq. 11.2)}$$

Where n is the subcritical crack index, V^* is a constant and K_0 is an arbitrary constant used to normalize K_I. The subcritical crack index depends on several properties such as grain size, grain mineralogy, cement type, porosity and environmental condition (Olson et al., 2001; Olson, 2004). Values for n can range from 20 for sandstones submerged in water to 250 for carbonate in dry conditions (Olson, 2004). Studies by Olson (1993) and Segall (1984) show that variation of subcritical crack index produces changes in spatial arrangement and the length distribution of fractures.

Prior to performing subcritical measurements I grooved the samples to obtain a pre-crack that will favor fracture propagation in a predefined position (Figure 11.7) and allow obtaining uniformity of conditions for the studied samples. Subcritical crack index measurements were done with a modification of the constant-displacement double torsion beam apparatus, used for Young's modulus measurements, and following the methodology described by Holder et al. (2001). The sample is located on top of four ball bearings, and load is incremented at a constant velocity in order to propagate a fracture at the bottom of the sample. Prior to crack growth measurements the specimen was incrementally preloaded with constant displacement steps (Zone A in Figure 11.8). The time at which load increment departed from a linear behavior (Zone B in Figure 11.8) was considered to be the beginning of the crack propagation; from here load decay was recorded during approximately 10 minutes (Zone C in Figure 11.8). These provided highly reproducible subcritical propagation velocity curves allowing calculation, through an Excel® spreadsheet template, of subcritical velocity exponent n from the slopes of the load-decay curves (Holder et al. 2001).

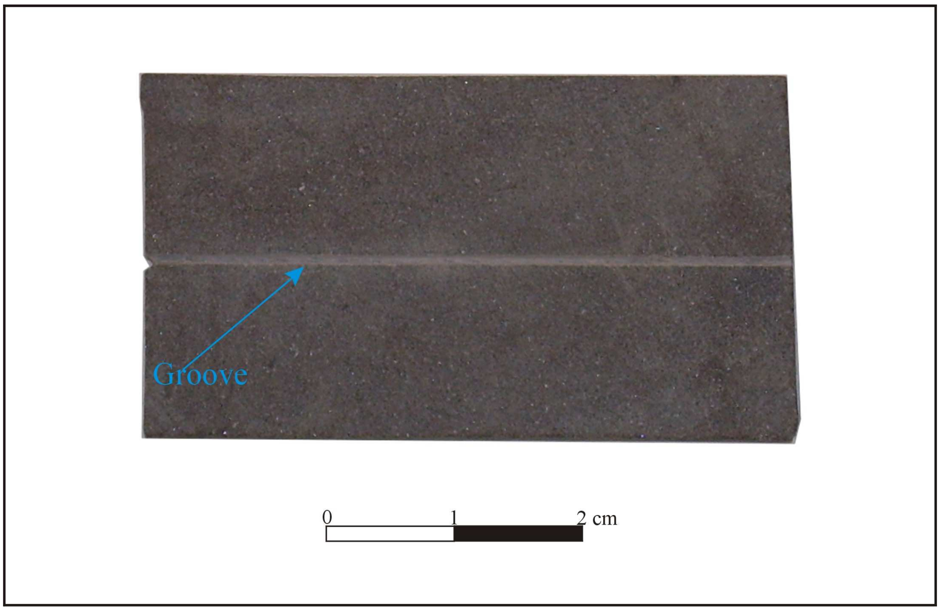

Figure 11.7: Slabs for samples H4 showing groove for subcritical crack index measurements.

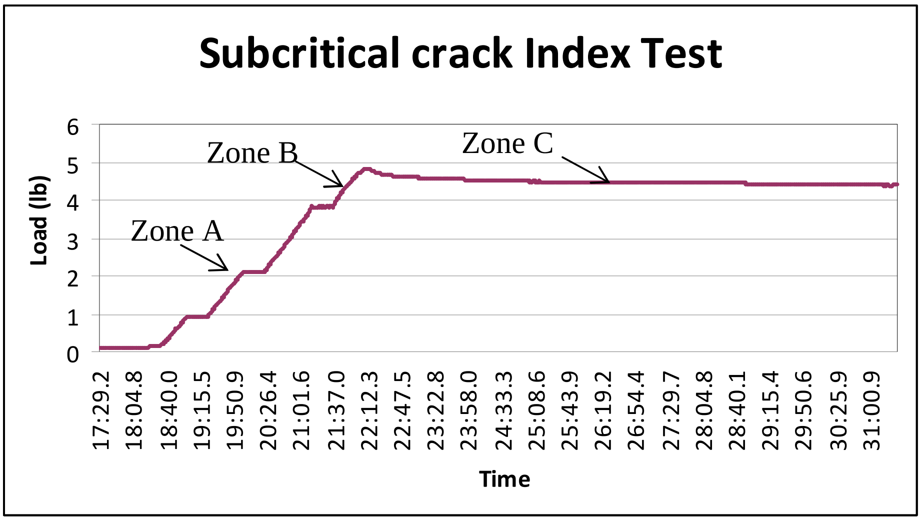

Figure 11.8: Load versus time measurement for sample H4. Zone A shows incremental preloads; zone B departure from linear behavior; zone c load decay.

Thirty-two measurements were done for twelve slabs of four samples. The number of samples is small because obtaining a sample suitable for analyses is even harder than for Young's modulus tests (the samples are fairly thin and break easily during handling). Figure 11.8 is a histogram of the values showing a normal distribution. The arithmetic mean value for subcritical crack index (n), considering all the measurements, is 47; this value is in agreement with the most common values of subcritical crack index for sandstones defined by Olson (Joints tutorial; Rijken, 2005). Once again, the small number of samples suitable for measurement and the absence of variation with respect to structural position precluded me from performing further analyses of the variation of this rock property with structural position.

Nevertheless, the influence of subcritical crack index in the fracture-related strain of the Devonian sandstones was assessed through bivariate analyses similar to the assessment presented for Young's modulus (see Table 11.1 and 11.2). Results are similar to those obtained for Young's modulus with an $R^2 = 0.3608$ for the correlation with Set I and $R^2 = 0.8196$ for Set II. In order to assess the validity of these results, I performed F tests (Table 11.3 and 11.4). From charts I obtained a critical F (with an $\alpha = 0.05$) of 18.61 for Set I and of 161.45 for Set II. Once again the null hypothesis (e.g. no correlation) cannot be rejected since the critic F values are larger than the calculated F values in both sets. This states that even when the R^2 value for the regression defined for Set II was close to 1, the regression is not valid. The lack of correlation between subcritical crack index and fracture related strain is somewhat expected since previous studies have defined the influence of subcritical crack index on fracture spacing arrangements (see references above) but not on fracture strain. As I mentioned in Chapter 9, I consider fracture related strain as independent of the number of fractures (e.g. more abundant narrow fractures or fewer wider fractures).

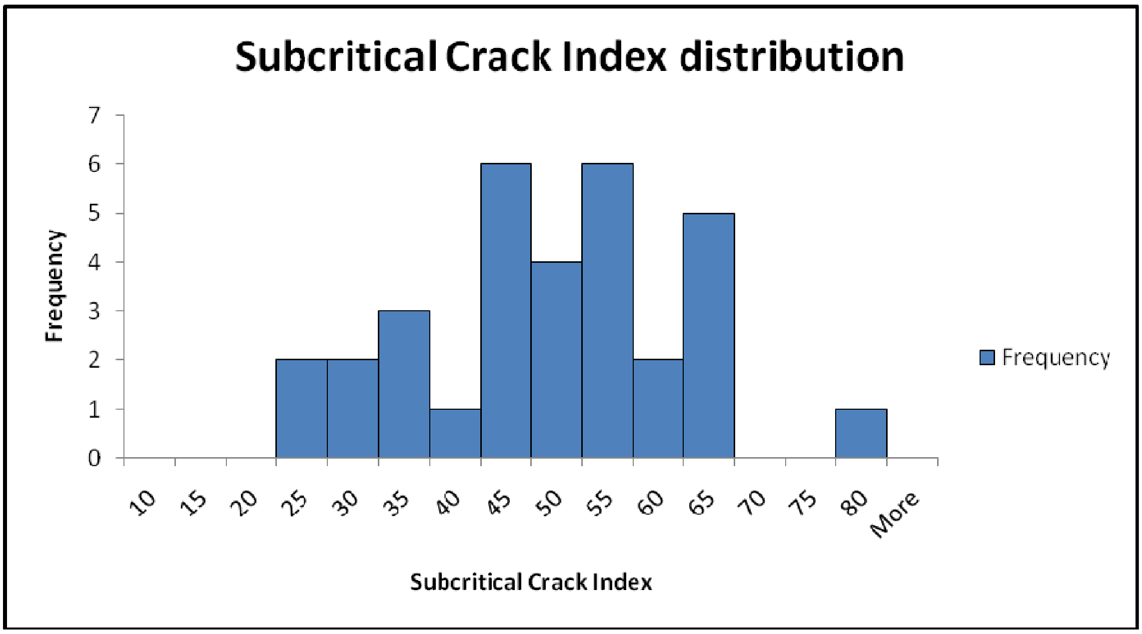

Figure 11.9: Histogram showing distribution of subcritical crack index measurements.

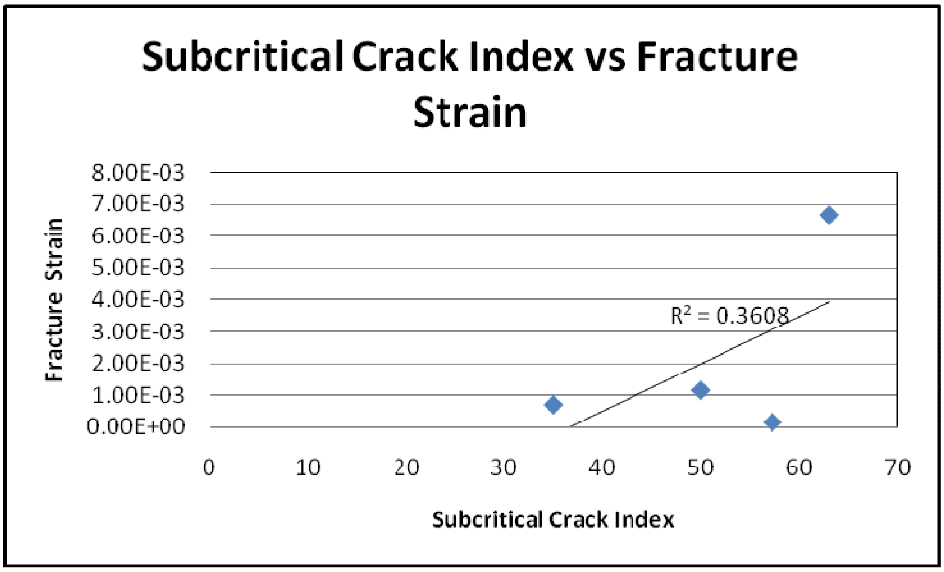

Figure 11.10: Scatter plot and lineal regression for fracture related strain of Set I and subcritical crack index.

Regression Statistics	
Multiple R	0.600627315
R Square	0.360753171
Adjusted R Square	0.041129757
Standard Error	0.002959305
Observations	4

ANOVA

	df	*SS*	*MS*	*F*	*Significance F*
Regression	1	9.884E-06	9.88E-06	1.128681927	0.399372685
Residual	2	1.751E-05	8.76E-06		
Total	3	2.74E-05			

Table 11.3: Output of regression analysis for fracture related strain of Set I and Subcritical Crack Index. F value does not allow rejection of the null hypothesis. Therefore, no relation can be defined between the two variables.

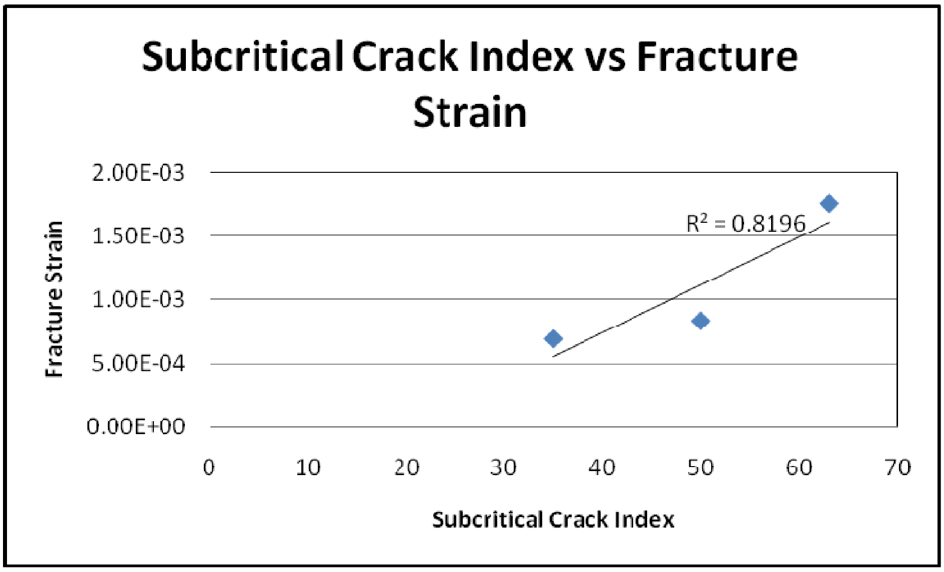

Figure 11.11: Scatter plot and lineal regression for fracture related strain of Set II and subcritical crack index.

Regression Statistics	
Multiple R	0.905320594
R Square	0.819605378
Adjusted R Square	0.639210757
Standard Error	0.00034795
Observations	3

ANOVA

	df	*SS*	*MS*	*F*	*Significance F*
Regression	1	5.5E-07	5.5E-07	4.543403	0.279261151
Residual	1	1.21E-07	1.21E-07		
Total	2	6.71E-07			

Table 11.4: Output of regression analysis for fracture related strain of Set II and Subcritical Crack Index. F value does not allow rejection of the null hypothesis. Therefore, no relation could be defined between the two variables.

CHAPTER 12: FRACTURE POROSITY AND PEREMEABILITY

Dual porosity reservoirs as the one of the Devonian sandstones in the Subandean Ranges are characterized by a complex porosity system that can be divided into the localized porosity associated to the fractures and the distributed porosity associated with the rock mass (or matrix). Permeability, the ability of a porous medium to transmit flow, also presents extremely contrasting values between matrix and fractures in this type of reservoir (Nelson, 2001). In the case of the Subandean Devonian reservoir, it is the presence of the fracture system what controls the productivity and defines the quality of the reservoir; because the permeability values for the matrix are extremely low (see Chapter 1). Conceptually dual porosity reservoirs are usually simplified, by considering a model in which matrix blocks contact each other through the fracture system, which is the only effective large scale permeability (Carlson, 2003). An example of this is the simple model developed by Warren and Root (1963), present in most reservoir engineering books, where the reservoir is conceptualized as a series of sugar cubes, separated by fractures of infinite length and evenly spaced (Figure 12.1). Researchers have developed the parallel plate model to describe fluid flow in a single fracture, in which the single fracture was conceptualized as a channel (Bear et al., 1993; Waite et al., 1999). However, as I presented in Chapters 7 and 8 fracture properties and arrangement can vary significantly between locations, and are far from presenting uniform distributions; specially when it comes to properties such as length or apertures, which have an enormous impact on aggregate properties such as porosity and permeability.

Philip et al. (2005) mentioned that due to the difficulties of defining fracture geometries for interwell regions, most reservoir models use data obtained from wells and outcrops and then employ statistical approaches to randomly populate and characterize a fractured field. In contrast, Philip et al. employ a mechanistic approach based on boundary conditions and rock properties to generate the fracture pattern. Philip et al. also superimpose the effects of diagenesis (cement deposits) on their numerically generated fracture patterns by systematically shrinking fracture apertures and closing narrow fracture segments. This has the effect of reducing the permeability of the system. With flow through both discontinuous fractures and matrix, they found that fracture length distribution and thus to some extent, degree of diagenetic overprint, had a major impact on the capacity of the fracture and matrix system to transmit fluid.

I used an approach that is a modification of the dual porosity, parallel plate, following the methodology described by Marrett (1996) and Gale (2002). This approach is essentially a parallel plate approximation, but one in which the apertures of the fractures has a range of sizes rather than a single value. A power law size distribution matches the size distributions found in some reservoir fractures (Marrett et al., 1999; Hooker et al, 2009). In this approach aggregate properties of fractures such as porosity and permeability are assessed in terms of individual fracture attributes (e.g. fracture aperture), and generalized with the scaling relations of those attributes. Marrett (1996) mentions that a number of factors should be considered when working with this methodology, such as the relation between the topology of the studied property and sampling topology (e.g. permeability is defined by a 3D tensor, while sampling in my thesis is given by one-dimensional scanlines); and the often ignored limits for fracture scaling properties (e.g. size distributions are valid for a certain range of scale). In addition, a number of limitations to this methodology apply particularly for my thesis and will be addressed later in this Chapter.

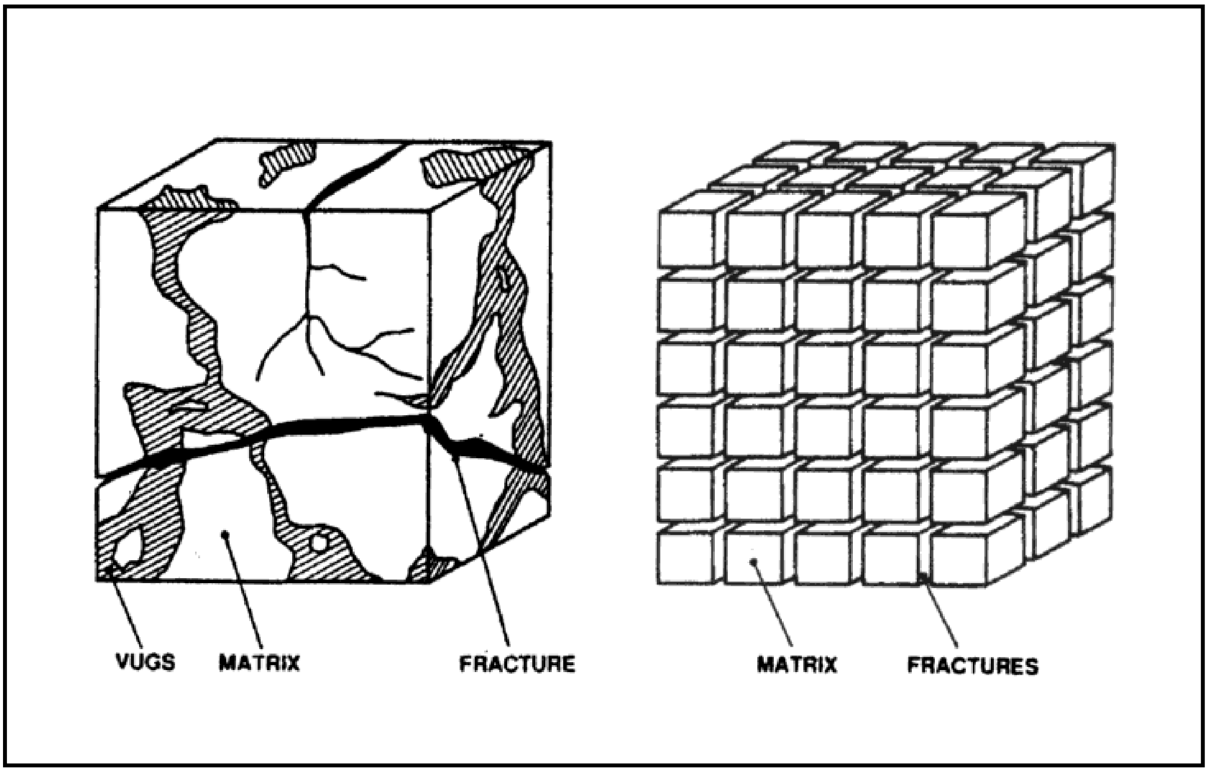

Figure 12.1: Scheme of actual reservoir and simplified reservoir model (from Carlson, 2003, based on Warren and Root).

12.1 Porosity

Fracture porosity of open extension fractures is in principle identical to extensional strains produced by veins (Marrett, 1996). Marrett (1996) defines the aggregate fracture porosity of a set in one dimensional sampling as

$$\phi_T = \sum \frac{b}{R_T} = \zeta\left(\frac{1}{C_T}\right)\frac{b_1}{R_T}$$

Where b is the extension fracture aperture (a in Chapter 9), R_T is the size of sampling domain (the length of the scanline), ξ is the Reimann z function, c_T is the exponent for the power law that relates the cumulative frequency and the fracture aperture, and b_1 is the aperture of the largest fracture sampled. This is how I defined fracture porosity. However, the application of this equation in my thesis presents a number of challenges. First of all, most of the samples I studied do not follow a clear power law aperture distribution (see Chapter 9) and are better described by exponential or log-normal arrangements. Moreover, some of the equations present a C_T exponent larger than one, which leads to a non-convergent infinite series of Reimann function. Therefore, porosity calculations with this methodology were done for just samples where a fair to good power law could be fit to the data and where the exponent of the equation was smaller than 1. This is restricted to Set I from samples H6, H13 and H8. Table 12.1 presents the power law equation, scanline length, the maximum aperture sampled, the porosity associated with this fracture and the total porosity result obtained for each of the samples. The results show that total fracture porosity is between 2.4 to 3.4 the porosity of the largest fracture.

Sample	Set	Power Law Equation	Maximum Aperture	Scanline Length (mm)	Reimann z Function	Φ_1(%)	Φ_T(%)
H6	I	$y=0.0048x^{-0.737}$ $R^2=0.9652$	0.180	81.47	3.40	0.22	0.75
H8	I	$y=0.0014x^{-0.66}$ $R^2=0.9418$	0.175	47.15	2.44	0.37	0.90
H13	I	$y=0.0054x^{-0.646}$ $R^2=0.9575$	0.129	34.8	2.55	0.37	0.95

Table 12.1: Porosity calculations based on aggregate properties of fractures. Here porosity is intra-fracture volume (IFV) and includes open fracture pore space and cement fracture volume.

In addition to the limitations related with distribution equations, the analysis performed above ignores the presence of cement filling the fractures, which reduces the amount of porosity. Note that *porosity* as used in this context is the space within the fractures not accounting for cements that may fill in all or part of the fracture. The quantity might better be termed intra-fracture volume. I interpreted the cement in the fractures of the Devonian sandstones, as synkinematic quartz. Philip et al. (2005) stated that presence of cement has an impact both on fracture propagation and in fluid flow. Therefore, it is important to clearly differentiate between intra-fracture volume (IFV) that includes open and cement fracture volume (this value is the one defined in Table 12.1) and porosity that would be the volume within fracture not occupied by cement as defined in Chapter 10.

Quartz cement is thought to fill fractures in a systematic way. Small fractures are filled first, while larger fractures are gradually filled as cement accumulates (Laubach, 2003; Laubach and Diaz-Tushman, 2009). In order to account for this an emergent threshold, defined as the aperture size above which fractures preserve some amount of porosity (Laubach, 2003) should be defined. I observed in SEM-CL images, that fracture porosity is only preserved in the largest fractures forming only 10% of the total kinematic aperture in this size range. Therefore, the results presented above should be carefully assessed because actual porosity will be smaller than the intra-fracture volume (IFV) obtained from aggregate analyses.

12.2 Permeability

A similar approach was used to define permeability values of the fractures I studied. Again the methodology presented by Marrett (1996) and Gale (2002) was followed to define the total permeability related to fractures. Marrett's (1996) calculation of permeability is expressed by the cubic law based on the parallel-plate model, where single-phase laminar flow is assumed. Fractures have infinite length and constant aperture. A range of aperture sizes is accounted for in Marrett's approach. Assuming the aperture sizes follow a power law, the equation that defines the permeability in terms of the largest fracture and the exponent of the scaling law is given by

$$K_T = \sum \frac{b^3}{12R_T} = \zeta\left(\frac{3}{C_T}\right)\frac{b_1{}^3}{12R_T}$$

The samples for which I defined permeability are the same as those for which I calculated porosity, since these most closely fit the assumption of a power law aperture distribution. Table 12.2 presents the set analyzed for each sample, the power law equation that defines the maximum aperture, the scanline length, the Reimann Z function, the permeability K_1 for the largest fracture and the total permeability K_t.

Sample	Set	Power Law Equation	Maximum Aperture	Scanline Length (mm)	Reimann z Function	K_1 (D)	K_T (D)
H6	I	$y=0.0048x^{-0.737}$ $R^2=0.9652$	0.180	81.47	1.08	6.087	6.557
H8	I	$y=0.0014x^{-0.66}$ $R^2=0.9418$	0.175	47.15	1.05	5.168	5.420
H13	I	$y=0.0054x^{-0.646}$ $R^2=0.9575$	0.129	34.8	1.05	9.630	10.136

Table 12.2: Permeability calculation based on aggregate properties of fractures.

It can be observed that permeability values obtained from this method are variable ranging from 6557 mD to 10136 mD. I found similar results as those of Marrett (1996) because the total permeability of the fracture population is almost completely defined by the permeability present in the largest fracture. Total permeability values are between 1.05 and 1.08 times the permeability of the largest fracture.

Once again in the reservoir a number of factors such as the presence of cement in the fractures will tend to reduce the permeability. Cement in the fractures reduces the free space for fluid flow. Also fractures are not of infinite length.

Philip et al. (2005) suggests that in a weakly connected fracture network it is the length of the fractures that seems to affect permeability the most. They argue that the presence of cement reduces the overall permeability, not by reducing the fracture aperture but rather by diminishing the length of the open volume of fractures and fracture network connectivity (another aspect of length, really). Fractures get narrower at the tips and the amount of void space for fluid flow diminishes or even disappears as cement accumulates.

With these considerations in mind, I conclude that the very high values of permeability calculated using the power-law size distribution and the parallel plate model are probably high. Marrett's power-law parallel plate model does underscore the importance of the largest fractures in overall fluid flow. My observations of fracture cement and fracture size distribution suggest that many of the smallest fractures (and much of the fracture porosity) is readily sealed by cement, but that larger fractures can retain porosity and conduct fluids. An analysis such as Philip et al.'s is probably more appropriate for obtaining realistic permeability values for these rocks. The rock property measurements I made for subcritical crack index, and the strain values I obtained from scaling analysis, are inputs needed for such refined analysis using the geomechanical model of Olson et al. (2009; see also Rijken, 2005).

CHAPTER 13: DISCUSSION

In the previous chapters I assessed several fracture properties, using a variety of methodologies over a wide spectrum of scale and compared the results to fold-related fracture models. As I mentioned in Chapter 1, the goal of my thesis is to better understand a fracture system, its origin and what geologic properties control it. Structural models and the fracture distributions that are predicted by classic fold-related-fracture models were discussed in Chapter 7. However, the homogeneity of deformation intensity (used by me as a surrogate of fracture abundance or intensity) that these models predict in the backlimb and hinge, fails to explain differences in production (presumably fracture related) for wells located in the folds. Moreover, these analyses are based on the paradigm that fractures are strictly controlled by folding during the Andean orogeny. In the Subandean Ranges, I compare production rate variations with reservoir quality changes related to variation of fracture properties estimated from the microfracture populations in the samples I studied. Therefore, even when the structural model predicts the same magnitude of deformation in different zones of the structural model, the same fracture intensity cannot be assumed.

Studying microfractures in subsurface samples provides statistical information on microfracture distribution and properties, which hopefully scale up to genetically related macrofractures distribution and properties. Nevertheless, microfracture analyses have the limitation of a specific location and predictions are necessary for interwell regions.

The third alternative I employed is to analyze fractures for an outcrop reservoir analog. In this case ubiquity of information allows comparing microfractures in samples collected in the field with changes of macrofracture distribution that can be related with macrostructural features. The caveat of this type of analyses is that geologic history is not the same for outcrop and subsurface rocks, so even when fracture origin may be related, fracture properties and distribution are not necessarily equal. Evidence of this is the difference in fracture related strain presented in Chapter 9.

Independently from the methodology employed to assess fracture distribution, there are multiple variables that will affect fracture arrangement and properties. However, in many cases only a few of these variables will have a tangible impact. In my study I consider structure, lithologic content and diagenetic effects as possible controlling factors on the fracture system in Devonian rocks. In order to assess these factors, I employ structural position (e.g. backlimb, hinge, and forelimb) as a proxy of structural control; quartz content as a proxy of lithological control; and quartz cement content as a proxy of diagenetic control. The effect of structural control is perhaps the easiest to understand, since as I showed in Chapter 7, deformation (represented either by curvature or strain) varies from one structural domain to another. Lithologic and diagenetic effects that control fracture attributes, can be understood by considering that quartz content and prekinematic quartz cement precipitation strengthen the rock framework (Storvoll et al., 2005; Makowitz et al., 2006) changing the rock mechanical properties. This will have an impact on fracture development since strain will be resolved differently according to the ability of the rock to accommodate strain in a more or less ductile way. In addition, precipitation of quartz during fracture opening, known as synkinematic cementation (Laubach, 1988 and 2003; Laubach et al., 2004), affects fracture properties by reducing fracture porosity and deposits within the fractures and the host rock may stiffen fractures (Laubach et al, 2004).

13.1 Multivariate Analyses

In Chapter 11, I evaluated the relation of fracture-related strain with Young's modulus and subcritical crack index, but no significant correlation was found. Usually a dependent variable, as is the fracture-related strain in my study, is affected by two or more regressors or independent variables. Multivariate analyses permits performance of simultaneous analyses of several variables (Donner and Barbossa, 2008). In my thesis this method allowed me to evaluate the effects of structural, lithological and diagenetic effects on fracture-related strain. Since each of these variables constitutes a dimension in the analyses, graphical representation of multivariate analyses is extremely hard to conceive. Therefore, it is easier to represent results in a numerical way.

To assess the relation between these properties I used multiple linear regression (Swan and Sandilans, 1995). The regression model takes the form

$$Y = \beta_0 + \beta_1 x_1 + \beta_2 x_2 + \beta_3 x_3 + \varepsilon$$

Where ε are random variables, with mean equal to zero and σ^2 variance; Y is the dependent variable; β_0 to β_3 are the partial regression coefficients; and x_1 to x_3 are the independent variables. In order to solve this equation I applied the regression function in Excel®. This function allows defining a square correlation coefficient (R^2) to assess the existence of a relation between the dependent and independent variables. In addition, an F test (Swan and Sandilans, 1995) such as the one I applied in Chapter 11 is performed. This allows testing a null hypothesis H_0 where $\beta = 0$ (i.e. no correlation), against H_1 where $\beta \neq 0$ (i.e. at least one of the coefficients is not zero). However, even when the null hypothesis is rejected this test does not tell us what is the correlation for each of the independent variables with the dependent one. In order to account for this, the t student test (Swan and Sandilans, 1995) is applied. This test allows defining the significance of the correlation coefficient for each of the variables considered (see Table 13.1 through 13.3)

Twenty one fracture-related strain values were assessed for fifteen samples both from subsurface and outcrop. My first step was to assess all of these values together independently from the origin of the sample (i.e. subsurface or outcrop) and the presence of different fracture sets (Set I and Set II). Table 13.1 is the regression result for this analysis. In order to perform the analysis the independent variables were represented as percentages for quartz and quartz cement content. Structural position was defined as a number being equal to 1 when the sample was located in the backlimb (low strain zone) and 2 when the sample was located in the hinge or forelimb (high strain zone). The F value obtained (2.5) is almost equal to the critic F value with a confident interval of 90% (F = 2.44). This allows rejecting the null hypothesis suggesting that some type of correlation between these variables is present. However, considering that the two values are so close raises uncertainties the validity of this assessment.

Regression Statistics	
Multiple R	0.553375045
R Square	0.30622394
Adjusted R Square	0.183792871
Standard Error	0.002316453
Observations	21

ANOVA

	df	*SS*	*MS*	*F*	*Significance F*
Regression	3	4.02639E-05	1E-05	2.50119	0.094177168
Residual	17	9.12212E-05	5E-06		
Total	20	0.000131485			

	Coefficients	*Standard Error*	*t Stat*	*P-value*	*Lower 95%*	*Upper 95%*	*Lower 95.0%*	*Upper 95.0%*
Intercept	-0.006986926	0.005421295	-1.289	0.21473	-0.018424859	0.004451	-0.0184249	0.004451007
Structural Position	0.000944128	0.001278199	0.739	0.4702	-0.001752637	0.0036409	-0.0017526	0.003640892
Quartz %	0.000176467	9.46042E-05	1.865	0.07949	-2.31307E-05	0.0003761	-2.313E-05	0.000376064
Quartz Cement %	-0.000115036	0.00017185	-0.669	0.51223	-0.000477607	0.0002475	-0.0004776	0.000247536

Table 13.1: Summary output for multiple regression analyses of all strain measurements. See text for explanation.

The independent variables coefficient suggests that quartz content is the most significant control in fracture-related strain. The t value of 1.86 gives more than 92% of confidence on this coefficient of determination. Structural position and quartz cement content do not have a statistical correlation.

A second step was to divide the strain magnitudes between those which correspond to fractures of Set I and those of fractures of Set II, based on the data presented in Chapter 9. By doing this I was forced to exclude five of the strain measurements, since they cannot clearly be assigned to one of the two sets. Table 13.2 represents the strain values for Set I and shows a square correlation coefficient of 0.7. The F value allows rejecting the null hypothesis with an $\alpha = 0.1$ (F = 3.62), suggesting that this correlation is valid. Once again quartz content is the most important factor influencing fracture-related strain. The t-test suggests that there is less than 4%

probability of spurious significance of this relation. Again structural position and quartz cement do not have a statistical correlation.

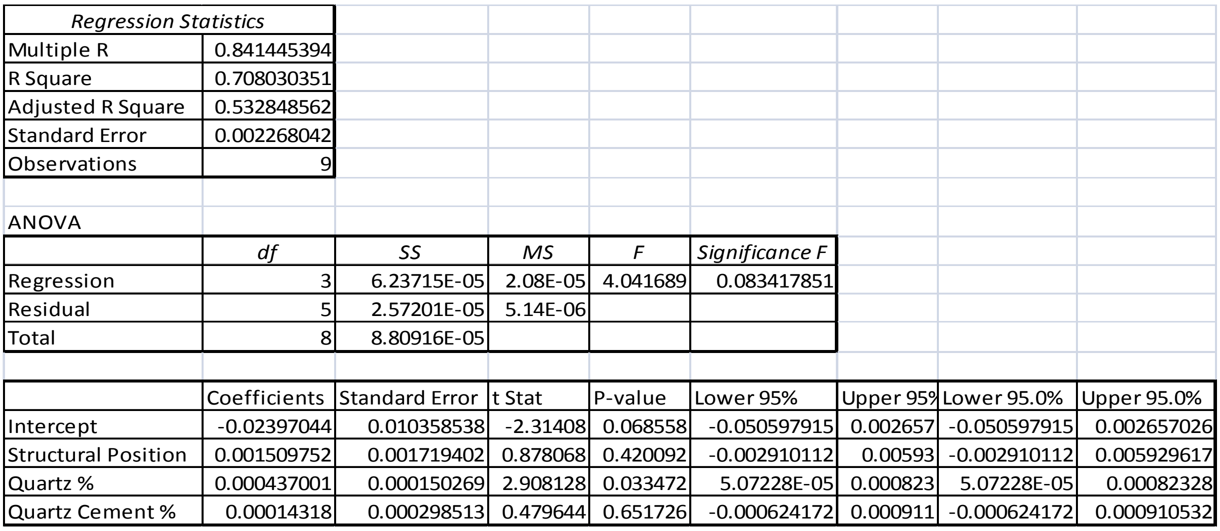

Regression Statistics	
Multiple R	0.841445394
R Square	0.708030351
Adjusted R Square	0.532848562
Standard Error	0.002268042
Observations	9

ANOVA

	df	*SS*	*MS*	*F*	*Significance F*
Regression	3	6.23715E-05	2.08E-05	4.041689	0.083417851
Residual	5	2.57201E-05	5.14E-06		
Total	8	8.80916E-05			

	Coefficients	Standard Error	t Stat	P-value	Lower 95%	Upper 95%	Lower 95.0%	Upper 95.0%
Intercept	-0.02397044	0.010358538	-2.31408	0.068558	-0.050597915	0.002657	-0.050597915	0.002657026
Structural Position	0.001509752	0.001719402	0.878068	0.420092	-0.002910112	0.00593	-0.002910112	0.005929617
Quartz %	0.000437001	0.000150269	2.908128	0.033472	5.07228E-05	0.000823	5.07228E-05	0.00082328
Quartz Cement %	0.00014318	0.000298513	0.479644	0.651726	-0.000624172	0.000911	-0.000624172	0.000910532

Table 13.2: Results of the analysis for strain values of Set I. See text for explanation.

Table 13.3 presents the multiple linear regression for Set II. The square correlation coefficient is 0.713. The F value obtained for this regression does not allow rejecting the null hypothesis, suggesting that there is no correlation. When we observe the values obtained in the t-test the strongest control on fracture-related strain is given by structural position, but there is a 12% probability of unreliable determination of this coefficient. The data presented in Chapter 9 shows that especially for subsurface samples, an increment in fracture-related strain is present as we move from the backlimb to the forelimb and hinge (see Table 9.3). For Set II oriented parallel to the structural axis trend it would be expectable to find a variation of strain as we assess different structural domains, since part of its development may be associated to curvature related strain (see

Chapter 8). Therefore, discarding this relation without further analyses seems inappropriate, and perhaps the fact that the F value is smaller than the critic F value could be related with the small number of samples being assessed.

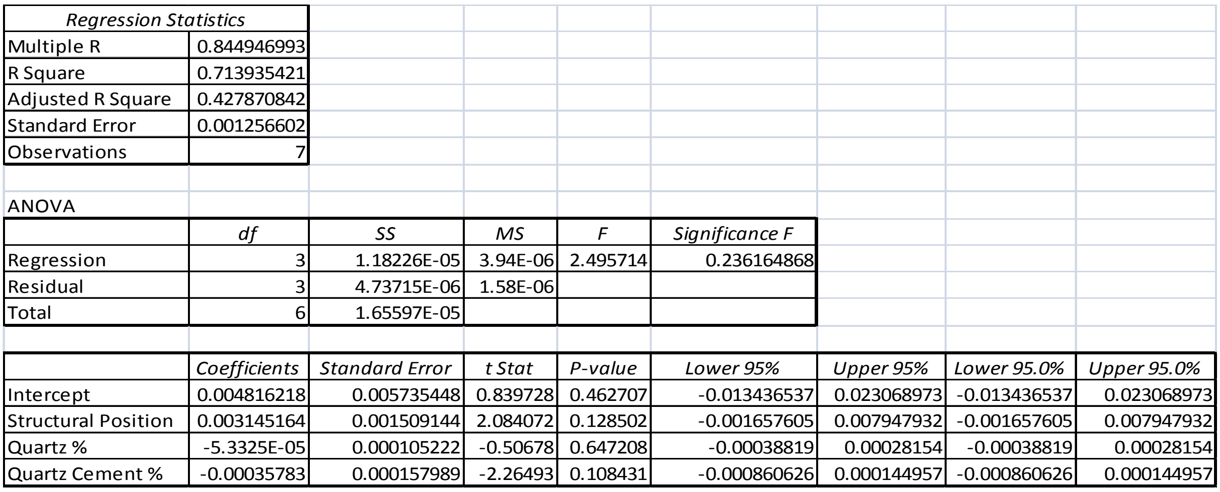

Regression Statistics	
Multiple R	0.844946993
R Square	0.713935421
Adjusted R Square	0.427870842
Standard Error	0.001256602
Observations	7

ANOVA

	df	*SS*	*MS*	*F*	*Significance F*
Regression	3	1.18226E-05	3.94E-06	2.495714	0.236164868
Residual	3	4.73715E-06	1.58E-06		
Total	6	1.65597E-05			

	Coefficients	*Standard Error*	*t Stat*	*P-value*	*Lower 95%*	*Upper 95%*	*Lower 95.0%*	*Upper 95.0%*
Intercept	0.004816218	0.005735448	0.839728	0.462707	-0.013436537	0.023068973	-0.013436537	0.023068973
Structural Position	0.003145164	0.001509144	2.084072	0.128502	-0.001657605	0.007947932	-0.001657605	0.007947932
Quartz %	-5.3325E-05	0.000105222	-0.50678	0.647208	-0.00038819	0.00028154	-0.00038819	0.00028154
Quartz Cement %	-0.00035783	0.000157989	-2.26493	0.108431	-0.000860626	0.000144957	-0.000860626	0.000144957

Table 13.3 Analysis for strain values of Set II. See text for explanation.

Some other variables that were not included in my analyses might have an impact on fracture distribution. Florez Niño et al. (2005) suggest that proximity to meter scale faults has a control of fracture intensity for the Abra del Condor anticline. However, assessing this feature in the subsurface is impossible since the faults, if present, are sub-seismic in resolution scale and thus proximity to small faults cannot be assessed. Another factor to consider is that these structures are formed by double plunging anticlines, so structural position in the N-S direction probably has an impact in strain changes.

13.2 Fracture Model

The origin to the fractures present in the Devonian sandstones of the Subandean Ranges is uncertain. The relative timing of fracture opening is commonly inferred from cross-cutting and abutting relations and orientation (Engelder, 1985; Hancock, 1985). Such observations are rarely sufficiently numerous to closely constrain deformation timing. Laubach and Ward (2006) argue that characterization of cement deposits and study of fluid inclusion within fractures can be used to retrieve information about the fracture history, when coupled with basin thermal curves. Unfortunately only one subsurface sample showed cementation features within microfractures feasible for study. Therefore, I based my interpretation on other information such as crosscutting relationships observed both in the field and with the microscope, fracture-related strain distribution and structural models.

Figure 13.1 is a schematic representation of the fracture distribution and history of the Devonian sandstones of the Subandean ranges. Set I is interpreted as the most common feature and was probably formed during an early stage of the Andean orogeny, developing parallel to the maximum compression direction and perpendicular to the structural trend. Engelder and Lash (2009) discuss the formation of such fractures. Probably at this same stage some small scale thrusts formed perpendicular to fractures of Set I.

Two different origins can be identified for Set II because the distribution and changes in cross cutting relations discussed in Chapter 8, allow more than one origin for this set. Bedding unfolding suggests that this set was formed during the early stages of deformation. Fractures that crosscut Set I could be related to both an internal rotation of stress distribution, when fractures of Set I reach a stage close to saturation (see Chapter 8); or to local strain associated to bending that would define a biaxial extension generating fractures. Strain analyses I presented in Chapter 7, suggest that this fractures should be located in a strip to the west of the hinge. However, if these fractures developed in early stages of folding, they should be found along the whole structure and not restricted to a particular position. From what I observed in the field, fractures of both sets appear to be present in both limbs of the anticline. Therefore, the structural model fails to address this issue.

A third stage is associated with the evolution and growth of the folds, this favors the development of fractures of Set II in hinge zones, either by developing new fractures or by reactivating older fractures. As a consequence of this, fracture-related strain for fractures of Set II seems to be controlled by structural position in the samples I studied (see Table 13.3). In accordance to this, curvature analyses presented in Chapter 7, suggests that maximum strain associated with local bending increases as we move to crestal regions.

A final stage in the fracture pattern evolution would be related to the reactivation of fractures of Set I as shear fractures, related to the strike slip faults described in Chapter 8. Florez Niño et al. (2005) argue that it is the increment in the amount of shear on these small fractures what leads to the development of metric scale faults such as the ones observed in the Abra del Condor region.

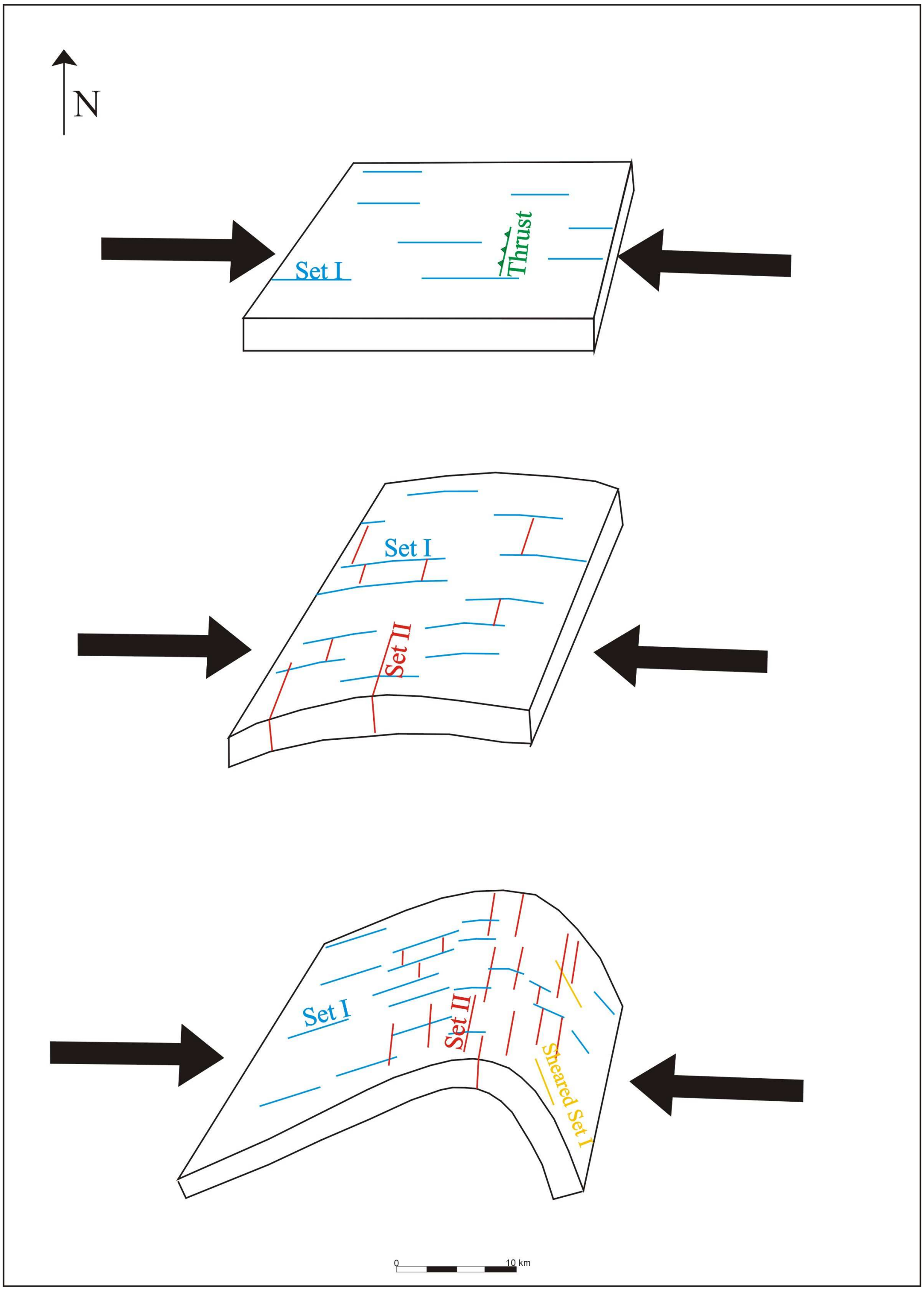

Figure 13.1: Fracture evolution model for a fold of the Subandean Ranges.

CHAPTER 14: C ONCLUSIONS

In this thesis I describe and explain fractures present in the Devonian sandstones of the Subandean Ranges, employing a variety of methodologies. From all the analyses performed I am able to conclude that

1. Microfractures can be used as a surrogate to analyze macrofractures. Evidence of this is the agreement of orientation between macrofractures observed in the field and microfractures observed in the lab from outcrop samples; and between macrofractures defined from microresistivity logs and microfractures observed with SEM-CL microscopy in core samples.
2. Two fractures sets, one perpendicular and one parallel to the structural trend of the Subandean ranges, are present. These have a variety of arrangements according to the studied location, going from mutual crosscutting, to Set II abutting against Set I.
3. The set perpendicular to the structural trend, defined by me as Set I is much more common, and the fracture-related strain associated with it is larger than that one of Set II. This strain magnitude is higher with increaing quartz content.
4. The set parallel to the structural trend, defined by me as Set II is less common and is controlled by structural position. Since fracture-related strain associated with it increases closer to the hinges.

5. Both sets are interpreted as formed during the early stages of folding. Increments of strain during flexure, favors reactivation and development of new fractures of Set II. An increment of shear in the final stages favors the reactivation of fractures of Set I as strike slip faults.
6. Both fracture sets record small amounts of strain (in terms of cumulative aperture for a given scanline length), comparable to those defined by Hooker et al. (2009) for subsurface fractures identified in horizontal core. Size distribution for the microfractures of these sets follow mostly log-normal distributions with uniform spacing, below an aperture size threshold of 0.015 mm. If larger sizes are considered the distributions show fair to poor power laws. In any case making prediction for larger fracture intensities from the equations is risky.
7. Structural models and strain and curvature analyses associated to them are useful tools to predict fracture distribution. However, the results obtained fail to address changes in fracture-related strain as we move along a particular structural domain. This is probably related to the fact that these models ignore rock mechanical properties and diagenetic effects.

APPENDIX A: STRATIGRAPHIC DESCRIPTION

This appendix includes a description of the stratigraphy present in the Subandean Region of Bolivia and Argentina. Figure A1 is a stratigraphic column showing the equivalent formations for the two countries.

Paleozoic

ORDOVICIAN

Zapla/Cancañiri Formation

The formation is formed by dark grey diamictites, with sandy matrix and contains disperse fragments of quartz, and metamorphic and granitic rocks. This formation is associated with a glacial event, and presents poor to massive stratification; locally it can present convolute lamination (Aceñolaza et al., 1999a). It discordantly overlies Mid-Ordovician sedimentary rocks, and its top is given by a hiatus or unconformity over which the deposits of the Lipeon Formation are found (Aceñolaza et al., 1999b). It reaches its maximum development in Bolivia with a thickness of 1,000 m (Suarez Soruco and Diaz Martinez, 1996).

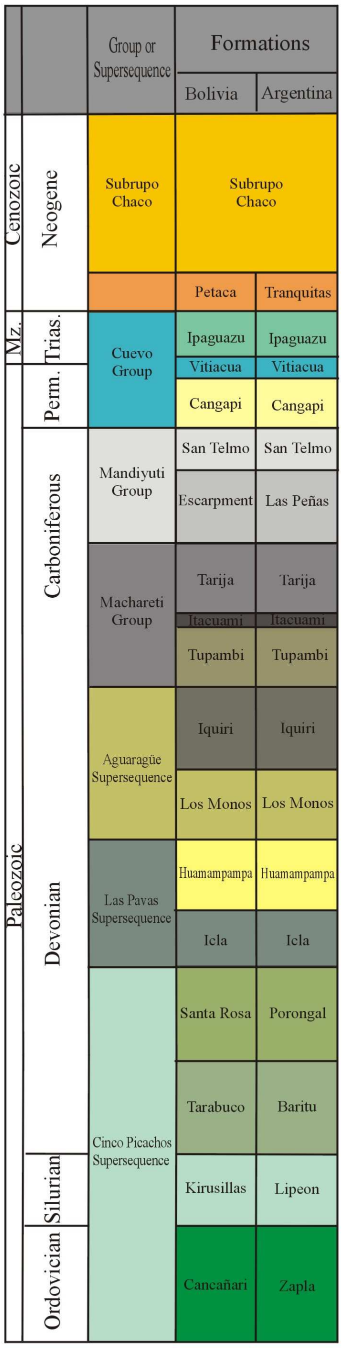

		Group or Supersequence	Formations	
			Bolivia	Argentina
Cenozoic	Neogene	Subrupo Chaco	Subrupo Chaco	
			Petaca	Tranquitas
Mz.	Trias.	Cuevo Group	Ipaguazu	Ipaguazu
			Vitiacua	Vitiacua
Paleozoic	Perm.		Cangapi	Cangapi
	Carboniferous	Mandiyuti Group	San Telmo	San Telmo
			Escarpment	Las Peñas
		Machareti Group	Tarija	Tarija
			Itacuami	Itacuami
			Tupambi	Tupambi
	Devonian	Aguaragüe Supersequence	Iquiri	Iquiri
			Los Monos	Los Monos
		Las Pavas Supersequence	Huamampampa	Huamampampa
			Icla	Icla
		Cinco Picachos Supersequence	Santa Rosa	Porongal
			Tarabuco	Baritu
	Silurian		Kirusillas	Lipeon
	Ordovician		Cancañari	Zapla

Figure A1: Stratigraphic column For the Subandean Region of Argentina and Bolivia

SILURIAN

Cinco Picachos Supersequence

This unit extends from the Silurian to the Early Devonian and comprises the Kirusillas/Lipeon, Tarabuco/Baritu and Santa Rosa/Porongal (Starck, 1995) formations. It is limited in its base by a big unconformity, which separates it from Ordovician rocks. Its top is represented by a maximum transgression surface that defines the beginning of the Las Pavas Supersequence.

Kirusillas/Lipeon Formation

This unit has a thickness close to 600 m and it is mostly formed by shale, dirty sandstones and highly bioturbated greywackes, which would correspond to a distal platform environment (Starck, 1999a). Close to its base, Vistalli (1999) described primary lens shaped structures associated with storm events. Distal tempestites have also been recognized for this formation.

In addition, this formation presents great interest for hydrocarbon prospection since it has been defined as a source rock, and is currently within the gas generation window (Cruz et al., 2001)

DEVONIAN

Tarabuco/Baritu Formation

This unit is formed by thin sandstones and shales, which corresponds to a proximal platform environment dominated by storm events (Starck, 1999a). Evidence of this, is the presence of hummocky structures defined at the base of the formation (Vistalli, 1999). In the uppermost portion of this unit, cross-stratification is recognized; allowing definition of a proximal platform environment. A continentalization of these deposits is interpreted as we move upwards in the sequence.

Santa Rosa/Porongal Formation

This formation is located on top of Kirusillas/Baritu Formation and the contact between the two is transitional. It is formed by quartzarenites, conglomeratic sandstones, and oligomictic conglomerates. The conglomeratic facies present evidence of uni- and bidirectional currents, as well as wave action. This allows defining a fan delta environment, where the sediments would be redistributed by the action of waves, tides and costal currents (Vistalli, 1999). The Santa Rosa Formation in Bolivia presents reservoir characteristics, and with adequate structures it can store hydrocarbons generated in the Kirusillas Formation (Suarez Soruco and Diaz Martinez, 1996).

Las Pavas Supersequence

This supersequence extends from Early to Mid Devonian and comprises the Icla and Huamampampa formations (Starck, 1995). It is limited in its base and top by flooding surfaces. It has a thickness close to 900 m, and presents grain and strata coarsening-upward sequences, controlled by the progradation of proximal facies over distal ones (Starck et al, 1992).

Icla Formation

This formation is concordantly deposited on top of Santa Rosa/Porongal Formation, and presents a thickness close to 500 m. It is mostly formed by black shales that locally present high content of organic matter (Suarez Soruco and Diaz Martinez, 1996). Within this shaly unit, less developed quartzose sandstone packages can be identified (Luquez et al., 2002). The basal portion of this unit would correspond to distal platform environment moving into a proximal platform as we move upwards (Vistalli, 1999).

Huamampampa Formation

The Huamampampa Formation is formed by intercalations of well developed quartzose sandstones and shale, and overlies concordantly the deposits of the Icla Formation (Luquez et al., 2002). It reaches a maximum thickness of 600 m. Its lower portion is represented by deposits that correspond to a distal platform environment; as we move upwards this grades into proximal platform deposits, and coastal sandstones with cross-stratification. The uppermost portion of the sequence corresponds to continental or mixed environments (Starck et al., 1992). The deposits of the Icla and Huamampampa formations are grouped in Argentina under the name of Areniscas Pescado (Aceñolaza et al., 1999a) or Pescado Formation (Vistalli, 1999).

Aguaragüe Supersequence

This supersequence extends from Middle to Late Devonian, and comprises the Los Monos and Iquiri formations (Starck, 1995). Its lower limit is defined by a flooding surface, and the deposits that form it are characteristic of a distal platform environment. As we move upwards in the sequence these deposits grade into proximal platform and coastal facies (Vistalli, 1999). Where it reaches its maximum development, this supersequence can present up to 1,000 m of thickness. However, this unit was affected by the Pre-Carboniferous unconformity; related with this, its deposits can be much thinner or even disappear, as it occurs in the Cordillera Oriental region (Starck et al., 1992).

Los Monos Formation

This unit concordantly overlays the deposits of the Huamampampa Formation, and presents a thickness close to 600 m (Luquez et al., 2002). It is formed by dark shales, which correspond to a distal platform environment. It presents minor sandstones intercalations, associated with sporadic storm events. These become, more common towards the top of the formation (Starck, 1999a). This formation has great importance in the development of the Subandean petroleum system, since the overpressured shales that form it, constitute an excellent hydrodynamic seal for the reservoirs of the Huamampampa Formation (Vaamonde, 2002).

Iquiri Formation

This unit is formed by sandstones that would correspond to facies of proximal platform and coastal environments (Vistalli, 1999). It overlays concordantly the deposits of the Los Monos Formation and its top is given by an unconformity that separates it from the Machareti Group.

CARBONIFEROUS

Machareti Group

As mentioned before this Group overlays discordantly the deposits of the Aguaragüe Supersequence. In Argentina three units are defined within this Group; these are Tupambi, Itacuami and Tarija formations (Starck et al., 1999b).

Tupambi Formation

This unit is mostly formed by white sandstones that present coarsening upwards arrangement. Its base is given by diamictites and shales. The sandstones of this Formation present ondulitic structures and cross-stratification. The unit is characterized by rapid facies and thickness changes, where the latter can go from 500 m to less than 10 m. Thickness variation is related with the fact that this unit is filling paleovalleys developed on the Devonian deposits, as a consequence of a eustatic change (Starck et al., 1993).

It is interpreted as part of a deltaic environment and the presence of subordinate diamictites will indicate glacial influence (Starck et al., 2002a).

Itacuami Formation

This unit is mostly formed by diamictites and dark shales, and presents thickness values close to 100 m (Azcuy and di Pasquo, 1999). It is concordantly deposited on top of the Tupambi Formation and presents in its base striae, which added to the presence of cadilites (given by isolated clasts with sizes between 5 and 10 cm); allow defining a strong glacial influence during the deposition of this Formation (Starck, 1999a).

Tarija Formation

This formation concordantly overlies the Itacuami Formation; it presents a thickness close to 600 m and is mostly formed by dark grey diamictites, with a limo-arcilitic matrix and clasts of variables sizes, which can reach up to 20 cm of size. These clasts are generally polished and present striae. Sandstone, shale and conglomerate layers are subordinate. The lack of internal structure of the diamictites, gives a massive character to this unit.

The presence of striae pavements allows definition of a glacial origin for these deposits, related to the climax of the gondwanic glaciations. The subordinate sandstones, could correspond to subglacial rivers or glacifluvial systems developed in a period of glacial retreatment (Starck, 1999a)

Mandiyuti Group

This group is separated from the deposits of the Machareti Group by an unconformity. This unconformity is related with a eustatic sealevel drop (Starck, 1995), which would have generated paleo-valleys on the Tarija Formation deposits.

Analogously to the Machareti Group, the basal fill of this Group is given by a fluvial system, which corresponds to the deposits of the Las Peñas Formation, confined to the paleo-valleys associated to the unconformity. On top of this, appear the glacial deposits of the San Telmo Formation (Starck et al., 1993).

Las Peñas/Escarpment Formation

This formation discordantly overlies the Tarija Formation deposits, and presents variable thicknesses, going from a few meters to 600 meters (Starck, 1999b). The dominant lithology is given by fine to medium grained quartzose sandstones. There are also subordinate lenses of conglomerates and grey and green shales (Azcuy and di Pasquo, 1999). This unit is interpreted by Starck (1999a) as part of a fluvial environment.

San Telmo Formation

These deposits overlie concordantly the deposits of the Las Peñas/Escarpment Formation (Reyes, 1972); the basal surface of this unit was interpreted by Starck (1999a) as a flooding surface. Its top is given by an erosive unconformity, which separates it from the Cuevo Group. To the south the pre-Cretaceous erosive unconformity, erodes the deposits of the Cuevo Group and tertiary deposits overlay the San Telmo Formation.

This unit presents highly variable thicknesses going from 50 m in Cordillera Oriental to 600 m in the Subandean Ranges. It is formed by an intercalation of diamictites, dark shale and coarse grained pink quartzose sandstones. This unit was deposited in a coastal environment with glacial influence, and grades as we move upwards to a periglacial lacustrine environment (Tapia, 1985).

PERMIAN

Cuevo Group

This group discordantly overlays the deposits of the Mandiyuti Group, and is formed by the Cangapi, Vitiacua and Ipaguazu formations. The latter is not present in Argentina since it was eroded by the pre-Cretaceous unconformity that limits the uppermost limit of the Cuevo Group (Starck, 1999b). In addition, the presence of this unconformity eroded the deposits of the Tacuru Group, present in Bolivia between the Cuevo Group and Tertiary deposits.

Cangapi Formation

This unit discordantly overlays the deposits of the San Telmo Formation, and presents a thickness close to 300 m. It is formed by tabular layers of green friable sandstone. These are either massive or present parallel stratification. Close to the top siliceous concretions that represent a transitional change into the Vitiacua Formation deposits (Starck, 1999b). Tomezzoli (1992) recognizes large scale cross-stratification for this unit and assigns an eolic environment for its deposition.

Vitiacua Formation

This deposit is formed by grey, blue and red limestones, and has large amounts of siliceous concretions. It has parallel stratification and is interpreted as shallowing-deepening sequences (Starck, 1999b). Tomezzoli (1996) defined a shallow marine platform environment for this unit, based on the presence of marine fossils.

Cenozoic

TERTIARY

Tranquitas/Petaca Formation

This unit is mostly formed by sandstones that correspond to a fluvial environment and present variable thicknesses, reaching a maximum of 700 m (Constantini et al. 2002a; Ramos 1999b). The basal deposits of this unit are represented by the Galarza Conglomerate, which presents a thickness close to 20 m in most parts of the basin. These deposits are interpreted as a residual lag associated to the advance of the deformation front, during the early development of Cordillera Oriental (Hernandez et al., 1999). The Serie Gris Neta Member concordantly overlays the Galarza Conglomerate, and is mostly formed by very friable, fine grained quartzose sandstones, which correspond to a fluvial environment with small fans (Constantini et al., 2002). The Serie de Transicion Member concordantly overlays the Serie Gris Neta Member, and is represented by an intercalation of red sandstones and shales. The top of this unit is defined by a flooding surface, which separates the Tranquitas/Petaca Formation from the Terciario Subandino deposits.

Subgrupo Chaco/Terciario Subandino

The Terciario Subandino is represented by 7,000 m of sediments, related with the Andean orogeny and the development of the foreland basin associated with it (Constantini et al., 2002). The Terciario Subandino Inferior of Argentina can be correlated with the Yecua Formation of Bolivia; presents 1,000 to 1,500 m of thickness and is mostly formed by fine grained red sandstones. This unit transitionally goes into the deposits of the Terciario Subandino Intermedio that can be correlated with the Tariquia Formation in Bolivia (Ramos, 1999b). The Terciario Subandino Intermedio is mostly formed by red shales and fine grained sandstones with sparse intercalation of grey tobaceous layers. The Terciario Subandino Superior is correlated with the Guandacay Formation of Bolivia and is formed by thick conglomerates, shale and red sandstones.

APPENDIX B: MICROFRACTURE DISTRIBUTION DATA

Distribution data of microfractures including aperture, position along scanline and non-weighted strike distribution, for the studied samples.

B1 Microfracture data for sample H1

Sample H1 sl1

Fracture cumulative N°	Aperture	Position Along Scanline	Didger Azimuth	Real Azimuth
1	0.022171	77.875	40.284	30.284
2	0.013033	47.739	24.262	14.262
3	0.005395	47.897	5.597	355.597
4	0.004532	47.801	175.773	165.773
5	0.004321	25.221	179.288	169.288
6	0.004041	77.433	150.981	140.981
7	0.004038	77.581	121.769	111.769
8	0.003695	34.363	146.751	136.751
9	0.003285	7.659	28.029	18.029
10	0.002824	31.712	48.088	38.088
11	0.002674	77.408	167.292	157.292
12	0.002646	5.935	48.534	38.534
13	0.002558	34.444	168.571	158.571
14	0.002522	33.925	155.379	145.379
15	0.00235	13.570	4.271	354.271
16	0.002013	21.919	65.345	55.345
17	0.001972	7.311	120.679	110.679
18	0.001926	33.896	172.820	162.820
19	0.00176	41.641	59.877	49.877
20	0.001647	29.809	15.461	5.461
21	0.001505	31.648	27.386	17.386
22	0.001489	4.904	116.387	106.387
23	0.001362	4.900	47.147	37.147
24	0.00131	17.438	49.162	39.162
25	0.000755	3.790	76.010	66.010

Sample H1 sl2

Fracture cumulative N°	Aperture	Position Along Scanline	Didger Azimuth	Real Azimuth
1	0.009643	4.777	1.419449217	81.419
2	0.00481	0.012737979	59.39880851	139.399
3	0.003267	30.64456779	20.70300856	100.703
4	0.002991	25.89064616	149.8545476	229.855
5	0.002737	32.3991007	26.65693309	106.657
6	0.002716	5.705721343	162.682172	242.682

7	0.002224	0.343463818	49.07031428	129.070
8	0.002115	25.93856475	139.6416259	219.642
9	0.001565	20.6296263	138.7371576	218.737
10	0.001384	17.49490241	113.1334438	193.133

B2 Microfracture data for sample H6

Sample H6

Fracture cumulative N°	Aperture	Position Along Scanline	Didger Azimuth	Real Azimuth
1	0.180416	36.602	180.000	304.000
2	0.10655	62.378	33.673	157.673
3	0.088293	39.740	12.148	136.148
4	0.044623	66.874	134.576	258.576
5	0.027033	53.012	29.185	153.185
6	0.020542	33.094	8.176	132.176
7	0.014474	26.354	137.529	261.529
8	0.011882	51.944	44.540	168.540
9	0.011522	47.493	162.323	286.323
10	0.011435	38.837	4.994	128.994
11	0.011379	53.375	160.137	284.137
12	0.009212	53.180	9.223	133.223
13	0.009009	24.003	178.848	302.848
14	0.008734	40.315	118.295	242.295
15	0.007603	24.529	3.436	127.436
16	0.007142	7.953	9.316	133.316
17	0.005883	13.077	151.579	275.579
18	0.005877	38.824	12.662	136.662
19	0.005578	42.392	120.148	244.148
20	0.005566	11.792	13.885	137.885
21	0.005417	52.001	46.544	170.544
22	0.005355	42.191	143.073	267.073
23	0.005083	12.605	158.645	282.645
24	0.004683	36.449	131.841	255.841
25	0.004614	38.560	152.520	276.520
26	0.004596	11.588	1.369	125.369
27	0.003851	14.081	174.215	298.215
28	0.003683	7.086	149.773	273.773
29	0.003325	48.193	5.029	129.029

30	0.003096	53.797	5.880	129.880
31	0.002962	43.677	59.813	183.813
32	0.002797	13.648	39.560	163.560
33	0.002749	30.718	171.906	295.906
34	0.002632	42.947	150.406	274.406
35	0.002469	2.300	157.549	281.549
36	0.002405	40.720	178.600	302.600
37	0.002356	14.134	13.815	137.815
38	0.002184	24.544	4.424	128.424
39	0.002171	12.369	176.407	300.407
40	0.001915	13.854	25.593	149.593
41	0.001691	20.980	12.555	136.555
42	0.001613	12.377	16.786	140.786
43	0.001437	38.704	178.807	302.807
44	0.000861	13.790	44.661	168.661
45	0.000806	49.478	66.896	190.896

B3 Microfracture data for sample H7

Sample H7 sl1

Fracture cumulative N°	Aperture	Position Along Scanline	Didger Azimuth	Real Azimuth
1	0.05262	40.8188204	165.4763338	95.476
2	0.038317	17.41722469	57.27509524	347.275
3	0.03219	4.109182094	159.8722981	89.872
4	0.013828	4.346013775	177.4824625	107.482
5	0.013666	1.086033091	8.511230554	298.511
6	0.012448	4.366566831	179.9999987	110.000
7	0.012379	3.356014854	1.247001815	291.247
8	0.01011	3.066515116	172.7964097	102.796
9	0.00791	17.04030354	57.06174193	347.062
10	0.007718	9.294322764	178.5504971	108.550
11	0.007233	39.5836836	8.374179615	298.374
12	0.006666	12.07477151	22.00866816	312.009
13	0.006467	34.68847391	168.4657497	98.466
14	0.006292	34.64692754	139.8017349	69.802
15	0.005122	35.84849891	1.298885143	291.299
16	0.004705	11.79676103	156.2106081	86.211
17	0.004305	5.232	147.3005524	77.301

18	0.003976	40.7084402	5.863626423	295.864
19	0.003859	8.604553057	178.985689	108.986
20	0.003723	14.34262655	45.22935423	335.229
21	0.003661	40.73210099	0.290765531	290.291
22	0.003547	0.019241822	12.64074101	302.641
23	0.003526	34.20058769	109.681199	39.681
24	0.003426	8.590875983	26.98586765	316.986
25	0.003359	3.196150572	22.14373154	312.144
26	0.003199	1.331941556	10.06330076	300.063
27	0.00315	5.65600798	31.3857321	321.386
28	0.002816	30.93941632	50.34338765	340.343
29	0.002772	40.20946598	18.39496075	308.395
30	0.00271	35.79407313	41.79639876	331.796
31	0.002702	15.32101866	22.27577541	312.276
32	0.002586	26.95215849	167.7796012	97.780
33	0.002458	5.689482497	31.96723904	321.967
34	0.002309	8.717261575	3.791980668	293.792
35	0.002306	6.270605885	4.759765603	294.760
36	0.0023	5.660914916	179.3725265	109.373
37	0.002277	15.16332358	168.8659596	98.866
38	0.002195	34.83409521	1.95218E-06	290.000
39	0.002157	14.19919341	168.5798531	98.580
40	0.002134	14.24526102	13.08566175	303.086
41	0.001999	18.79331664	24.12918735	314.129
42	0.001939	11.50354641	27.653931	317.654
43	0.001912	16.65639547	29.09689649	319.097
44	0.001826	18.54635356	33.27978572	323.280
45	0.001821	31.37291159	28.14649963	318.146
46	0.001705	5.154693733	38.17935346	328.179
47	0.001542	8.576810835	0.356759391	290.357
48	0.001457	34.12635354	5.910031066	295.910
49	0.001422	6.693205837	22.3236289	312.324
50	0.001413	18.73319022	51.9831937	341.983
51	0.001383	37.71190393	50.55596458	340.556
52	0.001309	18.77261698	26.08495865	316.085
53	0.001111	1.260684411	56.8539443	346.854

Sample H7 sl2

Fracture cumulative N°	Aperture	Position Along Scanline	Didger Azimuth	Real Azimuth
1	0.013329	3.695	5.000	205.000

2	0.011151	27.274	145.082	345.082
3	0.010462	7.747	5.011	205.011
4	0.007212	7.865	5.299	205.299
5	0.006944	29.373	60.366	260.366
6	0.006757	10.955	179.301	19.301
7	0.006649	11.045	8.527	208.527
8	0.006641	15.519	39.621	239.621
9	0.006503	20.311	133.812	333.812
10	0.006036	8.554	13.261	213.261
11	0.005830	7.422	177.239	17.239
12	0.005159	11.263	164.811	4.811
13	0.004894	32.486	126.152	326.152
14	0.004852	0.268	180.000	20.000
15	0.004381	16.186	175.332	15.332
16	0.004280	37.180	114.543	314.543
17	0.004243	0.867	149.010	349.010
18	0.004212	9.925	154.421	354.421
19	0.004203	7.371	173.145	13.145
20	0.004199	36.081	149.715	349.715
21	0.003887	15.484	37.004	237.004
22	0.003853	37.745	107.709	307.709
23	0.003842	13.200	150.696	350.696
24	0.003021	16.533	29.603	229.603
25	0.002989	14.068	53.782	253.782
26	0.002902	11.107	18.482	218.482
27	0.002732	3.102	111.006	311.006
28	0.002650	11.481	177.279	17.279
29	0.002568	31.691	62.086	262.086
30	0.002482	37.635	108.970	308.970
31	0.002332	29.116	139.352	339.352
32	0.002267	3.378	63.414	263.414
33	0.001937	38.194	102.646	302.646
34	0.001766	28.191	50.991	250.991
35	0.001766	25.212	37.689	237.689
36	0.001650	34.993	54.038	254.038
37	0.001250	9.029	68.390	268.390

B4 Microfracture data for sample H8

Sample H8 sl1

Fracture cumulative N°	Aperture	Position Along Scanline	Didger Azimuth	Real Azimuth
1	0.019530	50.032	121.561	121.561
2	0.006343	14.907	142.633	142.633
3	0.004820	9.813	35.899	35.899
4	0.003927	6.782	50.445	50.445
5	0.003817	46.580	24.419	24.419
6	0.002159	27.414	21.709	21.709

Sample H8 sl2

Fracture cumulative N°	Aperture	Position Along Scanline	Didger Azimuth	Real Azimuth
1	0.175194	10.371	9.834	279.834
2	0.010707	13.198	46.399	316.399
3	0.008451	15.091	4.536	274.536
4	0.008312	3.163	10.870	280.870
5	0.002114	30.762	28.513	298.513
6	0.001675	4.726	156.230	66.230
7	0.001466	1.495	35.425	305.425
8	0.001187	19.480	167.589	77.589

B5 Microfracture data for sample H13

Sample H13 sl1

Fracture cumulative N°	Aperture	Position Along Scanline	Didger Azimuth	Real Azimuth
1	0.128664	11.85019223	1.725963749	296.726
2	0.013191	24.12958787	9.782870614	304.783
3	0.010442	27.83124607	152.106757	87.107
4	0.008352	9.79538365	127.799034	62.799
5	0.007885	24.22080062	53.19132328	348.191
6	0.005945	0.006302836	151.7877778	86.788
7	0.005766	6.395243746	159.1735608	94.174
8	0.004295	8.440981313	34.54898576	329.549
9	0.003794	4.148404642	177.3658386	112.366
10	0.003675	25.08186843	8.703481057	303.703

11	0.003387	10.89983235	154.7451029	89.745
12	0.002984	3.309811524	165.6780778	100.678
13	0.002943	4.159994354	36.99036264	331.990
14	0.002852	24.01231008	137.933073	72.933
15	0.002804	28.67446411	16.3584172	311.358
16	0.002234	11.62468871	179.9125707	114.913
17	0.002208	5.247	144.5468616	79.547
18	0.002019	24.04158244	115.7269923	50.727
19	0.001972	27.85725599	152.8912367	87.891
20	0.001588	25.58326998	57.00687389	352.007
21	0.001487	11.53647609	175.7073999	110.707
22	0.001486	14.03891336	176.7703258	111.770
23	0.001485	14.00542045	175.8425357	110.843
24	0.001445	2.814071115	165.557337	100.557
25	0.001376	27.86186389	159.0226781	94.023
26	0.001361	10.40988715	23.07242372	318.072
27	0.001085	7.839064554	42.48560274	337.486
28	0.001041	16.9171959	8.159118368	303.159
29	0.000744	11.05225528	1.115005069	296.115
30	0.000732	10.88435516	168.7242171	103.724
31	0.000705	13.21975116	160.3784833	95.378
32	0.000504	29.31204867	132.6793946	67.679
33	0.000271	24.15790482	110.5970137	45.597

Sample H13 sl2

Fracture cumulative N°	Aperture	Position Along Scanline	Didger Azimuth	Real Azimuth
1	0.017542	20.14405659	153.2183841	358.218
2	0.014424	39.822643	162.2952635	7.295
3	0.012107	46.34482311	15.55369526	220.554
4	0.008493	20.20127406	173.3212549	18.321
5	0.006396	37.66212863	172.2922658	17.292
6	0.005483	30.76429369	163.2977801	8.298
7	0.005284	7.153718065	59.44441309	264.444
8	0.005108	51.3828705	26.08148873	231.081
9	0.003797	18.22450023	164.5149969	9.515
10	0.003696	17.1667583	10.5454051	215.545
11	0.003136	36.43829321	168.4726788	13.473
12	0.002875	32.62709267	114.7367006	319.737
13	0.002044	52.7383132	16.84108579	221.841
14	0.001946	42.99153331	178.91906	23.919

15	0.001914	0.747	16.16420451	221.164
16	0.001807	50.34372033	157.2354787	2.235
17	0.001743	50.3561174	141.707583	346.708
18	0.001644	37.77637789	34.73361394	239.734
19	0.001451	35.38154017	108.6116717	313.612
20	0.001209	44.57898749	116.3617629	321.362
21	0.001196	43.11010655	164.1060015	9.106
22	0.001128	30.72936747	176.8180282	21.818
23	0.001084	44.63496937	104.9923978	309.992
24	0.000950	14.93281575	78.87676721	283.877
25	0.000911	34.64524169	96.36219376	301.362
26	0.000875	34.9186395	95.31698761	300.317
27	0.000768	35.06445623	100.8442106	305.844
28	0.000523	30.69356729	20.26757109	225.268
29	0.000492	52.98984641	118.5468258	323.547

B6 Microfracture data for sample JI-02

Sample JI-02

Fracture cumulative N°	Aperture	Position Along Scanline	Didger Azimuth	Real Azimuth
1	0.002407	18.179	32.161	89.161
2	0.002265	20.664	178.546	235.546
3	0.001671	2.430	41.768	98.768
4	0.001653	58.627	32.214	89.214
5	0.001389	23.925	13.233	70.233
6	0.000769	25.920	85.066	142.066
7	0.000750	17.849	136.907	193.907

B7 Microfracture data for sample JI-03

Sample JI-03

Fracture cumulative N°	Aperture	Position Along Scanline	Didger Azimuth	Real Azimuth
1	0.013921	0.887	147.381	270.381
2	0.005515	56.247	163.062	286.062
3	0.004701	94.110	163.480	286.480
4	0.003156	75.035	147.425	270.425
5	0.002891	83.743	157.479	280.479
6	0.002591	21.582	139.538	262.538
7	0.002347	57.435	45.924	168.924
8	0.001985	57.377	58.352	181.352
9	0.001931	90.677	177.290	300.290
10	0.001832	87.415	1.027	124.027
11	0.001792	19.491	26.920	149.920
12	0.001774	46.505	170.446	293.446
13	0.001378	56.264	165.343	288.343
14	0.001330	46.432	158.839	281.839
15	0.001319	8.125	28.189	151.189
16	0.001218	5.484	24.737	147.737
17	0.001211	21.597	115.128	238.128
18	0.000970	52.256	139.108	262.108

B8 Microfracture data for sample JI-04

Sample JI-04

Fracture cumulative N°	Aperture	Position Along Scanline	Didger Azimuth	Real Azimuth
1	0.014610	55.578	22.675	326.675
2	0.011101	122.380	136.777	80.777
3	0.010529	104.427	12.391	316.391
4	0.009759	114.820	142.670	86.670
5	0.009515	102.493	19.132	323.132
6	0.008685	71.044	19.026	323.026
7	0.008169	85.038	164.367	108.367
8	0.007948	93.506	29.473	333.473

9	0.007911	92.275	20.553	324.553
10	0.007541	42.775	49.744	353.744
11	0.007204	70.976	20.686	324.686
12	0.007094	82.530	23.116	327.116
13	0.006781	104.582	43.159	347.159
14	0.006579	84.075	20.359	324.359
15	0.006302	25.843	32.415	336.415
16	0.006146	108.834	39.054	343.054
17	0.006104	87.885	16.324	320.324
18	0.006020	112.888	23.313	327.313
19	0.005976	2.758	23.018	327.018
20	0.005638	84.688	36.588	340.588
21	0.005464	133.595	56.331	0.331
22	0.005441	23.163	32.563	336.563
23	0.005310	77.659	145.668	89.668
24	0.005191	111.342	25.039	329.039
25	0.005034	37.561	179.484	123.484
26	0.004995	0.069	53.592	357.592
27	0.004881	111.708	11.940	315.940
28	0.004707	110.836	19.090	323.090
29	0.004599	30.019	155.498	99.498
30	0.004510	104.339	7.506	311.506
31	0.004403	106.722	15.266	319.266
32	0.004335	73.795	15.614	319.614
33	0.004315	86.241	164.805	108.805
34	0.004266	3.020	31.309	335.309
35	0.004249	22.835	52.113	356.113
36	0.004142	113.545	161.692	105.692
37	0.004121	8.819	129.963	73.963
38	0.003991	127.691	8.651	312.651
39	0.003990	30.287	7.867	311.867
40	0.003967	45.452	69.750	13.750
41	0.003916	82.624	27.881	331.881
42	0.003895	135.644	24.045	328.045
43	0.003836	4.631	53.317	357.317
44	0.003831	121.752	57.096	1.096
45	0.003698	86.004	37.906	341.906
46	0.003665	83.577	29.263	333.263
47	0.003446	59.658	3.578	307.578
48	0.003400	78.942	25.723	329.723

49	0.003390	115.915	17.748	321.748
50	0.003338	122.573	158.473	102.473
51	0.003337	41.171	65.708	9.708
52	0.003302	33.913	56.491	0.491
53	0.003237	76.739	23.890	327.890
54	0.003157	34.431	2.733	306.733
55	0.003144	22.884	140.538	84.538
56	0.003085	105.116	147.204	91.204
57	0.002933	96.650	125.398	69.398
58	0.002874	107.178	54.679	358.679
59	0.002846	42.015	2.314	306.314
60	0.002839	65.624	46.872	350.872
61	0.002801	65.478	9.873	313.873
62	0.002778	50.708	166.447	110.447
63	0.002754	39.901	4.665	308.665
64	0.002717	50.669	168.793	112.793
65	0.002541	45.219	34.095	338.095
66	0.002519	73.613	6.939	310.939
67	0.002499	52.043	63.337	7.337
68	0.002495	20.008	11.292	315.292
69	0.002491	127.846	68.943	12.943
70	0.002390	45.357	149.128	93.128
71	0.002366	18.844	53.410	357.410
72	0.002294	114.565	35.947	339.947
73	0.002293	51.112	47.763	351.763
74	0.002244	4.666	57.681	1.681
75	0.002241	41.932	49.868	353.868
76	0.002239	105.476	39.869	343.869
77	0.002239	110.517	171.533	115.533
78	0.002228	91.060	177.549	121.549
79	0.002206	24.789	11.313	315.313
80	0.002202	111.677	166.396	110.396
81	0.002193	49.192	36.836	340.836
82	0.002192	32.248	10.996	314.996
83	0.002185	43.700	177.756	121.756
84	0.002177	15.641	60.619	4.619
85	0.002172	51.720	57.750	1.750
86	0.002166	65.348	58.335	2.335
87	0.002155	116.287	16.846	320.846
88	0.002151	112.291	59.227	3.227

89	0.002119	73.311	111.418	55.418
90	0.002107	122.581	168.737	112.737
91	0.002061	24.968	176.826	120.826
92	0.002013	37.766	60.309	4.309
93	0.002007	45.791	65.088	9.088
94	0.001999	45.180	60.955	4.955
95	0.001981	112.744	61.822	5.822
96	0.001981	127.422	150.573	94.573
97	0.001963	27.654	161.368	105.368
98	0.001944	65.646	55.872	359.872
99	0.001935	7.800	159.031	103.031
100	0.001932	34.305	164.193	108.193
101	0.001895	112.971	49.322	353.322
102	0.001880	111.814	49.688	353.688
103	0.001866	30.342	61.786	5.786
104	0.001863	27.024	157.886	101.886
105	0.001840	84.814	33.693	337.693
106	0.001824	127.711	58.641	2.641
107	0.001813	116.439	51.357	355.357
108	0.001802	51.908	144.864	88.864
109	0.001799	18.002	174.232	118.232
110	0.001773	135.003	68.585	12.585
111	0.001743	43.927	64.496	8.496
112	0.001732	125.236	117.733	61.733
113	0.001702	98.225	65.870	9.870
114	0.001679	77.999	36.708	340.708
115	0.001675	115.532	61.978	5.978
116	0.001667	66.507	35.786	339.786
117	0.001666	73.591	141.335	85.335
118	0.001658	80.433	41.227	345.227
119	0.001634	42.878	37.284	341.284
120	0.001629	90.679	54.059	358.059
121	0.001597	53.474	66.687	10.687
122	0.001587	28.067	49.957	353.957
123	0.001577	100.362	0.269	304.269
124	0.001574	99.208	62.799	6.799
125	0.001570	135.943	63.268	7.268
126	0.001569	106.428	10.250	314.250
127	0.001547	52.017	0.369	304.369
128	0.001547	139.339	179.822	123.822

129	0.001539	62.940	174.270	118.270
130	0.001525	136.091	16.799	320.799
131	0.001519	82.475	14.326	318.326
132	0.001503	134.139	57.613	1.613
133	0.001489	120.724	158.056	102.056
134	0.001449	44.263	57.747	1.747
135	0.001446	37.443	58.845	2.845
136	0.001442	132.787	47.057	351.057
137	0.001431	99.017	58.851	2.851
138	0.001429	115.010	66.256	10.256
139	0.001428	71.892	72.689	16.689
140	0.001427	34.205	55.319	359.319
141	0.001422	121.634	173.489	117.489
142	0.001420	124.323	5.823	309.823
143	0.001393	64.415	60.104	4.104
144	0.001387	113.013	12.899	316.899
145	0.001386	116.483	49.056	353.056
146	0.001385	65.278	65.722	9.722
147	0.001378	73.655	11.361	315.361
148	0.001364	133.380	30.752	334.752
149	0.001363	35.420	163.923	107.923
150	0.001353	31.973	30.634	334.634
151	0.001344	10.552	25.718	329.718
152	0.001338	6.157	8.031	312.031
153	0.001330	111.841	51.009	355.009
154	0.001324	133.151	21.490	325.490
155	0.001318	92.127	20.020	324.020
156	0.001308	31.944	28.770	332.770
157	0.001291	53.255	22.943	326.943
158	0.001291	91.801	158.283	102.283
159	0.001289	54.048	67.439	11.439
160	0.001285	44.294	51.051	355.051
161	0.001283	74.898	154.838	98.838
162	0.001271	114.847	52.969	356.969
163	0.001270	47.782	53.816	357.816
164	0.001266	112.032	63.043	7.043
165	0.001235	36.129	60.372	4.372
166	0.001230	118.466	69.204	13.204
167	0.001220	131.717	64.069	8.069
168	0.001217	13.902	60.257	4.257

169	0.001212	135.652	64.259	8.259
170	0.001206	34.278	61.136	5.136
171	0.001198	11.496	36.313	340.313
172	0.001162	26.352	38.591	342.591
173	0.001152	47.646	65.502	9.502
174	0.001148	114.802	35.893	339.893
175	0.001138	7.153	62.264	6.264
176	0.001122	135.692	141.060	85.060
177	0.001099	117.003	60.254	4.254
178	0.001090	72.917	63.944	7.944
179	0.001086	117.392	67.012	11.012
180	0.001084	80.777	45.933	349.933
181	0.001081	136.879	67.810	11.810
182	0.001069	114.933	61.107	5.107
183	0.000979	41.816	2.526	306.526
184	0.000976	92.174	11.454	315.454
185	0.000969	62.530	171.259	115.259
186	0.000966	125.942	62.563	6.563
187	0.000959	51.133	45.344	349.344
188	0.000950	135.731	19.353	323.353
189	0.000884	23.919	55.380	359.380
190	0.000877	6.211	12.863	316.863
191	0.000877	28.213	64.185	8.185
192	0.000838	36.955	101.328	45.328
193	0.000828	111.772	65.184	9.184
194	0.000764	139.325	171.105	115.105
195	0.000714	132.738	1.472	305.472
196	0.000699	112.436	63.402	7.402
197	0.000689	116.647	14.851	318.851
198	0.000687	62.515	172.838	116.838
199	0.000679	112.109	161.261	105.261
200	0.000679	139.275	64.219	8.219
201	0.000651	131.150	23.740	327.740
202	0.000647	60.790	61.586	5.586
203	0.000616	107.288	29.866	333.866
204	0.000600	21.029	106.785	50.785
205	0.000482	99.254	46.193	350.193
206	0.000426	52.015	51.221	355.221
207	0.000317	107.301	63.020	7.020

B9 Microfracture data for sample JI-07

Sample JI-07

Fracture cumulative N°	Aperture	Position Along Scanline	Didger Azimuth	Real Azimuth
1	0.005968	41.782	144.751	47.751
2	0.004478	0.435	44.111	307.111
3	0.004259	47.723	152.631	55.631
4	0.002562	31.219	0.196	263.196
5	0.002242	47.307	36.804	299.804
6	0.002234	47.503	174.564	77.564

B10 Microfracture data for sample JI-10

Sample JI-10

Fracture cumulative N°	Aperture	Position Along Scanline	Didger Azimuth	Real Azimuth
1	0.007585	53.641	175.588	58.588
2	0.003081	38.143	136.104	19.104
3	0.001726	11.907	143.977	26.977
4	0.001085	15.731	45.743	288.743
5	0.000811	3.733	145.459	28.459

APPENDIX C: POINT COUNTING DATA

Point count data for all the studied samples presented as percentages. 300 points were counted for each sample.

C1 Point count data for the studied samples

C1 Point counting data

Sample	Monocrystaline Components								Rock Lithics Fragments					
	Mono Qtz	Poly Qtz	K Feld	Plag	Biot	Musc	Opaque	Chlorite	Sed Silt	Clay Stone	Sed Chert	Met Phyl	Met Plut	Volc Fels
H1	49.00	3.67	5.00	4.67	0.00	0.00	0.00	0.00	0.33	0.00	1.67	8.33	4.00	1.00
H4	45.00	5.33	3.67	2.33	0.00	0.67	0.00	0.33	3.33	1.67	1.33	2.00	0.00	0.67
H6	52.70	2.70	5.70	1.00	0.00	0.00	0.00	0.00	1.00	0.30	1.70	4.00	0.00	2.30
H7	62.00	9.33	2.00	0.67	0.00	0.00	0.00	0.00	0.00	1.00	1.00	2.67	0.00	3.33
H8	56.30	4.00	5.00	1.30	0.00	1.00	0.00	0.00	1.00	2.70	0.30	1.30	0.00	12.70
H9	41.70	3.00	8.30	1.00	0.00	1.30	0.00	0.30	0.30	1.30	1.70	16.70	0.00	7.00
H11	54.00	3.00	4.67	4.67	0.33	0.00	0.00	0.67	0.33	0.33	1.00	7.67	0.00	0.33
H12	51.67	2.33	4.33	2.33	0.33	0.33	0.00	0.33	0.33	1.00	1.00	9.33	5.00	0.67
H13	58.33	4.66	5.33	2.33	0.33	0.33	0.00	0.00	0.33	2.33	1.33	4.33	0.00	0.66
JI-02	51.33	2.00	1.67	3.67	0.33	0.67	0.00	0.67	0.33	2.00	1.67	7.00	1.00	0.33
JI-03	47.33	3.00	4.33	2.67	0.33	1.00	0.00	0.67	2.00	1.33	2.67	10.67	0.67	0.67
JI-04	56.00	4.00	2.33	1.33	0.33	0.67	0.33	0.00	1.33	2.00		4.00	0.00	2.67
JI_05	40.00	2.67	3.67	4.33	1.00	0.67	0.00	0.33	1.67	3.00	1.00	7.33	2.67	0.00
JI-07	46.67	2.33	2.00	4.00	2.33	2.67	0.00	0.33	1.00	3.33	0.67	8.00	0.67	0.00
JI-10	61.67	2.33	2.33	1.33	0.00	0.00	0.33	0.00	0.33	0.00	0.67	4.33	1.00	0.33

Sample	Matrix		Pseudomatrix	Diagentetic Components					Porosity			
	Silt	Clay	Clay clast	Qtz cmt (1)	Qtz cmt (2)	Carb cmt	Clay cmt	Org	Fracture	Primary	Secondary	Organic
H1	0.00	0.00	2.00	20.33	0.00	0.00	0.00	0.00	0.00	0.00	0.00	0.00
H4	0.33	0.00	3.33	13.67	0.00	1.67	1.33	13.33	0.00	0.00	0.00	0.00
H6	0.00	0.00	0.00	19.30	0.00	0.00	0.00	0.00	2.30	0.30	6.70	0.00
H7	0.33	2.00	0.00	10.67	2.33	1.67	0.00	0.33	0.67	0.00	0.00	0.00
H8	0.00	0.70	0.00	12.00	0.00	0.00	0.00	0.30	0.00	1.00	0.00	0.00
H9	0.00	2.30	0.00	10.00	0.00	0.60	0.00	0.60	2.30	0.00	1.30	0.00
H11	0.00	0.33	0.00	13.33	0.00	3.33	0.00	1.00	0.00	0.00	1.00	0.00
H12	0.00	1.00	0.00	15.33	0.00	1.00	0.00	0.67	0.00	0.67	0.67	0.00
H13	0.33	1.00	0.00	13.66	0.33	3.33	0.00	0.33	0.66	0.00	0.00	0.00
JI-02	0.00	1.00	0.00	16.67	2.00	0.00	0.00	5.67	0.33	0.33	0.00	1.33
JI-03	0.00	3.67	0.00	13.67	0.67	0.00	0.00	2.67	0.00	0.00	0.00	2.00
JI-04	0.00	0.00	3.00	16.33	2.33	2.00	1.00	0.00	0.00	0.00	0.33	0.00
JI_05	0.00	4.67	4.67	17.33	0.00	0.00	0.00	3.00	0.00	0.00	0.67	1.33
JI-07	0.00	0.67	0.00	17.33	1.33	0.00	0.00	0.33	0.67	0.33	1.33	4.00
JI-10	0.00	0.00	0.00	21.00	0.00	0.00	0.00	1.00	0.00	0.33	2.00	1.00

References

Aceñolaza, F.G., Buatois, L.A., Mangano, M.G., Esteban, S.B., Tortello, M.F. y Aceñolaza, G.F., 1999a. Cámbrico y Ordovícico del noroeste argentino. Instituto de Geología y Recursos Minerales. Geología Argentina, 29 (7), pp. 169-187.

Aceñolaza, F. G., Buatois, L. A., Mangano, M. G., Esteban, S. B., Tortello, M. F. y Aceñolaza, G. F., 1999a. Cámbrico y Ordovícico del noroeste argentino. Instituto de Geología y Recursos Minerales. Geología Argentina, 29 (7), pp. 169-187.

Aceñolaza, F. G., Aceñolaza, G. y Garcia, G., 1999b. El Silúrico-devónico del noroeste argentino. Instituto de Geología y Recursos Minerales. Geología Argentina, 29 (9), pp. 205-214.

Allan, U.S., 1989. Model for hydrocarbon migration and entrapment within faulted structures. AAPG Bulletin, v.73, pp. 803–811.

Antonellini M., 1998. Outcrop Characterization of Fractures in the Huamampampa Formation. EPTG Amoco. Non published report.

Aramayo Flores, F., 1999. Estructura de las Sierras Subandinas del Noroeste Argentino. Geología del Noroeste Argentino. XIV Congreso Geológico Argentino. G. González Bonorino, R. Omarini and J. Viramonte (eds.). I, pp. 401-414.

Aramayo Flores, F., 1999. Estructura de las Sierras Subandinas del Noroeste Argentino. Geología del Noroeste Argentino. XIV Congreso Geológico Argentino. G. González Bonorino, R. Omarini and J. Viramonte (eds.). I, pp. 401-414.

Araujo, A., and Clivio J. L., 2001. Tectonic Influence in the Productive Potential of the MGR-X3 Well in the Margarita Field, Bolivia. SPE 69509.

Atkinson, B. K., and Meredith, P. G., 1987. The Theory of Subcritical Crack Growth with Applications to Minerals and Rocks. In: Fracture Mechanics of Rock. Atkinson B. K. (ed.). Academic Press, San Diego, California.

Ayaviri, A., 2002. Geologic Map, Abra del Condor-Canaletas. Non published report.

Azcuy, C. L. and Di Pascuo, M., 1999. Carbonífero y Pérmico de las sierras Subandinas, Cordillera Oriental y Puna. Instituto de Geología y Recursos Minerales. Geología Argentina, anales 29 (11), pp. 239-260.

Baby, P., Hérail, G., Salinas, R., and Sempere, T., 1992. Geometry and kinematic evolution of passive roof duplexes deduced from cross-section balacing: example from the foreland thrust system of the southern Bolivian Subandean Zone. Tectonics 11, pp. 523–536.

Bai, T., Maerten, L., Gross, M.R., and Aydin, A., 2002, Orthogonal cross joints: Do they imply a regional stress rotation?: Journal of Structural Geology, v. 24, pp. 77–88.

Bai, T., and Pollard, D.D., 2000a. Fracture Spacing in Layered Rocks: A New Explanation Based on the Stress Transition. Journal of Structural Geology, 22, pp. 43-57.

Bai, T., and Pollard, D.D., 2000b. Closely spaced fractures in layered rocks: initiation mechanisms and propagation kinematics. Journal of Structural Geology, 22, pp. 1409-1425.

Bai, T., and Pollard, D.D., Gross, M. R., 2000. Mechanical prediction of fracture aperture in layered rocks. Journal of Geophysical Research. Vol 105, N°B1, pp. 707-721

Bear, J., Tsang, C.F., de Marsily, G., 1993. Flow and contaminant transport in fractured rock. Academic Press, San Diego.

Becker, A., and M. R. Gross, 1996. Mechanisms for Joint Saturation in Mechanically Layered Rocks –An Example from Southern Israel. Tectonophysics, 257, pp. 223-237.

Bergbauer, S., and Pollard, D.D., 2003. How to calculate normal curvatures of sampled geological surfaces. Journal of Structural Geology, 25, pp. 277-289.

Bergbauer, S., and Pollard, D.D., 2004. A new conceptual fold–fracture model including prefolding joints, based on field data from the Emigrant Gap anticline, Wyoming. GSA Bulletin 116, pp. 294–307.

Bellahsen, N., Fiore, P., and Pollard, D.D., 2006. The role of fractures in the structural interpretation of Sheep Mountain Anticline, Wyoming. Journal of Structural Geology, 28, pp. 850-867.

Bjørlykke, K., and Egeberg, P.K., 1993. Quartz Cementation in Sedimentary Basins. AAPG Bulletin, v. 77, pp. 1538-1548.

Boggs, S., and Krinsley, D., 2006, Application of Cathodoluminescence Imaging to the Study of Sedimentary Rocks, Cambridge Univ. Press, 165 p.

Casey, M., and Butler, W.H., 2004. Modelling approaches to understanding fold development: implications for hydrocarbon reservoirs. Marine and Petroleum Geology, 21, pp. 933-946.

Carlson, M.R., 2003. Practical Reservoir Simulation. PennWell corporation. 564 p.

Clark, M.B., Brantley, S.L., Fisher, D.M., 1995. Power-law vein-thickness distributions and positive feedback in vein growth. Geology 23 (11), pp. 975–978.

Cladouhos, T.T., and Marrett, R., 1996, Are fault growth and linkage models consistent with power-law distributions of fault lengths?: Journal of Structural Geology, v. 18, pp. 281-293.

Cohen, M. 2002. Caracterizacion del sistema de fracturas naturales de los campos San Pedrito y Macueta. V Congreso de Exploracion y Desarrollo de Hidrocarburos. Digital Acts.

Cohen M., and Ollier C., 2002. Log Porosity Calibration with Core data and Acoustic Imaging in Naturally Fractured Reservoirs: An example from San Pedrito Field, NW Argentina. 2002 SPWLA European Symposium.

Cooper, M., 2007. Structural style and hydrocarbon prospectivity in fold and thrust belts: a global review. In: Deformation of the Continental Crust: The Legacy of Mike Coward. A.C. Ries, R.W.H. Butler, and R.H. Graham (eds). Geologcial Society of London, Special Publications, 272, pp. 447-472.

Couples G. D., Lewis, H., and Tanner, P.W.G., 1998. Strain Partitioning during flexural slip-folding. . In: Structural Geology in Reservoir Characterization.

Coward M. P., T. S. Daltaban, and H. Johnson (eds.), Geological Society of London. Special Publication No127, pp. 149-166.

Constantini, L. A., Rodríguez, A., Fontana, C., Rodríguez Schelotto, M. L. y Hernández, R., 2002. Los Reservorios de la Formación Tranquitas y “Terciario Subandino”. Rocas Reservorio de las Cuencas Productivas de la Argentina. V Congreso de Exploración y Desarrollo de Hidrocarburos. M. Schiuma, G. Hinterwimmer, G. Vergani (eds.). pp. 767-786.

Cruz,C., Sylwan, C. y Villar, H., 2001. Source Rocks and Hydrocarbons South of the Santa Cruz Elbow, Bolivia and Northwest Argentina. AAPG Annual Conference, Denver.

Di Marco, L., 2004. Camino de Los Infernales, Geología de la Sierra del Alto Río Seco, Estructura San Pedro, Provincia de Salta. Facultad de Ciencias Exactas y Naturales, Universidad de Buenos Aires. Trabajo Final de Licenciatura (inedited), pp. 50-51.

Donner, R.V., and Barbosa, S.M., 2008. Nonlinear Time Series Analysis in the Geosciences: Application in Climatology, Geodynamics and Solar-Terrestrial Physics. Springer-Verlag, 390 p.

Disalvo, A. and Villar, H. J., 1999. Los Sistemas Petrolíferos del Area Oriental de la Cuenca Paleozoica Noroeste, Argentina. IV Congreso Exploración y Desarrollo de Hidrocarburos, Actas I, pp. 83-100.

Dunn, J. F., Hartshorn, K. G., and Hartshorn, P. W., 1995, Structural styles and hydrocarbon potential of the sub-Andean thrust belt of southern Bolivia, in A. J. Tankard, R. Suárez S., and H. J. Welsink, Petroleum basins of South America: AAPG Memoir 62, pp. 523–543.

Echeverria, L., Hernández, R., Allmendinger, R., and Reynolds, J., 2003. Subandean thrust and fault belt of northwestern Argentina; Geometry and timing of the Andean evolution. AAPG Bulletin, v. 87, pp. 965-985.

Egan, S.S., Buddin, T. S., Kane, S. J., Williams, G. D., 1997. Three-dimensional modelling and visualisation in structural geology: new techniques for the restoration and balancing of volumes. In: Proceedings of the 1996 Geoscience Information Group Conference on Geological Visualisation: the Intelligent Picture? Electronic Geology 1, pp. 67-82.

Engelder, T, 1985. Loading paths to joint propagation during a tectonic cycle: an example from the Appalachian Pleateau. JSG 7, pp. 459-476.

Engelder, T., and Lacazette, A., 1990, Natural hydraulic fracturing, In: N. Barton and O. Stephansson (eds.), Rock Joints, A.A. Balkema, Rotterdam, pp. 35–44.

Engelder, T., and Lash, G.G., 2009. Joint sets that enhance production from Middle and Upper Devonian gas shales of the Appalachian Basin. AAPG Bulletin, v.93, pp. 857-889.

Ericsson, J. B., McKean, H. C., and Hooper, R. J., 1998. Facies and curvature controlled 3D fracture models in a Cretaceous carbonate reservoir, Arabian Gulf. In: Jones, G., Q. J. Fischer, and R. J. Knipe (eds) Faulting, Fault Sealing and Fluid Flow in Hydrocarbon Reservoirs. Geological Society of London, Special Publications, 147, pp. 299-312.

FaultKinWin tutorial, 2001. www.geo.cornell.edu/geology/faculty/RWA/programs.html

Fischer, M., and Wilkerson S., 2000. Predicting the orientation of joints from fold shape: Results of pseudo-three-dimensional modeling and curvature analysis. Geology v28, no1, pp. 15-18.

Fleuty, M. J., 1964. The description of folds. Proceeding Geological Association of London, 75, pp. 461-492.

Folk, R. L., 1980. Petrology of Sedimentary Rocks. Hemphill Publishing Company, Austin, 184 p.

Gale, J. 2002. Specifyng Lengths of Horizontal Wells in Fractured Reservoirs. SPE Reservoir Evaluation and Engineering.

Gillespie, P. A., Howard, C. B., Walsh, J. J., and Watterson, J., 1993. Measurement and Characterization of Spatial Distributions of Fractures. Tectonophysics, 226, pp. 113-141.

Gillespie, P. A., Walsh, J. J., Watterson, J., Bonson, C. G., and Manzocchi, T., 2001. Scaling Relationships of Joint and Vein Arrays from The Burren, Co. 409 Clare, Ireland. In: Paul Hancock Memorial Issue. Dunne, W. M., I. S. Stewart, J. P. Turner (eds.). Journal of Structural Geology, 23 (2-3), pp. 183-201.

Giraudo, R., Limache, R., Requena, E., and Guerra, H., 1999. Geología estructural de la faja fallada y plegada del Subandino Sur, Bolivia. Boletín de Informaciones Petroleras, XVI (59), pp. 54-70.

Gomez, L., and Laubach, S., 2006. Rapid digital quantification of microfractures population. Journal of Structural Geology, 28, pp. 408-420.

Groeber, P., 1929. Líneas Fundamentales de la Geología del Neuquén, Sur de Mendoza y Regiones Adyacentes. Dirección Nacional de Geología y Minería, publicación 58, pp. 1-110.

Groshong, R. H., 2006. 3-D Structural Geology 2nd Edition. Sringer-Verlag Berlin Heidelberg. 400 p.

Gross, M. R., 1993. The Origin and Spacing of Cross Joints: Examples from the Monterrey Formation, Santa Barbara Coastline, California. Journal of Structural Geology, v.15, pp. 737-751.

Guzofski, C. A., Mueller, J. P., Shaw, J. H., Muron, P., Medwedeff, D. A., Bilotti, F., and Rivero, C., 2009. Insights into the mechanisms of fault-related folding provided by volumetric structural restorations using spatially varying mechanical constraints. AAPG Bulletin, v.93, pp. 479–502.

Hanks, C.L., Lorenz, J., Lawrence, T., and Krumhardt, A. P., 1997. Lithologic and Structural Controls on natural Fracture Distribution and Behavior Within the Lisburne Group, Northeatern Brooks Range and North Slope Subsurface, Alaska. AAPG Bulletin, v81, pp 1700-1720.

Hancock, P.L., 1985. Brittle microtectonics; principles and practice. Journal of Structural Geology, 7, pp. 437–457.

Heidbach, O., Tingay, M., Barth, A., Reinecker, J., Kurfe, D., and Müller, B. The World Stress Map based on the database release 2008, equatorial scale 1:46,000,000, Commission for the Geological Map of the World, Paris, doi:10.1594/GFZ.WSM.Map2009, 2009.

Hennings, P.H., Olson, J.E., Thompson, L.B., 2000. Combining outcrop data and three-dimensional structural models to characterize fractured reservoirs; an example from Wyoming. AAPG Bulletin, v. 84, pp. 830–849.

Hernández, R., Echeverria, L., Allmendinger, R., Reynolds, J., and Jordan, T., 2002. Las faja plegada y corrida subandina del noroeste argentino. Secuencias de precrecimiento y crecimiento, geometría estructural y tiempo de evolución de Los Andes. V Congreso de Exploración y Desarrollo de Hidrocarburos. (Digital acts).

Hooker, J.N., Gale, J.F.W., Gomez, L.A., Laubach, S.E., Marrett, R., and Reed, R.M., 2009. Aperture-size scaling variation in a low-strain opening-mode fracture set, Cozzette Sandstone, Colorado. Journal of Structural Geology, 31, pp. 707-718.

Holder, J., Olson, J.E., and Philip, Z., 2001, Experimental Determination of Subcritical Crack Growth Parameters in Sedimentary Rock, Geophysical Research Letters, Vol. 28, No. 4, pp. 599-602.

Horton, B. K., Hampton, B.A., and Waanders, G.L., 2001, Paleogene synorogenic sedimentation in the Altiplano plate and implications for initial mountain building in the central Andes. GSA Bulletin, v. 113, pp. 1387– 1400.

Hudleston, P. J., Treagus, S.H., and Lan, L., 1996. Flexural flow folding: does it occur in nature? Geology, 24, pp. 203-206.

Jaeger, J., and Cook, N.G., 2007. Fundamentals of Rock Mechanics 4th edition. Blackwell Publishing, 475 p.

Jamison, W. R., 1997. Quantitative Evaluation of Fractures on Monkshood Anticline, a Detachment Fold in the Foothills of Western Canada. AAPG Bulletin, v. 81, pp. 1110-1132.

Jordan, T. E., and Alonso, R.N., 1987, Cenozoic stratigraphy and basins tectonics of the Andes mountains, 20°–28° south latitude: AAPG Bulletin, v. 71, pp. 49–74.

Johnson, K. M., and Johnson, A.M., 2000. Localization of layer-parallel faults in San Rafael swell, Utah and other monoclinal folds. Journal of Structural Geology, 22, pp. 1455-1468.

Keating, D. P., and Fischer, M.P., 2008. An experimental evaluation of the curvature-strain relation in fault-related folds. AAPG Bulletin, v. 92, pp. 869-884.

Kley, J. and Monaldi, C., 1999. Estructura de las Sierras Subandinas y del Sistema de Santa Bárbara. Geología del Noroeste Argentino. XIV Congreso Geológico Argentino. G. González Bonorino, R. Omarini y J. Viramonte (eds.). I:, pp. 401-414.

Kozlowski, E. F. Aramayo Flores, and Hofmann, C.,. 2005. Gas en el Devónico de las Sierras Subandinas, Provincia de Salta, Argentina. In: Las Trampas de Hidrocarburos en las Cuencas Productivas de Argentina, E. Kozlowski, G. Vergani, and A. Boll (eds.). VI Congreso de Exploracion y Desarrollo de Hidrocarburos. pp. 17-35.

Kranz, R.L., 1983. Microcracks in Rocks-A Review. Tectonophysics, 100, 1-3, pp. 449-480.

Lander, R. H., Gale, J.F., Laubach, S.E., and Bonnell, L.M., 2002, Interaction between quartz cementation and fracturing in sandstone (abs.): AAPG Annual Convention Program, v. 11, pp. A98–A99.

Laubach, S.E., 1988, Subsurface fractures and their relationship to stress history in East Texas basin sandstone. Tectonophysics, 156, pp. 37-49.

Laubach, S. E., 1989, Paleostress directions from the preferred orientation of closed microfractures (fluid-inclusion planes) in sandstone, East Texas basin, U.S.A. Journal of Structural Geology, 11, pp. 603–611.

Laubach, S.E., 1997. A Method to Detect Natural Fracture Strike in Sandstones. AAPG Bulletin, v. 81, pp. 604-623.

Laubach, S., 2003. Practical approaches to identifying sealed and open fractures. AAPG Bulletin, v. 87, pp. 561-579.

Laubach, S.E. and Diaz-Tushman, K., 2009, Laurentian paleostress trajectories and ephemeral fracture permeability, Cambrian Eriboll Formation sandstones west of the Moine thrust zone, northwest Scotland. Journal of the Geological Society (London), v. 166, part 2, p. 349-362.

Laubach, S. E., Lander, R.H., Bonnell, L.H., Olson, J.E., and Reed, R.M., 2004. Opening histories of fractures in sandstone. In: The Initiation, Propagation, and Arrest of Joints and other Fractures. Cosgrove, J. W., Engelder, T. (Eds.), Geological Society of London Special Publication, vol. 231, pp. 1–9.

Laubach, S. E., and Lorenz, J.C., 1992, Natural fracture patterns in sandstones of the Frontier Formation, southwestern Wyoming (abs.). AAPG Bulletin, v. 76, pp. 1262.

Laubach, S.E., and K.L. Milliken, 1996, New fracture characterization techniques for siliciclastic rocks. In: Second North American Rock Mechanics Symposium M. Aubertin, F. Hassani, and H. Mitri, (eds),: Balkema, pp. 1209-1213.

Laubach, S. E., Olson, J.E., and Gross, M.R., 2009. Mechanical and fracture stratigraphy. AAPG Bulletin. In press.

Laubach, S. E. and Ward, M.E., 2006. Diagenesis in porosity evolution of opening-mode fractures, Middle Triassic to Lower Jurassic La Boca Formation, NE Mexico. Tectonophysics, 419, (1–4), pp. 75–97.

Lisle, R., 1992, Constant bed-length folding: three-dimensional geometrical implications. Journal of Structural Geology, 15, pp. 245–252.

Lisle, R. 1994. Detection of Zones of Abnormal Strain in Structures Using Gaussian Curvature Analysis. AAPG Bulletin, v78, p.1811-1819.

Lisle, R., and Robinson, J.M., 1995. The Mohr circle for curvature and its application to fold description. Journal of Structural Geology, 17, pp. 739-750.

Luquez, J., Hofman, C. y Constantini, L., 2002. Los Reservorios de las Formaciones Santa Rosa, Icla y Huamampampa. Rocas Reservorio de las Cuencas Productivas de la Argentina. V Congreso de Exploración y Desarrollo de Hidrocarburos. M. Schiuma, G. Hinterwimmer, G. Vergani (eds.). pp. 683-697.

Makowitz, A., R. H. Lander, and K. L. Milliken, 2006, Diagenetic modeling to assess the relative timing of quartz cementation and brittle grain processes during compaction. AAPG Bulletin, v. 90, pp. 873–885.

Marret, R. 1996. Aggregate properties of fracture populations. Journal of Structural Geology. 18 , pp.169-178.

Marret. R., In preparation. Fractal and Periodic Spatial Arrangement of Natural Fractures.

Marrett, R. and Allmendinger, R., 1991. Estimates of strain due to brittle faulting: sampling of fault population. Journal of Structural Geology, 13, pp. 735-738.

Marret R., Gale, J. F., Gomez, L.A., In preparation. Correlation Analysis of Fracture Arrangement in Space.

Marrett, R., and Laubach, S.E., 2001, Burial, tectonic, and exhumational fracturing, in R. Marrett, ed., Genesis and controls of reservoir-scale carbonate deformation, Monterrey Salient, Mexico, University of Texas at Austin, Bureau of Economic Geology, Austin, Guidebook 28, pp. 109– 122.

Marrett, R., Ortega, O., and Kelsey, C., 1999. Extent of power law scaling for natural fractures in rocks. Geology, V. 27, N° 9. pp.799-802.

McClay, K. R., 1992. Glossary of thrust tectonics terms. In: McClay, K. R (ed), Thrust Tectonics. Chapman and Hall, London, pp. 419-433.

Millani, E. J., 1997. Evolucao Tetono-Sedimenter e Estratigrafia da Bacia do Parana. Universidade Federal do Rio Grande do Sul, Tesis doctoral (inédita), Porto Alegre. In: V. A. Ramos, 1999. Rasgos Estructurales del territorio Argentino. Geología Argentina. Instituto de Geología y Recursos Minerales. Geología Argentina, anales 29 (24), pp. 716-759.

Milliken, K.L., and Laubach, S.E., 2000, Brittle deformation in sandstone diagenesis as revealed by scanned cathodoluminescence imaging with application to characterization of fractured reservoirs: Chapter 9, Cathodoluminescence in Geosciences, New York, Springer-Verlag, pp. 225-243.

Mingramm, A. and Russo, A., 1972. Sierras Subandinas y Chaco Salteño. In Leanza, A. F. (ed.) Geología Regional Argentina. Academia Nacional de Ciencias, pp.185-221.

Mitra, S., 1990. Fault-propagation folds: geometry kinematic evolution, and hydrocarbon traps. AAPG Bulletin, v74, pp. 921–945.

Moretti, I., 2008. Working in complexa reas: New restorations workflow base don quality control, 2D and 3D restorations. Marine and Petroleum Geology, 25, pp. 2505-218.

Moretti, I., Baby, P., Mendez, E., and Zubieta, D., 1996. Hydrocarbon generation in relation to thrusting in the Sub Andean Zone from 18 to 22jS, Bolivia. Petroleum Geosciences 2, pp. 17– 28.

Moretti, I., and Delos, V., 2006. Surfacic Restoration: flexural slip versus simple shear. 26th Gocad Meeting.

Moretti, I., Labaume, P., Sheppard, S., and Boulègue, J., 2002. Compartmentalisation of fluid migration pathways in the sub-Andean Zone, Bolivia. Tectonophysics, 348, pp. 5-24.

Moretti, I., Lepage, F., and Guiton, M., 2006. 3D restoration: geometry and geomechanics. Oil and Gas Technology 61 (2), 277–289.

Morettini, E., Thompson, A., Eberli, G.P., Rawnsley, K.D., Asyee, W., Christman, P., Cortis, T., Foster, K., Hitchings, V., Kolkman, W., and Van Konijnenburg, V.H., 2005. Combining high resolution sequence stratigraphy and mechanical stratigraphy for improved reservoir characterisation in the Fahud field of Oman. GeoArabia 10/3, 17–44.

Move tutorial, 2009. www.mve.com.

Mynatt, I., Bergbauer, S., Pollard, D.D., 2007. Using differential geometry to describe 3-D folds. Journal of Structural Geology, 29, pp. 1256-1266.

Narr, W. 1991. Fracture density in the deep subsurface; techniques with application to Point Argüello oil field. AAPG Bulletin, v75, pp. 1300-1323.

Narr, W., and Currie, J.B., 1982, Origin of fracture porosity- example from Altamont field, Utah. AAPG Bulletin, v66, pp. 1231–1247.

Narr, W. and Suppe, J., 1991. Joint spacing in sedimentary rocks. Journal of Structural Geology, 13, pp. 1037-1048.

Nelson, R. A., 2001. Geological analysis of naturally fractured reservoirs 2nd edition. Gulf Professional Publishing, 332p.

Olson, J. E. 1993. Joint pattern development: effects of subcritical crack-growth and mechanical crack interaction. Journal of Geophysical Research, 98, pp.12251-12265.

Olson, J. E., 2003. Sublinear scaling of fracture aperture versus length: An exception to the rule?. Journal of Geophysical Research v108, No B9, pp. 2413.

Olson, J. E. 2004. Predicting fracture swarms -the influence of subcritical crack growth and the crack-tip process zone on joint spacing in rock. In: The initiation, propagation, and arrest of joints and other fractures. Engelder, T., and Cosgrove, J. W. (eds). Geological Society of London, Special Publications, 231, pp. 73-87.

Olson, J. E, Laubach, S.E., and Lander, R.H., 2009, Natural fracture characterization in tight gas sandstones: Integrating mechanics and diagenesis. AAPG Bulletin, v. 93, no. 11.

Olson, J. E. and Pollard, D.D., 1989. Inferring paleostresses from natural fracture patterns: A new method. Geology 17, pp. 345-348.

Olson, J. E. and Pollard, D.D., 1991. The initiation and growth of en echelon veins, Journal of Structural Geology, 13, pp. 595–608.

Olson, J.E., Qiu, Y., Holder, J., and Rijken, P., 2001, Constraining the Spatial Distribution of Fracture Networks in Naturally Fractured Reservoirs Using Fracture Mechanics and Core Measurements, Society of Petroleum Engineers, SPE 71342

Ortega, O., and Marrett, R., 2000, Prediction of macrofracture properties using microfracture information, Mesaverde Group sandstones, San Juan Basin, New Mexico. Journal of Structural Geology, 22, pp. 571-588.

Ortega, O.J., Marrett, R., and Laubach, S.E., 2006, A scale-independent approach to fracture intensity and average spacing measurement: AAPG Bulletin, v. 90. pp. 193-208.

Pagel, M., Barbin, V., Blanc, P., Ohnenstetter, D. (eds.), 2000. Cathodoluminescence in Geosciences. Springer-Verlag.

Palma, M., and Irigoyen, V., 1987. Los Estratos de Botijuela en la Puna Catamarqueña. XX Congreso Geológico Argentino. Actas II, pp. 168-173.

Philip, Z.G., Jennings, J.W., Olson, J.E., Laubach, S.E., and Holder, J., 2005. Modeling coupled fracture-matrix fluid flow in geomechanically simulated fracture networks. SPE Reservoir Evaluation & Engineering, 8 (4), 300-309.

Pineau, A., 1985, Echantillonnage des espacements entre fractures:Une distribution exponentielle negative troque´e: Comptes Rendus de l’Acade´mie des Sciences, II, v. 301, pp. 1043– 1046.

Pollard, D., and Aydin, A., 1988. Progress in understanding jointing over the last century. GSA Bulletin, v.100. pp. 1181-1204.

Pearce, M.A., Jones, R.R., Smith, S.A., McCaffrey, K.J., and Clegg, P., 2006. Numerical analysis of fold curvature using data acquired by high-precision GPS. Journal of Structural Geology, 28, pp. 1640-1646.

Price, N. J., 1966. Fault and Joint development in brittle and semibrittle rock. New York: Pergamon Press.

Ramos, V. A, 1986. El Diastrofismo Oclóyico: un ejemplo de tectónica de colisión durante el Eopaleozoico en el Noroeste Argentino. Revista del Instituto de Geología y Minería. Universidad Nacional de Jujuy. 6, pp. 13-28.

Ramos, V. A., 1999a. Rasgos Estructurales del territorio Argentino. Geología Argentina. Instituto de Geología y Recursos Minerales. Geología Argentina, anales 29 (24), pp. 716-759.

Ramos, V. A., 1999b. Los Depósitos Sinorogénicos Terciarios de la Región Andina. Geología Argentina. Instituto de Geología y Recursos Minerales. Geología Argentina, Anales 29 (22), pp. 651-682.

Ramsay, J. G., 1967. Folding and fracturing of Rocks. Mc Graw and Hill.

Reyes, F. C., 1972. On the Carboniferous and Permian of Bolivia and Northwestern Argentina. Anales Academia Brasileña de Ciencias (Supl.), 4, pp. 261-277.

Ratliff, B. 2006. Litho-Tect tutorial. www.geologicsystems.com.

Rijken, P., 2005. Modeling naturally fractured reservoirs: from experimental rock mechanics to flow simulation. The University of Texas at Austin, Department of Petroleum and Geosystems Engineering, Unpublished PhD Dissertation. 275 p.

Rives, T., Razak, M., Petit, J.P., and Rawnsley, K.T., 1992, Joint spacing; analogue and numerical simulations, in J.-P. Burg, D. Mainprice, and J.-P. Petit, eds., Mechanical instabilities in rocks and tectonics; a selection of papers: Journal of Structural Geology, 14, pp. 925– 937.

Roeder, D. 1988. Andean-age structure of Eastem Cordillera (province of La Paz, Bolivia). Tectonics, 7, pp. 23-29.

Samson, P., and Mallet, J.L., 1997. Curvature analysis of triangulated surfaces in structural geology. Mathematical Geology, 29, pp. 391-412.

Sanders, C., Bonora, M., Richards, D., Kozlowski, E., Silwan, C., and Cohen, M., 2004. Kinematic structural restorations and discrete fracture modeling of a thrust trap: a case of study from the Tarija Basin, Argentina. Marine and Petroleum Geology, 21, pp. 845-855.

Sanguinetti M., Lúquez, J., and Clivio, J., 1998. Fracture Analysis of Paleozoic Sandstones in Ramos Field, Northwestern Argentina. AAPG International Conference & Exhibition, Rio de Janeiro, pp 492-493.

Schmidt, R.A., and Rossmanith, H.P., 1983. Basics of Fracture Mechanics. In Rock Fracture Mechanics, Rossmanith H.P. (ed.). Springer-Verlag, 477 p.

Segall, E., 1984. Formation and growth of extensional fracture sets. GSA Bulletin, 95, pp. 454-462.

Sempere,T ., Hérail, G., Olier, J., and Bonhomme, M.G., 1990. Late Oligocene-early Miocene major tectonic crisis and related basins in Bolivia, Geology 1, 8, pp. 946-949.

Starck, D., 1995. Silurian- Jurassic stratigraphy and basin evolution of Northwestern Argentina. In: A. J. Tankard. R. Suárez Soruco and H. J. Welsink (eds.): Petroleum basins of South America, American Association Petroleum Geologists, Memoir 62: 251-267.

Starck, D., 1999a. Los sistemas petroleros de la Cuenca de Tarija. IV Congreso de Exploración y Desarrollo de Hidrocarburos. Actas I, pp. 63-82.

Starck, D., 1999b. Evolución estratigráfica de la Cuenca de Tarija. Geología del Noroeste Argentino. XIV Congreso Geológico Argentino. G. Gonzáles Bonorino, R. Omarini, J. Viramonte (eds). I, pp. 227-234.

Starck, D., Gallardo, E., and Schulz, A., 1993. Neopaleozoic stratigraphy of the Sierras Subandinas Occidentales and Cordillera Oriental, Argentina. 12° International Congress Carboniferous-Permian. Comptes Rendus, 2, pp. 353-372.

Starck, D., Gallardo, E., and Schultz, A., 1992. La discordancia precarbónica en la porción argentina de la Cuenca de Tarija. Boletín de Informaciones Petroleras. Tercera época. 30, pp. 2-11.

Starck, D., Rodríguez, A., and Constantini, L., 2002a. Los Reservorios de las Formaciones Tupambi, Tarija, Los Monos y San Telmo. Rocas Reservorio de las Cuencas Productivas de la Argentina. V Congreso de Exploración y Desarrollo de Hidrocarburos. M. Schiuma, G. Hinterwimmer, G. Vergani (eds.). pp. 699-716.

Starck, D., Rodríguez A., and Constantini, L., 2002b. Análisis de algunos aspectos geométricos y evolutivos de las estructuras de la faja plegada subandina del norte de Argentina y el sur de Bolivia. V Congreso de Exploración y Desarrollo de Hidrocarburos. (Digital Acts).

Stearns, D. W., 1968, Certain aspects of fractures in naturally deformed rocks, in Riecker, R. E. (ed.), Rock mechanics seminar: Bedford, Terrestrial Sciences Laboratory, pp. 97–118.

Stewart, S. A., and Podolski, R., 1998. Curvature analysis of gridded surfaces. In: Coward, M. P., T. S. Daltaban, and H. Johnson (eds.). Structural Geology in Reservoir Characterization. Geological Society Special Publications 127, pp. 133-147.

Storvoll, V., Bjørlykke, V., and Mondol, N.H., 2005. Velocity depth trends in Mesozoic and Cenozoic sediments from the Norwegian Shelf. AAPG Bulletin, v. 89, p. 359–381.

Suárez Soruco, R. and Díaz Martínez, E., 1996. Léxico estratigráfico de Bolivia. 227 p.

Suppe, J., 1983. Geometry and kinematics of fault-bend folding. American Journal of Science 283, pp. 684–721.

Suppe, J., and Medwedeff, D.A., 1990. Geometry and kinematics of fault propagation folding. Eclogae Geologicae Helvetiae 83, pp. 409–454.

Swan, A. R. H. and M. Sandilands, 1995. Introduction to Geological Data Analysis. Blackwell Science, 446 p.

Tapia, E. J., 1985. Estudio de las sedimentitas neopaleozoicas en el rió Caraparí, Salta. Trabajo Final de Licenciatura, Facultad de Ciencias Exactas y Naturales, Universidad de Buenos Aires. Trabajo Final de Licenciatura.

Tomezzoli, R., 1992. Grupo Cuevo y referencias del Grupo Tacurú en las márgenes del río Bermejo (Dpto. de Orán, Salta. Dpto. de Tarija, Bolivia). Facultad de Ciencias Exactas y Naturales, Universidad de Buenos Aires. Trabajo Final de Licenciatura, 121 p.

Tomezzoli, R., 1996. Estratigrafía del Grupo Cuevo (Pérmico-Triásico Inferior) y del Grupo Tacurú (Jurásico) en las márgenes del río Bermejo (Orán, Salta y Tarija, Bolivia). Revista de la Asociación Geológica Argentina, 51 (1-4): 37-50.

Twiss, R. J., and Moores, E.M., 1992. Structural Gelogy. W. H. Freemand and Company, 532 p.

Vaamonde, D., 2002. La Formación Los Monos: Su Capacidad Como Roca Sello. V Congreso de Exploración y Desarrollo de Hidrocarburos. (digital acts).

Vistalli, M., 1999. Cuenca siluro-devónica. Geología del Noroeste Argentino. XIV Congreso Geológico Argentino. (Eds) G. Gonzáles Bonorino, R. Omarini, J. Viramonte. I, pp. 168-184.

Waite, M. E., Ge, S., Spetzler, H. A., 1999. A new conceptual model for fluid flow in discrete fractures: an experimental and numerical study. Journal of Geophysical Research 104 (B6), 13049–13059.

Warren, J.E., and Root, P.J., 1963. The behaviour of naturally fractured reservoir. SPE Journal, 9, pp. 245-255.

Welsink, H.J., Franco, A., and Oviedo G., 1995, Andean and pre-Andean deformation, Boomerang Hills area, Bolivia, in A. J. Tankard, R. Suárez S., and H. J. Welsink, Petroleum basins of South America: AAPG Memoir 62, pp. 481–499.

Zoback, M. L., and Zoback, M.D., 1980. State of stress in the conterminous United States. Journal of Geophysical Research, v. 85, No B11, pp. 6113-6156.

Vita

Juan Francisco Pedro Iñigo was born in Buenos Aires, Argentina, on April 28th, 1980, to Nicolas Iñigo Carrera and Adriana Laura Lesta. Juan graduated from the Facultad de Ciencias Exactas y Naturales of the Universidad de Buenos Aires in 2004, obtaining the degree of *Licenciado en Ciencias Geológicas*. In 2005 he joined the Department of Reserves Development in Pan American Energy, where he worked as a Structural Geologist for two years and a half. While working in Pan American Energy he pursued graduate studies, and in 2007 he obtained the degree of *Especialista en Ingenieria de Reservorio* from the Facultad de Ingenieria of the Universidad de Buenos Aires. In 2007 he obtained a Fulbright scholarship and became a student at the University of Texas at Austin to pursue his Master in Geological Sciences, with emphasis on natural fractured reservoirs.

Permanent address: Segurola 881, PB C, 1638 Vicente López, Buenos Aires, Argentina.
This thesis was typed by the author.